Influences of dynamic debris jams on a bridge pier

Zhang Wenjun

Thesis submitted in partial fulfillment of the requirements for the degree of

Doctorate in Philosophy Civil Engineering

Academic advisors: Prof. Ioan Nistor and Prof. Colin D. Rennie

University of Ottawa

Ottawa, Ontario, Canada

Abstract

Sediment material around the base of a bridge pier is moved by the flow velocity and associated turbulence. This phenomenon is generally termed as local scour and can lead to undermining the structure and increase its possibility of failure. Numerous factors can affect bridge pier scour and they have been investigated for decades. Debris jams, one of these factors, could significantly contribute to bridge failure as some field examples and experimental investigations pointed out. Woody debris accumulation on the front of either single or multiple bridge piers can result in deeper pier scour and extra load exerted on the pier. Several studies have already investigated the influence of woody debris on pier scour in terms of static woody debris. In addition, HEC-18 (2012) also proposed a design code to estimate scour depth in the presence of woody debris jam. However, in these studies, the woody debris jam was considered to be static, whereas a woody debris jam accumulates piece by piece, growing to a debris jam with a shape most akin to a half-cone, and then may even eventually break up and be carried in pieces downstream. Therefore, this research investigated the evolution of the loading onto and scouring around a bridge pier in the presence of dynamic debris jams.

In this study, the temporal evolution of the bridge pier scours was monitored during the development of dynamic debris jams. Experimental modeling was conducted to explore the influence of dynamic debris jam on bridge pier scour using a scale of 30 by employing both dowels and seedling trees. It was found that the dynamic debris jam of dowels could last 10-20 minutes and reach a critical size, then fail and subsequently reform. In addition, the first debris jam had an obvious influence on scour depth which correlated to the blockage generated by the debris jam; however, the influence of the subsequent debris jam depended on its size compared to the previously formed one. For the dynamic debris jam using seedling trees, the debris jam lasted for a longer time once it formed, and it could lead to twice the maximum scour depth compared to that generated in the absence of the debris jam, which is the same with dowels debris jam. In addition, the hydraulic head induced by the debris jam was correlated to the blockage of the debris jam and the flow Froude number irrespective of whether the dynamic debris jam was made of dowels or seedling trees.

Additionally, blank control tests in the absence of a debris jam were used along with previous data gleaned from the literature to develop and test new multigene genetic programming (MGGP) models for the temporal evolution of scour. The MGGP model, using the non-dimensional variables from the empirical equations, can reach a better accuracy than the empirical equations, which indicates the ability of the model to optimize the empirical equations.

The temporal evolution of load exerted onto the bridge pier with a dynamic debris jam was also measured. Experimental tests were performed to investigate the additional debris jam drag force exerted onto the bridge pier using both dowels and seedling trees in the presence of a fixed flume bed. Likewise, the dynamic debris jam of dowels lasted for about 10-20 mins, while those formed by the seedling trees, once formed, could last over 50 mins. The investigation demonstrated that the drag coefficient of the seedling trees jam was higher than that of the dowels jam. More importantly, a spike in the drag force was also observed irrespective of whether the jams were formed by dowels or seedling trees.

Detailed investigation of the flow field around the debris jam and pier provided insight into the mechanics of debris jams. Three half-cone-shaped debris jams of the same dimensions were designed and built. The three jams were fabricated using: a) 20 cm long dowels, b) 30 cm long dowels, or c) a 3D-printer. For each jam, four sections were measured using an Acoustic Doppler Velocimeter (ADV). The results indicated that the flow fields around the 20 cm length dowel jam and the 30 cm length dowel jam were similar. In

addition, the section behind the pier and debris jam showed divided zones termed herein as the accelerated high-velocity zone, the high shear transition zone, and the wake dead zone. As for the drag coefficient, the 20 cm length dowels jam and 30 cm length dowels jam shared a very close magnitude of 1.7, but the drag coefficient of the 3D printer debris jam was only 0.88 which indicated the debris jam built by individual pieces behaved differently than the block jam.

Acknowledgments

I want to thank my supervisors Prof. Ioan Nistor and Prof. Colin D. Rennie, who graciously provided me with endless help and give me a wonderful Ph.D. experience. I still remember the day when Prof. Nistor in Beijing interviewed and encouraged me to pursue a Ph.D. with him and continuously supported me to finish my thesis, while also providing me with life suggestions. I also clearly remember the heavily rainy day when Prof. Rennie brought the seedling trees for me to do experiments, and he always nicely responded to anything that I was confused about and needed. Many of those days, I am grateful for, what occurred during this period, that offered me the courage and persistence to be, what I was not able to be before, although I acknowledge that I still need to have more work to do.

I would like to thank the people who helped me a lot with my experimental work. Mr. Mark Lapointe, the technician of the hydraulic lab, tried his best to satisfy the demands of my experiments. I appreciated Mr. Leo Denner who also helped me a lot in my experiments. I also would like to thank the friends I met in Ottawa, Cao Huade, and Yan Xiaohui always provided me with some suggestions during my time of worry. Christopher Valela, Dario Sirianni, and Kate Neigel offered me significant help with my experiments.

I would like to express my gratitude to my parents who brought me into this world. As a second child in my family, my parents managed to provide me with educational opportunities, but they gave me a happy childhood in our rural village through their companionship. It's hard to imagine that I could have come this far without their countless selfless acts of support.

Lastly, I would also like to acknowledge the China Scholarship Council and the University of Ottawa for supporting my studies which provided me with the opportunity to study in Canada and pursued my Ph.D. at the University of Ottawa. Additionally, I want to appreciate the support of the fund of NSERC Discovery Grants of Profs. Nistor and Rennie for my studies.

Table of Contents

List of Figures

List of Tables

List of Acronyms

ADV Acoustic Doppler Velocimeter

AHRS High-precision high-reliability attitude and referencing system

AI Artificial intelligence

ANN Artificial Neural networks

AI Artificial Intelligence

3D Three-dimensional

DAQ Data acquisition system

DES Detached eddy simulation

GP Genetic Programming

GEP Gene Expression Programming

RANS Reynolds-Average Naiver-Stokes

RS Reynold shear stress

LES Large eddy simulation

SFM Structure from motion

MGGP Multigene genetic programming

MLR multiple linear regression

PSR Poisson Surface Reconstruction

PIV Particle image velocimetry

URANS Unsteady Reynolds-Average Navier-Stokes

US Ultrasonic wave sensor

WLR Weighted linear regression

List of Symbols

ΔA =Blockage ratio by the projected vertical area of debris jam (-)
ΔA^* =Blockage ratio by the horizontal plan area of debris jam (-)
A_w = Area of wetted debris based on the upstream surface elevation projected normal to the flow direction (m^2)
A_c = unobstructed cross-sectional flow in the contracted section (m^2)
A_0= Area of primary vortex (m^2)
A_t= Area of the developed vortex at any time t (m^2)
A_{vc} = the projected area of debris accumulation into the flow (m^2)
A_d = the increased projected area due to debris jam $A_d = A_{vc} - h_d D_p$
A_p = the horizon plane area of debris accumulation into the flow (m^2)
A_{hu} = Area of the vertically projected, submerged portion of the debris accumulation below the upstream water surface(m^2)
A_{hd} = Area of vertically projected debris jam submerged in the downstream(m^2)
$\Delta\tilde{A}$=Percentage rough blockage ratio
B = the blockage ratio caused only by the debris jam (-)
b = Width of flume(m)
b_d^* = effective width of a pier (m)
b_p = width of pier perpendicular to flow (m)
B_d = the breadth of debris dam (m)
C_d= Coefficient of drag (-)
C = a hydrodynamic mass coefficient (-)
c_w = Concentration of wood (-)
C_D = the coefficient of depth (-)
C_B = the blockage coefficient (-)
C_{str} = the coefficient of the building structure (-)
C_I = the impact coefficient (-)
C_o = the orientation coefficient (-)
D_{ep} = Effective width or diameter of the pier(m)
D_{e*} = Effective sediment size for particle level (m)
D_v = Primary vortex diameter (m)
D_p =Width or diameter of the pier(m)
D_d = Average debris log/pieces diameter (m)
d_{50} =Median size distribution of particles(mm)
d_s = Scour depth in the presence of woody debris jam at time t (m)
d_{s0} = Scour depth without the presence of debris jam at time t (m)
d_{se} =Equilibrium scour depth (m)
d_{sp} =Predicted scour depth at time t (m)
d_{eu} =Effective sediment size (m)

F_r =Froude number (-)

F_d = particle Froude number (-)

F_i = the impact force at the Stillwater elevation (N)

F_{df} = drag force (N)

$F_{d\beta}$ =Densiometric particle Froude number (-)

f =Coefficient of proportionality (-)

g =Gravitational acceleration (m s^{-2})

Δh = Debris-induced hydraulic head (m)

Δh_h =Difference in water surface elevation between the front ultrasonic distance sensor and the posterior one in the presence of woody debris (m)

Δh_{nh} =Difference of water surface elevation between the front ultrasonic distance sensor and the posterior one without woody debris (m)

Δh_u = Upstream head increase (m)

h =Approach flow depth (m)

h_d = Height of woody debris jam from the bottom of debris jam to the water surface (m)

h_d^* = the effective height of the debris jam (thickness) (m)

h_{cu} =vertical distance from the upstream water surface to the centroid of area (m)

h_{cd} = vertical distance from the downstream (m)

l_d =Length of woody debris jam in streamwise direction (m)

L_R = Reference length (m)

K_1, K_2= Coefficients of pier nose; correction factor (-)

K_3 = correction for bed condition (-)

K_d =Influence of debris jam on scour d_s/d_{s0} (-)

K_{d1} =for initial woody debris jam (-)

K_{d2} =for the subsequent woody debris jam (-)

K_{d1max} = the maximum value of K_d in the first woody debris jam (-)

K_σ, K_v = Parameters for Chang et al (2004) (-)

K_s = Streamwise diffusion coefficient (-)

K_n = Transverse diffusion coefficient (-)

K_θ = Angular diffusion coefficient (-)

k_E = the effective stiffness of debris (-)

k = turbulent kinetic energy (-)

k_s = Bed roughness (m)

P =the pressure

Q_{so} =Discharge of sediment transported out of scour hole (m^3 s^{-1})

R_e = Reynold number (-)

R_d = Blockage ratio in percentage (%)

R_{max} = the maximum response ratio assuming the approximate natural period

S =Flume slope (-)

s =Sediment relative density (-)

t = Time moment (s)

t_e =Time for equilibrium scour depth (s)
t_r =a reference time defined (s)
T_s = Transport-stage parameter (-)
t_o =Dimensionless time parameter in Oliveto and Hager (2002) (-)
t_A =Dimensionless time parameter in Aksoy et al. 2017 (-)
T^* = Non-dimensional time relative debris accumulated area (-)
Δt =Duration of impact(s)
$\tau_{p,t}$ = Bed shear stress (kg m^2 s^{-2})
τ_w = Water flow shear stress
N_S =Shape number, 1 for a circular pier and 1.5 for an abutment (-)
m = the weight of debris element (kg)
N = Number of moments to account for the error (-)
n = Manning's roughness coefficient (-)
n_1 = the 0.79 for rectangular debris, 0.21 for triangular debris (-)
w_d =Width of woody debris jam normal to flow (m)
U =Mean velocity of approach flow (m s^{-1})
U_d = the velocity of debris (m s^{-1})
$U_{d\max}$ = the maximum velocity of flow containing debris
u_* =Shear velocity (m s^{-1})
u_c =Critical mean flow velocity for sediment entrainment (m s^{-1})
u_i =the velocity component in the according directions
u_i' =the fluctuate velocity in the according directions; y_{mi} =measured value (-)
y_{pi} =predicted value (-)
$\overline{y}_m$ =mean measured value (-)
$\overline{y}_p$ =mean predicted value (-)
α =0.79 for rectangular debris and 0.21 for triangular debris (-)
β =-0.79 for rectangular debris and -0.17 for triangular debris, while β =0 when $l_d/h \leq 1.0$ (-)
χ =Parameter 0.32 or 3.2 (-)
κ =von Karman constant (0.41) (-)
σ =Sediment gradation (-)
λ =Scale factor (-)
ε = Coefficient to connect parameter K_d the first or previous woody debris jam, averaging close to 1.0 (-)
w = Rate of flow work (-)
ω_w = Angular velocity of wood (rad s^{-1})
w_f = fall velocity of sand (m s^{-1})
δ_w = Orientation of a log
v_w = Wood linear velocity (m s^{-1})
∅ = Sediment repose angle (°)

Δ = s-1 (-)

ρ_s = Density of sand (kg m^{-3})

ν =Kinematic viscosity (m^2 s^{-1})

ρ =fluid density (kg m^{-3})

ρ_d =fluid density (kg m^{-3})

δ_{ij} = Kronecker delta (-)

Chapter 1. Introduction

Wood logs or debris play an important role in river systems, and the appearance of debris also adversely influences infrastructure. Studies related to woody debris have involved many aspects such as the process of debris entering the river (Mazzorana et al. 2011; Mazzorana et al. 2009), debris volume estimation (Comiti et al. 2016; Gurnell et al. 2002; Tonon et al. 2018) and the influence on river morphologies (Klaar et al. 2011). The dynamics of wood debris involve the entrainment (Braudrick and Grant 2000), motion (Braudrick et al. 1997), and deposition (Braudrick and Grant 2001) processes. Gravity and buoyancy forces, drag force and friction force determine the movement of logs in the river, and the critical conditions are studied (Bocchiola et al. 2006; Braudrick and Grant 2000; Chen et al. 2019; Crosato et al. 2013; Haga et al. 2002). The transport process of debris is another important issue that determines for how long the debris can travel (Braudrick et al. 1997) and where it might stop (Davidson et al. 2015), and a model has also been proposed to describe the transport of woody debris (Persi et al. 2018). Woody debris can also increase the risk to infrastructure as Ruiz-Villanueva et al. (2014) indicated for a mountain village. In addition, the presence of debris significantly increases the possibility of bridge failures (Bradley et al. (2005).

Floods can be considered an important trigger that leads to the failure of a bridge, especially a flood scour as (Arneson et al. 2012) indicated that 23 bridge failures with a $15 million estimated cost occurred in the upper Mississippi basin in 1993. However, the report of (Diehl 1997) was also indicated that the debris accumulation around the pier of the bridge contributed to over one-third of bridge failures in the United States and regarded as one of the leading causes that link to bridge failures(Lyn et al. 2007). The risk of bridge failure could be significantly increased due to the accumulation of debris around the pier, Examples of accumulated wood debris around bridge piers are shown in Figure 1-1.

Figure 1-1(a) SRT view of the downstream railway bridge (Lyn et al. 2007) (b) large wood accumulations during the 2005 flood in Switzerland (Schalko 2018)

Woody drifts and debris captured by bridge piers advected from the upstream result in the formation of woody debris jams. The presence of woody debris jams leads to the reduction of cross-sectional area and strengthens downward flow close to the pier, which enhances the scour process at the base of bridge piers and causes greater scour depth (Pagliara and Carnacina 2013). In addition, woody debris jams can also result in an extra load on the bridge pier; thus, the presence of woody debris jams affects the stability of bridges and threaten their safety. Some failure examples are mentioned in Pagliara and Carnacina (2011a) and (Bradley et al. 2005)

The presence of debris could lead to an irregular flow pattern around the pier, which could exacerbate scour in front of the pier, thus there is increasing research to understand the influence of debris jams on bridge pier loading and scour.

1.1 Objectives

Woody debris jams on bridge piers have been drawing more research focus because they threaten the stability and safety of bridges, which complicates protecting bridges from potential failures. A comprehensive experimental and numerical investigation into woody debris jams on bridge piers was performed, which considered the dynamics of woody debris jam evolution during flood events. The specific objectives are as follows.

1. The influence of the evolution of woody debris jam on single bridge pier scour. Physical modeling was conducted to investigate scour depth while releasing woody debris to form a woody debris jam. The evolution of scour depth with and without the presence of woody debris was compared. In addition, two types of woody debris pieces (dowels and seedling trees) were applied to distinguish the difference between idealized and realistic model debris.
2. The evolution of woody debris jam load on a single bridge pier. Physical modeling was applied to investigate the time history of the force load on the pier during the evolution of the woody debris jam. In addition, seedling trees were used to simulate real woody debris.
3. The flow field in the presence of woody debris jam around the bridge pier. Understanding the flow field is necessary and fundamental to investigate the influence of woody debris jam and the mechanism of the effects of woody debris jam.
4. Application of artificial intelligence (AI) tools in the hydraulic field. The powerful AI tool is considered to have broad prospects. A Multigene genetic programming algorithm is applied to develop a temporal evolution scour depth model and evaluated by the experiment data.

1.2 Scope

The objective of this thesis focuses on the influence of debris jam on bridge pier scour and induced load as well as the flow field, and debris jam formed by dowels and seedling trees applied to simulate the formation process. Physical modeling was applied to accomplish the objectives. However, this thesis also has several limitations due to the resources and lab time.

- All experiment tests for scour depth lasted for one hour, and this did not reach the equilibrium scour stage which was typically over 5 hours. As the dynamic debris jam was applied, the debris pieces were manually released one by one which made it difficult to last for a long time as well as the battery limitation of the GoPro camera.
- The formation of debris jams continuously occurred as the distance of releasing position to the pier was not very long. However, the wood debris was transported by the river flow and might move for a very long distance in the field, and the debris piece might take a longer time and be not continuous.
- The debris jam built by dowels for flow field measurement was not that similar to a real debris jam. A wood frame was built and put the dowels inside, and steel wires and nails were used to fix the dowels to improve the stability of the structure. However, the porosity of the resulting debris jam was nonuniform.
- Numerical modeling was not applied in this thesis, but TELEMAC 3D and Open Foam were both tried to simulate the influence of woody debris jam. However, TELEMAC 3D did not

reliably reproduce the horseshoe vortex during scour prediction, and Open Foam had no reliable solver for sediment transport.

There were various scenarios in the field, and it might be hard to incorporate every detail in the lab experiments, so this thesis mainly focused on the influence of a continuously increasing dynamic debris jam within the limitation of lab instruments.

1.3 Contributions and Novelty of the Study

This thesis was pioneered to work on the dynamic debris jam on scour and load, and the contributions and the novelty of this thesis lie in 1) introducing the time scale for the development of debris jam, 2) firstly using MGGP to develop the model of temporal evolution scour depth, 3) firstly applying the seedling trees to represent debris, and 4) measurement of the flow field around a half-cone debris jam.

Multigene genetic programming is first applied to develop a new model for temporal evolution scour depth at a single bridge pier. The application of the algorithm in the hydraulic field is valid to be helpful and convenient to optimize the exiting models.

Dynamic debris jams were created by releasing debris upstream, which could be considered as introducing a time scale to the development of debris jams. In contrast, in previous studies, a whole block was imposed instantaneously, and its dimensions were independent of the flow condition. Even though some previous studies moved forward to using debris pieces to build a debris jam, the debris jam was still pre-set. This type of debris jam is defined herein as the static debris jam, and it is deemed to be less representative of real debris jams than dynamic debris jams.

Seedling trees were first applied to represent the debris in several of the present lab experiments. Dowels were previously used as the debris pieces, but some studies (Lyn et al. 2003; Panici and Almeida 2020) pointed out that it might not be that reasonable as debris jams formed by natural debris have a less regular shape, which influences local flow conditions. As such, seedling trees were directly used herein to represent natural debris, and it was found that debris jams formed from seedlings presented different characteristics compared to the dowels.

Half-cone debris jams were built for the flow field measurement. A half-cone frame was made from dowels and dowels were put inside the frame; this provided an approach to building a woody debris jam. The flow field around the dowel debris jam can provide insight view of the mechanism of how the debris jam affects the bridge pier. A 3D printer-built debris jam with the same size as the frame is used to represent static debris jams in recent studies, and this helps to figure out the difference between a realistic debris jam and an ideal debris jam.

1.4 Publications

1.4.1 Journal Articles

1) Zhang, W., Nistor, I., Rennie, C. D., and Almansour, H. (2022). "Influence of Dynamic Woody Debris Jam on Single Bridge Pier Scour and Induced Hydraulic Head." Journal of Marine Science and Engineering, 10(10), 1421. (https://www.mdpi.com/2077-1312/10/10/1421) (Thesis: Chapter 4)

2) Zhang, W., Rennie, C. D., Nistor, I. (2022). “A new model developed by MGGP for the temporal evolution of bridge pier scour” Journal of Canadian Civil Engineering. [Accepted] (Thesis: Chapter 3)

3) Zhang, W., Nistor, I., Rennie, C. D. (2022). “Temporal evolution of the hydrodynamic loading due to dynamic debris jam on bridge pier” Journal of Fluids and Structures. [In review] (Thesis: Chapter 5)

4) Zhang, W., Nistor, I., Rennie, C. D. (2022). “Influence of debris jam formed by trees on bridge pier scour” Journal of Hydraulic Engineering [In review] (Thesis: Chapter 6)

5) Zhang, W., Rennie, C. D., Nistor, I. (2022). “Experimental investigation of the hydrodynamic field around a debris jam on a bridge pier” Journal of Hydraulic Research [In review] (Thesis: Chapter 7)

1.4.2 Conference Proceedings

1) Zhang, W., Nistor, I., Rennie, C. D., and Almansour, H. (2022) “Pier debris jam dynamics and associated scour” 39th IAHR World Congress, Granada City, Spain

1.5 Outline of the Thesis

In order to complete the objectives outlined in section 1.2, several physical experiments were conducted to examine the time histories of bridge pier scour and pier loading in the presence of dynamic debris jams. Additional experiments were performed to elucidate the flow field in the presence of a debris jam. This thesis was organized into the following chapters:

- Chapter 2 provides a comprehensive literature review related to the topic of woody debris in terms of scour depth, loading, and flow field as well as numerical simulation. The comprehensive literature review summarizes current studies on woody debris jam and states the problem and research needs for the woody debris jam.
- Chapter 3 develops a new model by introducing multigene genetic programming (MGGP) to predict the temporal evolution of bridge pier scour depth. This MGGP model is trained by the data collected from previous studies and new lab experiments conducted at uOttawa. A new function is derived for the prediction which demonstrates the application of the algorithm.
- Chapter 4 investigates the influence of dynamic debris jam formed by dowels on bridge pier scour depth, based on physical modeling conducted at uOttawa. This study indicates that dynamic debris jams formed by dowels might involve several peaks including the formation, growth, failure, and rebirth of individual debris jams. In addition, it is also pointed out the first debris jam peak has a significant influence on the development of scour depth in clearwater scour conditions.
- Chapter 5 works on monitoring the temporal evolution of loads caused by the dynamic debris jams comprised of either dowels or seedling trees. The dynamic debris jams formed by seedling trees and dowels have different characteristics: dowel jams lasted for a shorter time while the seedling tree jams seldom failed once formed. A spike phenomenon was also observed and the load caused by debris jam might increase drastically in a short time.
- Chapter 6 examines the influence of dynamic seedling tree jams on scour depth and compares these results to scour induced by dynamic dowel jams. A laser scanner was also applied to obtain the bed elevation, and it indicated that the scour depth could increase 2 times in the presence of dynamic debris jam while the volume of scour hole might increase 8 times.
- Chapter 7 provides the measurements of the flow field around half-cone debris jams. Woody debris jam was framed by woody dowels of a certain size and put dowels inside the frame, and 3D printed debris jam was built in the same size Flow field around the three debris jams as well Reynold shear stress, integral time scale, turbulence kinematic energy, and vortices were obtained by the Acoustic Doppler Velocimeter **(**ADV) measurement.
- Chapter 8 further reviews the design codes for the woody debris jam based on the present experimental data.
- Chapter 9 summarizes the thesis on the topic of the woody debris jam and its influence on scour depth, loads, and flow field respectively.

Chapter 2. Literature Review

2.1 Woody debris

Before 1975, few studies focused on woody debris or drift in rivers, but since then more and more research has evaluated its influences on river systems in terms of hydraulics of flow, transfer of sediment and organic material, and geomorphological effects (Gurnell et al. 2002). Woody debris enters the river system and is advected by the river flow. It has been observed that woody debris can accumulate in front of both single or multiple bridge piers, and this could increase the load on the bridge and lead to higher scour depth (Lyn et al. 2003). The presence of woody debris jams in river systems threatens the stability and safety of bridges.

According to the field investigation of (Bradley et al. 2005), the classification of debris is as follows: (1) very small buoyant debris or no debris, the debris can be ignored; (2) small floating debris: that might include small limbs or, orchard pruning, tulles, leaves, and refuse, which come from trees and other vegetation that are introduced into a stream due to bank erosion, are easily transported by the stream and overland flow; (3) medium floating debris, it mainly contains trees limbs or large sticks which can accumulate at both culvert or bridge structures; (4) large floating debris, which consists logs or trees or drifts. Once these debris pieces are introduced into a stream during flood events, a jam might form due to a collection of debris. The size of the jam highly depends on the type of vegetation within the watershed and the channel characteristics transporting the material. Debris jamming is a significant problem at bridge structures due to its size, shape, and facility for entrapment on bridge piers, and it might include fine detritus, coarse detritus, boulders, flowing debris, and ice debris. Thus, several types of debris jams are formed like underflow jams, dam jams, deflector jams, and parallel jams defined and modified in Wallerstein and Thorne (1997) as shown in Figure 2-1.

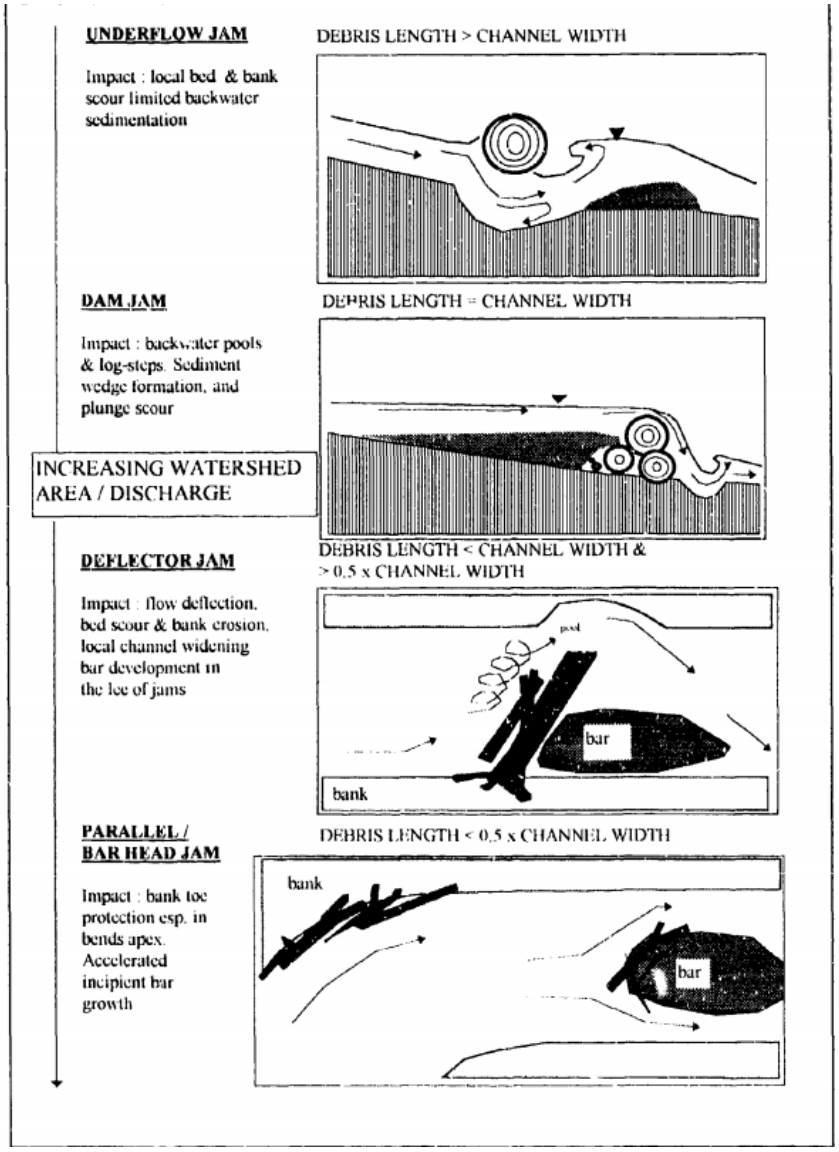

Figure 2-1 Debris Jam Classification Model (Wallerstein and Thorne 1997)

The evaluation method of debris accumulation should consider the potential for debris delivery to the site, the debris accumulation potential on an individual bridge element (as shown in Table *2-1*), and hypothetical accumulations for the entire bridge.

Table 2-1 Determining potential debris accumulation on a single pier (Bradley et al. 2005)

Accumulation Potential	Pier type	Location Category	Potential for Debris Delivery
Low	-	Sheltered	-
	Solid Pier	Bank/Floodplain	-
	Solid Pier	In the Channel	Low
	Piers w/ Openings	Bank/Floodplain	Low
Medium	Solid Pier	In the Channel	High
	Solid Pier	In the Path	Low
	Piers w/ Openings	Bank/Floodplain	High
	Piers w/ Openings	In the Channel	Low
High	Solid Pier	In the Path	High
	Piers w/ Openings	In the Path	Low
	Piers w/ Openings	In the Channel	High
High, Chronic	Piers w/ Openings	In the Path	High

In laboratory tests, two types of woody debris jam were used to simulate the woody debris jam. Firstly, a static woody debris jam means that the woody debris jam is simulated by a solid block with constant dimensions which are independent of the flow condition. This has been applied in the studies (Claps 2018; Ebrahimi et al. 2018; Lagasse et al. 2010; Pagliara and Carnacina 2011; Pagliara 2010) as shown in Figure 2-2. However, this type of woody debris jam does not realistically represent the formation and growth process of the debris jam, the ultimate size and shape of the debris jam, and the influence on the local flow field.

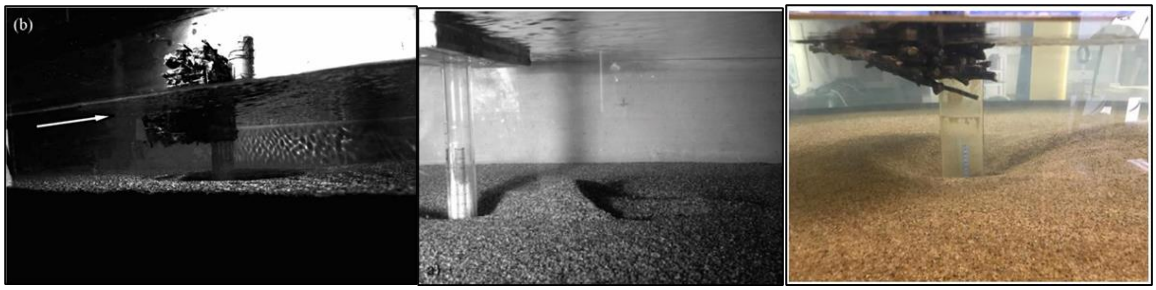

(a) (b) (c)

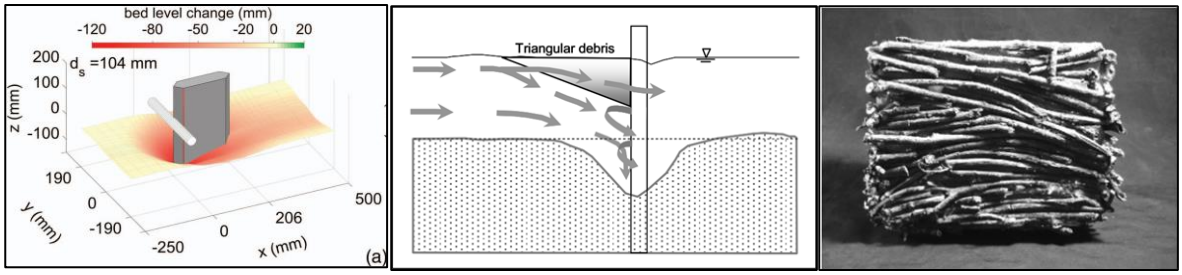

(d) (e) (f)

Figure 2-2 Static block debris (a)(Pagliara 2010) (b) (Pagliara and Carnacina 2011) (c) (Claps 2018)(d) (Ebrahimi et al. 2018) (e) (Lagasse et al. 2010) (f) (Pagliara and Carnacina 2013)

Dynamic (space- and time-evolving) woody debris jams have been recently used to simulate woody debris, and this type of woody debris jam was formed by releasing individual debris pieces. The woody debris flowed with water and accumulated in front of the bridge pier. Panici and de Almeida (2018)

investigated the maximum dimensions of woody debris jam in front of a bridge pier in terms of the characteristics of debris pieces and flow conditions. Schalko et al. (2019) released wood dowels to represent debris pieces to investigate the accumulation probability of congested or semi-congested jams. In addition, realistic debris was also applied to investigate the backwater rise due to woody debris jam (Schalko et al. 2018). Additionally, structure from motion (SFM) has been applied to directly capture the volume and porosity of a woody debris jam, and this technology was able to generate a high-quality point cloud and mesh model of a woody debris jam by the screened Poisson Surface Reconstruction (PSR) technique (Spreitzer et al. 2020) (Figure 2-3).

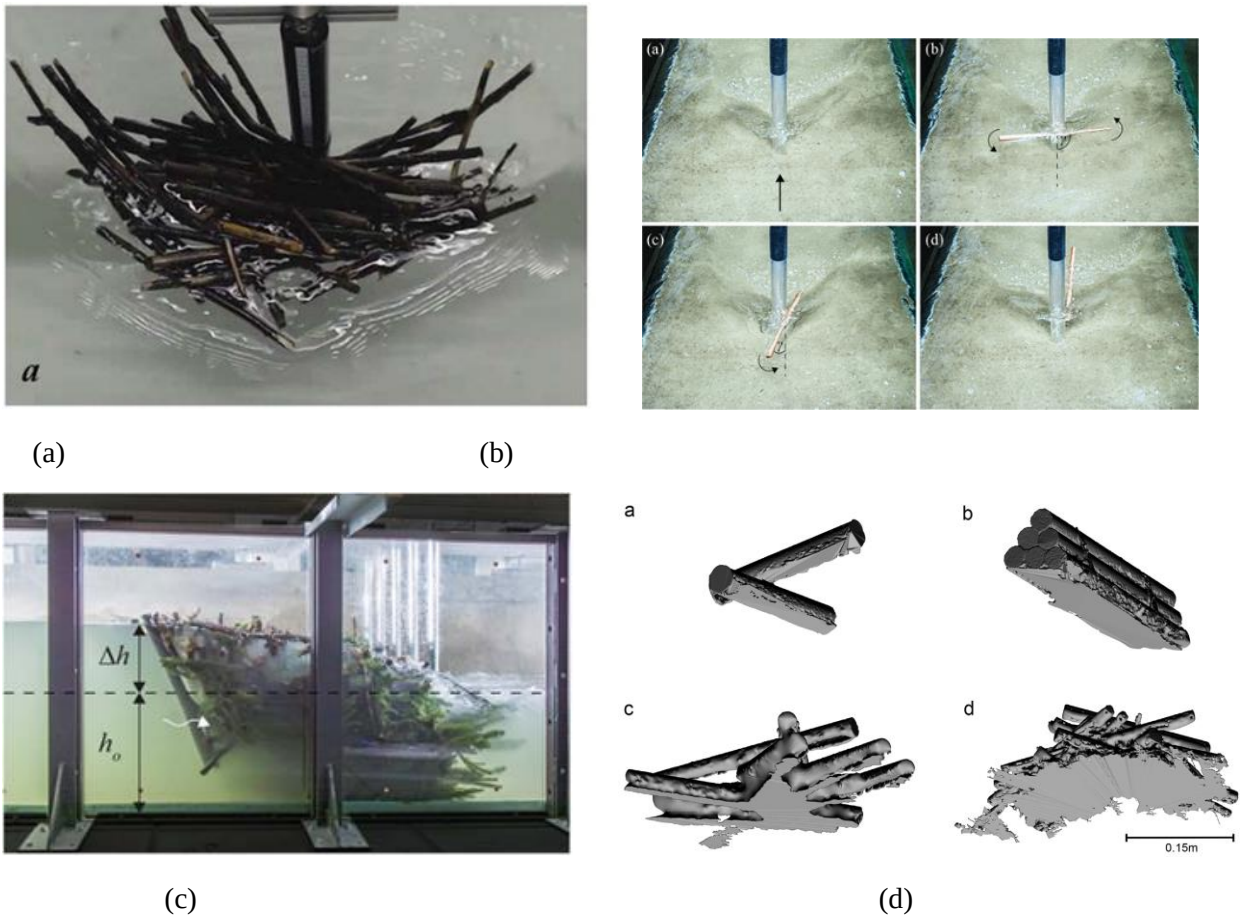

Figure 2-3 Dynamic debris (a) (Panici and de Almeida 2018), (b) (Schalko et al. 2019), (c) (Schalko et al. 2018), (d) (Spreitzer et al. 2020)

2.2 Woody debris and scouring

2.2.1 Scour process

Flow pattern dominates the process of scour, and the system of vortices especially horseshoe vortices have been long recognized as the basic mechanism of scour. Given the significance of flow patterns on scour, many researchers have investigated the eddy structure or vortices system. The pressure field induced by flow around the pier is considered to initiate a three-dimensional separation flow to form the horseshoe-vortex system, and the vortex filaments including the horseshoe vortex extend downstream with increased rotational velocities in the vortex core (Breusers et al. 1977). In addition, Breusers et al. (1977) cited the content of Melville and Raudkivi (1977) to explain the process that there is a strong vertically downward

flow developed in front of the cylinder as the scour hole enlarged. In these studies, downward flow and horseshoe vortex were considered to contribute to the development of scour, but the detailed mechanism for downward flow was not clear.

Dargahi (1989) investigated the dynamics of the vortex system around the cylinder, the mutual interaction of the horseshoe and wake vortices, and the characteristics of flow separation. The vortex system was described in detail for the first time at Reynold number 39,000, and the downward flow at the stagnation face led to the generation of the vortex system according to the kinematic laws of vortex behavior. More importantly, the pressure distribution along the stagnation line was measured and pointed to the existence of a pressure gradient which is caused by the non-uniform velocity distribution of approaching flow. In addition, the pressure gradient resulted in the formation of the first vortex. Ahmed and Rajaratnam (1998) also conducted a detailed experiment to understand the flow around bridge piers by examining the frontal downflow while considering the effects of bed roughness and the presence of scour holes. Pressure distribution upstream in front of the pier was measured; pressure was greater at higher levels and diminished gradually at lower levels, and there was a slight pressure increase near the bottom of the scour hole due to the downward flow hitting the bottom. In addition, the results showed that the bed roughness caused a steeper pressure gradient and resulted in stronger downflow in front of the cylinder, and Clauser's defect-type scheme described the velocity distribution better than either the log-law or the defect law. More importantly, the downflow velocity in front of the pier achieved 95% of the approach velocity inside a scour hole, while the maximum downflow in the absence of a scour hole was just approximately 35% of the approach velocity.

Although some uncertainties may remain regarding the detailed mechanics of vortex formation, there is general agreement that the presence of a pier leads to downflow and generation of a horseshoe vortex. Water flowing towards the pier is turned downward and a stagnation pressure is generated along the front of the pier. A pressure gradient forms due to the stagnation pressure that decreases with water depth, causing the increase of the water surface called a bore wave (Figure 2-4). Meanwhile, a horseshoe vortex system is also generated around the base of the pier, which transports sediment particles downstream. Erosion occurs due to the removal of sediment around the pier, and the scour hole develops corresponding to an increasing horseshoe vortex (Graf and Istiarto 2002; Graf and Yulistiyanto 1998; Manes and Brocchini 2015; Melville and Raudkivi 1977).

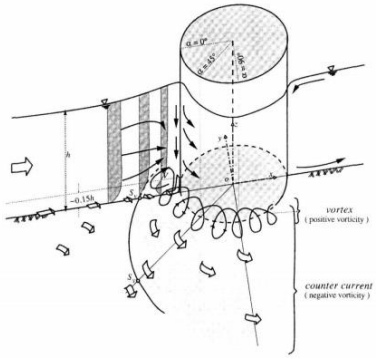

Figure 2-4 Scheme of the horseshoe-vortex system(Graf and Yulistiyanto 1998)

The horseshoe vortex system was widely accepted to illustrate the mechanism of scouring due to the presence of a bridge pier. Dargahi (1990) further investigated the mechanism of scour and the vortices system and showed that scour occurred through the combined actions of several vortices. This study argued that the rate of scouring at the side of the cylinder was much faster than in front of the cylinder (Figure

2-5a). Similarly, Hager (2007) investigated the evolution of scour hole and the development of the horseshoe vortex and clearly showed that downward flow occurred in the front of the cylinder (Figure 2-5 b). Scour developed rapidly in the initial stage, and a circulation flow was generated in the scour hole which means the vortices system formed. In addition, the strength or size of the circulation flow increased with time, and it finally achieved an equilibrium state, in agreement with the observations of Melville and Raudkivi (1977).

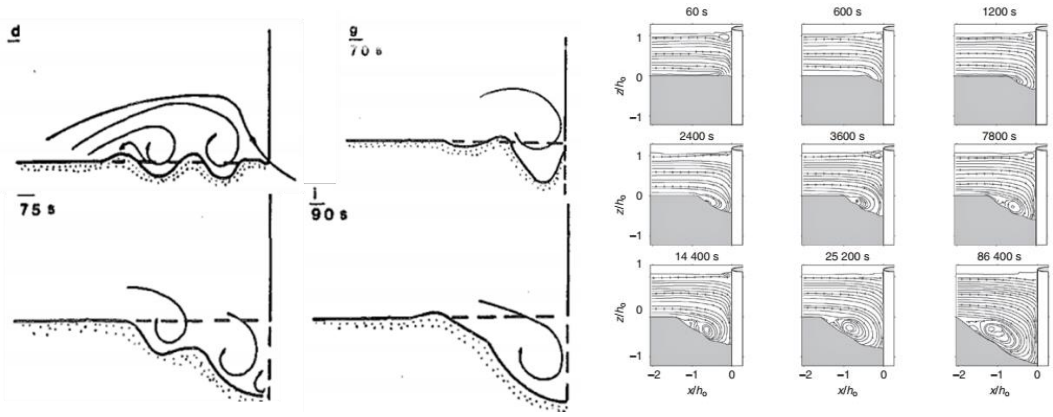

(a) evolution of scour (Dargahi 1990) (b) evolution of scour (Hager 2007)

Figure 2-5 Sketch of the scouring process

Bed shear stress has been used to describe the commencement of scour and to forecast the development of scour. Melville and Raudkivi (1977) studied the bed shear stress distribution upstream of the cylinder, and the maximum value of normalized shear stress was observed in front of the cylinder where the scouring occurred on the initial flatbed. In addition, erosion occurred below the rim of the scour hole which was formed by the circulation of downward flow, and this caused irregular sand avalanche collapses of the scour hole wall. The horseshoe vortex forced material up the slope and into the flow, which carried the sediment to the wake region. (Figure 2-6) It also should be noted that the bed shear stress in the equilibrium condition was generally smaller than that in the intermediate state, and this implied that the equilibrium condition was achieved by the combined effect of the temporal mean shear stress, the weight component and the turbulent agitation which everywhere added up to the local threshold condition for sediment transport. Finally, it also indicated that there is a tendency for the bed shear stress to be larger where the turbulence intensity is smaller and vice-versa.

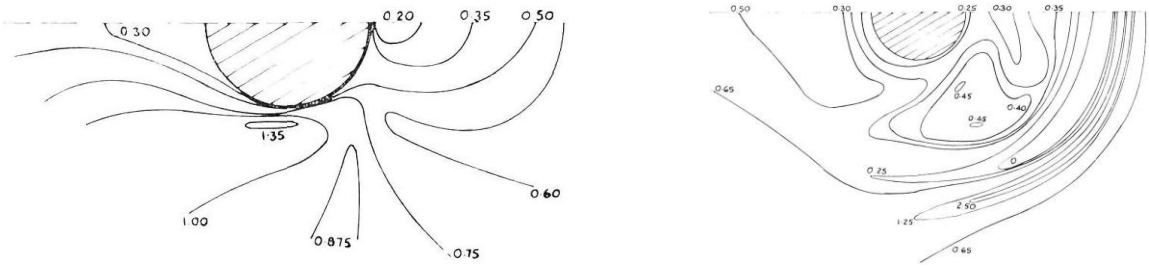

Figure 2-6 Bed shear stress contours normalized with respect to local slope adjusted critical threshold shear stresses on the initial flatbed (a) and the final equilibrium scour hole (b) surfaces(Melville and Raudkivi 1977)

Graf and Istiarto (2002) considered three methods to estimate the bed shear stress and measured the bed shear stress in the upstream and downstream of the cylinder in the symmetry plane. The measurements indicated that the bed shear stress upstream was slightly larger than that downstream (Figure 2-7), as was also observed by (Graf and Yulistiyanto 1998). Otherwise, the critical bed shear stress was not achieved along the scour hole, and shear stress returned to the same magnitude as the one upstream of the scour hole. It also should be noticed that the bed shear stress decreased considerably in the scour hole compared with its value outside the scour hole upstream.

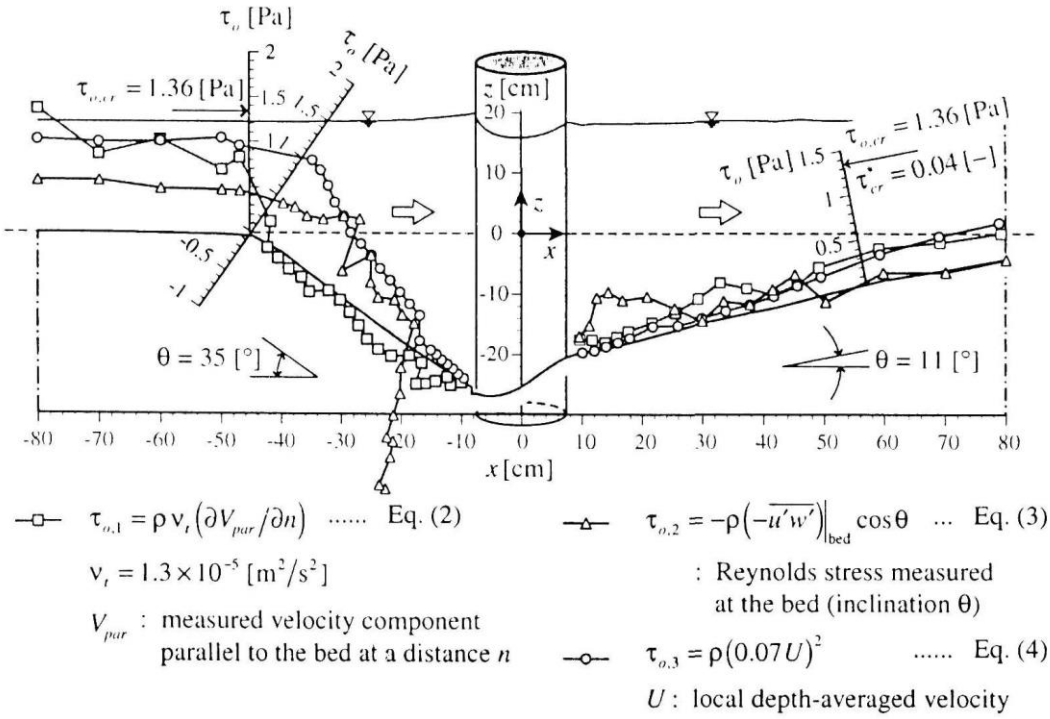

Figure 2-7 Estimated bed-shear stress in the plane upstream and downstream of a cylinder (Graf and Istiarto 2002).

Dey and Raikar (2007) investigated the temporal evolution of bed shear stress at different azimuthal planes and showed that the bed shear stress increased radially away from the pier achieving the maximum value in the middle portion of the scour hole, and its value then decreased and returned to the value on the flatbed (Figure 2-8). It also should be noticed that the magnitude of bed shear stress increased from the initial state and then reached its maximum state in the intermediate scour hole ($d_s = 0.5d_{se}$). Here d_s was the developing scour depth, and d_{se} was the scour depth at the equilibrium state. Finally, the bed shear stress in the symmetry plane at equilibrium scour was lower than critical shear stress, which coordinated with the previous studies, but this was not the case at other planes indicating a discrepancy between the measurement and estimated critical shear stress.

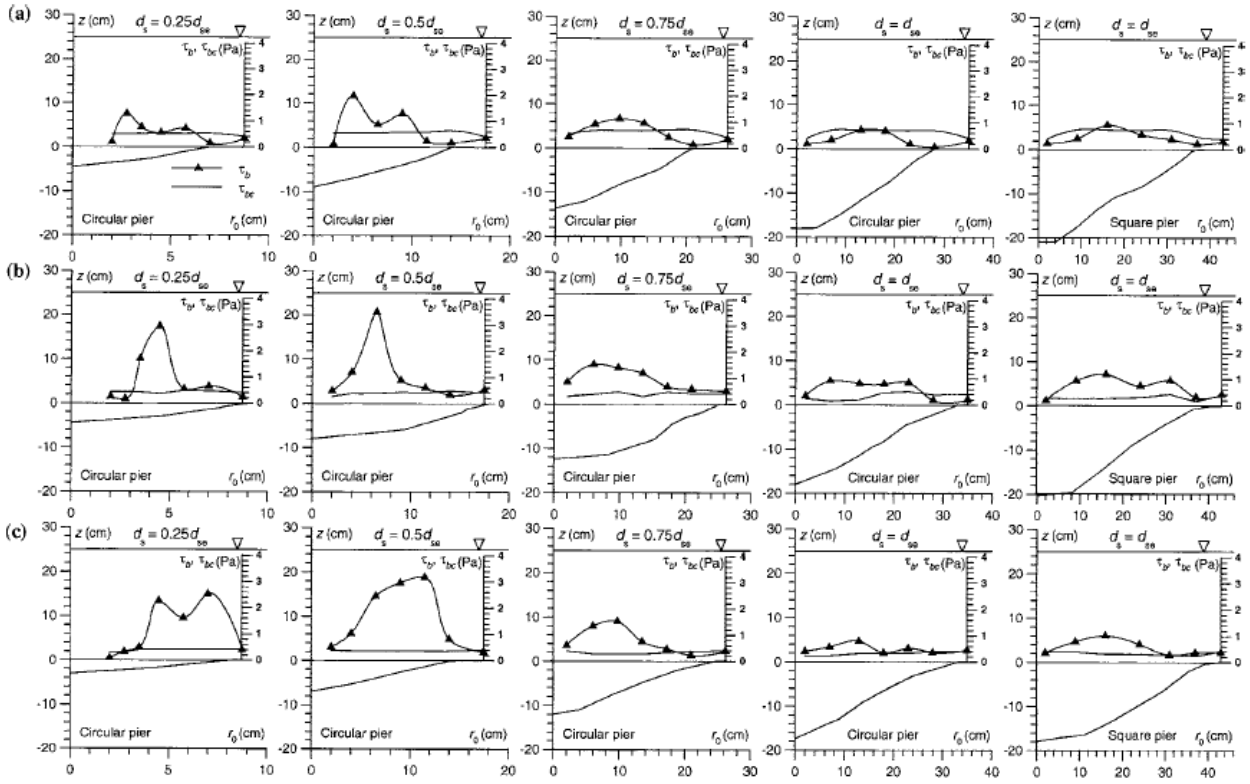

Figure 2-8 Distributions of bed shear stress and (in Pa) at azimuthal planes: (a) symmetry upstream (b) 45 degrees from the symmetry (c) 90 degrees from the symmetry (Dey and Raikar 2007)

In sum, strong downflow forms due to the stagnation pressure along the front of piers, which results in the development of horseshoe vortices around the base of the pier. The vortex system around the pier initiates a scour hole. As the scour hole enlarges, the size and circulation of the horseshoe vortex increase rapidly, and the velocity close to the bottom of the hole diminishes. The magnitude of the downflow appears to be directly associated with the rate of scour. The rate of increase of circulation diminishes as the scour hole develops and reaches a constant value at the equilibrium stage. The temporal bed shear stress and turbulence at the bed also contribute to the scour rate and tend to decrease as the scour hole enlarges until an equilibrium is achieved. Given the assumptions and observations above, Kothyari et al. (1992a) first proposed a method to calculate the temporal evolution of scour depth, and further improved models have been developed by (Dey 1999; Lu et al. 2011; Mia and Nago 2003)

2.2.2 Scour without debris

Analytical approaches for the temporal evolution of scour can be classified into three groups developed from (i) the sediment pick-up model; (ii) the horseshoe vortex model; and the (iii) the effective flow work model. According to sediment pick-up models, scour at a bridge pier is a sediment entrainment or bedload issue, but accompanied by a more complex flow condition. Yanmaz and Altinbilek (1991) proposed a semi-empirical model to predict the temporal evolution of scour depth around circular or square piers based on the sediment continuity equation, and the sediment pick-up function was introduced into the analysis of sediment entrainment around the pier.

According to the sediment continuity equation, the rate of volume change in the scour hole equates to the difference between the inflow and outflow of sediment at the scour hole. Clear-water scour was investigated in Yanmaz and Altinbilek (1991)'s study, so sediment carried into scour hole was ignored.

Dey (1999) acknowledged this perspective and further developed the model to be applied to live bed scour as well as non-uniform sediment. On the other hand, the sediment pick-up function adopted in Dey's derivation was based on van Rijn (1984)'s semi-empirical function and was formulated as

$$E = 0.00033\rho_s \left(\Delta g D_e\right)^{0.5} D_{*e}^{0.3} T_s^{1.5} \tag{2-1}$$

where E=the rate of sediment pick-up by scour; Δ=s-1; g=gravitation acceleration; D_e=effective sediment size; D_{e*}=effective sediment size for particle level; T_s= dimensionless of shear stress; s=sediment relative density.

It should be noted that the shape of the scour hole in the sediment pick-up model is assumed to be unchanged with time, so the volume of the scour hole could be obtained by the integral method. In addition, Yanmaz (2006) further improved the model based on Equation ((2-1)) to obtain a new function to compute the temporal evolution of scour depth. Yilmaz et al. (2017) extended this approach to dual bridge pier scours, and a model was proposed to calculate the time-dependent scour depth. Moreover, Yanmaz and Kose (2009) developed a model to calculate the temporal scour depth development at the base of the abutment based on this method.

In horseshoe vortex models for scouring, the horseshoe vortex system is considered to dominate the process of scour development, because the vortex system significantly affects the bed shear stress. (Kothyari et al. 1992a; Kothyari et al. 1992b) investigated the influence of uniform or non-uniform sediment and stratification on scour depth, and a model was proposed to calculate the scour depth, which was based on horseshoe vortex theory. The diameter of the primary vortex was assumed to be related to pier diameter and flow depth and was expressed as

$$\frac{D_v}{h} = 0.28\left(\frac{D_p}{h}\right)^{0.85} \tag{2-2}$$

where D_v=primary vortex diameter; h=flow depth in upstream.

Otherwise, the bed shear stress at the nose of the pier is assumed to be related to flow shear stress and the ratio of cross-section area between the primary vortex A_0 and developed vortex A_t, the expression is shown as

$$\tau_{p,t} = 4.0\tau_w\left(\frac{A_0}{A_t}\right)^{0.57} \tag{2-3}$$

where $\tau_{p,t}$=bed shear stress; τ_w=water flow shear stress; A_0= the area of the primary initial vortex; A_t= the area of developed (enlarged) vortex at any time t; t=time.

Since the bed shear stress decreases with the development of scouring, the removal of sediment around a pier base reduces, finally reaching an equilibrium scour depth. Mia and Nago (2003) continued this idea and further produced a model to calculate time-dependent scour depth, with the assumption that the scours hole shape remained unchanged with time. Kothyari and Kumar (2010) experimentally investigated the influence of sediment size on scour depth and further improved the horseshoe model though modifying the method to determine the value of the parameter. Lu et al. (2011) focused on the temporal variation of scour depth for a nonuniform circular pier, and the scour hole was divided into three zones. A model was further derived from Mia and Nago's model to compute scour depth with respect to different stages of scour development for the nonuniform pier.

Transport work rate was introduced by Bagnold (1966) to quantify sediment transport, and Lai et al. (2009) continued this idea to establish the relation between Γ-shaped hydrograph and equivalent scour duration. Based on the ratio of flow work and bed shear stress, the effective flow work on scoured sediment was assumed to be a function of flow intensity. Specifically, they used the flow intensity over the threshold value of flow intensity for sediment entrainment. Link et al. (2017) further developed the effective flow work model and adopted the referenced velocity to calculate the effective flow work.

Many studies have been conducted for scouring and found that temporal scour development is significantly influenced by flow intensity, pier size, sediment material, and so on. Several researchers have used multiple regression methods to build the relation to temporal scour depth, and the functions for temporal scour are shown in Table 2-2.

Table 2-2 Empirical functions to predict time-dependent scour depth

Researchers	Formulas	No.
Franzetti et al. (1982)	$\frac{d_s}{d_{se}} = 1 - \exp\left[-0.028\left(\frac{Ut}{D_p}\right)^{1/3}\right]$	(2-4)
Melville and Chiew (1999)	$\frac{d_s}{d_{se}} = \exp\left\{-0.03\left\lvert\frac{u_c}{U}\log\left(\frac{t}{t_e}\right)\right\rvert^{1.6}\right\}$	(2-5)
Oliveto and Hager (2002)	$\frac{d_s}{L_R} = 0.068\sigma^{-0.5} N_S F_d^{1.5} \log(T_o)$	(2-6)
Chang et al (2004)	$d_s = \begin{cases} 0.08K_\sigma K_\nu T_c^{-1.3} T & 0 \le t/t_e \le T_c \\ d_{se} - 0.27K_\sigma K_\nu \left(T^{-0.3} - 0.41\right) & T_c \le t/t_e \le 0.04 \\ d_{se} - 1.1K_\sigma K_\nu \left(T - 2.22T^{-0.45} + 1.22\right) & 0.04_c \le t/t_e \le 1 \end{cases}$	(2-7)
Kothyari et al. (2007)	$\frac{d_s}{L_R} = 0.272\sigma^{-0.5}\left(F_d - F_{d\beta}\right)^{2/3} \log(t_o)$	(2-8)
Aksoy et al. (2017)	$\frac{d_s}{D_p} = 0.8\left(\frac{U}{u_c}\right)^{1.5}\left(\frac{h}{D_p}\right)^{0.15}\left(\log t_A\right)^{0.6}$	(2-9)

where d_s= the temporal scour depth at time t; t_e=time for equilibrium scour depth in the study (Melville and Chiew 1999); d_{se}=equilibrium scour depth in the study(Melville and Chiew 1999) ; u_c=critical mean flow velocity for sediment entrainment; u_*=bed shear veloicty; L_R= a reference length, and equal to $\left(D_p h^2\right)^{1/3}$ for pier; t_o is the dimensionless time scale and equal to $\left\{t\left[\sqrt{d_{50}g(\rho_s-\rho_w)/\rho_w}/L_R\right]\right\}$; N_S=a shape number, 1 for circular pier and 1.25 for abutment; F_d is the densiometric particle Froude number equal to $\left\{U/\sqrt{d_{50}g(\rho_s-\rho_w)/\rho_w}\right\}$; $F_{d\beta}$ =Densiometric particle Froude number; K_σ =factor for adjusting sediment gradation; K_ν= the factor for adjusting flow intensity; d_{sec}=equilibrium scour depth of uniform sediment in the study (Chang et al. 2004); $t_c = [d_{sec}/(0.35K_\nu K_\sigma) - 0.31]^{-3.33}$ and ρ_s=density of sand, ρ_w=the water density; t_A = the dimensionless time scale and equal to $\left\{td_{50}\left[\sqrt{(\rho_s-\rho_w)/\rho_w g d_{50}}/D_p^2\right]\right\}$

Ettema (1980) investigated in detail the influence of nondimensional parameters on the development of scour depth, and a logarithmic function was proposed to describe the temporal scour depth. Shear velocity, sediment size, and pier size were considered to quantify the development of scour depth, as well as two empirical parameters that were determined by fitting experimental data. Franzetti et al. (1982) also conducted several experiments to obtain deep insight into the temporal scour depth and an exponential function for circular piers was derived to express the influence of duration on scour depth. Whitehouse (1997) further developed a similar exponential form of the formula to describe the temporal development of scour depth. Melville and Chiew (1999) systematically investigated the influences of several factors such as flow intensity, approach depth, and sediment size on scour depth and the time to reach equilibrium scour depth t_e was introduced to predict the time-dependent depth. In addition, the formula Melville (1997) used to predict the equilibrium scour depth was necessarily used to finish the calculation as well as the time to develop equilibrium scour depth. Oliveto and Hager (2002) studied the resistance force of piers on fluid flow and proposed an empirical function to predict the temporal evolution of scour depth based on hydraulic analogy by introducing Froude similarity, and it also should be noted that this method was further validated and developed by (Hager and Unger 2010; López et al. 2006; Oliveto and Hager 2005). Chang et al. (2004) thought that there was a critical sediment size corresponding to the equilibrium scour depth under the critical state, and a complex process was produced to calculate the equilibrium scour depth as well as the time required to develop into an equilibrium state. Moreover, this method could also apply to unsteady flow conditions. López et al. (2014) focused on the unsteady flow condition since the discharge of floods varies with time, and a new function was proposed to predict temporal scour depth based on the approach of (Oliveto and Hager 2002).

2.2.3 Scour process with the presence of debris

Scour hole depth in the presence of accumulated debris could be another problem of concern. As it has been discussed above, scour depth could significantly increase with the presence of accumulation debris. Thus, how to estimate the scour depth in the presence of accumulation debris could be an important problem. At present, the idea of the effective diameter of the pier is widely accepted and applied. An effective diameter pier was proposed by (Melville and Dongol 1992):

$$D_e = \frac{h_d^* D_d + \left(h - h_d^*\right) D_p}{h} \tag{2-10}$$

where D_e = the effective pier diameter; D_d = the diameter of debris jam; h_d^* = the effective height of the debris jam (thickness); and $h_d^* = 0.52h_d$; h_d = the height (thickness) of debris jam in the vertical plane.

By accounting for the accumulated debris by augmenting the pier diameter, functions for bridge pier scours without accumulation debris may be used to predict the scour depth. However, according to the research of (Pagliara and Carnacina 2011b), the accuracy of Meville's method was not good (Figure 2-9). Thus, a new parameter was created to quantify the influence of accumulation debris. The presence of both accumulation debris and the bridge pier could affect the area of the cross-section, thus Pagliara and Carnacina's theory considers blockage effects. Their proposed function for the influence of accumulation debris on blockage ratio R_d was:

$$R_d = \frac{\left(l_d - D_p\right) h_d}{h w_d} \cdot 100\% \tag{2-11}$$

where l_d = the length of debris in the direction of flow; h_d = the height (thickness) of debris jam in the vertical plane; w_d = the width of debris;

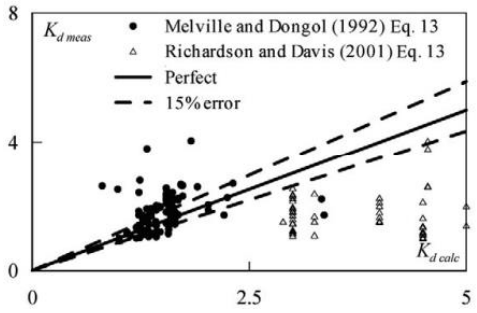

Figure 2-9 (Melville and Dongol 1992) design procedure (R^2=0.26 RMSE=0.048), and Richardson and Davis (2001) (RMSE=0.3)

Lagasse et al. (2010) continued this idea and further investigated the different geometry (rectangular and triangular) of debris and further developed Equation (2-10) to predict the influence of debris jam on scour depth:

$$D_{ep} = \frac{\alpha h_d w_d (l_d/h)^{\beta} - (h - \alpha h_d) D_p}{h} \tag{2-12}$$

where α = 0.79 for rectangular debris and 0.21 for triangular debris; β = −0.79 for rectangular debris and −0.17 for triangular debris for $l_d/h > 1$, and β = 0 when $l_d/h \leq 1$; l_d = the length of the woody debris jam.

In addition, a function for time-dependent equilibrium scour depth was proposed (Pagliara and Carnacina 2010):

$$\frac{d_s}{D_p} = \left(0.1868 \frac{U}{u_c} \cdot \Delta\tilde{A}^{0.4} - 0.1254\right) \ln\left(\frac{T^*}{10}\right) \tag{2-13}$$

where T^* = non-dimensional time relative debris accumulated area; $\Delta\tilde{A}$ = the percentage rough blockage ratio $\Delta\tilde{A} = \left(w_d - D_p\right) \cdot \left(h_d + D_d\right) \big/ \left(b \cdot h\right) \times 100$; D_d =average debris log diameter

Debris size and shape could also have a significant influence on scour depth. Ebrahimi et al. (2018) investigated the debris-induced scour around a sharp nose pier with the presence of different debris geometries like cylinder, half-pyramid, and plate in different flow conditions (Figure 2-10).

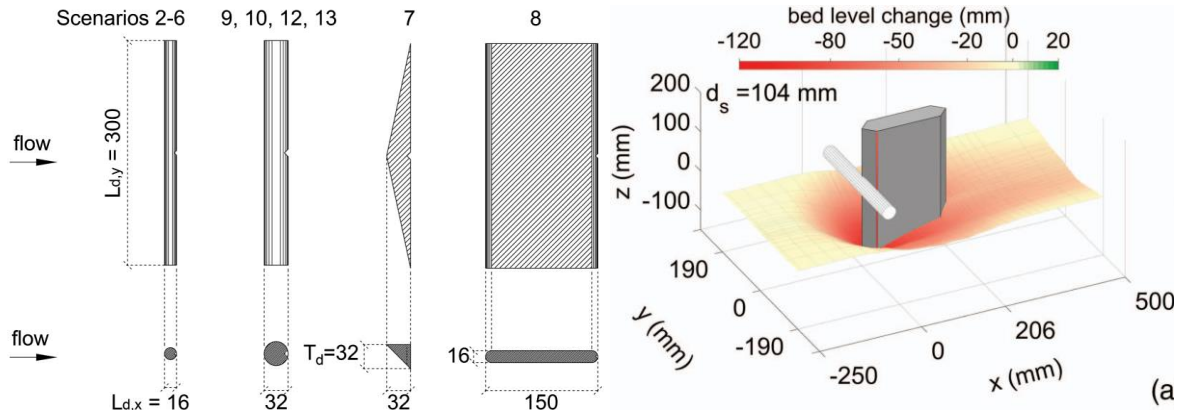

Figure 2-10 (a) Debris shape and size (b) Scour contour map (Ebrahimi et al. 2018)

The presented results indicated that the constant dimension debris will induce higher scour depth due to the increase of (horizontally and vertically) velocity and bed shear stress as the flow area reduces. Similarly, a larger height of debris (thicker) will increase the scour depth. On the other hand, inverted-pyramid debris causes smaller scour depth as the blockage ratio is smaller, which indicates the influence of debris geometry on scour. More importantly, this paper also explained the scour process:

"At the beginning of the experiments, the onset of scour was observed at the upstream nose of the pier, possibly due to the presence of a horseshoe vortex. However, as the scour progressed, downflow at the pier base was forced into the scour hole by the three-dimensional vortex generated by flow separation from the bed at the upstream edge of scour hole (Dey et al. 1995). This caused scour to quickly propagate downstream where vortex shedding from the two upstream lateral corners of the pier would further increase scour depth." (Ebrahimi et al. 2018). This indicated that downflow is caused by stagnation pressure, and it will be stronger in the presence of debris due to the reduction of flow area. Scour is initiated by the horseshoe vortices, and downflow enters the scour hole due to the effects of the three-dimensional vortices induced by the edge of the scour hole. Downflow loosens and lifts sediment particles, and the horseshoe vortices or shedding vortexes carry the sediment downstream.

It should be noted that the studies mentioned above are focusing on static debris in front of the pier, but it is not realistic due to the dynamic accumulation process of debris. Panici and de Almeida (2018) investigated the maximum size of debris accumulation considering the flow condition and debris characteristics (Figure 2-11) and demonstrated that higher velocity lead to a smaller debris jam size due to break-up or dislodgement of accumulations. This indicated the complexity of realistic debris jam formation and raised the question as to how long the debris jam could last and whether or not it would achieve an equilibrium or steady state. Actually, the debris jam could increase or decrease at any time which means the debris is time-dependent. Another question is how the debris jam was initiated and increased. Given this, Schalko et al. (2019) investigated the accumulation probability of debris to estimate the occurrence of debris jams, and Panici and de Almeida (2020) proposed a complicated and theoretical method to judge the formation and removal conditions of debris jams, but it involved too many parameters and complicated calculation process to get the results, which made it difficult to apply. Finally, (Panici and Kripakaran 2021) developed a novel debris retention system. These recent studies demonstrate the complexity of the debris accumulation process in a dynamic debris jam, which should similarly complicate the process of pier scour. However, the time history of pier scour in the presence of a dynamic debris jam remains to be investigated.

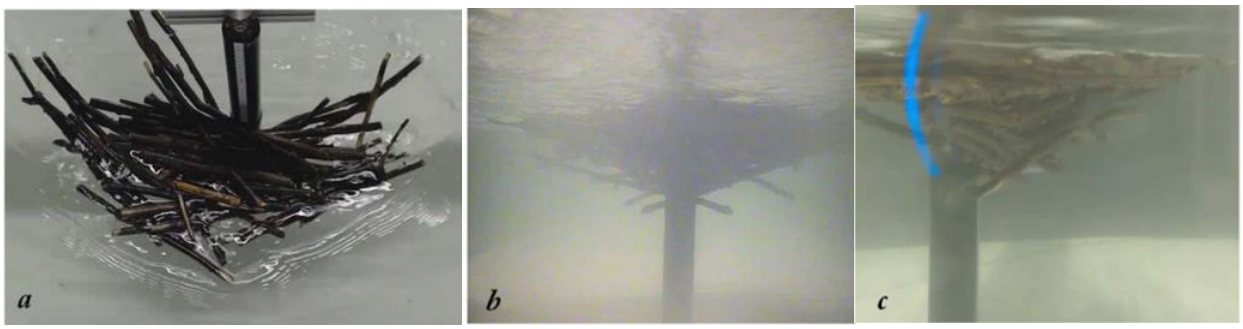

Figure 2-11 Typical accumulation shape during the stable phase for a nonuniform size debris test (debris length = 500 mm, D_p = 50 mm, U = 0.411 m/s resulting in λ = 10, and F_{rL} = 0.186). Images were captured at the same instant from (a) the top camera, (b) the underwater camera located downstream from the pier, and (c) the side camera (Panici and de Almeida 2018)

2.3 Woody debris and its load

Debris could significantly enhance the destruction caused by extreme flow events such as tsunamis or floods, and it has been focused on for a long time in coastal and hydraulic fields. A major 8.8 magnitude (Richter scale) earthquake occurred along the Pacific coast of Chile on 27 February 2010, and it was much more destructive due to the addition of debris (Figure 2-12). This event clarified that the impacts of debris should be carefully considered during tsunamis.

Figure 2-12 Tsunami damage due to the February 2010 Chile Tsunami. (Nistor and Palermo 2015)

Debris may also appear in a river channel, and this woody debris could form a debris jam in front of a bridge pier. Debris accumulation around the pier of a bridge could be an extra factor that links to the failure of the bridge (Bradley et al. 2005) and massive damage to civil properties. The first described woody debris disaster during a flood event occurred in the European Alps (Figure 2-13). Huge debris accumulation is considered one of the most destructive regional events, resulting in bridge obstructions which cause inundation and avulsions.

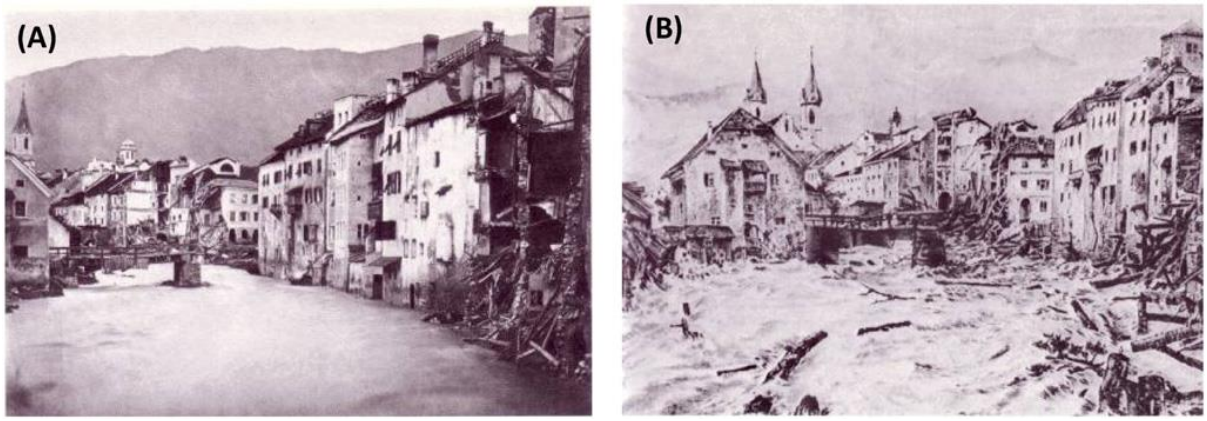

Figure 2-13 The Rienz River within the city of Bruneck/Brunico (south Tyrol, Italian Alps) was photographed after the large 1882 flood (A) and portrayed during the event (B). The painter included many floating logs in the flow, based on reports of local witnesses. (Comiti et al. 2016)

Hydraulic bores as a result of tsunamis or dam-release floods can induce extreme loads, sometimes with sufficient force to overturn concrete buildings (Nistor et al. 2017). Flood events with the company of debris including woody logs could significantly increase the power of these disasters which results in more severe damages. Thus, properly considering the effects of debris in flood events is necessary, including the development of associated codes for infrastructure design and construction.

Debris load threatens the safety of infrastructure during extreme flood events. Currently, the load due to debris has been poorly investigated especially for fluvial channels, but the load of debris in transient conditions has been studied. In addition, loads of debris are generally categorized into debris impact and debris damming (Yeh et al. 2014). Nistor et al. (2017) applied smart debris with a novel non-intrusive real-time tracking system and motion sensor to look at the dynamic path of debris entrained by a tsunami-like bore (Figure 2-14).

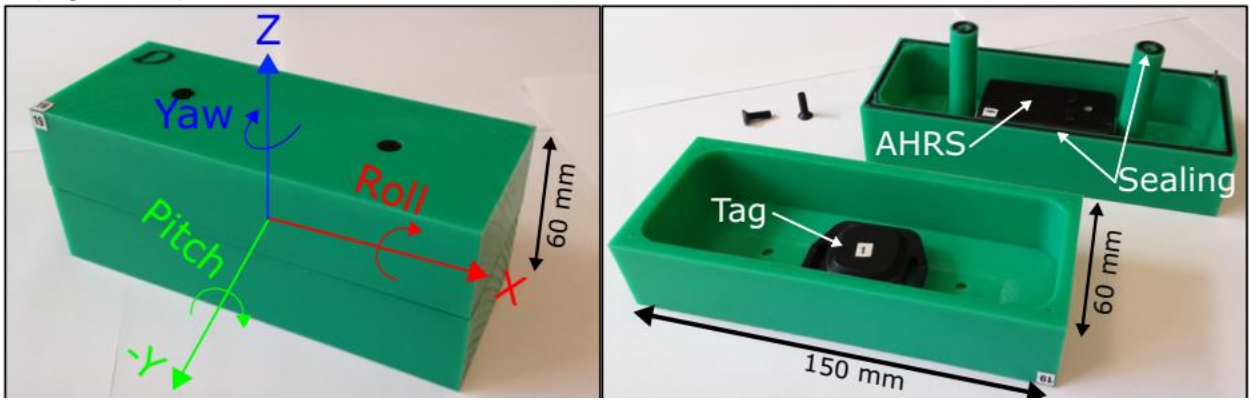

Figure 2-14 Downscaled 6.1-m (20-ft) shipping container model used as debris (Note: Tag = Quuppa locating tag; AHRS = high-precision high-reliability attitude and referencing system) (Nistor et al. 2017)

Derschum et al. (2018) also applied a smart debris scale to a shipping container (1:40) to investigate the impact and hydrodynamic force imposed on a rectangular structure in transient hydraulic conditions. The hydrodynamic force was extracted from the debris impact (Figure 2-15a), and the results also found that the debris impact velocity was about 63% of the wavefront velocity measured in the test. In addition, the debris was not able to reach the velocity of the bore wavefront, and a delay was observed between the wave and debris impacting the structure. On the other hand, an assumed linear centroid and observed centroid for the approach trajectory of debris were evaluated and turned out to be approximate, (Figure 2-15b), and the initial orientation of debris position was found not to have a significant influence on debris impact.

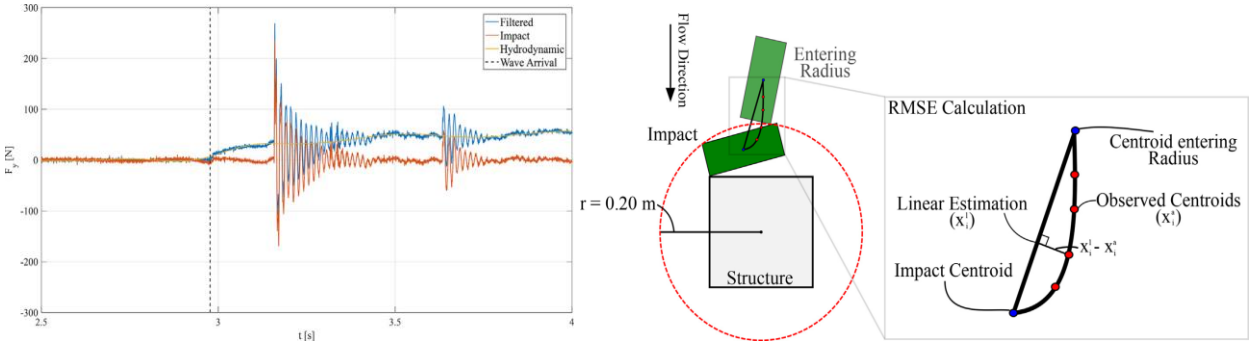

Figure 2-15 (a) Impact load filtering. The total force measured by the LC compared to the impact and hydrodynamic forces;(b) Definition of the RMSE. The comparison of the actual debris centroid positions with an assumed linear approach trajectory (Derschum et al. 2018)

Stolle et al. (2018a) also applied the smart debris in a tsunami-like bore to check the transport path of debris and compared with the results of (Naito et al. 2014), which claimed that lines ±22.5º from the centerline would be affected by debris, and the results showed that the range of debris was found to be consistent with the conclusion of Naito et al. 2014's study though a probability analysis.

Similarly, Spreitzer et al. (2019) also applied smart wood to test the movement behavior of large wood and assessed the effectiveness of the sensor. Further, Stolle et al. (2018b) investigated the damming load due to debris imposed to an obstacle in transient supercritical flow conditions; the load evolution with time was shown in Figure 2-16. Three types of debris (shipping container, board, and hydro pole) were applied. The shipping containers were easily captured and formed a debris jam in front of the ramp. In addition, the resistance coefficient for the three types of debris was consistent and related to Reynolds and Froude number.

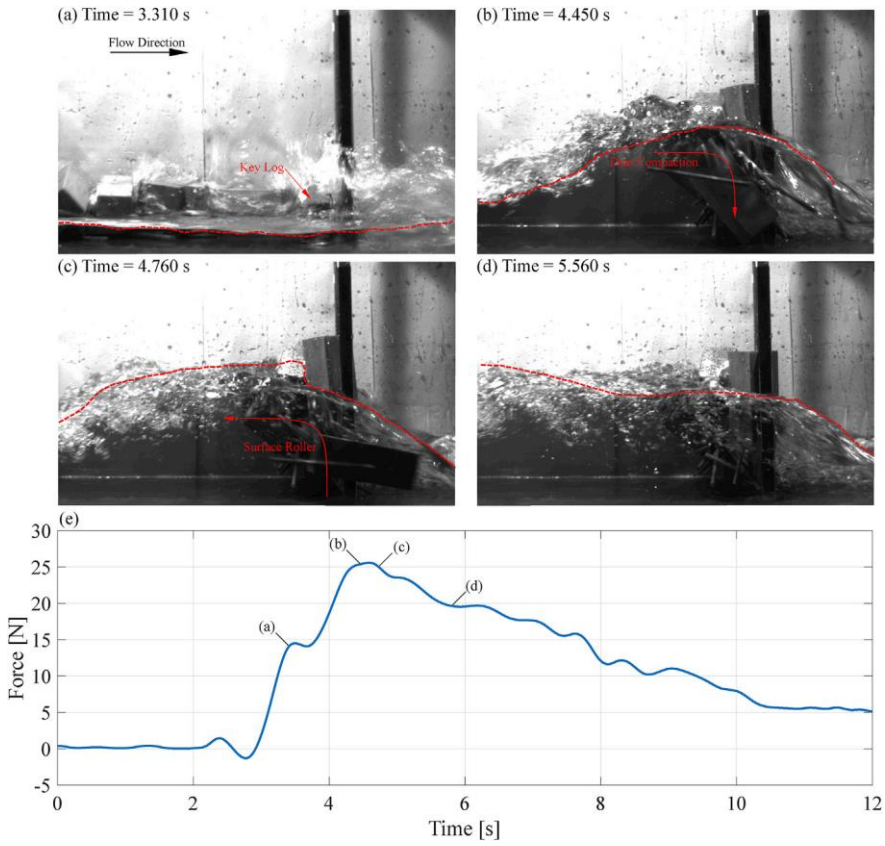

Figure 2-16 Debris dam formation for the case with 9 SC, 81 HP, 20 B, and 0.40 m impoundment depth. Panels (a)–(d) show still images from the HS at various key points. The red dashed line is marking the water's surface elevation. Panel (e) shows the force-time history for the experiment, the times corresponding to the above images are indicated within the figure (Stolle et al. 2018b)

For steady flow conditions, Mauti et al. (2020) applied an idealized debris dam with different heights, shapes, and porosities to test the damming load (Figure 2-17). The results showed that the force acting on a pier due to a debris dam was positively related to the dam height and Froude number and negatively to dam porosity. On the other hand, Panici and de Almeida (2018) also applied woody debris to investigate the drag force due to debris accumulation, and the drag coefficient was evaluated to be close to 1.

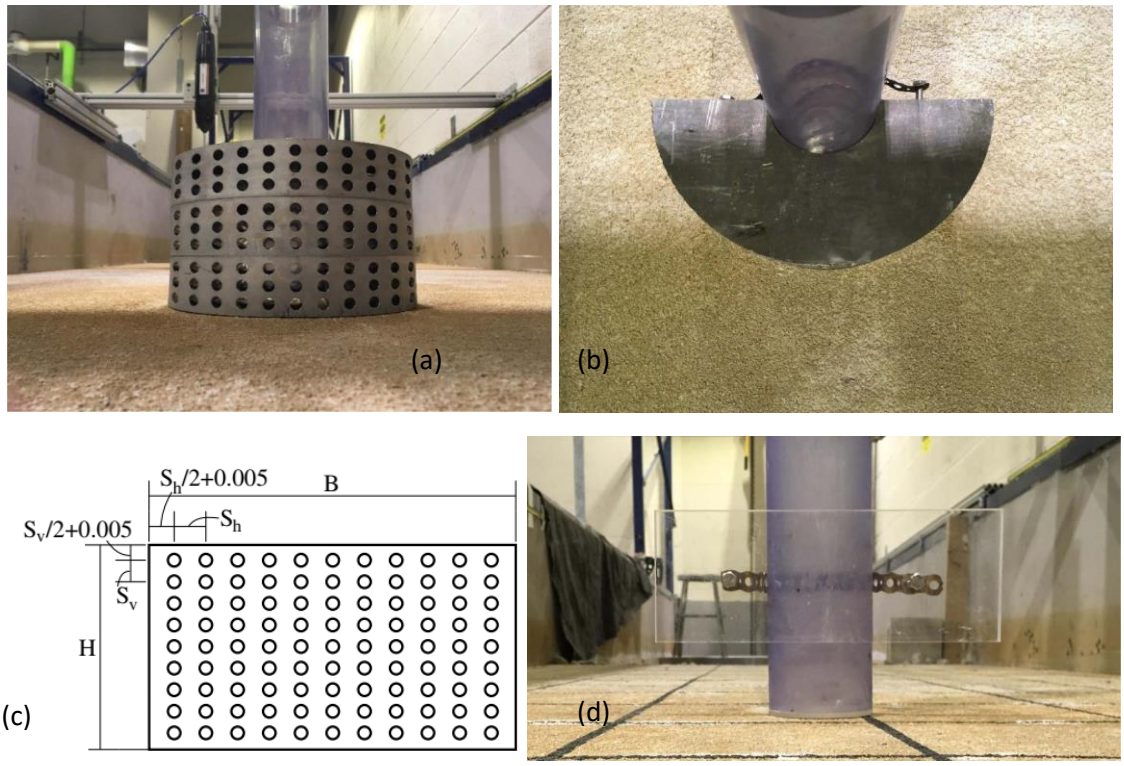

Figure 2-17 Debris dam specimens (m): (a) front view of cylindrical dam with 0.2 porosity and 0.15 m height; (b) top view of the cylindrical dam;(c) spacing of holes for porous debris dams; and (d) front view of the plate of 0.10 m height (Mauti et al. 2020)

Currently, the load of debris has been poorly studied for: (1) debris type, the idealized debris dam was fixed and static thus ignoring the formation of debris dam, in addition, the shape of the debris jam was not realistic; (2) flow condition, transient condition has not yet been studied for woody debris jam while steady flow condition has only rarely been investigated for debris.

2.4 Design codes related to debris jam

The design codes of buildings, which are used for guiding the construction of infrastructure, need to consider accurately the effects of debris imposed on structures. Debris effects in both unsteady and steady flow conditions have been introduced in terms of its load and associated scour.

2.4.1 Debris effects under unsteady flow

In terms of unsteady flow, the load on the structure is the main concern. As such, some design codes have been proposed for calculating debris load in transient flow conditions, especially for extreme conditions like tsunamis. The contents related to debris load were collected and compared including the load of impact force and damming force focusing on the differences between these codes (Macabuag et al. 2018). The design codes referred to were as follows:

(1) FEMA P646: Guidelines for Design of Structures for Vertical Evacuation from Tsunamis.

(2) FEMA P-55: Coastal Construction Manual Principles and Practices of Planning, Siting, Designing, Constructing, and Maintaining Residential Buildings in Coastal Areas (Fourth Edition)

(3) Tokyo University: STRUCTURAL DESIGN REQUIREMENT ON THE TSUNAMI EVACUATION BUILDINGS, Japan 2011

(4) The City and County of Honolulu Building Code (CCH) Chapter 16 Article 11 authored by the Department of Planning and Permitting of Honolulu, Hawaii

(5) SEI/ASCE 7-10: ASCE Standard. 2003. Minimum design loads for buildings and other structures.

(6) ASCE 7-16: Minimum design loads for buildings and other structures

Debris damming load on a structure

Debris damming effects trigger the accumulation of debris in front of a building, and FEMA P-464 (2019) recommends adopting the method of hydrodynamic force in ASCE 7-16 to calculate it. However, there is a formula proposed in FEMA P-464 (2012) to calculate the force of debris damming:

$$F_d = 0.5\rho_s C_d B_d (hU^2)_{\max} \tag{2-14}$$

where C_d = the drag coefficient, B_d = the breadth of the debris dam, h = the flow depth, and U = the flow velocity at the location of the structure. The value for C_d is recommended to be 2.0.

The momentum flux $(hU^2)_{max}$ can be obtained using a detailed numerical simulation model, and the debris damming force is assumed to act as a uniformly distributed load over the extent of the debris dam. The effects of debris damming should be evaluated at various locations on the structure to determine the most critical location.

Debris impact load on a structure

Debris impacting load, which is an impact force imposed in a very short time on a building by an object carried by the flow, should be considered due to its huge damages. Thus, several design codes have introduced formulae to calculate impacting force. Note that the impacting force in a river channel caused by flood events might not be obvious compared with a highly unsteady flow, but it might be a potential threat to a bridge pier.

(1) FEMA P-55

Several effects have been considered in the FEMA P-55 design code to calculate the impacting force of debris in an unsteady flow: (1) the size, shape, and weight (w) of waterborne objects (2) design flood velocity (U) (3) velocity of the waterborne object compared to the flood velocity (4) duration of the impact (assumed to be 0.03 s) (5) portion of the building to be struck. The equation to estimate debris load is as follows:

$$F_i = mUC_D C_B C_{str} \tag{2-15}$$

where F_i = the impact force at the Stillwater elevation, m = the mass of debris element, U = the velocity of water, C_D = the coefficient of depth, C_B = the blockage coefficient, C_{str} = the coefficient of a building structure.

The building structure coefficient, C_{str}, was developed based on ASCE7-10. A new formula was proposed to calculate the building structure coefficient:

$$C_{str} = \frac{3.14 C_I C_o R_{\max}}{2 g \Delta t} \tag{2-16}$$

where C_I = the impact coefficient 1.0; C_o = the orientation coefficient 0.8; Δt =s the duration of impact 0.03 s; $R_{\max}$ = the maximum response ratio assuming approximate natural period.

(2) The City and County of Honolulu Building Code (CCH) Provisions

The provisions contained were used to apply to the construction of all new buildings and structures, relocation and major alterations, additions, or reconstruction of existing buildings within the flood hazard districts as delineated on the flood boundary and floodway maps and flood insurance rate maps, and any amendments by the Federal Emergency Management Agency, on file with the department of land utilization, City and County of Honolulu. Considering the impact of debris in flow, the impact force in CCH is computed as follows:

$$F_i = m \frac{dU_d}{dt} \tag{2-17}$$

where m = the mass of debris, U_d = the velocity of debris (here evaluated to be the water velocity at the base of the structure); $\frac{dU_d}{d_t}$ = the acceleration or deceleration of the body.

Formula 2-19 was not convenient to use in practice, so the formula was further simplified by assuming a most critical or vulnerable location. In addition, the duration for the velocity reduction to zero was over a small finite time interval, and the approximation was made as:

$$F_i = \frac{31 U_d}{\Delta t} \tag{2-18}$$

where Δt = assumed to be the time interval over which impact occurs 1 s for wood construction; 0.1 s for structure material of reinforced concrete construction; 0.5 s for structure material of steel.

(3) FEMA P-646(2012)

Debris impact forces from waterborne objects such as floating driftwood, lumber, boats, shipping containers, automobiles, and buildings could be considered a dominant cause of building damage. Even though it is difficult to accurately calculate the force, it might be estimated by some methods.

Debris impact force is assumed to act locally on structures, unlike other forces, at the position of the water surface as shown in Figure 2-18, and the equation to estimate the magnitude of impact force is

$$F_i = 1.3 U_{d\max} \sqrt{k_E m (1 + c)} \tag{2-19}$$

where $U_{d\max}$ = the maximum velocity of flow containing debris; k_E = the effective stiffness of debris; and m =the mass of debris; c = a hydrodynamic mass coefficient.

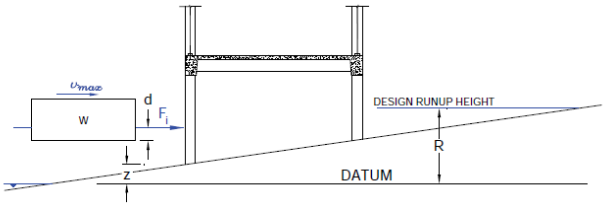

Figure 2-18 Waterborne debris impact force (FEMA P-646)

(4) Tokyo university: STRUCTURAL DESIGN REQUIREMENT ON THE TSUNAMI EVACUATION BUILDINGS, Japan 2011

A structure design method for tsunami evacuation buildings was developed after the 2011 Great East Japan earthquake due to the building damage from a tsunami. The process of structure design is indicated in Figure 2-19, which implies the necessary consideration of debris impact load.

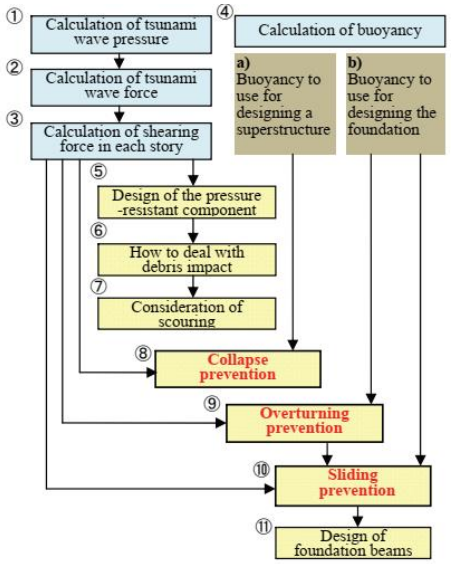

Figure 2-19 Process of the structural design of a tsunami evacuation building (adopted from STRUCTURAL DESIGN REQUIREMENT ON THE TSUNAMI EVACUATION BUILDINGS)

However, the existing methods of calculating debris impact load were very different from each other, and the types of debris were also limited. Thus, a unified evaluation method that could be feasible for various conditions has not been established yet.

Unfortunately, the method to calculate the impacting force of debris was not proposed, but it suggested that building protective equipment or facilities to prevent debris impact could be measured in the design code.

(5) ASCE7-02/ASCE7-10

The ASCE7 code considers impact load from logs, ice floes, and other objects hitting buildings and structures. The impacting force divides into three categories (1) normal impact loads resulting from isolated impacts of normally encountered objects (2) special impact loads that result from large objects like broken up ice floats and accumulation debris (3) extreme impact loads from very large objects like boats, barges

or collapsed buildings. Design for extreme impact load was not feasible for all/most buildings and structures. The method to calculate the magnitude of impact load was:

$$F_i = \frac{\pi m U_d C_I C_O C_B C_D R_{\max}}{2g\Delta t} \tag{2-20}$$

where $R_{\max}$ = the maximum response ratio for impulsive load determined; C_d , C_B = the depth coefficient and blockage coefficient separately determined; C_I = the impact coefficient determined, Δt =estimated to be 0.03 s. C_O = the orientation coefficient, here equal to 0.65;

In addition, special impact loads were proposed in the absence of a detailed analysis. Here the special load may be too small for some large accumulation of debris, and an alternative approach involving the application of the standard drag force expression was applied:

$$F_i = 0.5 C_d \rho A_{vc} U^2 \tag{2-21}$$

where U = flow velocity upstream of debris accumulation; A_{vc} = the projected area of debris accumulation into the flow; C_d= the drag coefficient equal to 1.0

(6) ASCE7-16

The most severe effect of impact loads within the inundation depth should be applied to the perimeter gravity load-carrying structural components located on the principal structure axes perpendicular to the range of inflow or outflow directions. Impact load is not necessarily applied simultaneously to all affected structural components. All buildings and other structures meeting the above requirement shall be designed for the impacts of wood poles, logs, vehicles, tumbling boulders, and concrete debris.

Simplified debris impact static load was estimated as the maximum static load, and this force was calculated by:

$$F_i = 1470 C_O C_I [kN] \tag{2-22}$$

where C_O = the orientation coefficient, here equal to 0.65, C_I = the impact factor.

While the nominal maximum instantaneous debris impact force can be determined by the following equation:

$$F_i = C_I C_O U_{\max} \sqrt{k_E m} \tag{2-23}$$

where U_{max} = the maximum flow velocity at the site occurring at depths enough to float the debris, k_E = the effective stiffness of the impacting debris or the lateral stiffness of the impacting structural elements.

Significant progress in this edition of ASEM was the guideline for the path of debris to assess its damage. Lines ±22.5º from the centerline shall be projected in the direction of tsunami flow as shown in Figure 2-20, and if the topography (such as hills) will bound the water from this 45º sector, the direction of the sector can be rotated to accommodate hill lines or the wedge can be narrowed where it is constrained on two or more sides.

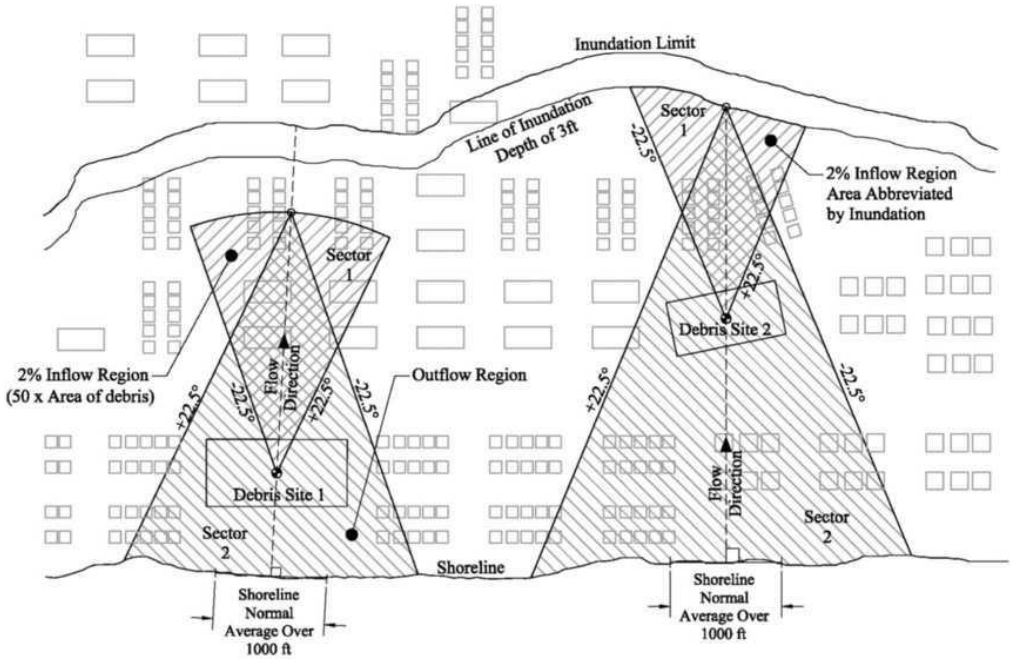

Figure 2-20 illustration of Determination of Floating Debris Impact Hazard Region (adopted from ASCE7-16)

Instructions for how to draw the directions of debris were expressed as follows: (1) "an arc of the impact of inflow should be drawn, one arc and two radial boundary lines of the 45º sector defines a circular sector region with an area that was 50 times the total sum debris area of the source, representing 2% concentration of debris." (2) "the debris impact hazard region for inflow and outflow should be determined by rotating the circular segment by 180º and placing the center at the intersection of the level or approved alternative boundary".

2.4.2 Debris effects under steady flow

Compared with unsteady flow conditions, debris effects in steady flow have focused on its influence on the safety of bridges. As such, the associated scour caused by debris was the main concern. There were also some design codes for in-channel wood debris, and they were developed by the US Federal Highway Administration.

(1) Federal Highway Administration (FHA), U.S. Department of Transportation (2005): Debris Control Structures Evaluation and Countermeasures (Third Edition), HEC-09

(2) Federal Highway Administration, U.S. Department of Transportation (2012): Evaluating Scour at Bridges (Fifth Edition), HEC-18

(3) Klohn Crippen Berger Ltd, BC Hydro (2018): Reservoir Boom Design Guideline (unpublished)

Loading on structure

Debris jam presented in front of a pier also imposes a load on the structure but drag force will be the main concern instead of impact force. For the hydraulic loading with debris accumulation, the hydrodynamic drag force is considered and the formula to calculate the drag force F_d is

$$F_d = C_d \gamma A_{vc} \frac{U_r^2}{2g} \tag{2-24}$$

where C_d = the coefficient of drag as shown in Table *2-3* ; A_{vc} = the area of wetted debris based on the upstream surface elevation projected normal to the flow direction; U_r = the reference velocity; γ = the specific weight of water.

Table 2-3 Drag coefficient for debris jam on bridge pier in HEC-09

Value of B	Value of F_r	C_D
B < 0.36	F_r < 0.4	1.8
B < 0.36	0.4 < F_r < 0.8	2.6 – 2.0F_r
0.36 < B < 0.77	F_r < 1	3.1 – 3.6B
B > 0.77	F_r < 1	1.4 -1.4B

Note*: B* means the blockage ratio which is the same as ΔA in this thesis.

The drag coefficient was related to the frontal blockage ratio ΔA and Froude number F_r as defined below:

$$\Delta A = \frac{A_{vc}}{A_{vc} + A_c} \tag{2-25}$$

where A_c = the unobstructed cross-sectional flow in the contracted section; A_{vc} = cross-sectional flow area blocked by debris

The total force on the structure due to hydrostatic pressure difference can be approximated as:

$$F_h = \rho g \left(h_{cu} A_{hu} - h_{cd} A_{hd} \right) \tag{2-26}$$

where h_{cu} =vertical distance from the upstream water surface to the centroid of the area; A_{hu} = the area of the vertically projected, submerged portion of the debris accumulation below the upstream water surface; h_{cd} = the vertical distance from the downstream, A_{hd} = area of debris jam vertically submerged downstream.

The total resultant force for debris should be computed as the summation of the drag force and the differential hydrostatic force. In practice, the transfer of load from debris to structure varies due to many factors including the characteristics of the debris accumulation and the degree to which streambeds and banks support the debris accumulation.

In the BC Hydro Reservoir Boom Design Guideline, a general current form of drag was also used considering the effects of the shape of the object in the flow and the flow velocity

$$F_{df} = \frac{w_w U^2 n^2 w_d l_d}{0.79 h^{1/3}} \tag{2-27}$$

where U = average velocity at surface, l_d = the length of debris in the direction of flow; w_d = the transverse dimension of debris; w_w = the unit weight of water; n = Manning's roughness coefficient.

Associated scour

Under steady flow conditions, the local pier scour associated with debris accumulation is another important issue. HEC-18 proposed a well know function to calculate the maximum pier scour depth:

$$\frac{d_s}{h} = 2.0 K_1 K_2 K_3 \left(\frac{D_p}{h} \right)^{0.65} F_r^{0.43} \tag{2-28}$$

where K_1 = the correction factor for pier nose shape; K_2 = the correction factor for an angle of the attack of flow; K_3 = the correction for bed condition

HEC-18 also recognizes the issue of a debris jam in front of the pier. The debris jam is idealized into either rectangular or triangular shapes for different situations. In addition, it found that the greatest amount of scour occurred when the dimensions of the debris jam in the flow direction reached the depth of approaching flow. On the other hand, it also showed that debris was very likely floating at the water's surface during a flood event.

As such, HEC-18 adopts the effective width of the pier to incorporate the prediction of scour depth in the presence of debris. The effective width of a pier D_p^* in the presence of rectangular and triangular shapes is proposed as:

$$D_p^* = \frac{K_4 \left(h_d w_d \right) + D_p \left(h - K_4 h_d \right)}{h} \tag{2-29}$$

where h_d = the height of the debris; w_d = the width of debris perpendicular to the flow direction; K_4 = the 0.79 rectangular debris, 0.21 for triangular debris; D_p = width of pier perpendicular to flow.

However, the design code also points out that this formula for debris jam has not yet been validated for the Florida DOT (FDOT) methodology. The presence of debris deflects a component of flow downward and leads to the increase of scour depth. In addition, the design code also suggests that the effects of debris diminish in a large water depth.

2.5 Flow Pattern in the presence of woody debris jam

The presence of accumulation of debris at bridge piers or abutments could significantly increase the possibility of bridge failure. Several investigations have focused on the accumulation of debris (Melville and Dongol 1992). The presence of debris could lead to an irregular flow pattern around the pier, and it might result in extra scour in front of the pier. Measurement and analysis of the flow pattern in the presence of debris have been conducted to obtain deeper insight.

Lagasse et al. (2010) summarized idealized flow patterns for local scour in the presence of accumulation debris (Figure 2-21). Reduction of cross-sectional flow area due to the presence of triangular accumulation debris led to the acceleration of flow velocity, and finally, it caused the increase of scour hole depth. In the case of rectangular accumulation debris, a second scour hole was observed in front of the bridge pier. These results conceptually described how the debris jam affected the scour process. However, idealized debris jams were studied, which might not have reflected realistic debris jams in terms of porosity and geometry. In addition, the results did not quantify the flow field.

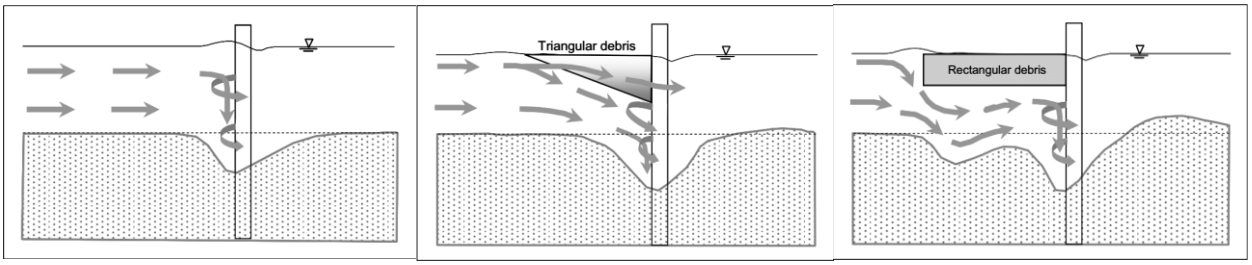

(a) at an unobstructed pier (b) at a rectangular debris cluster (c) at a triangular debris cluster

Figure 2-21 Idealized flow pattern(Lagasse et al. 2010)

As for the details of the flow field at the pier in the presence of accumulation debris, Pagliara and Carnacina (2013) used an Acoustic Doppler Velocimeter (ADV) to investigate the impacts of the accumulation debris with different roughness, in comparison to a pilot test (Figure 2-22). Due to the reduced area caused by the accumulation of debris, the flow was accelerated, and the accumulation of debris formed a boundary layer that deflected the flow downward to the base of the pier. In addition, the velocity distribution of the centerline was investigated, and velocity in the vertical direction was more irregularly distributed with increasing roughness of the accumulation debris.

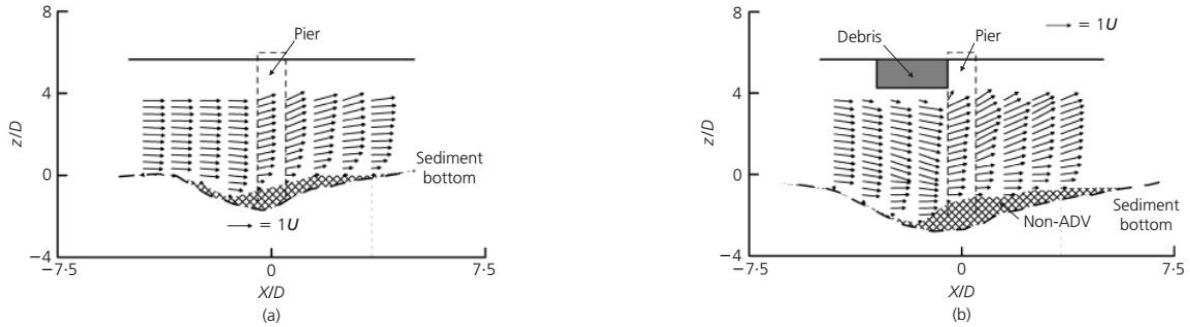

Figure 2-22 Final scour flow field at Y/D =0.55 for (a) test T1 (pilot test) and (b) test T4 with debris accumulation (Pagliara and Carnacina 2013)

Accumulation debris acted as a boundary layer at the water surface, so the velocity near the water surface decreased. Similar to an ice layer, the presence of accumulation debris influenced the vertical velocity distribution, and the maximum velocity in the vertical direction was found in the middle (Figure 2-23). The maximum velocity in the vertical direction was marked to quantify the change of vertical velocity distribution due to accumulation debris. This study indicated that the flow field was affected or contracted by the boundary layer at the bottom of the debris. It also showed that an increase in the kinetic energy of the flow, at the base of the pier caused by the debris, increased the capacity of flow to lift the sediment around the piers and carry the sediment downstream. Moreover, the roughness of the debris influenced the development of the boundary layer, and the maximum vertical velocity was observed close to the debris.

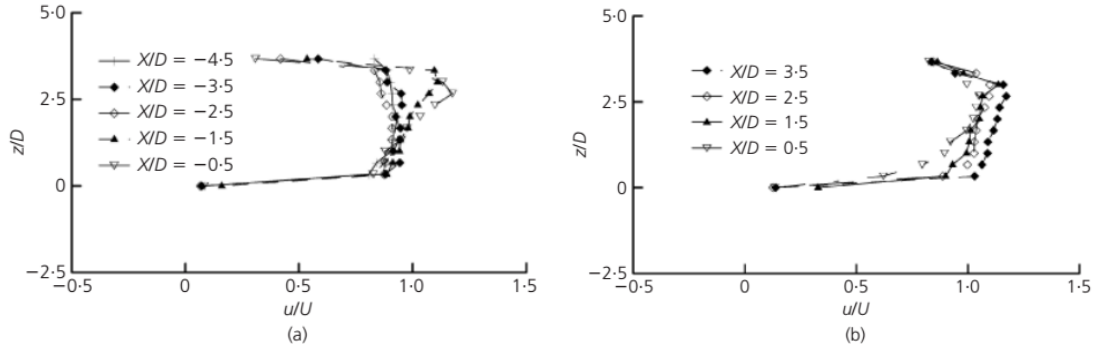

Figure 2-23 Test T4 flow velocities for fixed bed u/U against z/D_p (a) upstream ; (b) downstream (Pagliara and Carnacina 2013)

Okamoto et al. (2021) conducted flume tests to measure the flow field with driftwood accumulation by PIV. There were four stages monitored in the test, and a governing parameter for the accumulation process was examined. The instantaneous flow field measured by PIV is shown in Figure 2-24. The influence of woody debris jam on the profile of vertical velocity downward is shown in Figure 2-25. However, if the log jam reached spanwise wide, then the woody debris jam would not make the downward trend of vertical velocity, and the average velocity of the profile decreased.

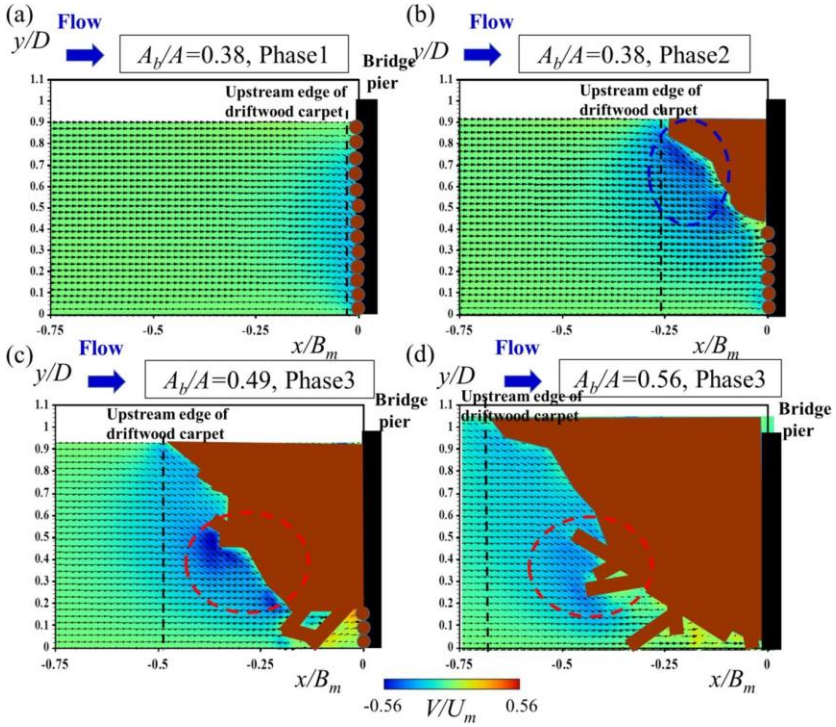

Figure 2-24 Contours of time-averaged vertical velocity (Okamoto et al. 2021)

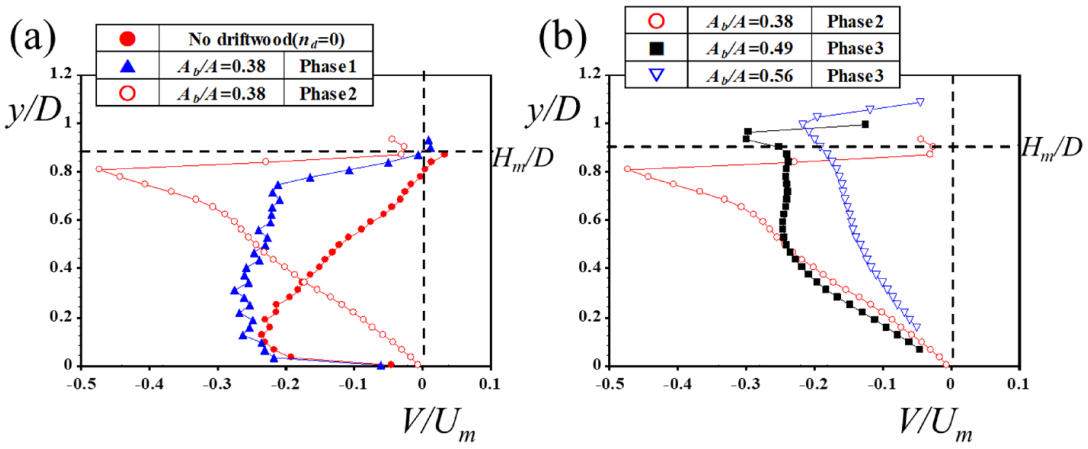

Figure 2-25 Vertical profiles of time-averaged vertical velocity at the upstream edge of driftwood carpet (Okamoto et al. 2021)

Understanding the flow field brings deep insight into the mechanism of hydraulic problems, and this was helpful to understand the effects of woody debris jams on scour. Current studies have focused on the woody block or fixed debris jam; this was not enough to have a comprehensive understanding of the influence of the presence of woody debris jam on scour.

2.6 Numerical simulation for woody debris jam

2.6.1 Simulation of a bridge pier in terms of turbulence model

Numerical models were also widely used to simulate the scour under bridge piers, and the influence of turbulence on scour in numerical models could be directly reflected and analyzed by comparing with experiments. Many different turbulence models have been applied to simulate the flow pattern and scour process. Olsen and Melaaen (1993) applied steady Reynolds-Average Naiver-Stokes (RANS) equations by omitting the transient terms, and further RANS $k-\varepsilon$ (Ali and Karim 2002) and $k-\omega$ (Roulund et al. 2005) models have been developed to simulate the bed shear stress and scour process, where k is the turbulence kinetic energy, ε is the dissipation of turbulence energy and ω is the specific rate of dissipation. Moreover, eddy-resolving models like large eddy simulation (LES) (Kirkil et al. 2008; Zhao and Huhe 2006) and detached eddy simulation (DES) (Escauriaza and Sotiropoulos 2011; Paik et al. 2007; Zeng and Constantinescu 2017) have also been applied to simulate the scour process, enabling greater insight into the sediment process interaction with flow structure and turbulence statistics.

Many studies of bridge pier scour used steady RANS models with a wall function to simulate bridge pier scour. Olsen and Melaaen (1993) applied steady RANS with the omission of the transient terms:

$$\bar{u}_j \frac{\partial \bar{u}_i}{\partial x_j} = \frac{1}{\rho}\frac{\partial}{\partial x_j}\left[-P\delta_{ij} - \rho\overline{u_i' u_j'} + \rho\nu\left(\frac{\partial \bar{u}_i}{\partial x_j} + \frac{\partial \bar{u}_j}{\partial x_i}\right)\right] \tag{2-30}$$

where P =the pressure; u_i =the velocity component in the accroding directions; u_i' =the flucuate velocity in the according directions; ρ =fluid density; ν =kinematic visocity; δ_{ij} = Kronecker delta.

Both bedload and suspended load were considered in the model, and the suspended load was calculated with the convection-diffusion equation and the $k-\varepsilon$ turbulence model:

$$\bar{u}_j \frac{\partial c}{\partial x_j} + w_f \frac{\partial c}{\partial x_z} = \frac{\partial}{\partial x_j}\left(\Gamma \frac{\partial c}{\partial x_j}\right) \tag{2-31}$$

where Γ =the diffusion coefficient (determined by $k-\varepsilon$ the model); w_f =sediment fall velocity.

As for the bedload transport, (Rijn 1984)'s formula was adopted to calculate the bed concentration. "Since the transient terms were neglected in the numerical model, the present study does not verify that the numerical model will be able to handle all cases of scour around obstacles." Olsen and Kjellesvig (1998) further developed the RANS with $k-\varepsilon$ a model including the transient turbulence terms (Eqs (2-31)and (2-30)), and the sediment processes also considered the sloping bed. This later model simulated better downstream, and the erosion process was modeled more correctly by considering the transient turbulence terms.

$$\frac{\partial \bar{u}_i}{\partial t} + \bar{u}_j \frac{\partial \bar{u}_i}{\partial x_j} = \frac{1}{\rho}\frac{\partial}{\partial x_j}\left[-P\delta_{ij} - \rho\overline{u_i' u_j'}\right] \tag{2-32}$$

$$\frac{\partial c}{\partial t} + \bar{u}_j \frac{\partial c}{\partial x_j} + w_f \frac{\partial c}{\partial x_z} = \frac{\partial}{\partial x_j}\left(\Gamma \frac{\partial c}{\partial x_j}\right) \tag{2-33}$$

Richardson and Panchang (1998) applied a computational fluid dynamic model named FLOW-3D which included the three-dimensional, transient, Navier-Stokes equations. Here the turbulence model combined Prandtl's mixing length theory and the renormalized group (RNG) $k-\varepsilon$ theory. In this study, the turbulence flow could be properly simulated on a flatbed, but the scouring process was incorrectly simulated due to an approximate model for sediment transport, even though drag force and local pressure were included in the scour process. Due to the significance of turbulence in the scouring process, more studies focused on applying a variety of turbulence models to obtain a more accurate result for the simulation. Ali and Karim (2002) applied FLUENT CFD to investigate the bed shear-stress for rigid beds using the standard $k-\varepsilon$ and RNG $k-\varepsilon$ turbulence models, and the computed results were further used to calculate the scour process. Salaheldin et al. (2004) used FLUENT's multiphase formulation (volume of fluid; VOF) method to capture the variation of water surface to achieve a more reasonable result for scour. Furthermore, several turbulence models, including standard $k-\varepsilon$, RNG $k-\varepsilon$, realizable $k-\varepsilon$ and Reynolds stress model (RSM), were also applied to simulate the velocity distribution and bed shear stress, which were then compared with experiments. It was found that the RSM could give a more satisfactory result for simulating the velocity field, bed shear stress and water level variation in the scouring process.

Roulund et al. (2005) investigated the influence of boundary layer thickness, Reynolds number and the bed roughness on horseshoe vortex at bridge pier scour by applying RANS $k-w$ SST (shear-stress transport) model. This turbulence model was selected as the best one to simulate the adverse-pressure-gradient flow case among a series of $k-w$ models, based on comparison with experimental results. Furthermore, a morphologic model including the bedload, sediment sliding, and mass balance of sediment was introduced to calculate the scouring process. Zhao et al. (2010) further improved the RANS $k-w$ SST model by introducing an Arbitrary Lagrangian Eulerian (ALE) scheme which took the effect of mesh moving speed into account, and the scouring process also included both suspended sediment and bedload as well as the skin friction and bed slope. Here the influence of turbulence on scour could directly be reflected by the equation:

$$\frac{\partial c}{\partial t}+\left(\overline{u}_j-\overline{u}_{jp}\right)\frac{\partial c}{\partial x_j}-w_f\frac{\partial c}{\partial x_z}=\frac{\partial}{\partial x_j}\left(\sigma_c\nu_t\frac{\partial c}{\partial x_j}\right) \tag{2-34}$$

where $\overline{u}_{jp}$ =velocity of the computatonal mesh movement; ν_t = the turbulence viscosity; σ_c = a constant. The experimental and numerical results showed that the scour process was governed by the combination of horseshoe vortex and vortex shedding, and the horseshoe vortex steepened the bed slope in front of the cylinder, and vortex shedding was observed to be important to the scour process in the wake of the cylinder.

The turbulence models mentioned above mainly focused on the steady Reynolds-Average-Navier-Stokes (RANS) models. RANS approaches continue to play an important role in scour mechanism research with further model improvements considering more factors in the sediment transport model (Baykal et al. 2015; Xiong et al. 2016). In addition, considering the computational cost of three-dimensional modeling, two-dimensional models for scour simulations including the turbulence influence (e.g., Liang et al. 2005; Noh et al. 2012) could be a more efficient and practical method to estimate the scour evolution. However, the mean flow and turbulence predictions obtained by RANS simulation with wall function in steady state were of questionable accuracy owing to the flow complexity (Ettema et al. 2017).

Given the significant role of turbulence in the scour process, Unsteady Reynolds-Average Navier-Stokes (URANS) models may yield more accurate results for the development of scour. (Paik et al. 2004) applied a URANS $k-\varepsilon$ model with a wall function to simulate a complex shape of an obstacle, and it was found that the URANS model can capture very complex, large-scale instabilities of mean flow and the low-frequency vortical rolls in the wake boundary layer. (Ge et al. 2005; Ge and Sotiropoulos 2005) further developed unsteady RANS and turbulence closure equations using a finite-volume method that was second-order accurate both in space and in time. Furthermore, URANS was applied to sandbed and included the bed transportation for diamond, square, and circle piers, and it was found that for the pier with blunt leading edges like circular and square piers, the URANS model cannot resolve the energetic horseshoe vortex system. It was necessary to use ad hoc empirical corrections to modify the calculated critical bed shear stress to reflect the scouring process.

Steady and unsteady RANS models can simulate the moveable bed, but these methods were not yet sufficiently reliable to predict scour depth for bridge pier design. (Ettema et al. 2017) pointed out that both steady and unsteady RANS models can not accurately predict massively separated flows or flows with adverse pressure gradients, and RANS models failed to describe the aspects of separated flows dominated by unsteady vortex shedding and large-scale vortex interactions. Thus, the RANS cannot correctly predict the structure of the horseshoe vortex system at the initial stage of scouring as well as the bimodal nature of large-scale oscillations of the horseshoe vortex.

Eddy resolving models can give more detailed information for the mean flow field and the turbulence structure which might be difficult to observe in experiments. Such models might also successfully simulate the coherent structures controlling the bed erosion phenomenon. Eddy resolving models demonstrate the role turbulence plays in the scour process, as the simulations achieve much better results when the instantaneous flow field is taken into account.

Tseng et al. (2000) investigated the flow pattern around circular and rectangular piers by employing a finite volume method using MacCormack's explicit predictor–corrector scheme to solve weakly compressible hydrodynamic flow equations combined with Smagorinsky's SGS turbulence model (Large Eddy Simulation, LES). Sung-Uk and Wonjun (2002) also investigated the flow field with or without scour hole and compared the behaviors of LES and RNG $k-\varepsilon$ models, and it was observed that LES could

simulate the flow field and scour hole more properly. Zhao and Huhe (2006) investigated the turbulence flow field and scour mechanism around a pier employing the LES method; the instantaneous flow pattern calculated in the study was reasonably computed as shown in Figure 2-26. The authors noted that "turbulence plays an important role in the scouring process." The turbulence intensity increased when the scour depth increased, which was not consistent with the experimental results discussed above.

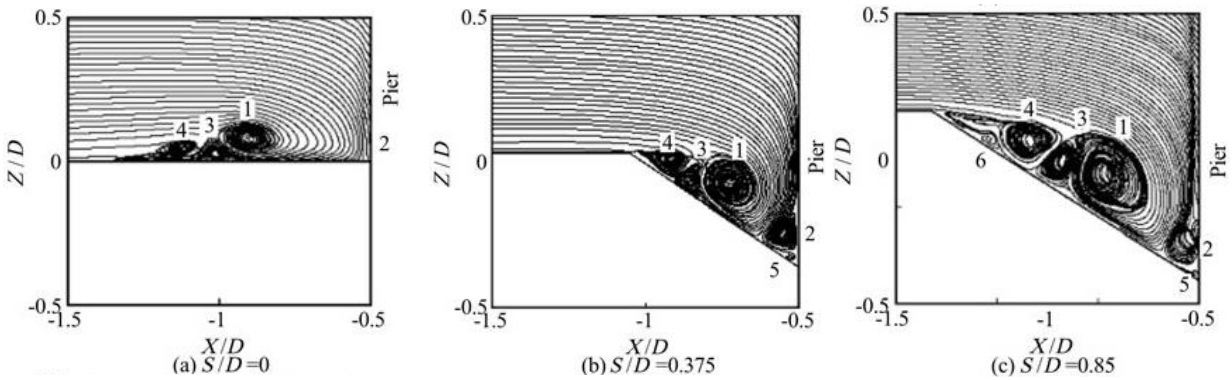

Figure 2-26 Instantaneous flow patterns of the horse vortex system in the upstream of the pier (Zhao and Huhe 2006)

Considering the advantages of LES for detailed computation of the flow pattern and turbulence structure, numerous studies adopted the LES method to simulate the scour process around a pier or obstacle. Koken and Constantinescu (2008a); Koken and Constantinescu (2008b) investigated comprehensively the scouring process around a spur dike including the initiation and final stage of erosion and deposition states by the LES method, and the bed shear stress and pressure fluctuation inside the horseshoe vortex were reasonably well simulated. Kirkil et al. (2008) used LES to investigate the flow field around a circular cylinder located in a scour hole considering the interaction of the horseshoe vortex system. It was found that the structure of the horseshoe vortex varied significantly with space and time even though a large and stable primary necklace vortex was evident in the scour hole (Figure 2-27). Kirkil and Constantinescu (2012); Kirkil and Constantinescu (2015) further applied this model to simulate the necklace horseshoe vortex system in both laminar and turbulent flow, and the large-scale coherent structures (necklace vortices, vortex tubes shed in the separated shear layers (SSLs) and roller vortices shed in the wake) were well captured.

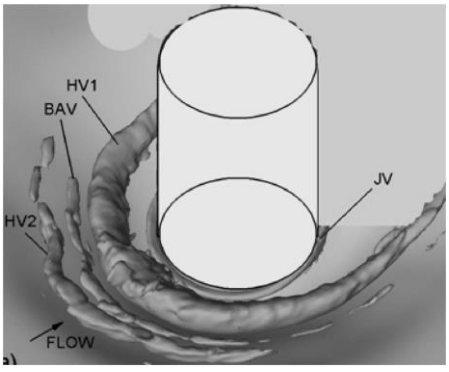

Figure 2-27 Visualization of the main necklace vortices inside the scour hole using the Q criterion(Kirkil et al. 2008)

Hybrid RANS-LES methods such as detached eddy simulation (DES) were another important set of approaches to capture the turbulent flow structures and scour around bridge piers. Paik et al. (2007) further developed the DES method with an unsteady RANS model, and this turbulence model become more widely used due to its ability to simulate flow without using wall functions. Escauriaza and Sotiropoulos (2011a); Escauriaza and Sotiropoulos (2011b); Escauriaza and Sotiropoulos (2011c) investigated the horseshoe vortex as well as initial erosion and bedload transport using unsteady incompressible Reynolds-averaged Navier–Stokes with DES turbulence model, demonstrating that the DES model could capture the coherent-structure and simulate the interaction of turbulence flow and sediment erosion. (Kirkil and Constantinescu 2009) investigated the dynamics of large-scale coherent eddies in the flow around a circular pier, their interactions, and their role in sediment entrainment in the scour process using the DES method. The flow structure, turbulence statistics, and instantaneous bed shear stress could be reasonably obtained by this model (Figure 2-28). Moreover, considering the good predictions of the DES model, it was further applied to investigate the erosion process around a vertical plate (Kirkil et al. 2009), piers with complex shape or multiple columns (Chang et al. 2013) and piers in shallow water (Zeng and Constantinescu 2017). It also should be pointed out that by employing RANS near the wall the DES method captures less flow physics, and it may be significantly more dissipative, compared with well-resolved LES.

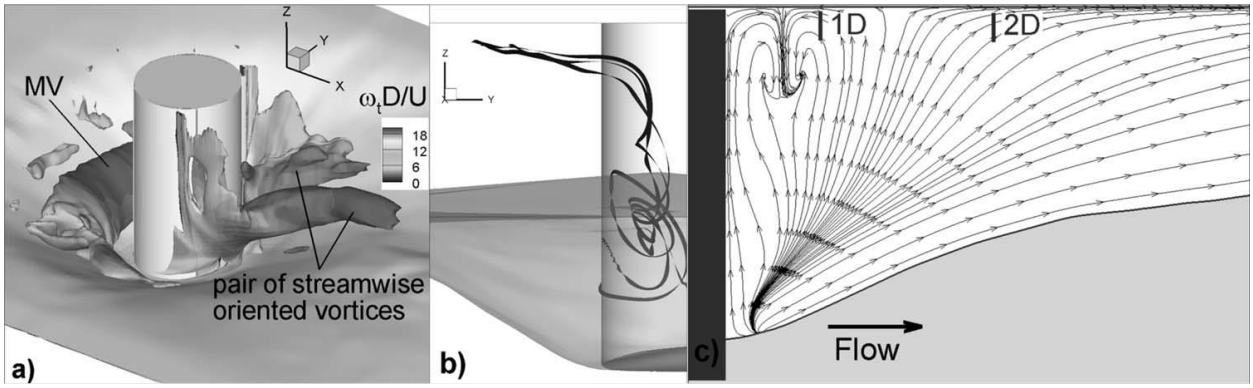

Figure 2-28 Visualization of the flow structure behind the pier: (a) Q isosurface; (b) 3D stream traces; and (c) mean-flow 2D streamline patterns in the symmetry plane(Kirkil et al. 2009).

2.6.2 Simulation of woody debris

Simulation of woody debris jams has not yet caught much attention, but some studies have already stepped into this field. In the study of Mendonça et al. (2019), a metal mesh was used to shape the woody debris jam, and then Flow-3D was applied to simulate the scour depth in the presence of triangular and rectangular debris as shown (Figure 2-29). However, the numerical results did not compare well with the experimental data, demonstrating that 3D simulation of scour was much more time-consuming and difficult to get a reasonable result.

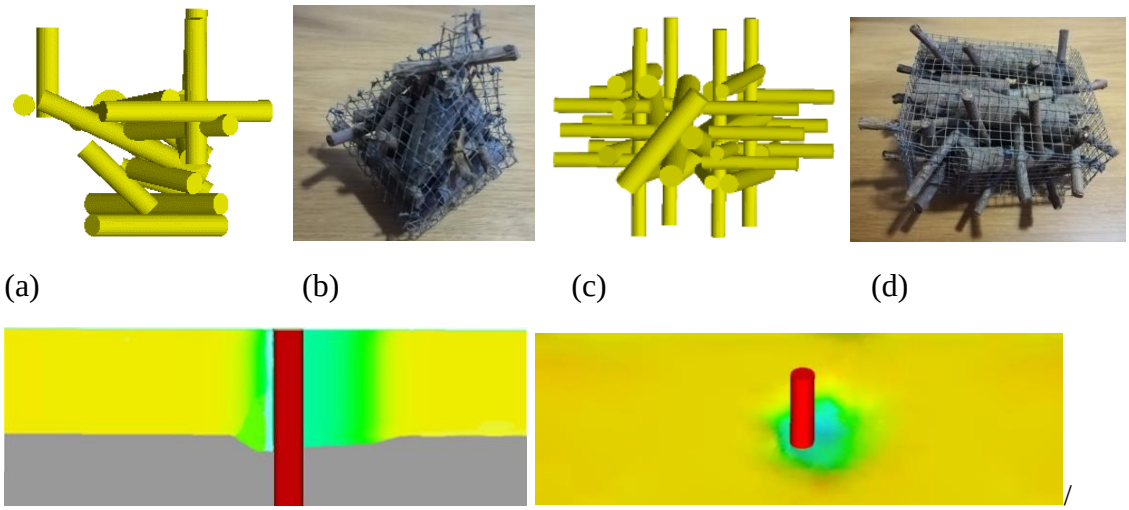

(a) (b) (c) (d)

(e) (f)

Figure 2-29 debris geometry (a) triangular debris in Flow-3D (b) triangular debris in experiments (c) rectangular debris in Flow-3D (d) rectangular debris in the experiment; (e) the side view of Flow-3D results (f) the 3d view of Flow-3D results (Mendonça et al. 2019)

In contrast to modeling the accumulation of the woody debris, Meninno et al. (2019) aimed to simulate the wood transport and the motion of wood debris. They used an advection-diffusion equation for floating debris by applying a mass conservation equation:

$$\frac{\partial c_w}{\partial t} + \nabla c_w v_w = K_s \frac{\partial^2 c_w}{\partial s^2} + K_n \frac{\partial^2 c_w}{\partial n^2} \tag{2-35}$$

$$\frac{\partial \delta_w}{\partial t} + v_w \nabla \delta_w + \omega_w \frac{\partial \delta_w}{\partial \theta} = K_s \frac{\partial^2 \delta_w}{\partial s^2} + K_n \frac{\partial^2 \delta_w}{\partial n^2} + K_\theta \frac{\partial^2 \delta_w}{\partial \theta^2} \tag{2-36}$$

where c_w = the concentration of wood; δ_w = the orientation of a log; v_w = the wood linear velocity; ω_w = the angular velocity of wood; K_s =the streamwise diffusion coefficient; K_n = the transverse diffusion coefficient; K_θ = the angular diffusion coefficient.

In their model the concentration of wood c_w timing a probability density function δ_w was used to express the mass conservation, and the diffusion coefficient was considered to correspond to the rate variance of particle position. The coefficients were determined with physical experiments. Persi et al. (2020) further tested the behavior of the model with spherical and cylindrical wood in semi-congested and single-body release methods in an open channel.

The moving particle semi-implicit (MPS)-type particle method had also been tested to simulate the motion of wood and deposition pattern (Kang et al. 2020). The motion of driftwood was expressed by assigning eight spheres in series to simulate the rotation and collision process, with the number of spheres corresponding to the aspect ratio of the driftwood (Figure 2-30). The motion of each sphere was separately calculated, and the gravity center was calculated by coordinating all the spheres. Then calculating the linear velocity and angular velocity at the center of the wood, the spheres were rearranged in a straight line.

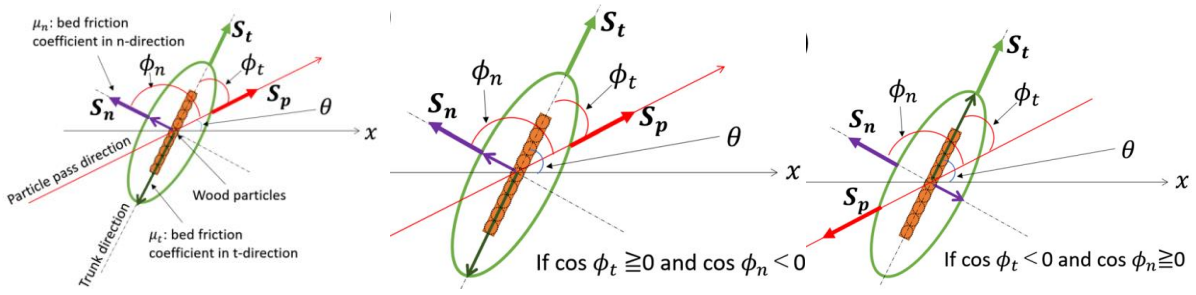

(a) (b) (c)

Figure 2-30 driftwood motion tracking process (a) basic domain (b) type of positive particle pass direction to the x-axis (c) type of negative particle pass direction to x-axis (Kang et al. 2020)

Kimura and Kitazono (2019) applied a Eulerian-type three-dimensional flow model coupling a Lagrangian-type two-dimensional driftwood model to simulate the motion and jamming process of woody debris, and the discrete element method (DEM) was used to model the collision effect of driftwood. Experiments for the driftwood jamming were done, and the physical tests were used as reference data for the numerical model (Figure 2-31). The driftwood Richardson number was proposed to quantify the three-dimensional behavior. However, the results demonstrated that the 2D model was not able to well simulate the water surface and the velocity in front of the obstacles.

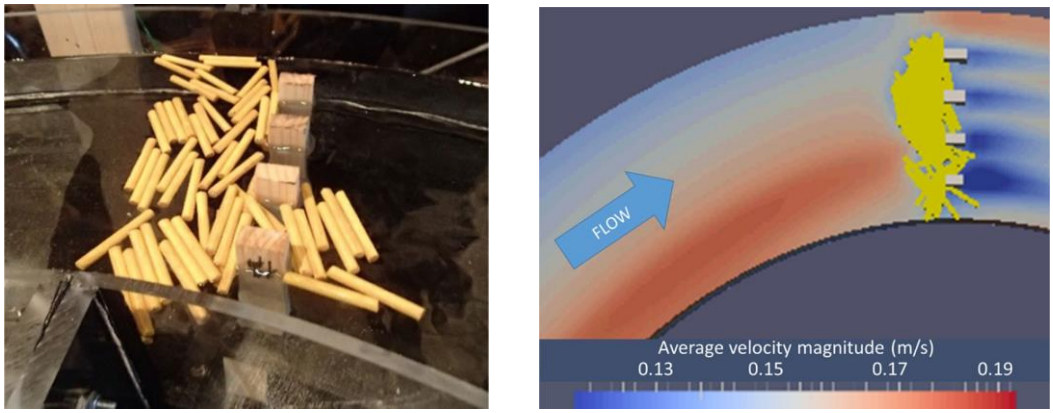

(a) Deposition and driftwood jamming (b) i-RIC simulation of debris jamming

Figure 2-31 physical and numerical modeling of driftwood jamming (Kimura and Kitazono 2019)

Current numerical studies have focused on the transportation, motion, and deposition of woody debris in rivers, all of which were essential processes. However, the interaction of woody debris and fluvial channel and structure has not yet been investigated in detail. FLOW-3D has been used to investigate the influence of woody debris jam on sand bed scour, but the results were far from satisfying.

2.7 Research Needs and Problem Statement

The presence of woody debris influences the hydro-morpho dynamics and ecosystems of rivers. Further, its influence on river infrastructure can be consequential, as it might threaten the stability and safety of bridges. It is common to observe that the woody debris accumulates in front of both single and complex bridge piers, resulting in flow obstruction (Diehl 1997). These woody debris jams decrease the area of the

cross-section and lead to an increase in flow velocity, which can result in deeper scour at the base of the pier.

Several studies have already investigated the influence of woody debris on pier scour in terms of static woody debris jam (Lagasse et al. 2010a; Lagasse et al. 2010b) and the maximum dimension of woody debris jam and drag coefficient of woody debris (Panici and de Almeida 2018; Panici and de Almeida 2020). In addition, HEC-18 was also proposed as a code to estimate the scour depth in the presence of woody debris jam and was further improved by Transportation Research Board (Lagasse et al. 2010). However, in these studies, the woody debris is thought to be static and a block without evolution, which does not consider the fact that a woody debris jam accumulates piece by piece, growing as a block with a shape most akin to a half-cone, and may even eventually break up and wash downstream. In other words, the dynamics of woody debris jam evolution and associated pier scour have not yet been considered. Thus, in the present study dynamic woody debris jams that evolve over time will be examined, and their influence on the flow field, pier loading, and pier scour will be investigated experimentally. In addition, AI tool has been widely used in the hydraulic field, so an algorithm of multigene genetic programming was introduced to develop a new model for temporal evolution to validate the application of AI tool.

Chapter 3. A new model developed by MGGP for the temporal evolution of bridge pier scour

3.1 Introduction

The removal of bed material around bridge piers caused by water flow is described as scouring. Scour at bridge piers could significantly lead to bridge failure, especially during flood events, and several investigations (Kandasamy and Melville 1989; Richardson and Richardson 1993; Sutherland 1986) pointed out that scour may be the leading cause of bridge failures. Therefore, significant attention has been paid to predicting local scour in order to avoid or mitigate the influence on bridges.

Local scour depth at the front of a pier is used to quantify the degree of scouring. If the maximum scour depth undermines the bridge foundation, this can cause structural instability, finally leading to bridge failure. Many methods have been developed to predict maximum scour depth or equilibrium scour depth (Kandasamy and Melville 1998; Melville 1997), and recently Shahriar et al. (2021) categorized four pier scour models for the equilibrium scour depth. Anderson (1963) pointed out that the scour depth varied with time, and the practical equilibrium depth could be reached in a relatively short time. However, while an equilibrium scours may be obtained after a long period of steady clearwater flow, the concept of an equilibrium scour depth has less utility when applied to field situations with unsteady and live bed flows. The peak flood flow might last only a few hours or days in the field, and there may be insufficient time during short flood events to generate an equilibrium depth (Melville and Chiew 1999). Similarly, Kothyari et al. (1992a) hypothesized that the maximum scour depth could not be reached with certainty when the discharge did not run for a long enough period. On the other hand, long-duration moderate floods may induce as much scour as short-term larger flood peaks (Link et al. 2017). The temporal evolution of scouring is therefore thought to be more realistic to reflect the development of scour.

Erosion occurs due to the removal of sediment around the pier, and the scour hole develops corresponding to an increasing horseshoe vortex (Graf and Istiarto 2002; Graf and Yulistiyanto 1998; Hager 2007; Melville and Raudkivi 1977). With the development of Artificial Intelligence (AI) technology, more and more AI models have been applied to predict scour depth (Azamathulla 2011; Azamathulla et al. 2010; Khan et al. 2011). These AI methods provide another potential approach to developing a more robust and accurate model for scouring prediction.

The present study aims to provide insight into the temporal evolution of pier scour. First, a comprehensive review of available analytical/theoretical models and empirical models is presented to introduce the fundamental processes and important variables for the prediction of scour depth with time. A brief review follows previous deep learning approaches to predict the temporal evolution of scouring. Novel new approaches for the prediction of scouring evolution are then developed using multigene genetic programing (MGGP). These MGGP models and previous empirical models are then assessed for accuracy of scour prediction, using an independent data set obtained from both new experiments and previously reported data.

3.1.1 State of the art

Due to the high risk of bridge failure caused by scouring, many formulas have been suggested to describe the development of scour depth with time. Chabert and Engeldinger (1956) were pioneers in the study of time variation of scour depth. During the period of the 1960s and 1970s, there were several researchers (Breusers 1967; Liu et al. 1961) who experimentally investigated the time-dependent scour depth, but the functions were either too complex or too inaccurate to reach a satisfying prediction.

Present studies related to time-dependent scour can be categorized into theoretical and empirical models. Current theoretical studies related to the temporal evolution of scour under the clear water regime can be classified into three groups developed from (i) sediment pick-up model; (ii) horseshoe vortex model; (iii) effective flow work model. According to sediment pick-up models, bridge pier scour is described as sediment entrainment or a bedload problem but accompanied by a more complex flow condition. Yanmaz and Altinbilek (1991) proposed a semiempirical model to predict the temporal evolution of scour depth around circular and square piers based on the sediment continuity equation, and the sediment pick-up function was introduced into the analysis of sediment entrainment around the pier. According to the sediment continuity equation, the rate of volume change in the scour hole equates to the difference between the sediment inflow and the outflow of the scour hole. Clear water scour was investigated by (Yanmaz and Altinbilek 1991), so sediment carried into the scour hole was ignored. Dey (1999) further developed the model to be applied to live bed scours as well as non-uniform sediment. In addition, Yanmaz (2006) further improved the model to obtain a new function to compute the temporal evolution of scour depth. Yilmaz et al. (2017) extended this approach to dual bridge pier scour, and a model was proposed to calculate the time-dependent scour depth. Moreover, Yanmaz and Kose (2009) developed a model to calculate the temporal scour depth development at the base of the abutment using this method. Chen et al. (2022) also applied this method to develop a mathematical relation for the scour hole dimensions and the scour depth.

In horseshoe vortex models for scouring, the horseshoe vortex system is considered to dominate the process of scour development, as the vortex system significantly affects the bed shear stress. Kothyari et al. (1992a) investigated the influence of uniform or non-uniform sediment and stratification on scour depth, and a model was proposed to calculate the scour depth, which was based on horseshoe vortex theory. This method was further applied to live bed scour (Kothyari et al. 1992b).

The bed shear stress decreases with the development of scouring, and the removal of sediment around a pier base finally reaching an equilibrium scour depth. Mia and Nago (2003) continued this idea and further produced a model to calculate time-dependent scour depth, and the assumption that scours hole shape remained unchanged concerning time was also introduced. Kothyari and Kumar (2010) experimentally investigated the influence of sediment size on scour depth and further improved the horseshoe model. Lu et al. (2011) focused on the temporal variation of scour depth for a nonuniform circular pier, and the scour hole was divided into three zones. Thereby, a model was further derived from Mia and Nago's model to compute scour depth with respect to different stages of scour development for the nonuniform pier.

Transport work rate was introduced to quantify sediment transport, and Lai et al. (2009) continued this idea to establish the relationship between a Γ-shaped hydrograph and equivalent scour duration. Based on the rate of flow work τu and bed shear stress $\tau \sim \rho u^2$, and u is the approaching flow velocity, the effective flow work on scour sediment was assumed to correspond to the flow intensity exceeding the threshold value of flow intensity. Link et al. (2017) further developed an effective flow work model and adopted the referenced velocity to calculate the effective flow work.

On the other hand, numerous studies have applied Artificial Intelligence (AI) methods to build new models in recent years, and several studies are focusing on the scour depth which turned out to be able to achieve a better prediction. Azamathulla and Ghani (2010) applied genetic programming (GP) to develop a model for predicting the scour depth and compared its performance with models generated by Artificial Neural networks (ANN). They showed that the overall performance of GP behaves better than ANN models. Azamathulla (2011) adopted GEP (Gene Expression Programming) and ANN to build the functions to predict the equilibrium scour depth at abutments, and it was found that the GEP function can achieve a better result. Azamathulla (2012) further applied the GEP method to generate a new function to estimate the scour depth downstream of sills, and the new function gave a satisfactory prediction. Mohammadpour et al. (2013) compared the results of time scale scour depth at short abutments predicted by GEP, ANN, and MLR (multiple linear regression) methods, and showed that GEP and ANN were more practical

approaches. In addition, Muzzammil et al. (2015) used the GEP method to generate a new function to predict the scour depth at bridge piers in cohesive beds. Khan et al. (2011) used the GEP method to predict the equilibrium scour depth at bridge piers. Jamei and Ahmadianfar (2019) applied MLR, GEP, and locally weighted linear regression (LWLR) to develop a new model respectively for the prediction of scour depth in the presence of debris jam and concluded that the LWLR can reach a satisfactory result. Among these AI models, GP and GEP models have the advantage of yielding an explicit model, especially compared with ANN.

A new approach for GP is the multigene genetic programming method (MGGP), which works with several traditional GP models together to develop a more robust and accurate, explicit model. A comparison of several machine learning methods turned out the MGGP has a successful estimation for solving civil engineering problem (Uncuoglu et al. 2022). In addition, MGGP has been used to develop models for soil water retention curve (Garg et al. 2014), permeability in oil reservoirs (Kaydani et al. 2014), and initial dilution of buoyant jets (Yan and Mohammadian 2019), and these studies suggested that the MGGP model achieved a more precise prediction compared to other AI models like ANN, ANFIS (neuro-fuzzy inference system), and GP. The MGGP algorithm is a convenient and efficient method to build new functions, but MGGP has not yet been applied to the prediction of the temporal evolution of bridge pier scour.

In the present study, the multigene genetic programming method (MGGP) is applied to develop a new empirical function for the temporal evolution of scour depth. The procedures are (1) collecting the necessary data, and its division into input data for the development of new functions and independent validation data for the evaluation of model performance; (2) normalizing the variables for scour depth predictions; (3) selecting parameters for developing a new MGGP model; (4) distributing input data into different percentages of training and testing data; (5) development of the new MGGP model; (6) evaluating the error of the developed MGGP model and comparing it with the existing empirical functions.

Many studies have been conducted for scouring and found that temporal scour depth development is significantly influenced by flow intensity, pier size, sediment material, and so on. Several researchers have used regression methods to build empirical relations to predict temporal scour depth as a function of relevant parameters.

3.1.2 Analysis of Temporal scour depth

Ettema (1980) investigated in detail the influence of nondimensional parameters on the development of scour depth, and a logarithmic function was proposed to describe the temporal scour depth. The function considered shear velocity, sediment size, and pier size, and two additional fitting parameters were determined using experimental data. Franzetti et al. (1982) also conducted several experiments to obtain deeper insight into the temporal scour depth, and an exponential function for circular piers was derived to express the influence of duration on scour depth. Whitehouse (1997) further developed a similar exponential form of the formula to describe the temporal development of scour depth. Melville and Chiew (1999) systematically investigated the influences of several factors such as flow intensity, approach depth, and sediment size on scour depth which resulted in equation (1). Their formula for d_s requires the time to reach equilibrium scour time t_e, and the equilibrium scour depth (d_{se}) which they obtained from the formula in Melville (1997). Oliveto and Hager (2002) studied the resistance force of piers on fluid flow and proposed an empirical function to predict the temporal evolution of scour depth based on hydraulic analogy by introducing Froude similarity. This method was further validated and developed by (Hager and Unger 2010; López et al. 2006; Oliveto and Hager 2005). Chang et al. (2004) thought that there was a critical sediment size corresponding to the equilibrium scour depth under the critical state, and a complex process was produced to calculate the equilibrium scour depth as well as the time required to develop into an equilibrium state for nonuniform sand. Moreover, this method could also apply to unsteady flow conditions. López et al. (2014) focused on the unsteady flow condition since the discharge of floods varies with time, and a new

function was proposed to predict temporal scour depth based on the approach of (Oliveto and Hager 2002). Aksoy et al. (2017) further considered the influence of pier diameter on scour, and a new empirical equation was proposed to calculate the temporal evolution of scour depth based on the (Yanmaz and Altinbilek 1991)'s model. Typical empirical functions are summarized in Table 3-1 .

Table 3-1 Empirical functions to predict time-dependent scour depth

Researchers	Formulae	No.
Melville and Chiew (1999)	$\frac{d_s}{d_{se}} = \exp\left\{-0.03\left\|\frac{u_c}{U}\ln\left(\frac{t}{t_e}\right)\right\|^{1.6}\right\}$	(3-1)
Oliveto and Hager (2002)	$\frac{d_s}{L_R} = 0.068\sigma^{-0.5}N_S F_d^{1.5}\log(t_o)$	(3-2)
Chang et al (2004)	$d_s = \begin{cases} 0.08K_\sigma K_v t_c^{-1.3}(t/t_e) & 0 \le (t/t_e) \le t_c \\ d_{\sec} - 0.27K_\sigma K_v\left((t/t_e)^{-0.3} - 0.41\right) & t_c \le t/t_e \le 0.04 \\ d_{\sec} - 1.1K_\sigma K_v\left((t/t_e) - 2.22(t/t_e)^{-0.45} + 1.22\right) & 0.04 \le t/t_e \le 1 \end{cases}$	(3-3)
Aksoy et al. (2017)	$\frac{d_s}{D_p} = 0.8\left(\frac{U}{u_c}\right)^{1.5}\left(\frac{h}{D_p}\right)^{0.15}(\log t_A)^{0.6}$	(3-4)

where d_s= the temporal scour depth at time t; t_e=time for equilibrium scour depth in the study (Melville and Chiew 1999); d_{se}=equilibrium scour depth in the study(Melville and Chiew 1999) ; u_c=critical mean flow velocity for sediment entrainment; L_R= a reference length, and equal to $\left(D_p h^2\right)^{1/3}$ for pier; t_o is the dimensionless time scale and equal to $\left\{t\left[\sqrt{d_{50}g(\rho_s-\rho_w)/\rho_w}/L_R\right]\right\}$; N_S=a shape number, 1 for circular pier and 1.25 for abutment; F_d is the densiometric particle Froude number equal to$\left\{U/\sqrt{d_{50}g(\rho_s-\rho_w)/\rho_w}\right\}$, ; K_σ =factor for adjusting sediment gradation; K_v= the factor for adjusting flow intensity; $d_{\sec}$=equilibrium scour depth of uniform sediment in the study (Chang et al. 2004); $t_c = [d_{sec}/(0.35K_vK_\sigma) - 0.31]^{-3.33}$ and ρ_s=density of sand, ρ_w=the water density; t_A = the dimensionless time scale and equal to $\left\{td_{50}\left[\sqrt{(\rho_s-\rho_w)/\rho_w g d_{50}}/D_p^2\right]\right\}$

3.2 Methodology

3.2.1 Data collection

The data used in the present study were sourced from both previous literature and a new experiment conducted by the authors to obtain data independent from previous studies. Physical modeling was applied to investigate the influence of the evolution of scour depth in front of a single bridge pier in the University of Ottawa Hydraulic Lab. The flume in the lab was 30 m long, 1.5 m wide, and 0.7 m deep (Figure 3-1). Two flow straighteners were set up close to the flume inlet to ensure flow uniformity. A 0.2m high false floor was initiated 18.3 m downstream of the flume inlet to create a 3.15 m long mobile bed test area within which the model pier and instrumentation were placed.

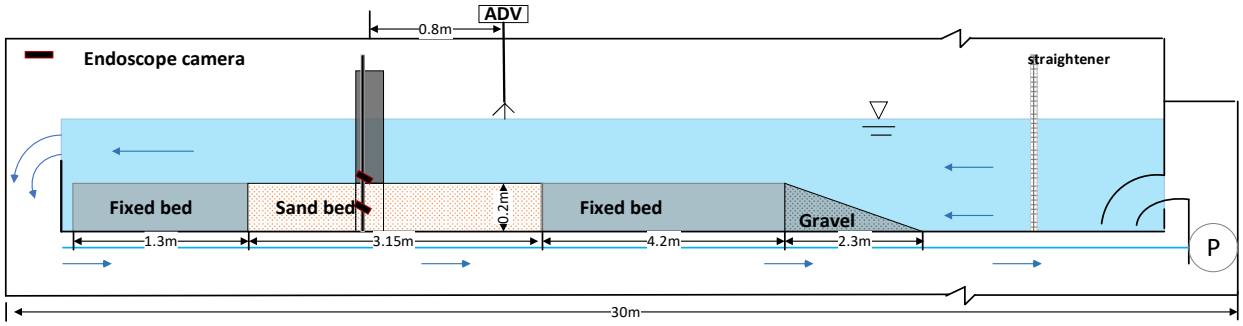

Figure 3-1 sketch of the experimental flume（not to scale）

The mobile bed test area was filled with sand with d_{50} of 1.16mm and a gradation of 1.22. A circular pier with a diameter D_p=0.09m was placed in the center of the sand bed test area. A Vectrino Acoustic Doppler Velocimeter (ADV) (https://www.nortekgroup.com/products/vector-300-m) was used to measure the vertical distribution of velocity 0.8m upstream of the pier, and a fitting equation was used to get the vertical distribution of velocity so that the mean velocity was obtained (see Zhang et al. (2022). A filter developed by (Rennie and Hay 2010) was applied to remove the noise of ADV data, and time-averaged velocity was obtained for each point. The mean velocity was computed by the depth-averaged method. The flow condition for each experimental test is presented in Supplementary III Table S0.

All tests were conducted under clear water scour flow conditions and lasted for 60mins. To initiate each test, the discharge was slowly increased to avoid any entrainment of the sand bed until reaching a pre-determined inlet valve opening position for the designed flow condition. After the flow stabilized (average of 2 minutes) then the time evolution of scour depth was recorded using an endoscope camera (5.0 MP USB Endoscope, NIDAGE 50FT Inspection Camera) inside the pier focussed on a ruler attached to the front of the pier, and the endoscope camera had image size of 2592×1944. The results of time history scour depth for each flow condition are presented in Figure 3-2. The measurement of temporal scour depth by endoscope camera was calibrated with an average error of 4.38%. As for the reason for employing 60min test durations, this study focused on the temporal evolution of scour depth instead of equilibrium scour depth. Further, given that initial scour develops quickly, capturing the first hour of the process is most useful for assessing the current models. In addition, the correct simulation of the rapid initial scour is important for predicting scour depth in flood events. Lastly, other previous studies have already done tests with longer durations (Lança et al. 2010), and their data sets are also incorporated herein to validate the models.

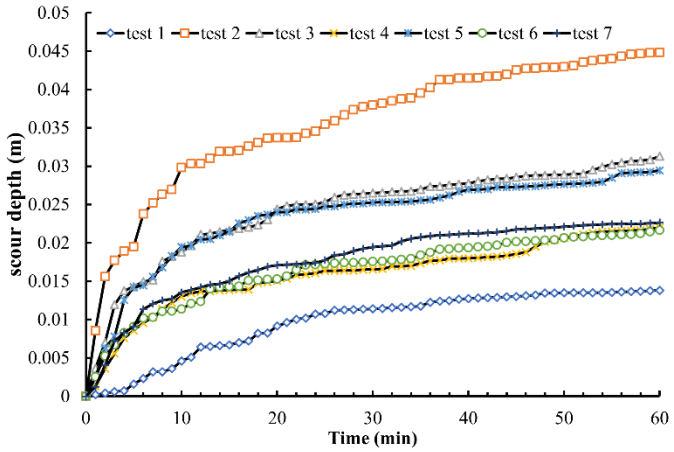

Figure 3-2 Temporal evolution of scour depth in front of the pier

The previous literature data to be used as input data were sourced from Alabi (2006), Chang et al. (2004) and Aksoy et al. (2017), Mia and Nago (2003) 665 data points in total were used to develop MGGP

model for the temporal evolution of scour at a circular bridge pier. The validation data included data from Lança et al. (2013) and the new experimental data from the present study (889 data points in total). The validation data are independent of previous studies and thus can be used to conduct an error evaluation. A detailed overview of the range of data is shown in Table 3-2.

Table 3-2. Summary of data sets

	Experiments	U(m/s)	h(m)	U/u_c	$\boldsymbol{D_p}$(m)	d_{50}(mm)	σ
Input Data	Alabi (2006)	0.195-0.248	0.115-0.23	0.7-0.89[a]	0.073-0.115	0.53	1.23
	Chang et al. (2004)	0.227-0.39	0.015-0.03	_	0.1	0.71-1.0	1.2-3.0
	Aksoy et al. (2017)	0.369-0.441	0.176-0.194	0.48-0.56[b]	0.04-0.2	3.47	1.39
	Mia and Nago (2003)	0.313-0.389	0.16-0.30	0.71-0.82[c]	0.06	1.28	1.29
Validation data	Lança et al. (2010)	0.252-0.295	0.13-0.16	-	0.063-0.080	0.86-1.28	1.40-1.46
	Present study	0.223-0.311	0.18-0.32	0.506-0.707[a]	0.09	1.16	1.28

Note: Critical mean velocity u_c is determined by [a]: (Aksoy et al. 2017)[b]: (Melville and Sutherland 1988): from the (Mia and Nago 2003) [c]

3.2.2 Normalizing the variables

The temporal evolution of scour depth is affected by sediment material (size d_{50}, gradation σ, density ρ_s); pier characteristics (alignment, shape, size D_p), although the present study is limited to circular piers; flow variables (depth h, velocity U, viscosity μ, water density ρ_w); gravitational acceleration g, and time t (Melville and Chiew 1999):

$$d_s = f\{\{h,U,g,\rho_w,\mu,S\},\{d_{50},\rho_s,\sigma\},\{D_p\},t\} \tag{3-5}$$

where h =approaching flow depth; d_s =the temporal scour depth at the time t; U=approaching average flow velocity; d_{50}=mean sediment size; ρ_s=density of sand; S=energy slope; t=time; σ=nonuniformity of sediment $\sqrt{d_{84}/d_{16}}$, and d_{84} and d_{16} are the grain diameter at 84% and 16% passing. Often, non-dimensional parameters are utilized via dimensional analysis to establish the function to predict the development of scour depth.

Non-dimensional analysis is necessary to start the MGGP model development, and Buckingham nondimensional methods were applied. The diameter of the pier D_p, mean velocity U, and density of water $\rho_w$were used as repeat variables, and the following non-dimensional variables were obtained: $\Pi_1 = d_{50}/D_p$, $\Pi_2 = h/D_p$, $\Pi_3 = \rho_w U D_p/\mu$, $\Pi_4 = \sigma$, $\Pi_5 = Ut/D_p$, $\Pi_6 = U/\sqrt{gD_p}$, $\Pi_7 = d_s/D_p$, $\pi_8 = S$, $\pi_9 = \rho_w/\rho_s$. It should be noted that π_8 was ignored in the subsequent analysis due to a lack of available data, and π_9 was neglected because it had a constant value in the data set. Finally, the standard non-dimensional equation for the temporal scour depth was obtained.

$$\Pi_7 = \Pi_1\Pi_2\Pi_3\Pi_4\Pi_5\Pi_6 \tag{3-6}$$

In addition, previous empirical formulas also proposed their nondimensional form, and the variables series of d was used to distinguish the standard nondimensional variable. Three groups of normalized variables were applied in the present study:

$$\begin{cases} d_9 = \dfrac{d_s}{d_{se} = d_1 d_2 d_6} = f\left(d_6, d_7\right) \\ d_{10} = \dfrac{d_s}{L_R} = f\left(d_3, d_4, d_5\right) \\ d_{11} = d_s / D_p = f\left(d_2, d_6, d_8\right) \end{cases} \tag{3-7}$$

where group one $\{d_1, d_2, d_6, d_7, d_9\}$; group two $\{d_3, d_4, d_5, d_{10}\}$; group three $\{d_2, d_6, d_8, d_{11}\}$; $d_1 = d_{50}/D_p$; $d_2 = h/D_p$; $d_3 = F_d$; $d_4 = \sigma$; $d_5 = T_o$; $d_6 = U/u_c$; $d_7 = t/t_e$; $d_8 = t_A$; $\mathrm{t_o} = t\left[\sqrt{d_{50} g(\rho_s - \rho_w)/\rho_w}/L_R\right]$; $t_A = \left\{t d_{50}\left[\sqrt{(\rho_s - \rho_w)/\rho_w g d_{50}}/D_p^2\right]\right\}$; $F_d = U/\sqrt{d_{50} g(\rho_s - \rho_w)/\rho_w}$; $L_R = \left(D_p h^2\right)^{1/3}$

It should be noted that Eq. (3-7)group one is adopted from Melville and Chiew (1999), while Eq.(3-7) group two is adopted from Oliveto and Hager (2002); likewise, Eq. (3-7) group three is from Aksoy et al. (2017). These normalizing styles are all applied separately to determine a better function for the temporal evolution of scour depth.

3.2.3 Multigene Genetic Programing method

Multigene Genetic Programing (MGGP), which is an extension of the GP approach, is a search model involving computer programs such as mathematical expressions, decision trees, polynomial constructs, and logical expressions. Both MGGP and Gene Expression Programming (GEP) are advancements of the GP method, although the algorithm structure is different. GEP computer programs are encoded into linear chromosomes and further expressed into expression trees (Ferreira 2001). The differences between MGGP, GEP, and GP are shown in Mehr and Safari (2020).

MGGP develops new models through an evolution process, and it is not necessary to input the structure of the function, thereby avoiding bias in the model definition. In addition, MGGP, as a branch of GP, uses a lower depth of GP trees leading to simpler functional forms, while multi-genes are applied to ensure the good fitness of the model. The mathematical expression of MGGP is formed by adding several genes together, and a bias term is used to incorporate them:

$$f(y) = a_0 + a_1(Gene_1) + a_2(Gene_2) + \cdots + a_i(Gene_i) + \cdots a_N(Gene_N) \tag{3-8}$$

where a_0 = the bias term; $\mathrm{Gene_i}$ = the ith gene involved to form the model; N = the number of genes; $a_1 \ldots a_i \ldots a_N$ is the weight of the corresponding gene.

Multigene are developed to form the function and are distributed with different weights. Among these genes, genetic operations are involved to evolve the generation of the model. The operation processes mainly include crossover, mutation, and reproduction. An example to show how it works is shown in Supplementary II Figure S0. Compared with traditional GP, the MGGP also involves the evolution of the model by exchanging the subtree term. More detailed information about MGGP can be seen in (Garg et al. 2014; Yan and Mohammadian 2019)

The MGGP model applied in the present study is based on the MATLAB codes of toolbox GPTIPS2 (Searson 2015), which is an open-source algorithm and able to be modified. Firstly, the input data sets were randomly divided into various proportions of "training set" and "testing set" data. Secondly, the variables were input into the MGGP model based on the normalizing shown in Eq. (3-7). Thirdly, the parameter of model architecture also needs to be determined such as the maximum number of generations of evolution, the number of genes, and the population size. A sensitivity analysis on the maximum generations showed that using maximum generations=2000 would be more than sufficient to ensure RMSE convergence which is around 300 generations (Supplementary II Figure S1).

Similar sensitivity analyses were also performed to determine the number of genes and the population size. The population size set in the model was 500 with a maximum number of generations of 2000, and 4 genes were applied. The probability of a Pareto tournament is 0.3 which works for the preference of simplicity. The function set enabled for defining the MGGP model is the default setting with +, -, *, /, exp, log, abs, cube, exp, square, tanh, sqrt, and neg, and the setup is summarized in Supplementary III Table S1.

3.3 Results and evaluation

3.3.1 Criteria of error evaluation

To evaluate the accuracy of the models, the following error metrics were used: root means square error (RMSE), normalized root mean square error (NRMSE), Nash-Sutcliffe coefficient (NASH), and Pearson correlation coefficient (R^2). Smaller values of RMSE and NRMSE mean higher accuracy of the model, whereas the E value and R^2 , when close to 1 corresponds to a better match of the model. A correlation coefficient R^2 of 0 means that there is no linear relationship between the variables. Collectively, these criteria can comprehensively quantify the error and correlation of the model.

$$RMSE = \sqrt{\frac{1}{n}\sum_{i=1}^{n}\left(y_{mi} - y_{pi}\right)^2} \tag{3-9}$$

$$NRMSE = \frac{RMSE}{\bar{y}_m} \tag{3-10}$$

$$NASH = 1 - \frac{\sum_{i=1}^{n}(y_{mi} - y_{pi})^2}{\sum_{i=1}^{n}(y_{mi} - \overline{y_{mi}})^2} \tag{3-11}$$

$$R^2 = \left(\frac{\sum_{i=1}^{n}(y_{mi} - \bar{y}_m)\cdot(y_{pi} - \bar{y}_p)}{\sqrt{\sum_{i=1}^{n}(y_{mi} - \bar{y}_m)^2 \cdot \sum_{i=1}^{n}(y_{pi} - \bar{y}_p)^2}} \right)^2 \tag{3-12}$$

where y_{mi} =measured value; y_{pi} =predicted value; $\bar{y}_m$ =mean measured value; $\bar{y}_p$ =mean predicted value; N= number of points.

3.3.2 Sensitivity analysis

MGGP models were developed using the variables determined by the Buckingham non-dimensional method Eq. (3-6). Further, the influences of each variable on the MGGP model were evaluated; the same apportions of training and testing data (3:1) were applied, and the influence of each variable was obtained by deactivating the variable. It might also be pointed out that 3: 2 splitting of the input data for the training and testing data was also tested, and it was found that, although the individual model errors varied somewhat between 3:2 versus 3:1 splitting, this did not change the results of sensitivity analysis for the role of each variable. The resulting equations are shown in Supplementary II Table S2, and the error analysis for each equation is shown in Table S3. The error of prediction without Π_1, Π_2, Π_3 does not exhibit a significant change, and this indicates that sediment size, flow depth, and viscosity have minimum influences on the prediction of input data. However, the time scale plays the most significant role in the predictions as the error significantly increases without the time scale. In addition, sediment gradation and mean velocity can also, apparently, affect the predictions of the scour depth in terms of time.

Error evaluation was further applied to the validating data, and the sensitivity analysis results are shown in Table S4. The MGGP model reached a reasonable prediction when deactivating the$\Pi_2 = h/D_p$, $\Pi_3 =$

$\rho_w UD_p/\mu$, and $\Pi_4 = \sigma$, and the prediction was much worse when deactivating $\Pi_5 = Ut/D_p$, $\Pi_6 = U/\sqrt{gD_p}$. This implied that sediment gradation, time scale, and mean velocity had a greater influence on the prediction of scour depth, especially with respect to time.

3.3.3 MGGP models with variables based on previous equations

Three types of normalized variables were executed to develop MGGP models, based on Eq. (3-7) . The results of the MGGP models are all presented in the Supplementary III Tables. Different proportions of training and testing data were separately tried to develop new models to achieve a better prediction. As Table S1 shows, the splitting proportions of input training and testing data evaluated for the development of a new model were (0.6, 0.4), (0.75, 0.25), (0.90, 0.10), and (1.0, 0.0). In addition, multigene gene programming can return to single gene programming when the gene number is set as 1.

Table S5 shows the MGGP models developed using Eq. (3-7) group one variable from the empirical function of Melville and Chiew (1999), and their error statistics are shown in Table S6. The functions based on the nondimensional form of Eq. (3-7) group one are generally far from satisfying accuracy. Eq. (S2) behaves best among them, for both the input data and validating data. Thus, the MGGP model developed with a higher proportion of training data performed better for the input data, and its behavior for validating is also expected to improve.

The second type of MGGP model based on the empirical function of Oliveto and Hager (2002) uses Eq. (3-7) group two to develop new functions, and the results are presented in Table S7. Likewise, different proportions were applied to develop new MGGP models to ensure the best performance of the model. Error evaluations were applied to quantify the performance or accuracy of these MGGP models, and the results are presented in Table S8. The predictions made by the models were surprisingly good for both input data and validating data while Eq. (S8) behaves the best for the input data, its performance for validating data is not the best one. In addition, the biases of Eq. (S7) and Eq. (S9) are too large to indicate true correlations. The MGGP models developed by a higher proportion of training data here did not lead to better performance for validating data, but, generally, Eq. (S8) has the best prediction for both input data and validating data. Otherwise, it is difficult for single-gene programming to reach a satisfying degree of accuracy with its simple expression.

The third type of MGGP model, based on Aksoy et al. (2017)'s empirical function variables Eq. (3-7) group three, is presented in Table S9. The same data split method in terms of propositions of training and testing data was applied to develop new models or functions. The error evaluations are also conducted using the same criteria, and the results are presented in Table S10. Generally, these models have a good agreement for the input data, which involves the model development, and Eq. (S14) has the best prediction among them. However, it also indicates that this type of non-dimensional form generally behaves poorly for validating data. In addition, the model developed using a higher proportion of training data can behave better for the input data, but this does not result in a good performance for the validating data.

3.4 Discussion

The MGGP method has been utilized herein to propose several functions to predict the temporal evolution of scour depth. By comparing Tables S4, S6, S8, and S10, it is interesting to note that the MGGP models based on non-dimensional variables derived from Buckingham Π dimensional analysis (Supplementary Tables S2) were outperformed by MGGP models derived using non-dimensional variables obtained from previous predictive models (Tables S5, S7, S9). The most successful of these latter MGGP models will now be compared to some typical empirical and mathematical models available in the literature for the temporal prediction of scour depth. Error evaluation based on the input data for these previous

models and the best MGGP models is shown in Table 3-3 as well as the Multiple Linear Regression and Genetic Algorithm (GP) is also presented.

Table 3-3 Summary of error evaluations for typical empirical functions and MGGP models on input data

	RMSE	NRMSE	NASH	R^2
Oliveto and Hager (2002)	0.034	0.499	0.119	0.535
Aksoy et al. (2017)	0.032	0.458	0.259	0.426
Melville and Chiew (1999)	0.039	0.561	-0.113	0.485
Chang et al (2004)	0.034	0.498	0.122	0.413
Mia and Nago (2003)	0.036	0.522	0.036	0.410
Kothyari et al (1992)	0.033	0.482	0.177	0.521
MLR (Pandey et al. 2018)	0.055	0.789	1.21	0.449
GP(Pandey et al. 2018)	0.0498	0.720	-0.836	0.429
MGGP-Eq. (S2)	0.021	0.307	0.667	0.683
MGGP-Eq. (S8)	0.015	0.223	0.825	0.834
MGGP-Eq. (S14)	0.017	0.250	0.779	0.779

Melville and Chiew (1999), Oliveto and Hager (2002), and Aksoy et al. (2017) are considered the typical empirical functions. Among them, Aksoy et al. (2017) had the best accuracy for input data as its RMSE is the smallest; however, this is not an independent test, as an important part of the input data is from (Aksoy et al. 2017), which might contribute to its good performance for the input data. On the other hand, compared with typical empirical functions, all three of the MGGP models resulted in better performance. This indicates the advantage of MGGP models to develop relatively better functions. In addition, it was also observed that the performance of the GP and MLR model developed by Pandey et al. (2018) is relatively weak.

The typical empirical, mathematical models, as well as MGGP models, were also applied to conduct an error evaluation in terms of validating data, which is shown in Table 3-4. The validating data are independent of the existing functions and were also not involved in the MGGP model's development; thus, the validation data provide a good test of each model's extension and robustness for the prediction of unknown causes. Firstly, the Melville and Chiew (1999) function has the smallest error among these typical empirical functions, while Kothyari et al. (1992) have the best performance for R^2. In addition, the model of Aksoy et al. (2017) exhibits relatively good performance, although not as good as the input data. Secondly, not all types of MGGP models can induce a better performance for validating data, as it is found that Eq. (S14) behaves poorly compared with Melville and Chiew's function. However, the MGGP model based on Oliveto and Hager variables (Eq. S8) has the smallest error overall, better than any of the existing empirical functions while the GP and MLR models still have relatively weak performance.

Table 3-4 Summary of error evaluations for typical empirical functions and MGGP models on validating data

	RMSE	NRMSE	NASH	R^2
Oliveto and Hager (2002)	0.043	0.605	0.468	0.676
Aksoy et al. (2017)	0.040	0.558	0.547	0.899
Melville and Chiew (1999)	0.033	0.462	0.689	0.852
Chang et al. (2004)	0.047	0.666	0.356	0.640
Mia and Nago (2003)	0.038	0.539	0.577	0.876
Kothyari et al. (1992a)	0.036	0.515	0.615	0.912
MLR (Pandey et al. 2018)	0.0632	0.892	-0.156	0.735
GP (Pandey et al. 2018)	0.0641	0.905	-0.192	0.535
MGGP-Eq. (S2)	0.024	0.340	0.832	0.877
MGGP-Eq. (S8)	0.022	0.314	0.857	0.913
MGGP-Eq. (S14)	0.029	0.404	0.762	0.910

Notably, the correlation criteria of NASH and R^2 are relatively high for the Kothyari et al. (1992a) and Aksoy et al. (2017) empirical functions, but the error of these is also very high, suggesting bias in the predictions. The predicted and measured scour depths for Aksoy et al. (2017), Kothyari et al. (1992a), and Melville and Chiew (1999), as well as the three MGGP models developed in the present study, are shown in Figure 3-3.

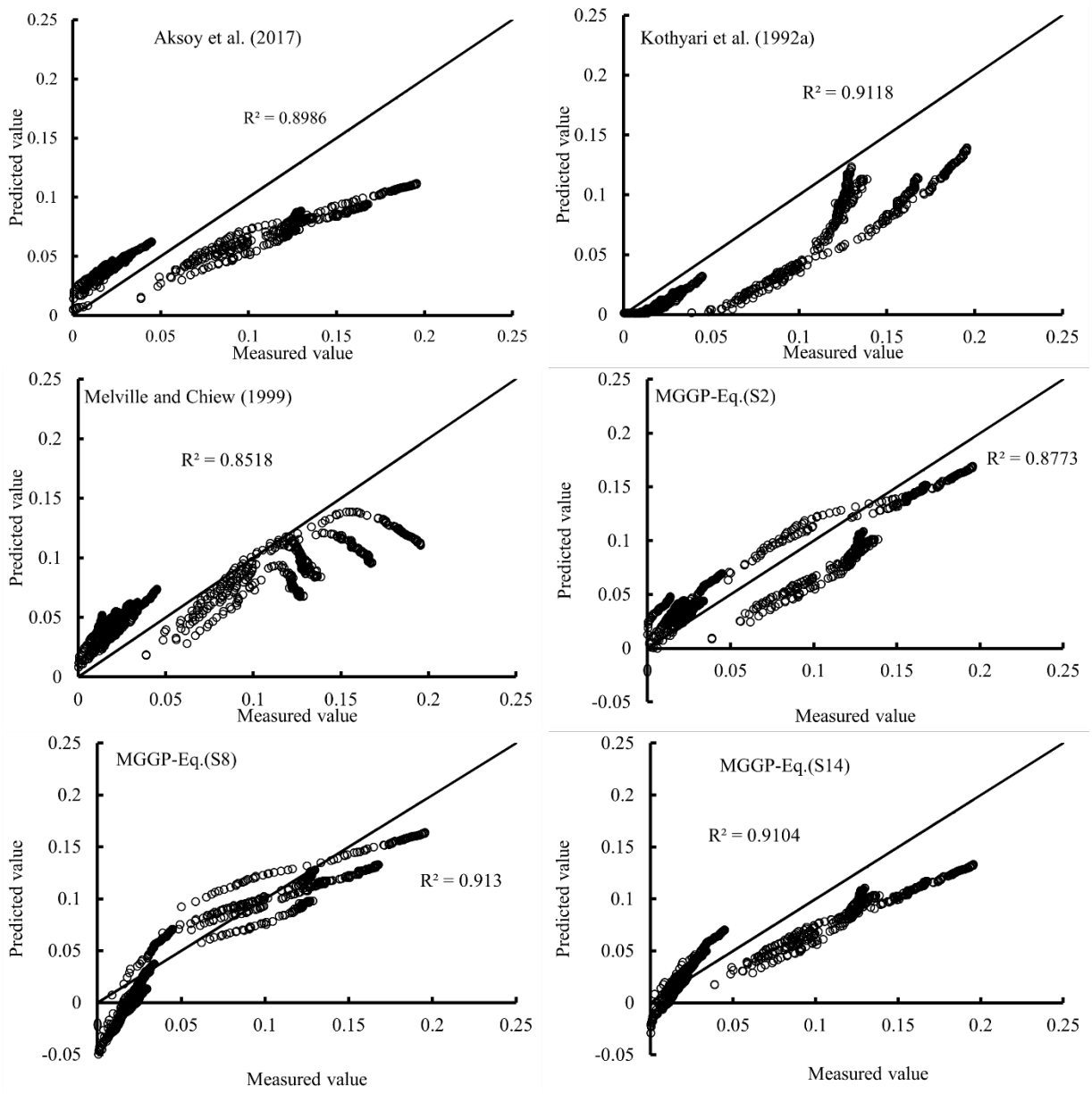

Figure 3-3 Comparison of the measured value and predicted values for the typical empirical function for validating data

As surmised, Kothyari et al. (1992a) achieved a very high correlation for validating data, but its error is also very high due to negative bias. Thus, R^2 cannot completely represent the accuracy of the model, and RMSE and NASH criteria are also helpful to quantify the accuracy of the model. Of the MGGP models, Eq. (S8) has the smallest RMSE and best Nash coefficient, but it is also found that there are many meaningless negative points; this is due to the utilization of log functions in the MGGP. In contrast, the MGGP model Eq. (S2) has a better physical meaning due to fewer meaningless points and a consistent trend with the measured value. It is worth noting that the MGGP model Eq. (S2) has fewer input variables and is thus less prone to overfitting and likely better applied to predict the evolution of scour depth.

Herein, it has been shown that different MGGP models with different reliability can be generated if the proportion of training and testing data used to develop the model is varied (Tables S5-S10). Even more importantly, additional independent validating data must be reserved to evaluate the generated models. As

with all empirical models, MGGP models are subject to overfitting, thus validating data should not be involved in the development of AI models to ensure fair and objective evaluation. Nonetheless, it should be recognized that MGGP models should not be applied for the prediction of situations beyond the range of parameter values considered in model development. This could also be observed in GP and MLR (Pandey et al. 2018) models, and this is also the reason that their models could not reach a good performance in this study. In the present case, the data sets selected to evaluate the time-dependent scour models are mainly from lab experiments, so field data might be necessary to further develop and evaluate the models. It should also be pointed out that some models have special application conditions; for example, Lu et al. (2011) worked for nonuniform pier diameter, while Chang et al. (2004) and Link et al. (2017) predicted temporal scour depth at bridge piers in unsteady flow conditions. Wang et al. (2022) investigated the scour depth in the double-layered sediment considering the mixture of coarse, medium, and fine sand. The selected non-dimensional variables are also important for MGGP models to develop a good function; this indicates that MGGP is helpful to determine the relevant parameters and structure of the predictive formula. In some cases, insensitive variables are not utilized in the developed MGGP (e.g., Π_3, see Table S3). Lastly, it should be noted that empirical models and MGGP models might also lead to meaningless negative points if log functions are utilized.

3.5 Conclusions

A comprehensive review of the models of the temporal evolution of bridge pier scour was presented in this study. Existing models for time-dependent scour development were summarized and categorized into mathematical models and empirical models as well as artificial intelligence models according to the derivation. Several experimental data from the laboratory were used to develop MGGP models for temporal scour depth at a bridge pier. The accuracy of typical mathematical, empirical models and MGGP models developed herein was evaluated using the criteria of root mean square error (RMSE), normalized RMSE, NASH coefficient, and Pearson's coefficient. It was found that an appropriate set of non-dimensional variables was necessary to develop a high-accuracy MGGP model. The MGGP model developed based on Melville and Chiew's (1999) non-dimensional variables performed best, outperforming the existing empirical and mathematical functions for both input data and validating data.

Chapter 4. Influence of Dynamic Woody Debris Jam on Single Bridge Pier Scour and Induced Hydraulic Head

4.1 Introduction

Woody debris from the upstream watershed attached to bridge piers often results in the formation of woody debris jams. The presence of woody debris jams leads to the reduction of cross-sectional flow area and strengthens downward flow close to the pier, which enhances the scour process at the base of bridge piers. This can induce greater scour depth than design guidelines prescribe. In addition, woody debris jams can also result in an extra load on the bridge such as the impact loads on the piers which occurred in the initial contact of debris with the pier (Haehnel and Daly 2004; Hasanpour et al. 2021; Stolle et al. 2018) or on the superstructure (Hasanpour et al. 2022), and the damming load on the superstructure (Istrati et al. 2020; Oudenbroek et al. 2018) in the extreme fluvial events. Thus, the presence of woody debris jams affects the stability of bridges and threatens their safety. Some documented failure examples were mentioned in (Pagliara and Carnacina 2011).

Beyond the adverse influence on bridge infrastructure, wood logs or debris play an important role in river systems. Studies related to woody debris have involved many aspects such as the process of debris entering the river (Mazzorana et al. 2011; Mazzorana et al. 2009), debris volume estimation (Comiti et al. 2016; Ruiz-Villanueva et al. 2016; Tonon et al. 2018) and their influence on river morphology (Klaar et al. 2011). The dynamics of wood debris involve entrainment (Braudrick and Grant 2000), motion (Braudrick et al. 1997), and deposition (Braudrick and Grant 2001) processes. Gravity force, dragging force, and friction force determine the movement of logs in the river, and critical conditions have been investigated in previous studies (Bocchiola et al. 2006; Braudrick and Grant 2000; Chen et al. 2019; Crosato et al. 2013; Haga et al. 2002). The transport process of debris was another important issue that determined how far the debris can travel (Braudrick et al. 1997) and where it might accumulate (Davidson et al. 2015). A debris motion model was also proposed to describe the transport of woody debris (Persi et al. 2018). In addition, the presence of debris significantly increased the possibility of bridge failures as clarified by Diehl (Diehl 1997).

Scour is the engineering term for the erosion of bed material caused by water around the base of the bridge pier (Arneson et al. 2012), and related studies have been going on for several decades. Basing on the critical shear stress velocity of a given sediment d_{50}, the critical mean velocity could be obtained (Melville 1992), and if $U/U_c < 1$, clear water scour occurs whereas for $U/U_c > 1$, it is live bed scour. In clearwater scour conditions the spatio-temporal evolution of scour depth continues until it reaches a value independent of time called the equilibrium scour depth. Kothyari et al. (Kothyari et al. 1992) proposed a mathematical method to calculate time-dependent scour depth considering the influence of the growth of a vortex on bed shear stress. This method was further developed for live bed scour (Kothyari et al. 1992), nonuniform circular piers (Lu et al. 2011), and continual development by modeling the vortex which initiated scour (Mia and Nago 2003). Yanmaz and Altinbilek (Yanmaz and Altinbilek 1991) employed a sediment transport model using a sediment pick-up model to derive a mathematical method to predict the temporal evolution of scour depth. Dey (Dey 1999) and Yanmaz (Yanmaz 2006) continued this idea of using different sediment pick-up models to develop a new model. Some studies applied this idea to different objects like bridge abutments (Yanmaz and Kose 2009) or dual bridge piers (Yilmaz et al. 2017).

On the other hand, empirical functions have also been widely used and developed based on experiments using non-dimensional analysis (Aksoy et al. 2017; Chang et al. 2004; Melville and Chiew 1999; Oliveto and Hager 2002). As for equilibrium scour depth or maximum scour depth, Melville (Melville 1997)

investigated the influence of the flow intensity, water depth, sediment size, gradation, and pier shapes on equilibrium scour depth, and an empirical formula was proposed to predict scour depth. A design method, HEC-18, proposed by the US Federal Highway Administration (FHWA), is widely used to estimate maximum scour depth.

Woody debris significantly changes the flow field and causes additional scour depth. The presence of a woody debris jam obstructs the cross-section of water flow, and the reduction of the flow area leads to an increase in velocity and downward flow (Lagasse et al. 2010; Pagliara and Carnacina 2013). Melville and Dongol (1992) applied a model of steady woody debris to investigate its influence on scouring; an effective diameter of bridge piers was proposed to include the influence of accumulated debris:

$$D_{ep} = \frac{0.52h_d w_d - (h - 0.52h_d)D_p}{h} \tag{4-1}$$

where D_{ep} = the effective width or diameter of the pier; h_d = the height of the woody debris jam from the bottom of the debris jam to the water surface; w_d = the width of the woody debris jam normal to the flow; h was the approach flow depth; D_p = the width or diameter of the pier without the debris jam.

Lagasse et al. (2010) continued this idea and further investigated the different geometry of debris and improved the Equation (4-1) to include the influence of the length of debris jam:

$$D_{ep} = \frac{\alpha h_d w_d (l_d/h)^{\beta} - (h - \alpha h_d)D_p}{h} \tag{4-2}$$

where α = 0.79 for rectangular debris and 0.21 for triangular debris; $\beta = -0.79$ for rectangular debris and −0.17 for triangular debris, β = 0 when $l_d/h \leq 1$; l_d = the length of the woody debris jam.

Lagasse et al. (2010) and Pagliara and Carnacina (2011) investigated rectangular, triangular, and cylindrical shapes of debris accumulation, as well as the roughness and porosity of debris jams (Pagliara 2010) and countermeasures for the scour depth (Pagliara et al. 2010). Their research showed that the blockage ratio caused by the debris jam mainly determines its impact on scour, and the flow contraction caused by the debris jam accelerated the scour process and increased the bridge failure possibility.

Furthermore, Pagliara and Carnacina (2011) also considered the effects of the length of the debris jam on scour depth, and they highlighted the influence of the downstream extension of the debris jam. In addition, Ebrahimi et al. (2018) used various dimensions of the debris block to investigate its influence on sharp nose-pier scour. They found that the height of the debris jam determined the effects on scour depth.

$$\frac{d_s}{d_{s0}} = 1 + \chi(h_d/h)^{1.237} \tag{4-3}$$

where d_s = the equilibrium scour depth in the presence of a woody debris jam; d_{s0} = the equilibrium scour depth without the presence of a debris jam; χ = 0.32 or 3.2 depending upon the experimental source data.

A static debris jam, which meant that the debris jam was shaped like a block (rectangular or triangular) and was quasi-independent of the flow condition, was widely used in the mentioned studies. Static debris jams might not realistically reflect the characteristics of woody debris jams. Moreover, the dimensions of debris were assumed constant while the realistic formation of the debris jam normally includes entrainment, growth, and failure.

A dynamic debris jam, in which the debris jam is formed piece by piece of woody debris and adapted to flow conditions, can directly reflect the process of formation and characteristics of debris jams. Panici and

de Almeida (2018) investigated the formation, growth, and failure process of debris jams via dynamic debris jams. In that study, the debris Froude number was used as the key factor to illustrate the critical dimensions of woody debris jams. Schalko et al. (2019) also used dynamic woody debris pieces to investigate the accumulation probability of debris.

Few studies have examined the influence of dynamic woody jams on bridge pier scour. A static debris jam in the form of a manual debris block cannot properly represent the debris jam formed in reality as it has no relation to flow conditions and the process of debris formation and growth. In order to bridge this gap, the present study applied a dynamic debris jam to investigate its influence on single bridge pier scour in clear water conditions, and the hydraulic head induced by the woody debris jam was also inspected.

4.2 Materials and Methods

4.2.1 Experiment Setup

A comprehensive experimental program was developed to investigate the influence of a dynamic woody debris jam on a single bridge pier scour. The physical model tests were conducted in a flume in the Hydraulic Laboratory of the University of Ottawa, Canada. The flume was 30 m in length, 1.5 m in width, and 0.7 m in depth (Figure 4-1). Two flow straighteners were set up close to the inlet of the water flow to ensure the uniformity required for the flow. A 0.2 m high false plate was set downstream in the flume and was used as a test area for the experimental setting.

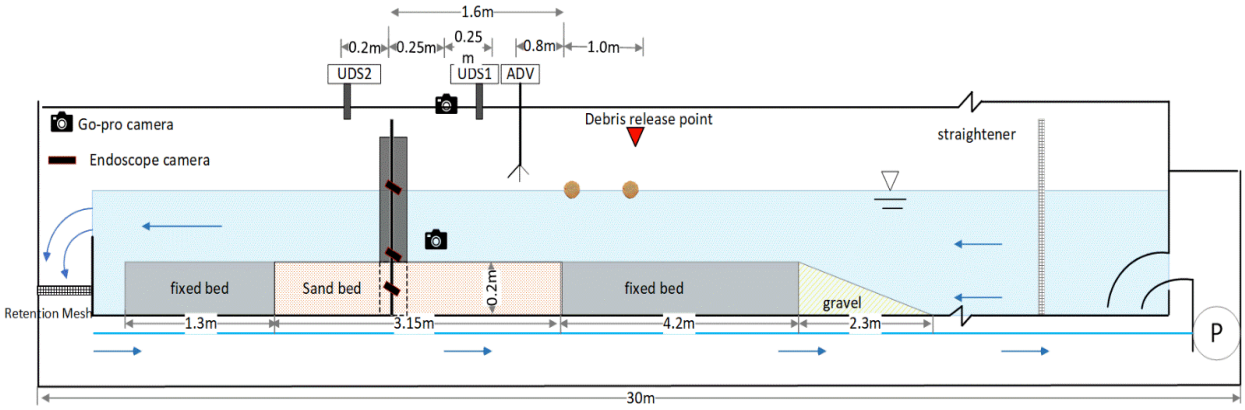

Figure 4-1. Experimental setting (not at scale).

A pier with a diameter D_p= 0.09 m was placed in the sand bed at the test area and the d_{50} for the sand was 1.16 mm with a gradation σ of 1.22. Woody dowels were used to represent woody debris; these were cut into 30 cm sections with the same diameter of 1.27 cm as Figure 4-2 (a) was shown. In total, 792 woody pieces were prepared for the tests.

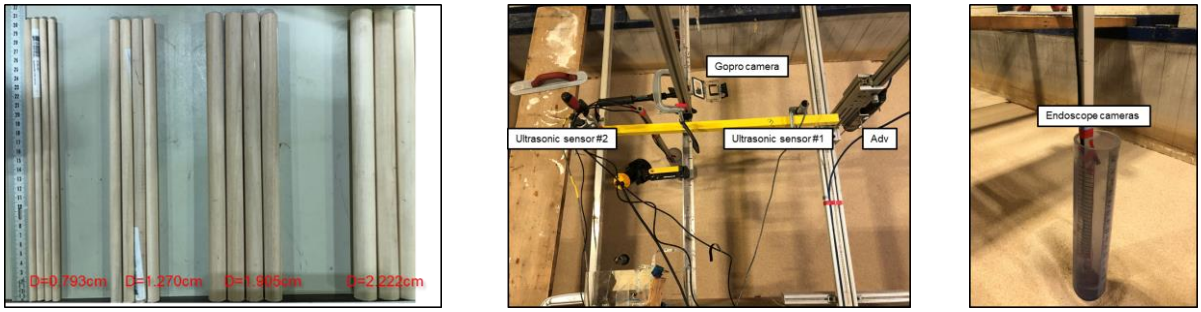

(a) (b) (c)

Figure 4-2. (a) Dowel with length 30 cm and diameter 1.27 cm compared with various diameters dowels (b) instruments set up (c) location of the highest located endoscopic camera

Various instruments were applied to monitor and record the necessary data for analysis, and the arrangement of instruments was shown in Figure 2(b). Two HERO5 Black GoPro cameras (https://gopro.com/en/us/update/hero5, assessed on 29 September 2022) were set up to capture the dimensions of the woody debris jam and a Linear model with a sampling rate of 60 fps was applied. One GoPro camera was fixed at the top of the flume at a height of 1.74 m above the sand bed while the other one was placed underwater in a transversal direction near the sidewall from upstream of the pier. Three endoscope cameras (5.0 MP USB Endoscope, NIDAGE 50FT Inspection Camera) were used and set inside the bridge pier as Figure 2(c) was shown, and the sampling rate of 20 fps with an image size of 2592×1944. One endoscope camera was installed at the top and positioned near the water surface of each test while the other two endoscope cameras were placed at an angle to obtain a wider view with one of the heights of about 5 cm above the sand bed and another one of 6 cm below the sand bed to capture the scour depth. A ruler was installed along the center line inside of the pier to facilitate observing the vertical development of the scour hole close to the pier. In addition, two MassaSonic PulStar ultrasonic distance sensors (https://www.massa.com/industrial/ultrasonic-sensors/pulstar, assessed on 29 September 2022) were applied to record the time history of the water level around the woody debris jam with a sampling rate of 5 Hz. One was fixed upstream of the pier at a distance of 0.5 m close to the centerline, and another one was fixed at 0.2 m behind the pier. A Vectrino Acoustic Doppler velocimeter (ADV) (https://www.nortekgroup.com/products, assessed on 29 September 2022) was applied to measure the vertical distribution of velocity at 0.7 m upstream of the pier. Each ADV point measurement had a duration of 2 min with a sampling rate of 100 Hz. A filter developed by Rennie and Hay (2010) (Rennie and Hay 2010)was applied to remove the noise of ADV data, and time-average velocity was obtained for each point.

4.2.2 Instrument Calibration and Error Evaluation

The accuracy of the MassaSonic PulStar ultrasonic distance sensors was 0.25 mm. The sensors were calibrated using different known water levels such that a relation between the electronic signal and water level was derived. The Go-pro cameras were also calibrated and found that the linear model was able to capture the dimensions of the debris jam at a linear error of 0.673%. The endoscope cameras placed inside the pier directly read the scour depth by recording the time-varying reading of the sand bed level during each test. A wide-angle was used to monitor the range of scour depths, and the endoscope cameras were calibrated with an average error of 4.38% due to angular perspective.

4.2.3 Experiment Matrix

Uniform and steady flow were applied to investigate scour depth under various flow conditions in the presence of the woody debris jam. A vertical distance of 2 cm was set as the flow velocity measuring space interval close to the water's surface while 1 cm was used closer to the sand bed. As a down-looking ADV

was utilized, a log law formula (Rennie and Church 2010) for vertical velocity distribution was obtained by linear regression and was then used to calculate the velocity magnitude close to the water's surface.

$$u = \frac{u_*}{\kappa} ln(z) + \frac{u_*}{\kappa} ln\left(\frac{30}{k_s}\right) \tag{4-4}$$

where u = the local velocity at height z ; z = water level elevation; u_* = the shear velocity; κ = the von Karman constant (0.41), and k_s = the bed roughness. Fitted velocity profiles are shown in Figure 4-3, from which the depth-averaged velocities for each test were calculated by integration.

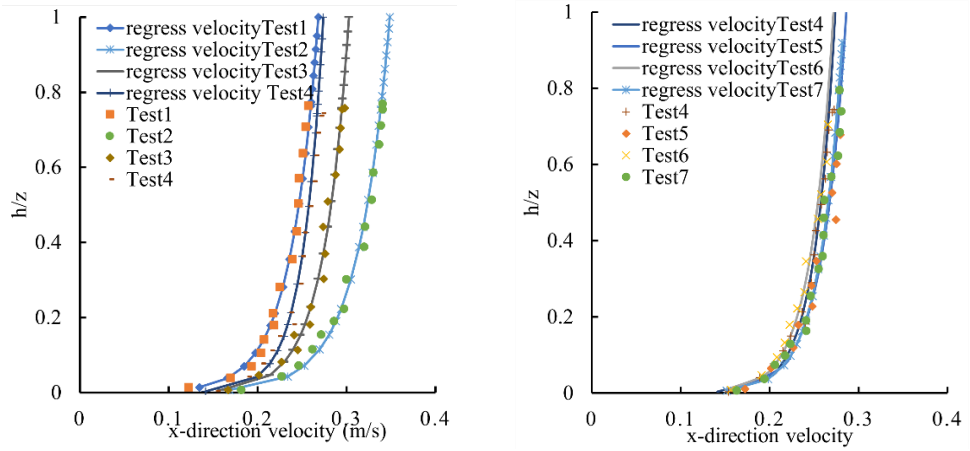

(**a**) (**b**)

Figure 4-3 U component normalized by the water depth h (**a**) with an approximate water depth (**b**) with an approximate mean velocity.

The mean flow velocity was in the range of 0.223 to 0.311 m/s and the water depth varied between 0.185 and 0.326 m. The detailed information for the hydraulic conditions of each test is presented in Table 4-1. It was noticeable that the flow intensity U/u_c was smaller than 1.0 to ensure that only clear water scour occurred for all tests.

Table 4-1 Experiment matrix.

Test Number	Water Depth h (m)	Mean Velocity U (m/s)	Shear Velocity u_* (m/s)	Froude Number F_r	U/u_c	Dowel Size Applied
1	0.284	0.223	0.0129	0.157	0.506	30 cm in length and 1.27 cm in diameter
2	0.278	0.311	0.0150	0.221	0.707	
3	0.281	0.273	0.0119	0.193	0.620	
4	0.286	0.250	0.00959	0.175	0.566	
5	0.184	0.256	0.0112	0.214	0.617	
6	0.234	0.246	0.0105	0.186	0.573	
7	0.326	0.257	0.0106	0.172	0.572	

Note: Hydraulic radius was used for the reference length for the Froude number, U_c was calculated according to the reference (Aksoy et al. 2017).

4.2.4 Scale Effects

The relation between the prototype object and the model object was described by the parameter

$$\lambda = \frac{\text{Prototype value}}{\text{Model value}} \tag{4-5}$$

Based on Froude's similitude, a value of $\lambda = 30$ would mean the length of the prototype log was 9 m while the pier diameter was 2.7 m. Based on the scale factor of λ, the length of the prototype log would be

9 m while the pier diameter would be 2.7 m. A debris length of 9 m is typical in prototype debris jams on bridge piers, although even longer pieces have also been observed in the field (Diehl) (Diehl 1997). Prototype flow conditions were at a range of 1.15–1.71 m/s for mean velocity and 5.53–9.78 m for water depth. In addition, Reynolds number Re in present tests was in the range of 47,104~86,458, and the flow was fully developed. Based on the Hjulström diagram values of U_c for given particle sizes, and equivalent U/U_c the ratio in lab and prototype, the prototype sediment size would be approximately 20 mm (i.e., coarse gravel). Note that the sediment scale factor deviates somewhat from λ.

4.2.5 Procedures

For each test case, a base case test without debris was studied under the same flow condition. In addition, the woody dowels also need to be submerged in water completely for 2 days before being applied to the experiments. Firstly, the pump valve was opened with a small discharge to slowly increase the water level in the flume to first wet and submerge the sand bed to avoid scour from occurring before the designed flow condition was achieved. Prior to the flow condition reaching the prescribed valve position, the endoscope video camera was turned on to monitor the scour depth in front of the pier. Then, the time was recorded when the designated test flow rate was applied. The ADV was used during the base case bank tests (without debris) to measure the vertical distribution of mean velocity with a sampling rate of 100 Hz. The test flow rate was then used for the experimental run. The same procedures were used for the test in the presence of a woody debris jam to reach the set flow conditions. The endoscope video cameras with a sampling rate of 20 fps and GoPro camera with a sampling rate of 60 fps as well as the ultrasonic distance sensor (US gauge) operating at a sampling rate of 5 Hz were also turned on before the set flow rate condition was achieved. Then, debris pieces were released 2.6 m upstream of the pier at a frequency of 12 pieces per minute (an average of one piece every 5 s) after the steady flow condition was reached. There were some unavoidable unstable flow conditions that occurred when the flow rate reached its set value for each test. Thus, a 2-min time interval was used for the stable flow conditions to occur; the time ending of the interval was then used as the scour initiated. Some light scours occurred for some sets prior to this time of origin, but as shown by the endoscope video camera had already been turned on and had recorded the video images of the scour, this had a minimal influence on the scour results. The duration of all the tests was one hour, and it might not reach an equilibrium scour. The reason for selecting one hour was to consider the feasibility and respect the fact that the initial one hour could cover the rapid change period of scour depth. A retention mesh and collection box located behind the flume end weir were used to capture the woody debris.

4.3 Results

4.3.1 Scour Depth

The time evolution of the scour depth was determined using the video capture by the endoscope camera. The time evolution of the scour depth of all tests in the presence or not of the debris jam is shown in Figure 4-4.

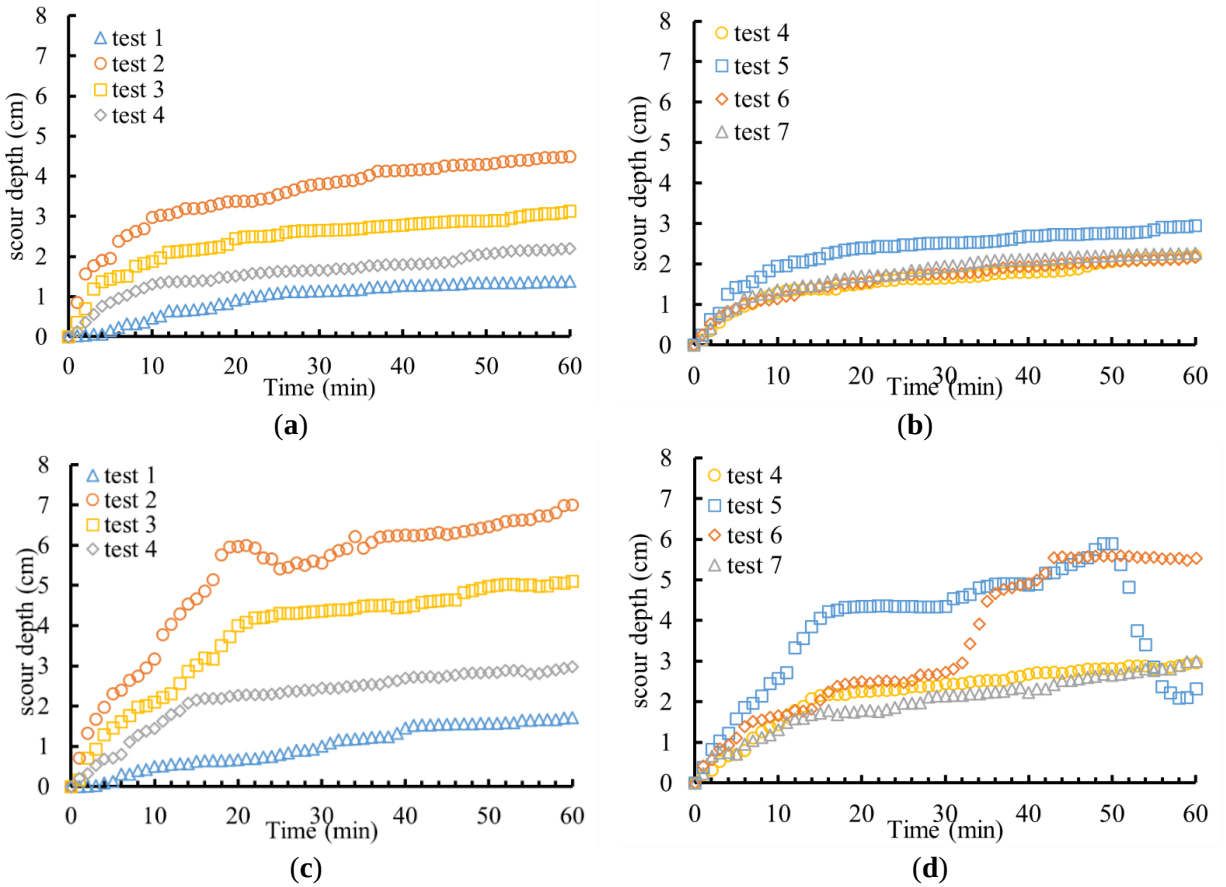

Figure 4-4 Temporal evolution of scour depth in front of the pier every minute: (**a**,**b**) tests without debris jam, (**c**,**d**) equivalent tests in the presence of debris jam.

Blank tests, with no debris involved, are presented in Figure *4-4*a,b. The tests shown in Figure *4-4*a have the same water depth but varied mean velocity; the results clearly indicated that the increase of mean velocity results in greater scour depth. This has already been clarified in previous studies (Melville 1997; Melville and Sutherland 1988), as U/U_c was used as a variable to compute the equilibrium scour depth in their studies. In addition, the evolution of scour depth in the presence of woody debris is shown in Figure *4-4*c,d, demonstrating that scour depth was substantially increased compared to the test without debris: generally, 1.2–2.5 times greater scour depth. On the other hand, the process of scour depth development in the presence of woody debris was much more irregular due to the irregular flow caused by the woody debris jam. Further analysis of the influence of woody debris on scour depth is provided in the following sections.

4.3.2 Woody Debris Jam

The formation of the woody debris jam was initiated by one or several woody debris pieces, which are defined in the literature as the key debris or log as Manners and Doyle (Manners and Doyle 2008) defined. The first key debris or several key debris pieces formed a stable structure in front of the pier, Then, the woody debris jam continued to grow as more debris pieces were captured by the key debris. It is also noted that when the debris jam exceeded a certain critical size, the woody debris jam failed. This has already been clarified by (Panici and de Almeida 2018; Panici and de Almeida 2020). In the present tests, the duration of a woody debris jam from formation to failure was on average 15–20 min, and at least 3 woody debris jams was formed for tests 2–7 during a one-hour duration. A typical case (test 1) for growth, failure, and rebirth was shown in Figure 4-5.

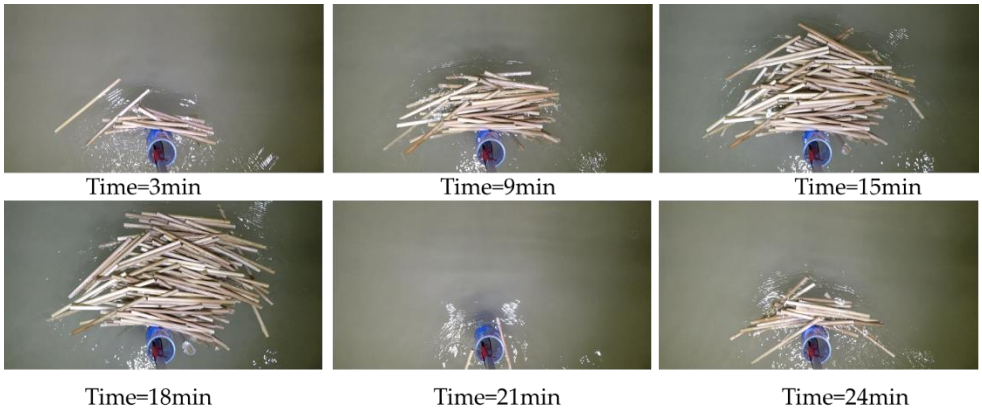

Figure 4-5 A typical case for the growth, failure, and rebirth of dynamic debris jam (test 1).

The time evolution of the dimensions of the woody debris jam was recorded by the GoPro video camera. The plane area of the woody debris jam was obtained by employing an open-source software, ImageJ (https://imagej.nih.gov/ij/, accessed on 29 September 2022). ImageJ was based on Java programming language and is used to analyze the information on video images and was developed by the National Institutes of Health and the Laboratory for Optical and Computational. ImageJ helps deal with the irregular geometry of woody debris jams and can provide the plane area of the debris jam by outlining its geometric boundary. The number of woody debris pieces was also analyzed by counting how many pieces were captured and remained attached to the front of the pier; meanwhile, the number of debris pieces left in the debris jam was also counted by analyzing the video recordings every second. The results of tests 2 and 4 are shown in Figure 4-6 a,b. The temporal evolution of the dimensions of the debris jam as well as the horizontal plan area was also presented in Figure 4-6 c,d. The height of debris jam h_d referred to the distance between the bottom of the debris jam to the water surface in front of the pier. The length of debris jam l_d referred to the maximum longitudinal distance of the debris jam along the centerline in the water surface, and the width of the debris jam w_d referred to the maximum width of debris jam in the lateral direction in front of the pier.

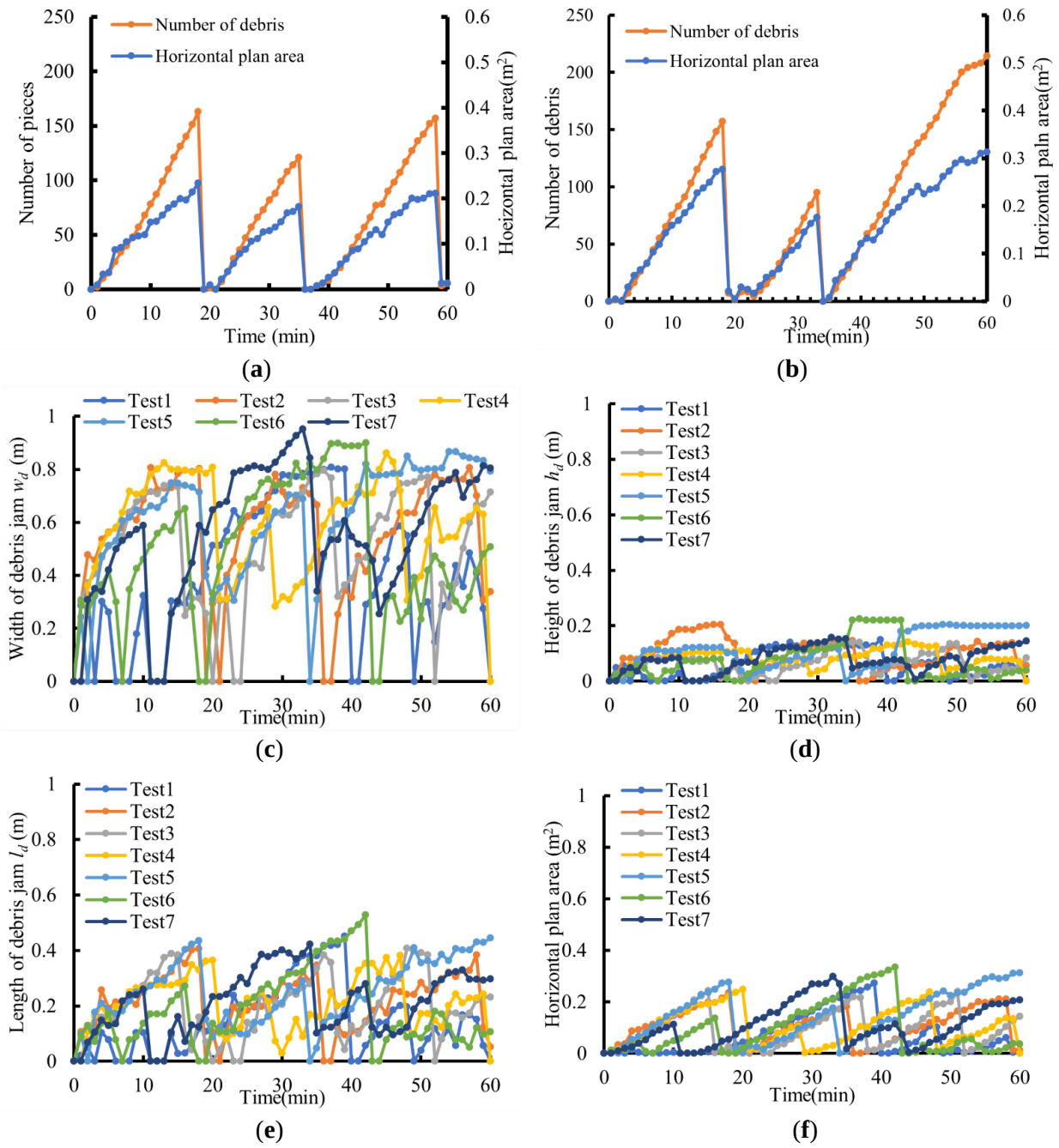

Figure 4-6 Temporal evolution of woody debris pieces in front of the pier as well as the corresponding plane area of the woody debris jam (**a**) test 2; (**b**) test 4, and (**c**–**f**) referred to the temporal evolution of width, height, length, and horizontal plan area of dynamic debris jam.

4.3.3 Time-History of the Water Level

Ultrasonic distance sensors (US Gauge) were used in the present study to record the time history of the elevation of the water surface and the results are shown in Figure 6. Two ultrasonic distance sensors were used: one of them was set up in front of the bridge pier while the other one was set up behind the pier. A fitting curve app in MATLAB was also applied to smooth the water level fluctuations. The difference in the water surface elevation with and without the pier was small in the absence of the woody debris jam as shown in Figure 4-7a. It was observed that the difference between the two ultrasonic distance sensors

significantly increased in the presence of the woody debris jam at the face of the pier (Figure 4-7b). In order to quantify the water rise caused by the woody debris jam, the hydraulic head induced by the woody debris jam of one set was used and defined as:

$$\Delta h = \Delta h_h - \Delta h_{nh} \quad (4\text{-}6)$$

where Δh_h = the difference in the water surface elevation between the front ultrasonic distance sensor and the one behind the pier in the presence of woody debris; Δh_{nh} = the difference in water surface elevation between the front ultrasonic distance sensor (US gauge) and the one behind the pier without the presence of woody debris.

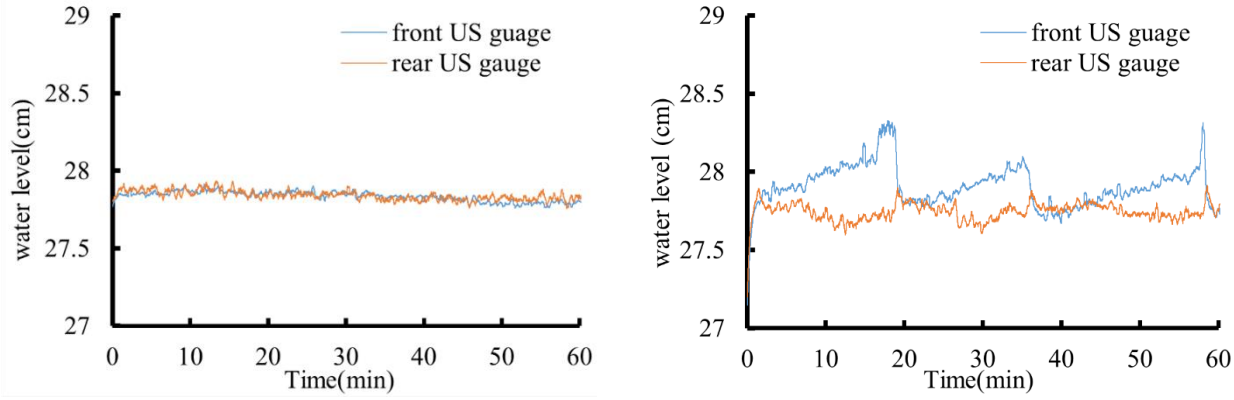

Figure 4-7 Time history of the water level captured by the ultrasonic distance sensors (**a**) without the presence of woody debris in test 2; (**b**) in the presence of woody debris in test 2.

Based on Equation (6), the debris-induced hydraulic head was computed and presented in Figure 4-8, as a function of the number of woody debris pieces, for test 2. It was observed that the woody debris jam debris-induced hydraulic head was directly correlated with the number of woody debris pieces accumulating in the debris jam—as such, a larger number of woody debris pieces accumulated into the formed jam generated a larger hydraulic head.

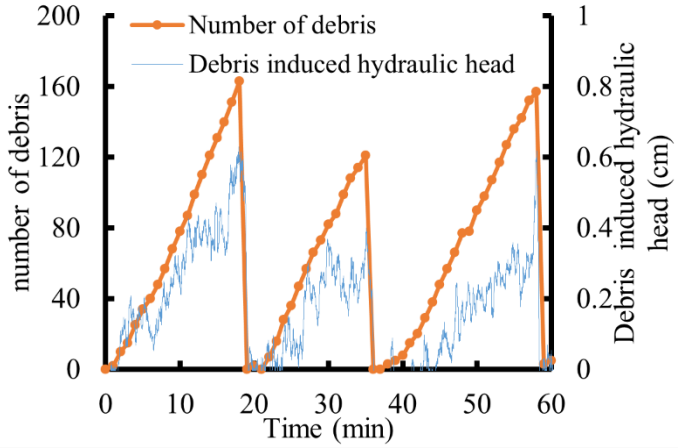

Figure 4-8 Time-history of the hydraulic head and the number of debris pieces in front of the pier test 2.

4.4 Analysis

Debris-induced hydraulic head or scour depth was correlated to the flow parameters (h, u, F_r, R_e, u_*), debris characteristics (L, d_d), dimensions of the woody debris jam (l_d, w_d, h_d), and the pier size D_p and sediment characteristics (d_{50}, σ).

$$\Delta h = \{(h, u, F_r, u_*, R_e), (l, d_d), (l_d, w_d, h_d), (d_{50}, \sigma), D_p\} \quad (4\text{-}7)$$

where F_r = the Froude number; R_e = the Reynold number; L = the length of the debris piece.

4.4.1 Debris Jam-Induced Hydraulic Head

As the woody debris pieces accumulated at the front of the pier, the water surface level was not consistent in front and behind the pier. The hydraulic head was influenced by the number of woody debris pieces accumulated in front of the pier.

Nondimensional analysis was applied though using the flow depth approach, while the debris characteristic was not changed, such that the relative hydraulic head caused by the woody debris jam was mainly related to the hydraulic condition and the dimensions of the woody debris jam:

$$\frac{\Delta h}{h} = \{(h, u, F_r, u_*, Re), (l_d, w_d, h_d), (D_p)\} \quad (4\text{-}8)$$

Various approaches have been tried before to find the correlation between woody debris jams and debris-induced hydraulic heads. According to experimental observations in this study, as the woody debris jam was growing through an increase in the number of woody debris pieces captured, its various dimensions grew commensurably. Thus, it was not appropriate to apply only one dimension like the height or width to quantify the influence caused by the woody debris jam. Finally, the results indicated that the blockage ratio, which was referred to as the ratio of the flow opening blocked by the maximum debris jam (vertical projected area) in stream cross-section consistent with (Parola et al. 2000), can generally be considered to quantify the effects of a woody debris jam on the hydraulic head:

$$\Delta A = \frac{0.5 h_d w_d}{bh} \quad (4\text{-}9)$$

where ΔA = the blockage ratio while the geometry of the woody debris jam is approximated to be triangular, b = the width of the flume; h = the approach flow depth before the debris jam formation.

The Froude number F_r, a non-dimensional parameter characterizing the flow, was used as a common denominator. Thus, results from all tests can be plotted together to investigate the possible relation between the blockage ratio generated by the debris jam and the relative hydraulic head as a function of the Froude number as shown in Figure 4-9. When more debris pieces were captured in front of the bridge pier and thus formed a larger debris jam, this caused an increase of blockage ratio, and the relative hydraulic head was also larger.

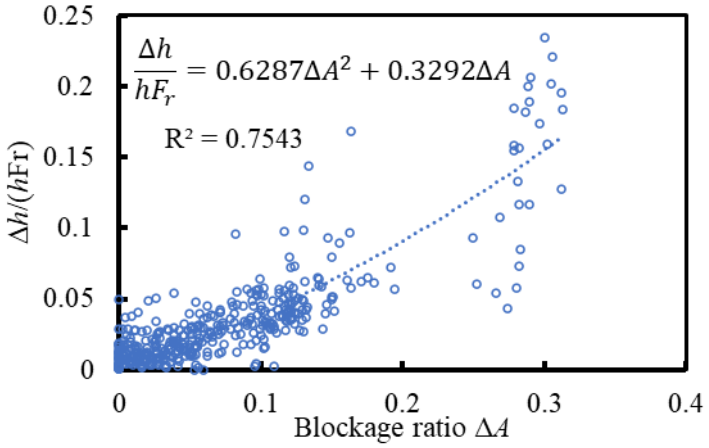

Figure 4-9 Correlation between the debris-induced hydraulic head and blockage ratio ΔA.

The height of woody debris jams h_d, referred to as the distance from the bottom of the debris jam to the water surface, was obtained by the endoscope video camera placed inside the pier—only the maximum height closest to the pier was obtained. Considering the fact that the height of the woody debris jam is difficult to obtain, especially during a natural flood event, the plane (horizontal) area of the woody debris jam was then used to determine the relationship between the woody debris jam and the debris-induced hydraulic head. The correlation between the horizontal plane area of the woody debris jam and the projected vertical area of the woody debris jam is shown in Figure 10a. These results showed that the plane area of the woody debris jam was well correlated with the vertical debris jam area; thus, one should consider both the plan and vertical dimensions of the debris jam to quantify its influence. The coefficient α was defined to relate the plane area of the woody debris jam with the vertical area:

$$\alpha = \frac{0.5 h_d w_d}{A_p} \tag{4-10}$$

where α = 0.266; A_p = the horizontal plane area of woody debris obtained by Image J analysis.

The horizontal plane area of the woody debris jam can be feasibly captured in practice as several approaches can be used to take photos of the woody debris jam in a safe way, especially during flood events. Thus, applying the horizontal plane area of the woody debris approach instead of the vertical area is more feasible to represent the area of the woody debris jam as its boundary can be outlined no matter how irregular it is. Thus, the equilibrium blockage ratio ΔA^* was defined as

$$\Delta A^* = \alpha \frac{Area_{plan}}{bh} \tag{4-11}$$

where ΔA^* = the equilibrium blockage ratio.

The relation between the equilibrium blockage ratio with the relative hydraulic head is presented in Figure 4-10. The equilibrium blockage ratio can achieve an even better correlation than the blockage ratio. This also implied that the geometry of the woody debris jam was irregular, and one could obtain a better correlation if the area of the woody debris jam can be better described. Finally, the debris-induced hydraulic head can be related to the blockage ratio and equilibrium blockage ratio:

$$\frac{\Delta h}{h} = F_r(0.629\Delta A^2 + 0.329\Delta A) \tag{4-12}$$

$$\frac{\Delta h}{h} = F_r(1.58\Delta A^{*2} + 0.206\Delta A^*) \tag{4-13}$$

Generally, the volume taken up by the woody debris in front of the pier blocked the flow and led to the occurrence of water level increase upstream, inducing hydraulic head, which indicated the increase in flood risk. It also needed to point out that the Froude number of the current study was limited, and more experiment data was required to support the effects of the *F*r number on the hydraulic head.

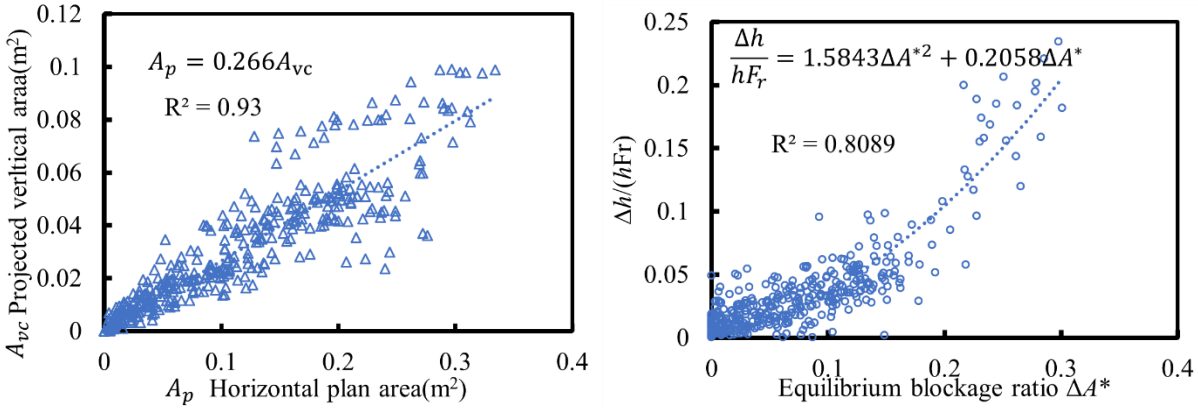

Figure 4-10 (**a**) Correlation between the horizontal plane area of woody debris jam with the projected vertical area of woody debris jam; (**b**) Correlation between the equilibrium blockage ratio with the hydraulic head.

4.4.2 Scour Depth Influenced by Woody Debris Jam

The spatio-temporal evolution of a woody debris jam leads to additional scour and can lead to unexpected failure of bridge piers during flood events. The influence due to woody debris jams on scour needs to be quantified for the purpose of safe design. Non-dimensional parameter K_d was defined to represent the change in scour depth caused by woody debris jams:

$$K_d = d_s/d_{s0} \tag{4-14}$$

where d_s = the scour depth in the presence of a woody debris jam at time t; d_{s0} = the scour depth without the presence of a woody debris jam at time t.

The change in scour depth was generated by the presence and evolution of a woody debris jam as the flow conditions remained unchanged. Therefore, K_d was considered to be correlated to the evolution of a woody debris jam:

$$K_d = \{(l_d, w_d, h_d), \Delta A, \Delta A^*\} \tag{4-15}$$

Several physically meaningful variables were considered to derive K_d. Finally, the equilibrium blockage ratio was applied to better reflect the evolution of the woody debris jam. The temporal evolution of K_d and of the equilibrium blockage ratio ΔA^* was shown in Figure 4-11 and Figure 4-12. Tests 1 to 4 had a similar approach flow depth but varying mean velocity and it was observed that K_d increased with the growth of the woody debris jam for the first peak. However, K_d changed little in the subsequently forming woody debris jams as their dimensions generally did not exceed the peak size of the first debris jam. The K_d value was close to constant after the first woody debris jam provided that the subsequent woody debris jams were smaller or close to the first one. This could first be explained by the scour hole remaining constant, such that the additional scour depth caused by the first debris jam will remain the same and would lead to a greater value of K_d, irrespective of the size of the subsequent woody jam. Secondly, for the first peak of a woody debris jam, the respective base case scour hole was relatively small such that the effects of the woody debris jam were more apparent, and the good agreement with K_d was clear. However, following the first peak, since the scour hole has already formed, the effects of scour depth from the subsequent small woody debris were less significant.

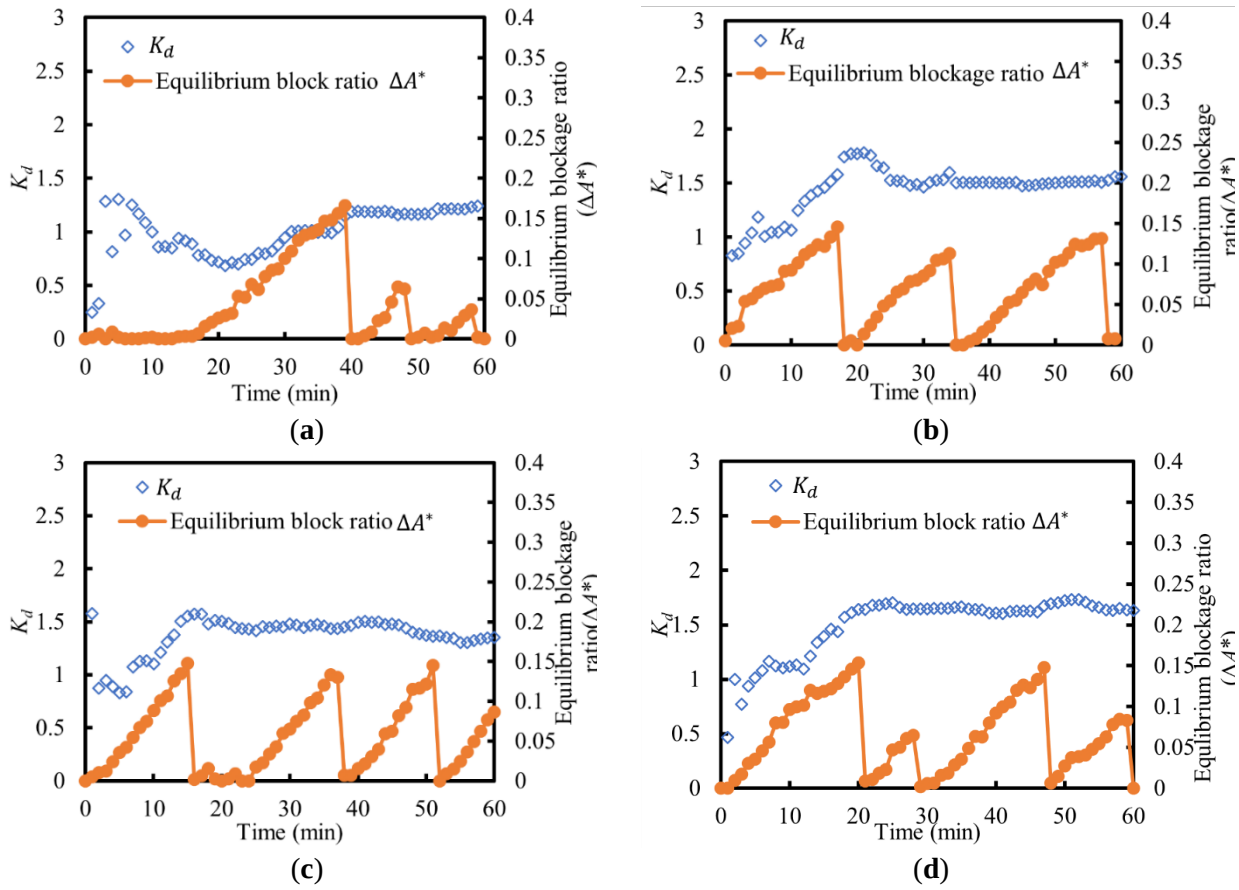

Figure 4-11**.** Time-history of the evolution of the relative scour depth K_d and equilibrium blockage ratio ΔA^* (**a**) test 1; (**b**) test 2; (**c**) test 3; (**d**) test 4.

The development of K_d and the equilibrium blockage ratio for tests 4 to 7 is presented in Figure Figure 4-12. The mean velocity of these tests was relatively similar, but the approach flow depth varied. Following the formation of the first woody jam, the K_d value also had a small change if the subsequent woody debris jams did not exceed the first one. However, it was also observed that if the subsequent woody debris jams were larger than the first or one of the previous ones, the value K_d further increased as shown in Figure 4-12b,c. As for the decrease of K_d, as shown in Figure 4-12b, it was recorded by the endoscope camera that the woody debris jam grew significantly and expanded very close to the sand bed, even filling in the scour hole in front of the pier.

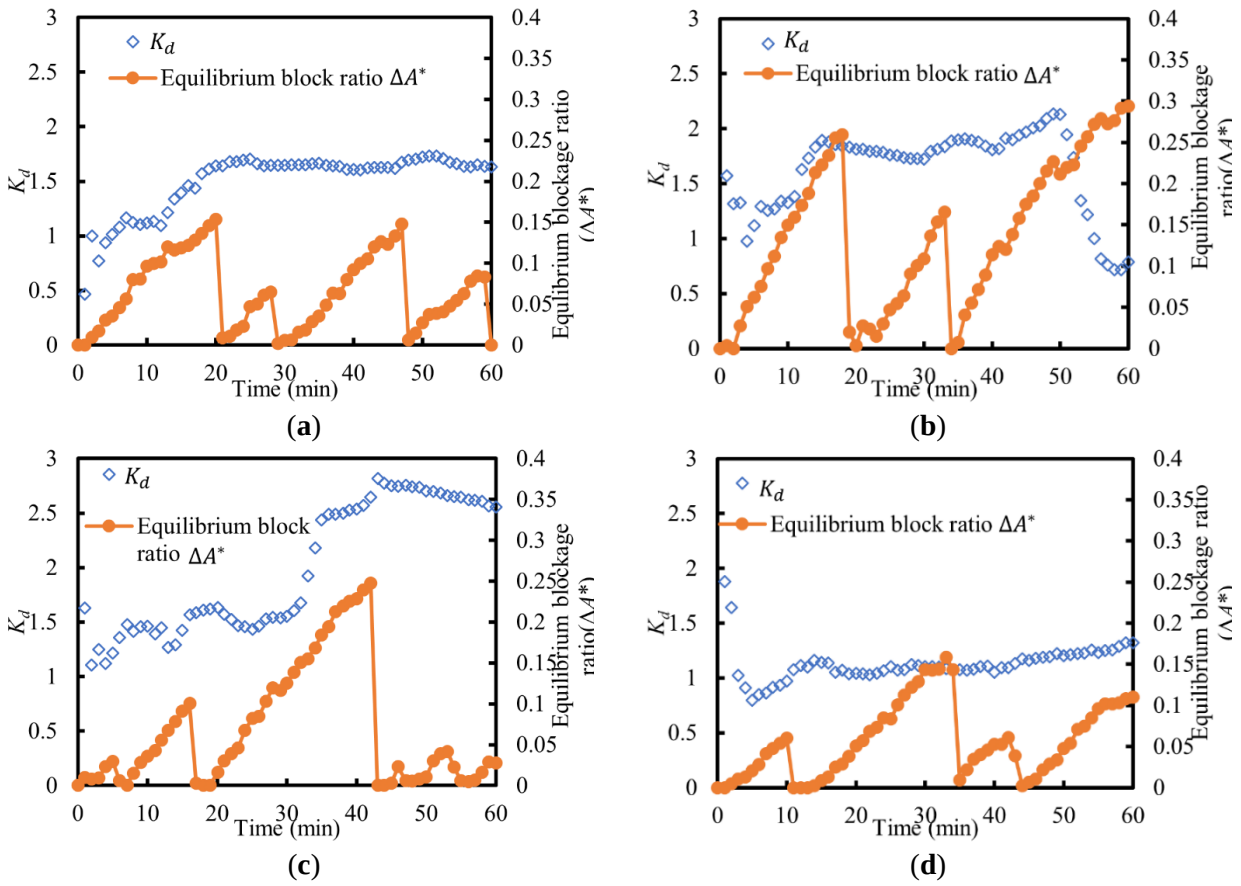

Figure 4-12 Time-history of the evolution of the relative scour depth K_d and equilibrium blockage ratio ΔA^* (**a**) test 4; (**b**) test 5; (**c**) test 6; (**d**) test 7

Based on the analysis above, the first debris jam had a clear relation to the development of additional scour depth. The subsequent woody debris jam had a small influence on the scour depth when its dimensions did not exceed the previous one. All test data related to the first debris jam were integrated and presented in Figure 4-13.

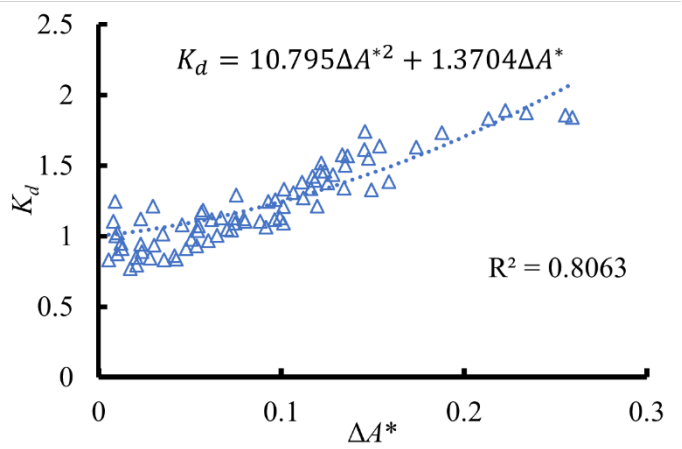

Figure 4-13 Correlation between the equilibrium blockage ratio, ΔA^*, and K_d.

Thus, the relation between K_d and the equilibrium blockage ratio, ΔA^* was described as:

$$K_{d1} = f_1 = 10.8\Delta A_1^{*2} + 1.37\Delta A_1^* + 1 \quad (4\text{-}16)$$

$$K_{d2} = \begin{cases} \varepsilon K_{d1max}, \Delta A_2^* \leq \Delta A_{1max}^* \\ f_2, \Delta A_2^* > \Delta A_{1max}^* \end{cases} \quad (4\text{-}17)$$

where K_{d1} = the non-dimensional parameter for the first woody debris jam; K_{d2} = for the subsequent woody debris jam; K_{d1max} = the maximum value of K_d for the first woody debris jam; ε =a coefficient to connect parameter K_d of the first or previous woody debris jam, averaging close to 1.0; f_2 = the relation of subsequent K_d with the equilibrium blockage ratio that exceeded the dimensions of the previous debris jam.

It should also be pointed out that K_{d1} was used to quantify the influence due to the woody debris jam during the initial stage of scour in clear water conditions. If the scour occurred after the first woody debris jam, then the growth of the woody debris jam may have a comparably small effect on scour depth provided that its dimensions were smaller than those of the previous one. However, if the subsequent woody debris jam continued to grow and exceeded the size of the previous one, then the scour depth further increased, as it was affected by the development of the woody debris jam and described by the parameter f_2. An explicit function for f_2 is not given here, as it is believed that more tests with debris jams, which exceeded the previous one, should be included. It is however recommended to apply $f_2 = f_1$ in order to estimate K_d and the authors argue for using ε = 2.0 for a conservative design purpose.

4.5 Discussion

The debris jam forming in front of a bridge pier can occur in various shapes and different types of woody debris jams cause various effects on piers. Applying a steady size-uniform woody block (Ebrahimi et al. 2018; Pagliara and Carnacina 2011; Pagliara and Carnacina 2011; Pagliara and Carnacina 2013; Pagliara 2010) to represent a woody debris jam is an idealized approach to investigate the influence caused by debris jams, and it may be reasonable if the woody debris jam was built before being captured by the pier or if the debris jam was stably formed in a short period. However, this type of steady, size-uniform woody debris jam ignores the processes of formation and failure of woody debris jams, particularly if the debris jam formed and developed over a longer period during natural flood events, as observed in (Diehl 1997). The investigation of dynamic woody debris jams, formed by woody pieces can provide more realistic insight into the life cycle of woody debris jams (their formation, growth, and failure) as well as their characteristics and effects. In addition, the dimensions of dynamic woody debris jams exhibited a certain correlation between their vertical areas and plane areas as shown in Figure 4-10a. This is an important difference between the steady, size-set woody block and the dynamic woody debris jam, as the dimensions of the steady, size-set woody debris jam may be independent of each other as well as with respect to flow conditions. The use of dynamic woody debris jams may have a substantial advantage over the use of size-set woody debris jams.

As seen in test 5, a reduction in the scour depth in front of a pier may occur when the woody debris jam becomes significantly large, and its lower limit reaches close to the sand bed, exceeding the scour hole. In test 5, scour depth was observed to decrease when the woody debris jam further developed starting from t = 50 min. The woody debris jam grew, and some debris pieces reached very close to the bottom of scour hole while the debris jam continued growing, as determined by analyzing the video captured by the endoscope camera as Figure 4-14a was shown. Then, scour occurred in front of the woody debris jam (as shown in Figure 4-14b) while the approach flow which moved close to the bed entrained sand to fill in the initial scour hole which had formed in front of the pier as the debris jam formed. This results in a decrease in scour depth right in front of the pier.

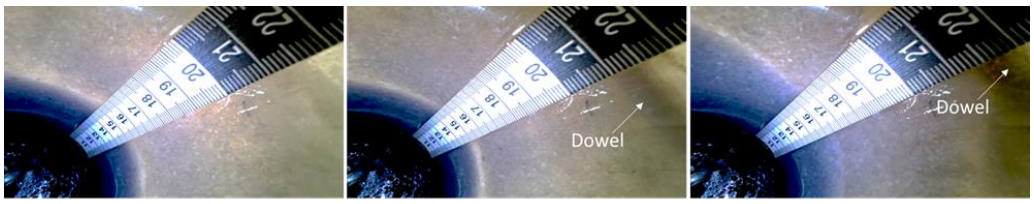

(**a**) The dowels approached the scour hole

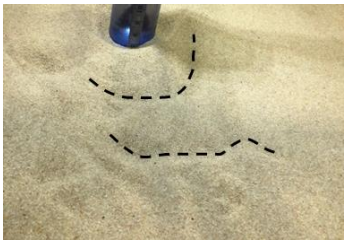

(**b**) final elevation of the sand bed

Figure 4-14 The debris jam reached the bed near the scour hole in test 5.

Few studies have investigated the effect of dynamic woody debris jams on scour depth, so the results from steady, size-set woody debris jams will be compared and discussed. Ebrahimi et al. (Ebrahimi et al. 2018) applied a set height of woody debris over the water depth to estimate the influence due to the woody debris jams on scour and derived two empirical formulas. In the present study, these formulas were applied to compare the relation between h_d/h and the scour depth. Additionally, data collected from several previous researchers (Ebrahimi et al. 2018; Melville and Dongol 1992; Pagliara and Carnacina 2011) were also included. As shown in Figure 4-15, the empirical formula based on the height of woody debris jams could provide the range to estimate the influence of the woody debris jams on scour, but without adequate correlation, and this could attribute to the shape's difference of the debris jam.

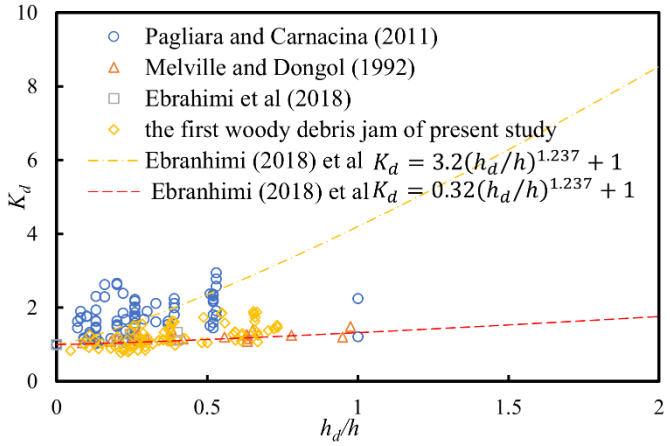

Figure 4-15 Comparison of the experimental data from (Ebrahimi et al. 2018; Melville and Dongol 1992; Pagliara and Carnacina 2011) with the results from the present study.

The blockage ratio was also applied to the results from the study by (Pagliara and Carnacina 2011), and it demonstrated a good agreement with their experimental data (shown in Figure 16). As scour occurred in front of single bridge piers, it was reasonable to introduce the blockage ratio to quantify the influence due to woody debris jams as the decrease of flow cross-sectional area caused by woody debris jams further increased flow velocity and enhanced the downward flow which finally resulted in additional scour. Thus, the blockage ratio was also introduced in the present study to incorporate the effects of a woody debris jam; the proposed formula also showed good agreement with experimental data. It can also be seen in Figure 4-16 that the current study showed less scour due to debris compared to the equations of Pagliara and Carnaica. This was firstly attributed to less flow intensity of the current study. The minimum flow intensity of Pagliara and Carnaica (2011) was 0.75 which was higher than the max one of the current study. In addition, Pagliara and Carnaica (2011)'s experiments had already implied that the geometry of the debris jam might affect the results as the rectangular or triangular debris jam has a greater influence on the scour

depth compared to the cylindrical debris jam. The geometry of the dynamic debris jam was near to half-cone even though the shape was not smooth or regular. Furthermore, the size of our dynamic debris jams gradually increased during the scour process while the static block debris jam in Pagliara and Carnaica had a constant size during the whole scour process.

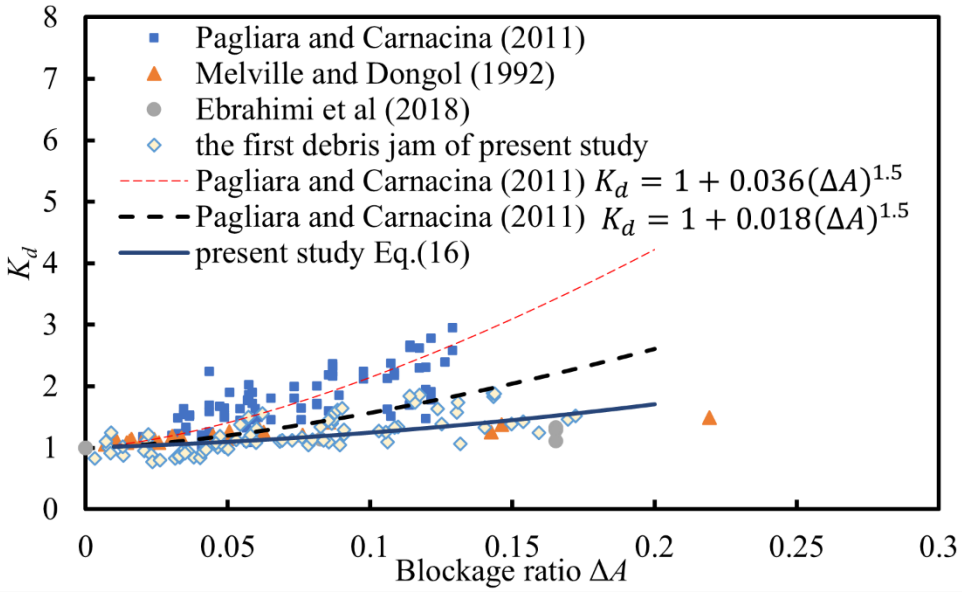

Figure 4-16 Formula by (Pagliara and Carnacina 2011) against experimental data from (Ebrahimi et al. 2018; Melville and Dongol 1992; Pagliara and Carnacina 2011); Pagliara and Carnacina (Pagliara and Carnacina 2011) $K_d = 1 + 0.036\Delta A^{1.5}$ for rectangular and triangular debris jams and $K_d = 1 + 0.018\Delta A^{1.5}$ for cylindrical debris jam, blockage ratio here was consistent with the (Pagliara and Carnacina 2011). (Noting: the data from (Melville and Dongol 1992) blockage percentage less than 0.3)

4.6 Conclusions

A new approach to determine the influence of dynamic woody debris jam formation, growth, and decay on scour and its associated hydraulic head was introduced in this study. The life cycle of formation, growth, and failure of woody debris jams provided new insights into their effects. Several characteristics which had not been investigated in previous studies which mostly involved steady, size-set woody debris jams were investigated in this study: (1) the spatio-temporal variation of the dimensions of woody debris jam; (2) the processes of formation, growth, and decay of the dynamic woody debris jams; (3) the space and time progression and influence of the series of dynamic woody debris jams over a longer period.

As the debris-induced hydraulic head was non-dimensionalized by the approach flow depth, it is found that the Froude number can represent the influence of the flow condition on the dynamic debris jams. A blockage ratio was derived to quantify the effects of the dynamic woody debris jams, and it was correlated with the hydraulic head generated by the presence of the debris jams. In addition, as the vertical area and plane area of woody debris jams were found to be correlated, the plane area was shown to be more accurately captured for an irregular woody debris jam. It also should point out that this approach to estimating the vertical projected area might be a limitation of the present study. However, using adequate engineering judgment, this could provide a potentially convenient method to estimate the blockage ratio—fully validating it may require further studies to prove its reliability.

The presence of dynamic woody debris jams generally leads to a deeper scour depth than in their absence. The defined blockage ratio was found to be a useful parameter to quantify their influence. An empirical relation between the equilibrium blockage ratio and ds/ds_0 of the first debris jam was derived and even

further compared with experimental data from previous studies. Over a period, the influence of the sequence of woody debris jams varies depending on their individual size. Several limitations of the present study are acknowledged by the authors: (1) wooden dowels are applied to model real debris; however, they do not completely reflect the complex geometry and properties of real debris; (2) the duration of each experimental test was approximately one hour due to the limitation of the experimental facilities and the total number of debris pieces released.

Chapter 5. Influence of Dynamic Debris Jam formed by Trees on Bridge Pier Scour

5.1 Introduction

Bridge pier scour is of critical concern for the design and construction of bridges over rivers. Sediment material removed by water flow at the base of a bridge pier affects the structure's stability and may lead to bridge failure. Of 383 bridge failures caused by floods, 25% involved pier damage, and 75% involved abutment damage according to a national study by Federal Highway Administration (FHA), and specifically, 23 bridge failures resulted in $15 million in damage costs in the 1993 Mississippi flood (Arneson et al. 2012). Further, over one-third of bridge failures in the US have been attributed to debris accumulation (Diehl 1997). The presence of a woody debris jam causes a decrease in the effective bridge opening and possibly increases the scour depth (Lyn et al. 2003). The Report from FHA (Bradley et al. 2005) addressed a need to quantify the influence of woody debris on scouring.

Previous studies related to woody debris jams can be categorized into static and dynamic debris (Table 5-1). In a static debris jam, the geometry and size of the debris jam do not evolve with time and are independent of the flow conditions. Melville and Dongol (1992) used idealized debris jams that were smooth and impermeable blocks with cylindrical, conical, and elliptical shapes in plan view. An effective pier diameter D_e was proposed to quantify the influence of debris jams.

$$D_e = \frac{0.52h_d d_d - (h - 0.52h_d)D_p}{h} \quad (5\text{-}1)$$

where h_d = the height of debris jam to free water surface; d_d= the diameter of debris jam applied in their study; h=the water depth of approaching flow before the debris section; D_p=the pier diameter.

Table 5-1 Evolution of debris jams applied in the previous studies

Studies	Topics	Debris type	Debris material
Pagliara and Carnacina (2011)	Maximum scour depth	Static	Real Debris pieces, block jam
Pagliara (2010)	Temporal scour depth	Static	Block jam
Ebrahimi et al. (2018)	Maximum scour depth	Static	3D printer jam
Lagasse et al. (2010)	Flow pattern and maximum scour depth	Static	Block jam
Claps (2018)	Scour depth	Static	Half cone, debris pieces
Pagliara and Carnacina (2013)	Flow pattern	Static	Rectangular block, debris pieces
Panici and de Almeida (2018)	Critical dimensions of debris jam	Dynamic	Real debris pieces
Schalko et al. (2019)	Debris jam accumulation probability	Dynamic	Dowels pieces
Cantero-Chinchilla et al. (2021)	Temporal evolution of scour depth	Static	Flow-dependent debris jam based on Panici and de Almeida (2018)
Zhang et al. (2022)	Scour depth	Dynamic	Dowels pieces

Lagasse et al. (2010) further developed an effective pier diameter to incorporate rectangular and triangular debris jams. Pagliara and Carnacina (2011a) applied rectangular, triangular, and cylindrical shapes of debris jams to investigate the effects on final scour depth, and the blockage ratio was introduced to predict the influence of debris jams on scour depth. Pagliara and Carnacina (2011b) further developed the prediction function to incorporate the effects of the longitudinal center position of the debris jam versus the pier center and the longitudinal length of the debris jam using a block woody jam. Ebrahimi et al. (2018) focused on the position of debris in water along the pier mainly using block cylindrical debris jams, and the height of debris jam normalized by water depth was proposed to estimate the influence of debris jam on scour depth. This type of block debris jam in a static state might not well represent debris jam characteristics such as roughness and porosity, so static debris jams built from debris pieces have also been applied to study effects on the temporal evolution of scour (Pagliara and Carnacina 2010), flow pattern (Pagliara and Carnacina 2013) and scour depth (Claps 2018). Debris jams built of debris pieces better represent realistic debris jams than block jams, but the static debris jams might still not well reflect the formation of debris jams in the field. A field investigation by FHA (Lyn et al. 2007) recorded the generation of a debris jam by a frontal camera fixed on the bridge pier. Their study clearly indicated that the debris jam did not suddenly form and appeared as a block in front of bridge in a static state; rather, the debris jam formation grew and evolved with time.

A dynamic debris jam evolves with time and its formation is dependent on the local flow condition. Panici and de Almeida (2018) applied the dynamic debris jam by manually releasing debris pieces into the flow to simulate the debris accumulation which included the processes of formation, growth, and failure. In addition, the debris Froude number was proposed to predict the critical dimensions of debris jam. Schalko et al. (2019) also applied dynamic debris pieces to predict the debris accumulation possibility.

Bridge pier scour evolves with a debris jam, so dynamic debris jams should be implemented to examine scour in the presence of debris jams; however, few studies investigated the influence of dynamic debris jams on scour depth. Zhang et al. (2022) studied scour due to dynamic debris jams comprised of wood dowels. Moreover, the material of which a debris jam is composed might also influence scour. Panici and Almeida (2020) pointed out that dowels might be not a good choice to represent real-world debris jams, and Lyn et al. (2003) suggested avoiding using dowel jams. The present study fills this research gap by studying the influence of scour of dynamic debris jams comprised of real trees. For the first time, seedling trees, instead of dowels, were applied to investigate the influence of dynamic debris jams on scour depth. The time evolution of single-bridge pier scour was measured in clear-water conditions as dynamic debris jams formed and grew while individual seedling trees were released continuously from upstream.

5.2 Methodology

5.2.1 Experiment setup

Physical modeling was conducted in the Hydraulic Laboratory of the University of Ottawa, Canada. The flume is 30m in length, 1.5 m in width, and 0.7m in height (Figure 5-1). A false floor with a height of 0.2m was built at the downstream end of the flume within which a 3.2 m long mobile bed test section was filled with sand with a median size of $d_{50} = 1.16\text{mm}$ and gradation of $\sigma = 1.22$. A flow straightener was positioned at the upstream end of the flume, and a gravel slope was placed immediately upstream of the false floor to ensure the approaching flow was uniform and steady. A plexiglass pier with a diameter of D_p=0.09m was installed in the center of the sand bed, and a ruler was attached to the inside front of the pier.

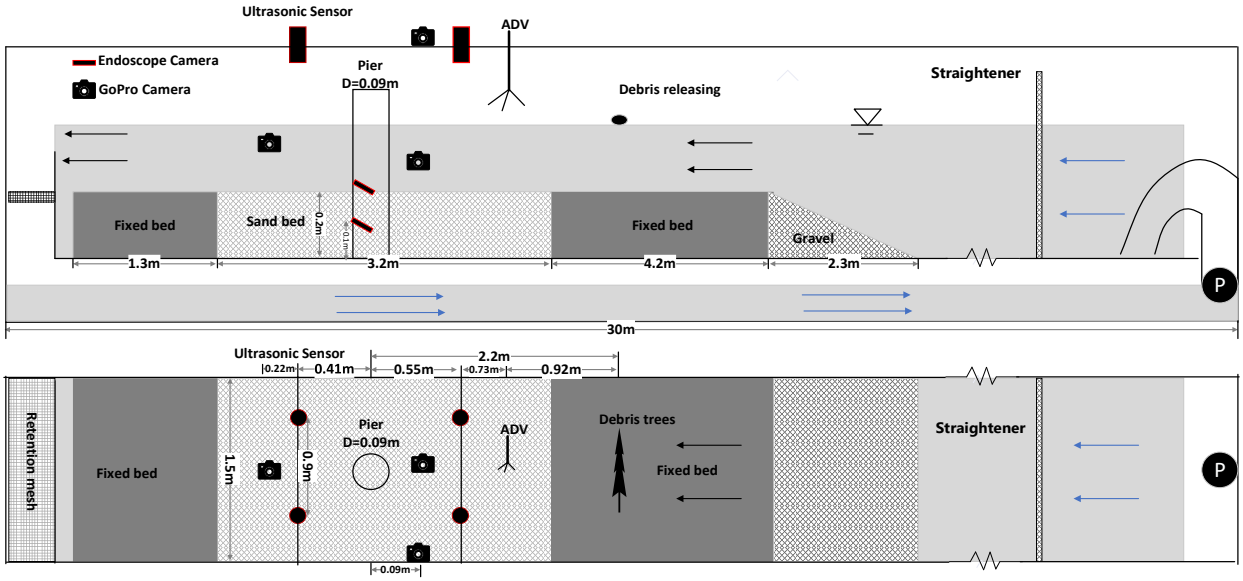

Figure 5-1 Sketch of setup for the experiment (not to scale).

White spruce seedling trees were applied to represent real-world debris. On average, the length of the seedling trees was 30.38 cm with a stem diameter of 2.2 mm. This type of debris kept the roots and leaves (Figure 5-2). In addition, GoPro cameras (https://gopro.com/en/us/update/hero5) were installed 0.41 m behind the pier (submerged), on the side of the flume wall (submerged), and on the top of the flume. The distance between the side and top GoPro was adjusted in the pre-test at a distance of 0.09 m in the longitudinal direction and a vertical distance of 1.65 m to the sand bed with a transverse distance of 0.75m. In addition, two endoscopic cameras (5.0MP USB Endoscope, NIDAGE 50FT Inspection Camera) were installed (https://www.amazon.ca/gp/product/B08LVPG18X/ref=ppx_yo_dt_b_asin_title_o08_s00?ie=UTF8&psc=1) at an angle inside the pier to monitor the development of scour depth in front of the pier with the help of a ruler inside of the pier. The upper endoscope was near the sand bed surface while the downward one was at 0.1 m above the bottom of the flume. Ultrasonic sensors (https://www.massa.com/industrial/ultrasonic-sensors/pulstar) were applied to obtain the induced hydraulic head caused by the debris jam. Two ultrasonic sensors were installed symmetrically 0.55 m upstream of the pier, while another 2 sensors were installed 0.41 m downstream of the pier. In addition, a Leica P50 Terrestrial Laser Scanner (Lidar) (https://leica-geosystems.com/products/laser-scanners/scanners/leica-scanstation-p50) was also used to obtain the sand bed elevation at the end of each experiment.

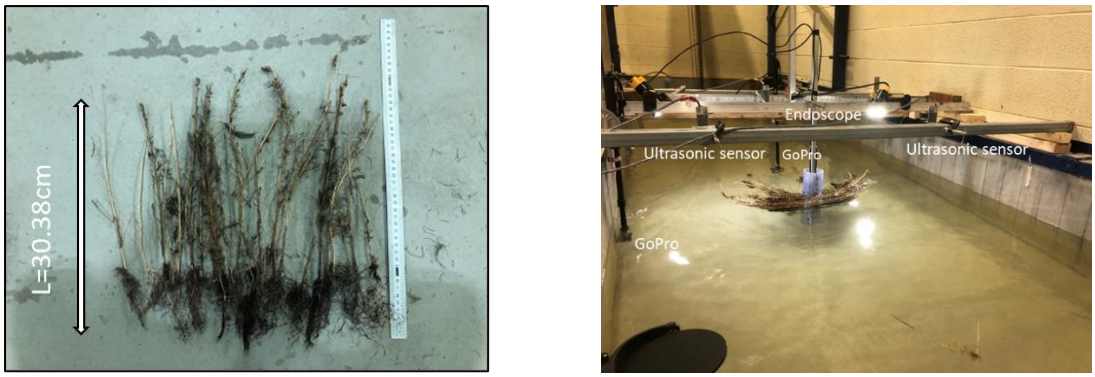

Figure 5-2 Seedling trees applied in the experiment (a) and the setting up of instruments (b).

A Vectrino Acoustic Doppler Velocimeter (ADV) (https://www.nortekgroup.com/products) was also used to measure the mean velocity of the approaching flow at the flume centreline 1.28 m upstream of the pier. A side looker ADV with a sampling rate of 100 Hz was applied to measure the flow velocity for 2mins, and the measurement points were vertically distributed with an increment of 1cm near the bed and a 2cm increment applied when above 15cm. The data measured by ADV was also filtered, time-averaged, and de-spike by the method of Jamieson et al. (2010). The vertical profile of streamwise velocity (u component) for each measured flow condition is shown in Figure 5-3. A depth-average method was used to calculate the mean velocity.

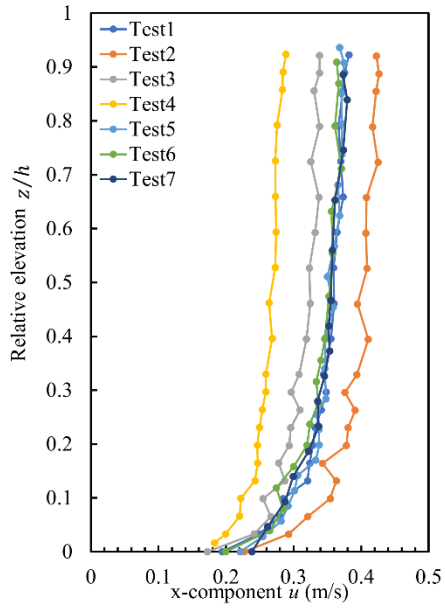

Figure 5-3Vertical distribution streamwise velocity (u component) for the approach flow of each experiment.

The test matrix for the experimental program is presented in Table 5-2. Tests 1-4 had a similar water depth but with a varied mean velocity in a range of 0.26-0.39 m/s, while tests 5-7 had a similar mean velocity but with a varied water depth in a range of 0.21-0.35 m. As for the debris, all tests were conducted both in the presence of tree jams and with no debris as an accompanying control blank test.

Table 5-2 Tests matrix in terms of flow conditions.

Test	Mean velocity U(m/s)	Water depth h(m)	F_r	Debris used
Test-1	0.34	0.30	0.24	No/trees
Test-2	0.39	0.30	0.27	No/trees
Test-3	0.31	0.30	0.21	No/trees
Test-4	0.26	0.30	0.18	No/trees
Test-5	0.34	0.35	0.22	No/trees
Test-6	0.34	0.25	0.25	No/trees
Test-7	0.34	0.21	0.27	No/trees

Note: No/trees means without and with seedling tree jam.

A pre-test was run for all tests to determine the flow condition, and then the blank test was first conducted. The water depth was slowly increased with very low discharge to avoid disrupting the sand bed, and when it reached a certain water depth, all cameras (GoPro and endoscope), as well as the ultrasonic sensors, were turned on to record the data. Then, the pump was applied to the designed flow discharge. The ADV was used to measure the velocity during the blank test. The same flume-filling procedures were applied to the test in the presence of debris jam. Seedling trees were applied in the centreline of the flume and manually released 10 cm normal horizontally to flow direction above the water surface at a frequency of 12 pieces per minute on average for a duration of one hour. During each run, the seedling trees were collected in a retention mesh at the flume outlet for re-use in subsequent tests while ensuring the condition of the trees was similar between tests. After the test, the flume was carefully drained, and the Lidar was used to measure the sand bed elevation throughout the area extending 1 m upstream and downstream of the pier. Four targets with known coordinates were used to calibrate the coordinate system. The measured bed surface was gridded with x spacing of 0.00796m and 0.00756 in y spacing and plotted using Surfer.

5.2.2 Scale effects and error evaluation

The Froude similarity was applied to consider scale effects. Froude numbers ($F_r = U/\sqrt{gh}$) for the present experiments are shown in Table 5-2. Applying a scale factor λ=30 in the present study, the prototype diameter of the pier would be 2.7 m and the prototype debris would be 9 m in length. This compares well to field observations of pier debris jams (Diehl (1997), in which the length of debris pieces was in the range of 0-24 m, and the debris length was generally less than the channel width. It is worth noting, however, that the seedling trees were more flexible than full-grown trees. It should also be noted that the dynamic debris jam experimental duration of one hour (5.5 hours at prototype scale) employed in the present study was a limit set by available equipment and materials. The experimental flow depths and velocities (Table 5-2) would have equivalent prototype flow conditions in the range of mean velocity of 1.4 - 2.1 m/s and water depth of 6.4 -10.6 m. Shields scaling of particle entrain ability would suggest a prototype bed sediment median size of 0.019 m (i.e., coarse gravel). Reynolds number of the present study was in the range of 56946-84382.

The ultrasonic sensors, MassaSonic PulStar, have a measurement resolution of 0.25 mm, and a sampling rate of 10 Hz was applied in the present study. The endoscope camera, 5.0MP USB Endoscope NIDAGE, was applied with a sampling rate of 20 fps with a size of 2592×1944. Due to inclination, the error of the

endoscope camera after calibration was 4.99%. The GoPro camera, with a sampling rate of 60 fps linear model, was used to get the dimensions of the debris jam with the help of Image J (https://imagej.nih.gov/ij/). The GoPro was also calibrated and had an error of 0.85% after using the reference mesh. ADV was applied with a sampling rate of 100 Hz, and the Lidar showed a resolution of 0.009m.

5.3 Results and Analysis

5.3.1 Dimensions of debris jam

Other than minor adjustments as each debris jam consolidated, once formed, each experimental debris jam continuously increased in size as debris pieces were constantly released from upstream; the debris jams were very stable and did not dislodge from the pier. Through analysis of the GoPro camera imagery, the evolution of the debris jam dimensions was obtained, as shown in Figure 5-4 for each experimental test. The debris jam's height, h_d, was defined as the distance between the bottom of the debris jam to the water surface in front of the pier. The width of the debris jam, w_d, was defined as the maximum transverse dimension of the debris jam normal to the flow direction. The length of debris jam, l_d, was defined as the maximum longitudinal distance from the pier to the debris jam boundary at the surface. In addition, the frontal vertical area of the debris jam A_{vc} in the cross-section was also calculated by:

$$A_{vc} = 0.5 h_d w_d \tag{5-2}$$

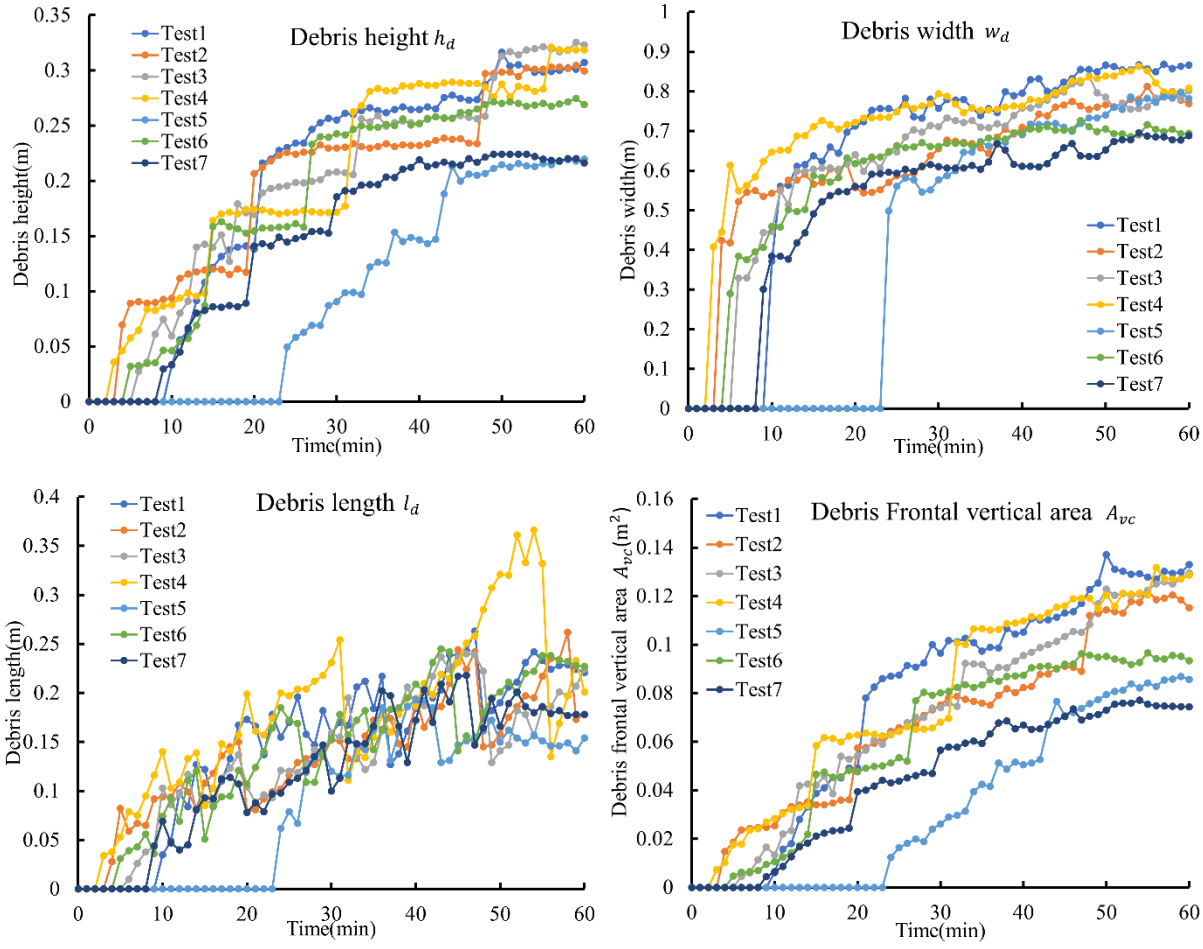

Figure 5-4 Evolution of dimensions of debris jam (a) the debris jam height (b) the debris jam width (c) the debris jam length (d) the frontal area of the debris jam.

5.3.2 Scour depth

Pier scour was quantified by the scour depth in front of the pier obtained by the endoscope cameras, and the evolution of scour depth is presented in Figure 5-5. Without the presence of a debris jam, scour depth increased smoothly with time. In addition, the development of scour depth in tests 1-4 indicated that higher flow intensity led to deeper scour depth, and the development of scour depth in tests 1,5-7 had a similar trend even though the water depth was varied. In contrast, the presence of a debris jam enhanced the development of scour depth leading to a much deeper scour depth. Further, except for Test 7, the growth of each debris jam in time led to increasing scour. It is worth noting that in Test 7 it was observed that the debris jam was so large that it reached the sand bed surface, with the consequence that the scour depth directly in front of the pier decreased near the end of the run.

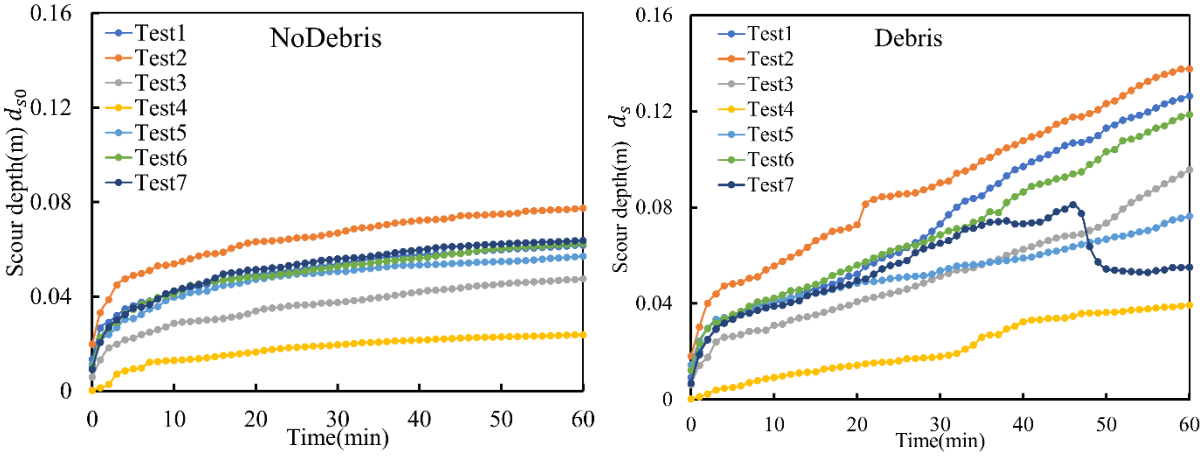

Figure 5-5 Scour depth time history without the presence of debris (a) and scour depth in the presence of debris (b).

The scour depth ratio K_d was used to quantify the influence on scour depth caused by the debris jam

$$K_d = \frac{d_s}{d_{s0}} \tag{5-3}$$

where d_s= the scour depth in the presence of debris jam at the time t; d_{s0}= the scour depth without the presence of debris jam at the same time t in the same flow condition.

The blockage ratio in percentage R_d was introduced to quantify the size of debris jam which was also applied in Pagliara and Carnacina (2011a).

$$R_d = \frac{A_{vc} - D_p h_d}{A_f} \times 100\% \tag{5-4}$$

where A_f=the cross-section area of approaching flow;

The evolution of scour depth ratio and blockage ratio for test 1 and test 3 is presented in Figure 5-6. The scour depth ratio before the formation of a debris jam was close to 1, then it increased continuously as the blockage ratio increased with the growth of the debris jam.

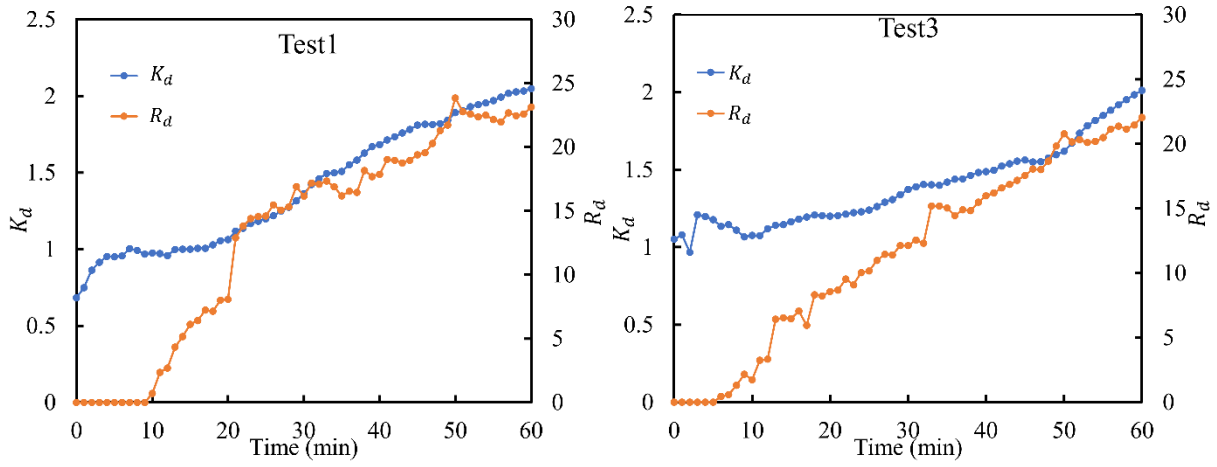

Figure 5-6 Evolution of scour depth ratio K_d (left axis) varied with the blockage ratio in percentage R_d (right axis) for example Test 1 (a) and Test 3 (b).

All test data were integrated to determine the relation between scour depth ratio K_d and the blockage ratio in percentage R_d (Figure 5-7). The intercept was set to 1 (because without debris, K_d= 1), and a polynomial function with 2nd order was derived to describe the function, so the relation was:

$$K_d = 0.0022R_d^2 - 0.102R_d + 1 \quad (5\text{-}5)$$

In addition, it was also observed that previous studies (Pagliara and Carnacina 2011) preferred to use a power function to describe the relation, so a power law function was also derived:

$$K_d = 0.001R_d^{2.1054} + 1 \quad (5\text{-}6)$$

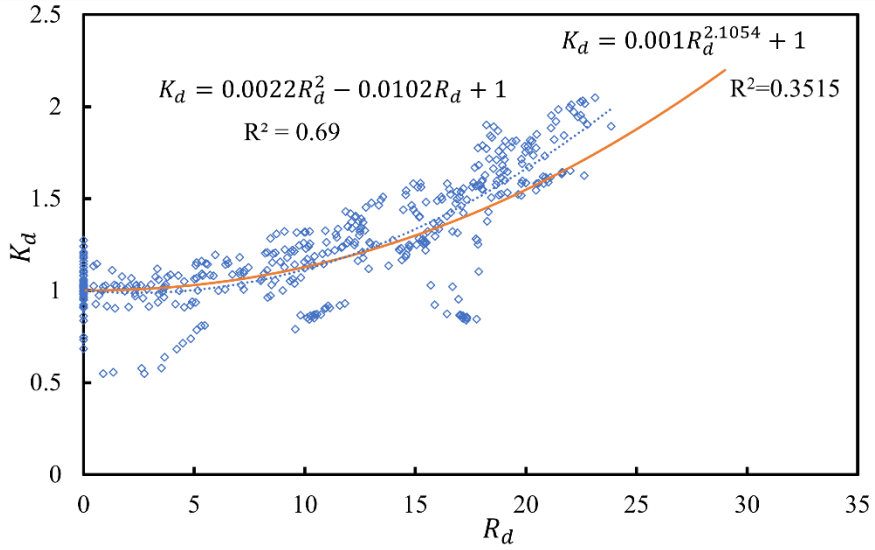

Figure 5-7 Relation between the scour depth ratio K_d and the blockage ratio in percentage R_d.

5.3.3 Debris jam Induced hydraulic head

Dynamic debris trees accumulated in front of the pier can lead to an increase in the water surface upstream of the debris jam, which possibly increases the flood risk. The water level increase caused by the debris jam was defined as an upstream head increase Δh_u, which was calculated from the upstream ultrasonic sensor water level data by subtracting the initial water level before releasing debris. Likewise, the instantaneous difference in water level between the upstream and downstream of the pier was defined as the head difference across the pier (Δh). Time series of the upstream head increase Δh_u and head differences across the pier during each experiment are presented in Figure 5-8.

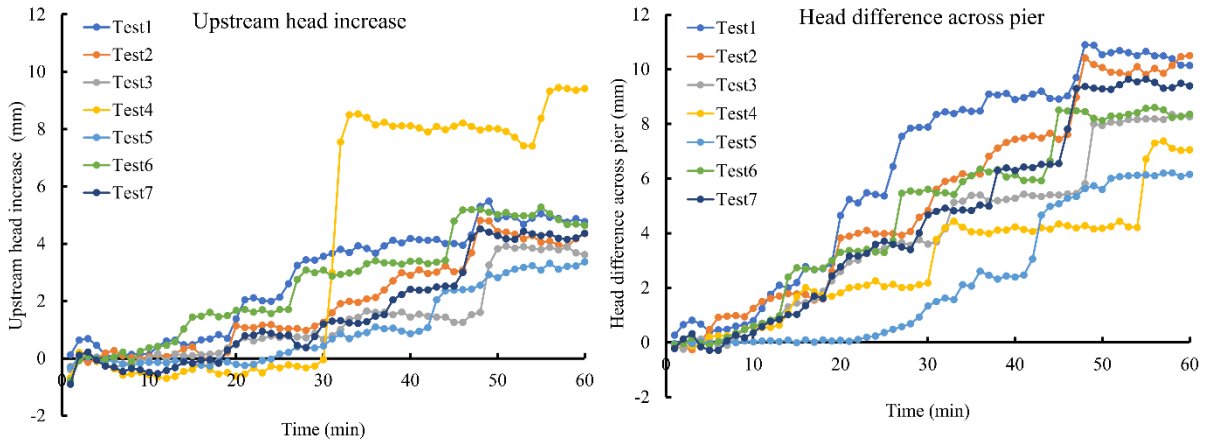

Figure 5-8 Upstream head increase Δh_u and head difference across pierΔh

The evolution of the head difference across pier (Δh) with time as well as the blockage ratio in percentage R_d for Test 1 and Test 3 are shown in Figure 5-9. It can be seen that head difference across the pier increased with the blockage ratio as the debris jam grew in time.

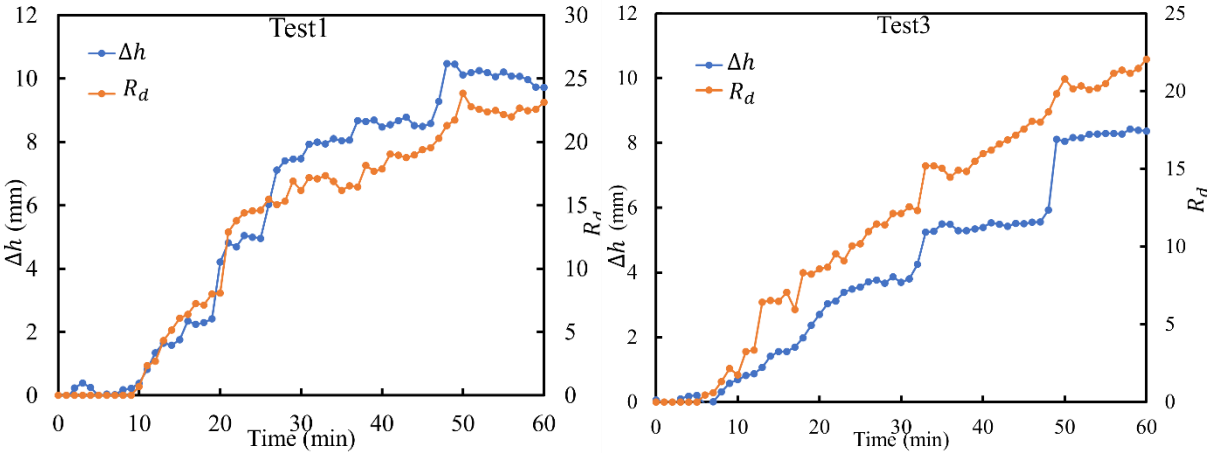

Figure 5-9. Evolution of debris jam head difference across the pier (Δh) (left axis) with time accompanied by the blockage ratio R_d (right axis) for Test 1 (a) and Test 3 (b).

Both the upstream head increase and the head difference across the pier for all the experimental test data were nondimensionalized by the local water depth of the approaching flow without the debris jam (h) as well as the Froude number (F_r) to account for flow conditions (Schalko et al. 2018), as presented in Figure

5-10. This collapsed the data to which a single linear function was fit, yielding the following relations for the hydraulic head induced by a dynamic debris jam:

$$\Delta h = 0.0061 R_d F_r h \tag{5-7}$$

$$\Delta h_u = 0.0035 R_d F_r h \tag{5-8}$$

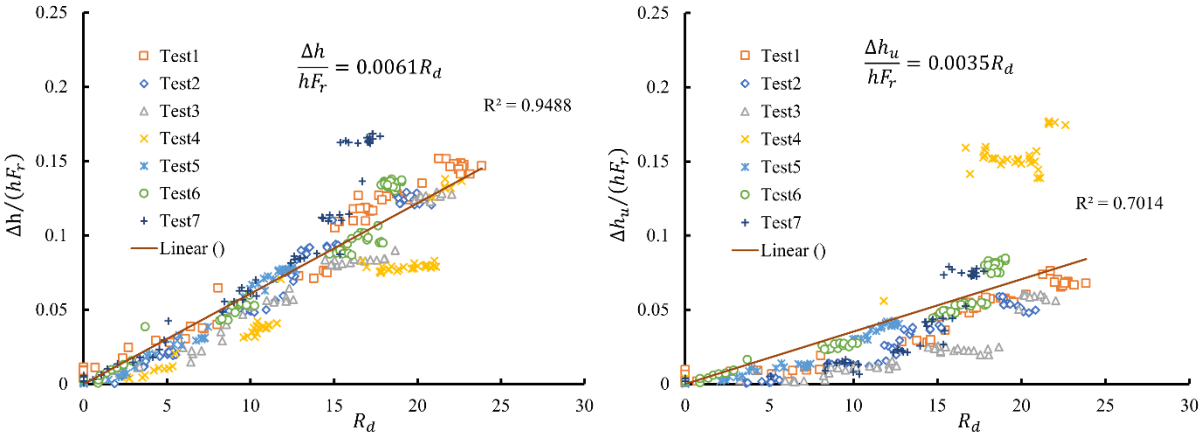

Figure 5-10. Relation of non-dimensional head difference across the pier $\Delta h/(hF_r)$ and upstream head increase $\Delta h_u/(hF_r)$ with blockage ratio R_d.

5.3.4 Bed elevation

The post-run bed surface elevations are shown in Figure 5-11. For each test case without a debris jam, the scour hole formed into a regular shape. On the other hand, with the presence of a debris jam, the scour holes were both much larger and irregular in shape. As explained above, in Test 7 the debris jam reached the sand bed surface; while the scour depth directly in front of the pier decreased (see Figure 6), the scour area around the pier was enlarged.

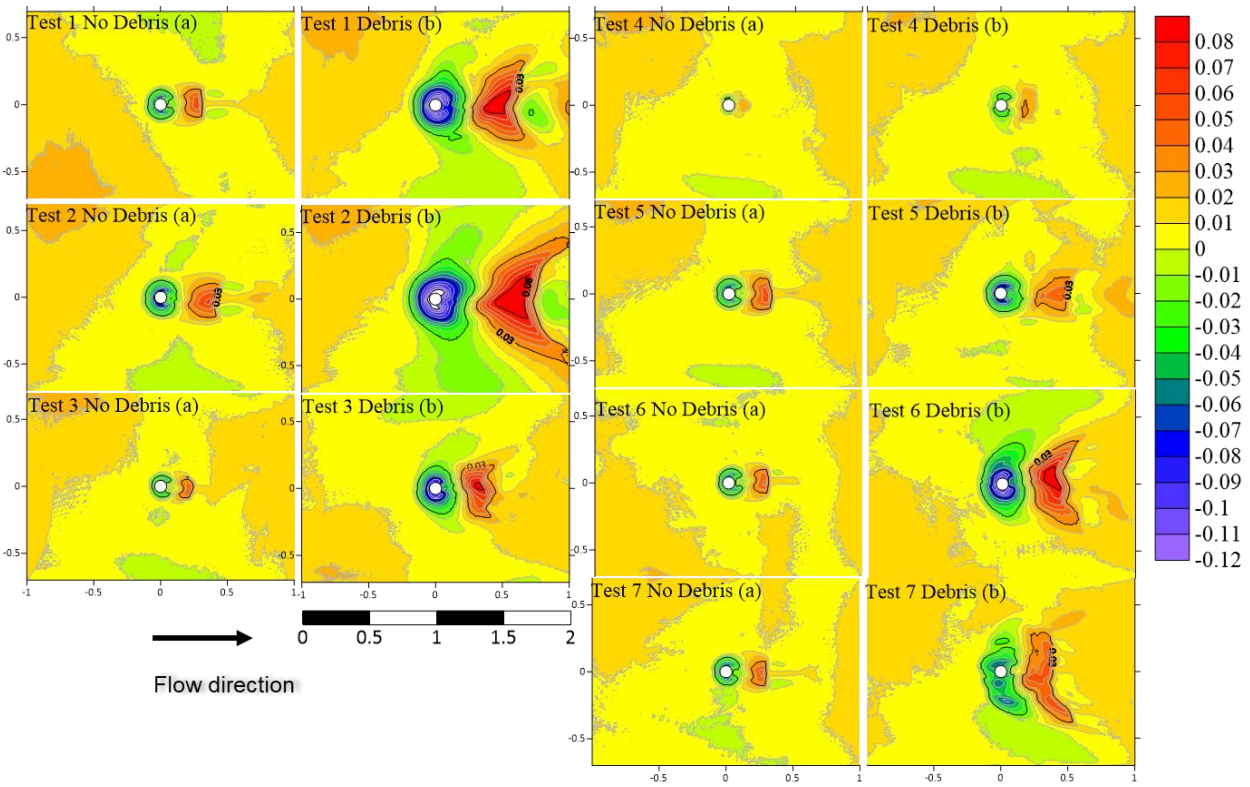

Figure 5-11. Final bed elevation obtained by laser scanner for Tests 1-7 both without(a) debris and (b) with the presence of a dynamic debris jam.

The volumes of the scour hole around the pier in cases with and without a debris jam were also calculated and compared (Table 5-3). Note that the pier volume is excluded from these scour volumes. The volume of a scour hole quantifies the size of the scouring. The presence of a dynamic debris jam can lead to the removal of more than six times the volume of sediment than the case without a debris jam. The effect of a dynamic debris jam on scour volume was even larger than on the scour depth as the maximum depth change ratio was 2.05. Furthermore, this might imply that focusing on scour depth might be not fully enough to comprehensively quantify the influence of dynamic debris jams.

Table 5-3 Scour hole volume and scour depth increase caused by dynamic debris jam over the scour hole without debris jam.

Test No	Debris	Scour hole Volume(m^3)	Scour depth(m) at t=60min	Volume Change ratio	Depth change ratio
Test1	No debris	0.0012	0.0617	7.82	2.05
	Debris	0.0094	0.1263		
Test2	No debris	0.0021	0.0774	6.75	1.78
	Debris	0.0144	0.1377		
Test3	No debris	0.0005	0.0476	8.98	2.01
	Debris	0.0041	0.0957		
Test4	No debris	0.0001	0.0238	6.47	1.65
	Debris	0.0005	0.0393		
Test5	No debris	0.0010	0.0571	2.48	1.34

	Debris	0.0024	0.0763		
Test6	No debris	0.0009	0.0624	8.43	1.90
	Debris	0.0073	0.1186		
Test7	No debris	0.0011	0.0637	4.45	0.87
	Debris	0.0048	0.0551		

5.4 Discussion

Field investigations (Lagasse et al. 2010) have indicated that natural debris jams can have various geometries, thus previous laboratory studies have employed rectangular, cylindrical, and triangular-shaped model debris jams to examine the influence on scour depth (Ebrahimi et al. 2018; Lagasse et al. 2010a; Melville and Dongol 1992; Pagliara and Carnacina 2011). However, the size and shape of these imposed static debris jams may not have reflected the local flow condition. In contrast, the dynamic debris jam formation process employed herein automatically resulted in jams with size and shape conforming to the specific local flow condition.

The elevation of the debris jam has been a focus of several previous studies (Ebrahimi et al. 2018; Lagasse et al. 2010b) as field observations suggest some debris jams are submerged at mid-depth rather than at the water surface. This was probably caused by an increase in woody debris density when the field debris was wet for a long time. In the current study, the density of debris pieces was controlled to maintain consistency. Nonetheless, in Test 7 the scour depth reduced in front of the pier partway through the test when the elevation of the debris jam was near the sand bed. This occurred because the debris jam increased in size continuously, finally, the debris jam reached the sand bed, and the debris entered the scour hole. This was also observed in a debris jam comprised of wood dowels (Zhang et al. 2022). When the debris pieces accumulated and occupied the scour hole, additional debris started to accumulate at the front edge of the debris jam immediately above the bed. This process is shown conceptually in Figure 5-12. Thus, sediment entered the scour hole reducing the scour depth, but then additional scour occurred in front of the new debris accumulation. As such, the scour hole volume was still greater than the case without the debris jam (Figure 11).

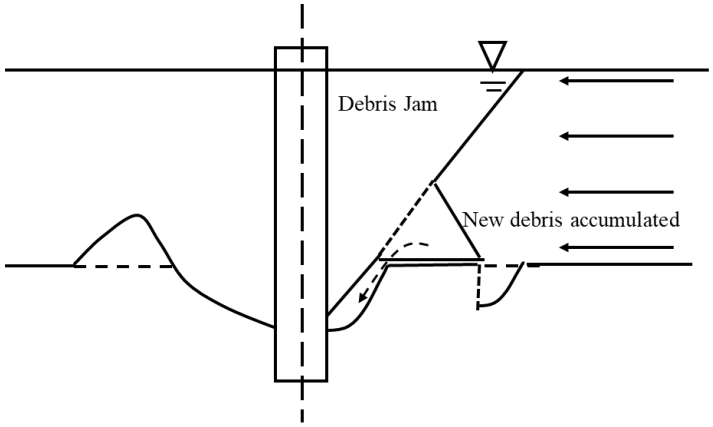

Figure 5-12. Conceptual sketch for the decrease of scour depth in Test 7

The present study utilized real seedling trees to form debris jams, while Zhang et al. (2022) applied the same procedure with dowels to reproduce the accumulation of debris. Once formed, debris jams comprised of real trees were more stable and lasted for a very long time, while dowel jams generally lasted less than

20 minutes before dislodging from the pier after which the debris jam growth process was reinitiated. The two types of debris james are compared using Test 2 (dowels) from Zhang et al. (2022) and Test 3 (seedling trees) from the present study (Figure 5-13). These two tests had the same experimental set-up and approximately similar flow conditions. The size of the seedling tree jam grew smoothly and continuously with a smaller slope, but the dowel jam accumulated quickly with a greater slope. In addition, the scour depth ratio increased smoothly for the seedling trees jam but the dowel jam rapidly influenced the scour depth ratio. Note that the first dowel jam was greater in size (blockage ratio R_d ~ 17) than the subsequent two dowel jams, and the scour depth ratio was likewise greatest for the first jam. That, not until the blockage ratio for the tree jam reached a similar value of R_d ~ 17 at t ~ 45 minutes did the scour depth ratio (K_d) for the tree jam exceed that of the dowel jam case. The slow but continuous development of the seedling tree jam can be attributed to the relatively thin, flexible, and rough surface of the trees. The seedling trees interwove and compacted together, eventually creating a relatively smooth and stable debris jam.

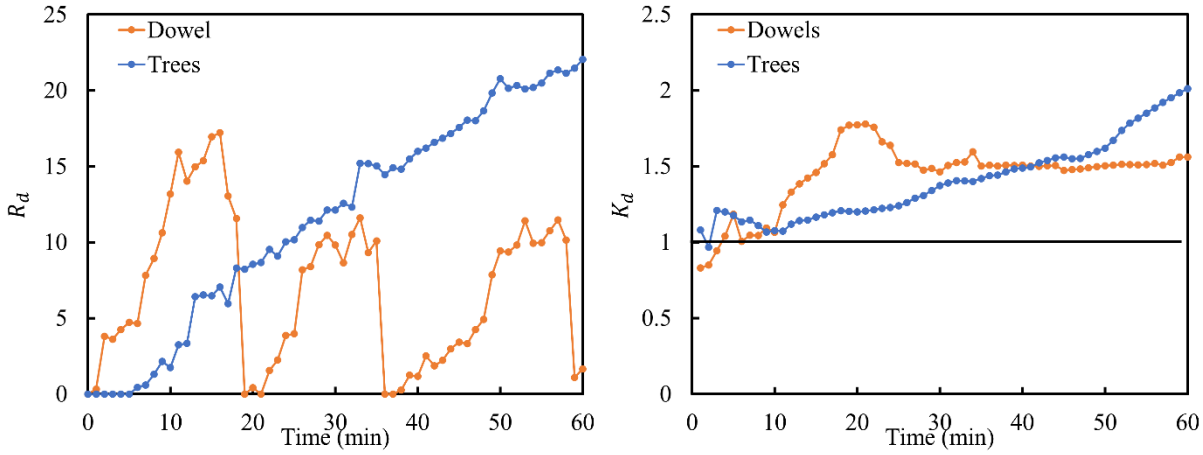

Figure 5-13 Comparison of debris jams comprised of debris trees (Test3, h = 0.30 m, U = 0.31 m/s, Fr = 0.21) versus dowels (as reported by Zhang et al., 2022: Test 2 therein, h = 0.28 m, U = 0.31 m/s, Fr = 0.22). Evolution of the blockage ratio in percentage R_d (a) scour depth ratio K_d (b)

Ebrahimi et al. (2018) argued debris jam height can be used to quantify the influence of the debris jam and proposed two formulas to predict the scour ratio. Data from (Ebrahimi et al. 2018; Melville 1992; Pagliara and Carnacina 2011; Zhang et al. 2022) and the present study are integrated into Figure 5-14 as well as these two formulas ignoring the shapes of the debris jams. Generally, the data of the present study were consistent with previous studies within a reasonable range, and the lower value function was also able to reflect the trend of the present study. The higher value function deviated from the present study, and this probably was due to shape differences; specifically, different proportions of the three dimensions of debris jams.

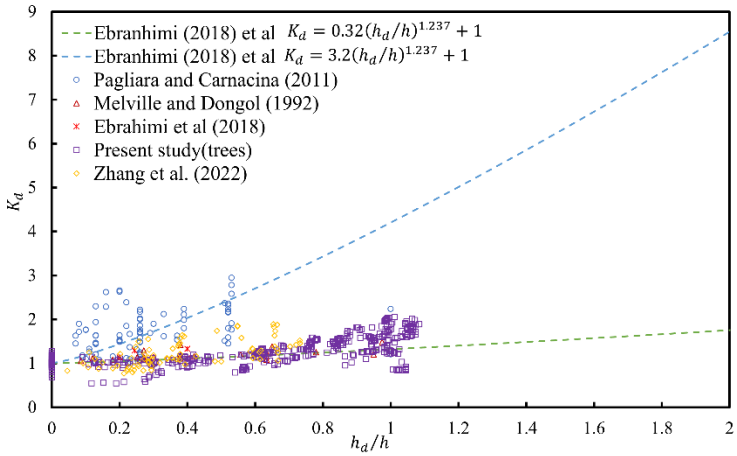

Figure 5-14 Influence of non-dimensionalized debris jam height h_d/h on scour depth integrating the data from (Ebrahimi et al. 2018; Melville 1992; Pagliara and Carnacina 2011; Zhang et al. 2022)

On the other hand, debris jams block the cross-sectional flow area, and this could constrict the flow and induce the enhancement of scouring. Thus, the blockage ratio of the debris jam may be important for scour, which considers two dimensions of the debris jam instead of just debris height. Two functions were proposed by (Pagliara and Carnacina 2011) to predict the influence of debris jam blockage ratio on scour depth, a lower value function for cylindrical debris jams and a higher value function for rectangular and triangular debris jams. Zhang et al. (2022) also suggested a similar function for dynamic debris jams comprised of dowels, while Equation 6 is a best-fit function for the present debris jams formed dynamically using real seedling trees. These four functions, along with data from the present and previous studies, are presented in Figure 5-15. It is clear that the function varies a great deal depending on the debris jam shape. In addition, the predicted increase in scour for a dynamic debris jam was lower for the same blockage ratio. This is likely because the size of a dynamic debris jam increased throughout the experimental test, whereas the full final size of a static block jam was immediately imposed. Thus, it can be expected that a dynamic debris jam will have a lower scour ratio.

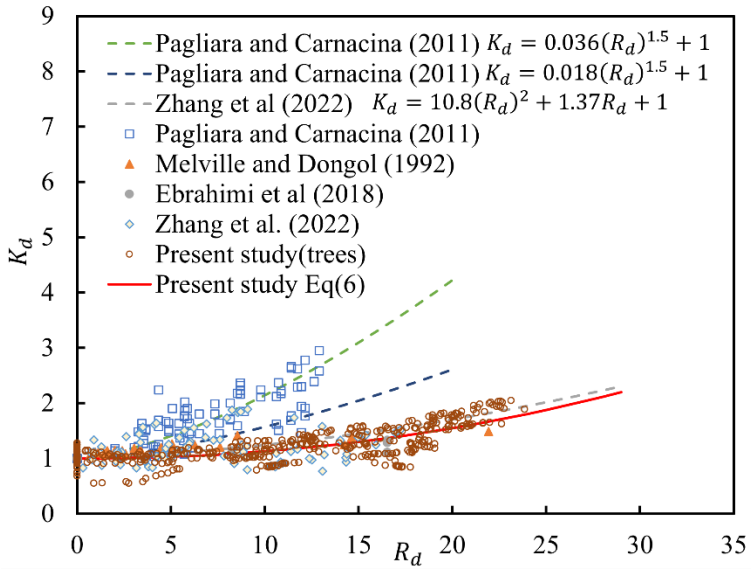

Figure 5-15 Influence of blockage ratio on scour depth by integrating the data from (Ebrahimi et al. 2018; Melville 1992; Pagliara and Carnacina 2011; Zhang et al. 2022) (Noting: the data from (Melville and Dongol 1992)blockage percentage less than 30%)

The presence of debris jams significantly increased scour hole volumes, which warrants a discussion of whether the scour depth alone is sufficient to assess the safety of a bridge pier when a debris jam is present. To explore this question, Figure 5-16 presents a concept sketch of a scour hole volume being enlarged due to a debris jam without an increase in scour depth. For simplicity, considering only the vertical direction, assuming the foundation bearing capacity balances gravitational weight, the bridge pier is stable if upward lift and buoyancy are balanced by the downward friction force applied by the soil around the contact with the pier surface. An increased scour depth due to a debris jam would lead to a decrease in friction force and corresponding stability. However, even without an increase in scour depth, an increase in scour hole volume due to a debris jam would lead to a decrease in confining stress for the remaining soil around the pier, which, in turn, would also reduce the friction force and thereby stability. Thus, an increased scour hole volume as well as scour depth may need to be considered when evaluating bridge instability in the presence of woody debris jams. Future studies, preferably with even longer test durations, could measure the confining stresses and pressure distribution around the pier to investigate the failure condition of the pier.

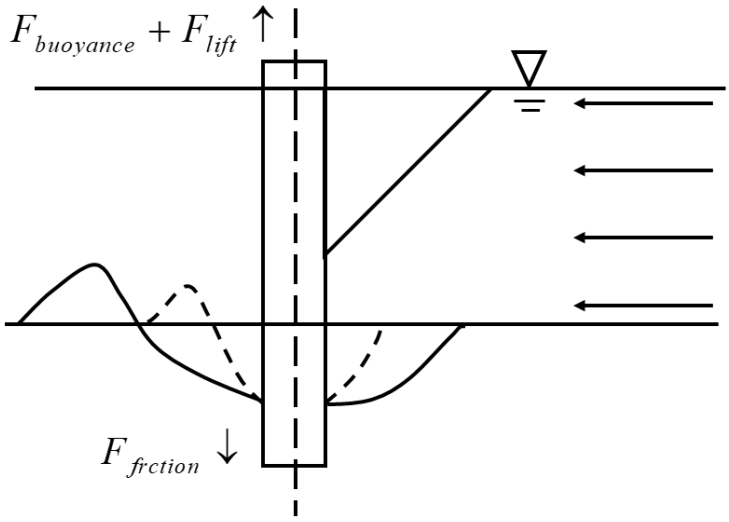

Figure 5-16 Sketch demonstrating a change of the scour hole volume with the same scour depth.

5.5 Conclusions

For a better representation of the natural debris jams and their influence on pier scour, real seedling trees were utilized for the first time to form dynamic debris jams in front of a single pier. The dynamic debris jams considered the time scale of debris jam formation and its relation to scour. Through the process of formation without imposition, dynamic debris jams obtain reasonable dimensions with respect to the local flow condition. The key conclusions of the study are as follows:

(1) Dynamic debris jams formed from real seedling trees as opposed to dowels were more stable and continuously increased in size, eventually leading to greater scour depth.

(2) Debris jam shape influences scour depth ratio. (Pagliara and Carnacina 2011a) found that rectangular and triangular shapes can lead to a much more significant scour ratio while cylindrical debris jams caused less scour ratio. However, dynamic debris jams had the lowest scour ratio, presumably because both the debris jam and the associated scour evolved mutually with time.

(3) In addition, to scour depth, the scour hole volume should be considered. In the presence of a dynamic debris jam comprised of real seedling trees, the scour hole volume was as much as six times the volume without the debris jam. This ratio was much greater than the final scour depth ratio which was about two times the depth without the jam.

Chapter 6. Temporal evolution of the hydrodynamic loading due to dynamic debris jam on bridge pier

6.1 Introduction

Woody debris plays an important role in rivers and its influences involve many aspects such as the flow dynamics, river hydro-geomorphological characteristics, and the river ecosystem. Studies of woody debris dynamics have focused on how the debris was entrained and entered rivers (Braudrick et al. 1997), their decomposition (Braudrick and Grant 2001; Mazzorana et al. 2011), and volume estimation (Spreitzer et al. 2020). A force analysis has been applied to a single wood log to determine its critical entrainment condition, buoyance, drag, and friction forces (Bocchiola et al. 2006; Braudrick and Grant 2000; Chen et al. 2019; Crosato et al. 2013; Haga et al. 2002). While Gurnell et al. (2002) focused on the relationship between woody debris accumulation and the hydro-geomorphological characteristics, the wood budget was also investigated to track the spatial and temporal distribution of debris in the channel. As for the role of woody debris in the ecosystem, Daniels (2006) summarized that the woody debris resulted in the promotion of biological production and diversity, as well as improved habitats. These studies indicated that woody debris in river systems is a common concern, and it plays various roles in various specific situations. However, river engineers have mainly focused on the threat of woody debris to river infrastructure and its dynamics.

Woody debris accumulated at bridge structures has been a widespread concern among bridge engineers. The presence of woody debris jam reduces the capacity of bridge openings and results in extra scour and increased lateral loading onto the pier. Diehl (1997) pointed out that woody debris jams were responsible for over one-third of the bridge failures in the US. Bradley et al. (2005) also indicated that the unsatisfactory performance of bridge structures was frequently caused by the accumulation of debris. Thus, consideration of debris accumulation has been of great importance and required consideration in the design of the bridge structures.

Debris jams can contribute to bridge failures and flood risk in three ways, as Panici and de Almeida (2018) summarized. Firstly, extra load occurs on the bridge infrastructure when subjected to a debris jam. As Panici and de Almeida (2018) showed, the drag force exerted on the pier could increase by an order of magnitude due to debris jams compared to the hydrodynamic loading. Secondly, the hydraulic head induced by debris jams, and the associated increase of water level upstream of the debris, is another issue caused by the presence of debris jams. This is due to both roughness of the debris jam and the reduction of the bridge openings caused by the accumulation of debris jams around piers. Gippel et al. (1996) defined the upstream water level increase as afflux, which resulted in an increase in the flood threat upstream of the bridge. Finally, the presence of debris jams can also significantly increase scour depth at the river structure, as mentioned in the findings of several researchers (Diehl 1997; Lagasse et al. 2010; Lyn et al. 2007).

In terms of the studies of the lateral loading caused by debris jams, the dynamics of the bridge pier were analyzed by (Parola et al. 2000):

$$F_s = F_D + (F_{hu} - F_{hd}) \tag{6-1}$$

where F_s = the lateral or streamwise force; F_D = the drag force; F_{hu} = the hydrostatic force upstream of obstruction; F_{hd} = the hydrostatic force downstream of the obstruction.

This method was also further adopted by US Federal Highway Administration (Bradley et al. 2005) for bridges over river channels. In addition, the drag coefficient was considered to be related to the flow

blockage ratio due to the presence of debris jams. Meanwhile, Stolle et al. (2018) applied 3 types of debris and investigated their drag resistance coefficient (including the drag force and the increase in the hydrostatic force due to flow obstruction) in transient supercritical flow conditions, the drag coefficient was found to be related to the Reynolds' and Froude number. In addition, Mauti et al. (2020) used idealized semicylinders and plates in plastic or aluminum material with varying porosity to investigate the effects of the debris jam porosity, shape, and height on hydrodynamic load due to debris jam. They showed that the effective resistance coefficient had no significant correlation to the porosity of the idealized debris jam. Panici and de Almeida (2018) also used dynamic debris jam to investigate the drag coefficient in terms of varied flow conditions and characteristics of debris like length or uniformity. They observed that the drag coefficient was in the range of 1.0-2.0 no matter the flow conditions or debris characteristics. Derschum et al. (2018) also pointed out that the impact force of debris distinguished from the hydrodynamic force was dominant in rapidly transient flow conditions. Thus, in extreme flood events, the streamwise force might also need to include the impact force F_i, even though the latter might be not too significant for woody debris in a fluvial channel.

Currently, modeling debris jams does not adequately represent the real debris jam, especially considering their size and local flow conditions. Mostly static and solid block debris jams have been applied to investigate the influence of debris jams on scour depth. Melville and Dongol (1992) applied a woody block to represent a debris jam and proposed an effective pier diameter to quantify its influence on scouring, similar also to the work of (Lagasse et al. 2010). Pagliara and Carnacina (2011) used woody debris jams with a cylindrical, rectangular, and triangular shapes and used their blockage ratio to quantify their influence on scour depth around piers. As mentioned before, Mauti et al. (2020) used an idealized debris jam to investigate the drag coefficient. Dynamic debris such as those employed by (Panici and de Almeida 2018) and (Schalko et al. 2019) need to be applied to simulate the formation of the debris jam and its load during the growth process.

Few studies have focused on the temporal evolution of loading caused by dynamic debris jams on the bridge structure. Such studies play an essential role to understand better the mechanism of debris formation which affects bridges. To be able to properly estimate the additional load exerted by the presence of the debris jam, the correct estimation of their drag coefficient – a difficult task - is crucial. Panici and de Almeida (2018) attempted to determine the critical size of the debris jam under specific flow conditions so that the maximum load caused by the debris jam could be estimated. However, it was difficult to determine whether the threat to the pier stability caused by the debris jam was only due to the maximum load or if this could have also come from the impulse load caused by the presence of the dynamic debris jam. Furthermore, studies utilizing dowels or debris without branches may be not able to well represent real debris as Lyn et al. (2003) and Panici and Almeida (2020) pointed out. In fact, no previous laboratory studies have used natural trees to investigate debris loading on bridge piers.

The present study introduces the time scale to investigate the temporal evolution of the loading induced by dynamic debris jams on a bridge pier. Idealized debris (dowels) and natural debris (seedling trees) were both used and compared to investigate the spatiotemporal characteristics of the dynamic debris jams and their hydraulic and loading characteristics. The time histories of both the force on the pier and the upstream hydraulic head (backwater water level increase) were monitored during the temporal formation and growth of the dynamic debris jams, such that the loading process could be elucidated more fully.

6.2 Methodology

6.2.1 Experiment setup

The physical modeling of dynamic debris jam impact on the cylindrical pier was conducted in the Hydraulic Laboratory at the University of Ottawa, Canada. The flume used is 30 m in length, 1.5 m in width, and 0.7m in height. A solid false bed with a height of 0.2 m and a length of 8.7 m was constructed over the last longitudinal third section of the flume. A wave straightener was installed at the upstream end of the flume to ensure a uniform approach flow, while a 2.3 m gravel prism with an upward slope of 0.087 was built immediately upstream of the false bed. A cylinder pier model with a diameter $D_p = 0.09$ m was installed 2.5 m upstream of the flume outlet. Debris was manually released every 5s for a period of one hour from a vertical distance of 5cm from the water surface and 2.2 m upstream of the pier location. The debris was released normally in the streamwise direction as the focus of this study was on the growth and development of debris jams. The sketch of the lab flume is shown in Figure 6-1.

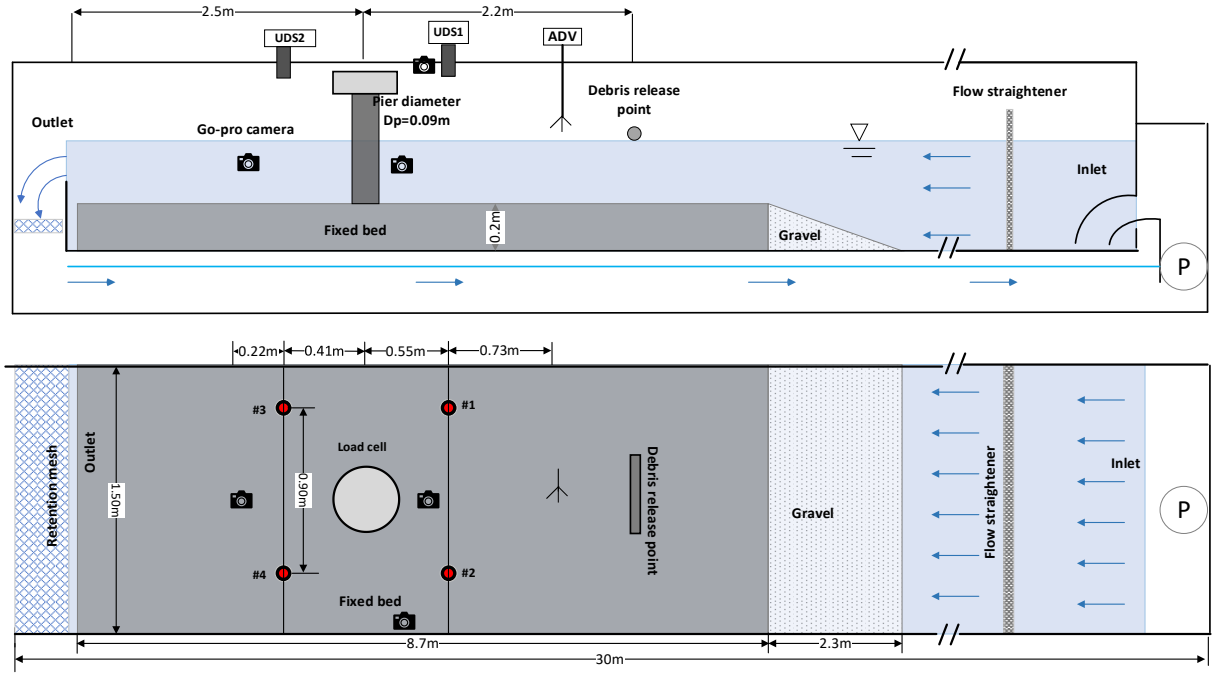

Figure 6-1 Sketch of loading tests of dynamic debris jam (not to scale).

The load and size of the dynamic debris jam were monitored during the development of the debris jam in front of the pier. Three HERO5 Black GoPro cameras (https://gopro.com/en/us/update/hero5) with a sampling rate of 60 fps in linear mode and a 1920*1080 resolution were installed to capture the spatial evolution of the dynamic debris jam. The first camera was submerged behind the pier at a downstream distance of 0.63 m, while the second one was fixed above the flume. The third one was submerged close to the flume side wall to record the development of debris jam. All cameras were adjusted before each test to ensure that the formation of each debris jam was fully captured. Four MassaSonic PulStar ultrasonic sensors (https://www.massa.com/industrial/ultrasonic-sensors/pulstar) with a measurement resolution of 0.25 mm and a sampling rate of 10 Hz were used to measure the water level. Two of the sensors (#1,#2) were set 0.55 m upstream of the pier, while the two others (#3,#4) were positioned 0.41 m downstream of the pier (see Figure 1). An Interface load cell was installed and connected to the bridge pier at its upper end to

monitor the time-history of the loading exerted on the pier by the woody debris jam. The Interface's 6-axis (6A154B) (https://www.interfaceforce.com/products/multi-axis-sensors/6-axis/6a-series-6-axis-standard-capacity-load-cells-fx-fy-fz-mx-my-mz/) loadcell model can simultaneously measure forces and moments along the three coordinate axes. The measurement range of the load cell was 100 N in the x-direction, 100 N in the y-direction, and 200 N in the z-direction; a sampling rate of 1000 Hz was used to ensure adequate capturing of the temporal evolution of the load onto the pier. In addition, A Vectrino Acoustic Doppler Velocimeter (ADV) (https://www.nortekgroup.com/products) set at a sampling rate of 100 Hz was used to measure the velocity profile 1.28 m upstream of the pier without debris. The measuring points were spaced in increments of 1-2 cm in the water depth direction with a duration over the 90s. A filter developed by (Jamieson et al. 2010; Rennie and Hay 2010) was applied to reduce the measurement noise of the ADV data, and the time-average velocity was obtained for each measuring point. The load cell and ultrasonic sensors were integrated into one synchronized data acquisition system (DAQ) manufactured by HBM GmbH, type of QuantumX MX440B and MX840B (https://www.hbm.com/en/). The details of the instrumentation used are presented in Table 6-1.

Table 6-1 Characteristics of the instrumentation used in the current study.

Instrument type/Manufacturer	Model	Sampling Rate (Hz)	Resolution
Ultrasonic Distance sensor(UDS)/MasaSOnic PulSar	M-5000/220	20	0.25mm
6-Axis Load Cell/Interface	6A154B	1000	±0.1%
Acoustic Doppler Velocimeter (ADV)/ Nortek	Vectrino	100	±0.5%
GoPro Camera	Black Hero 5	1080/60/Linear	
Data Acquisition System (DAQ)/ HBM GmbH	QuantumX MX440B and MX840B		

6.2.2 Experiment matrix and material

Dynamic debris jams were generated under various flow conditions (Table 6-2). The mean flow velocity upstream of the bridge pier for each test was obtained using an ADV located along the longitudinal centerline of the flume. The distribution of the u-component velocity over the normalized water depth for each test condition is shown in Figure 6-2, from which a depth-averaging method was used to calculate the mean flow approach velocity for each test.

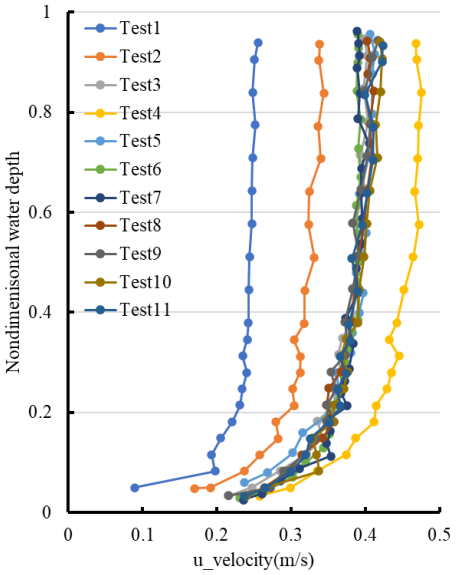

Figure 6-2 u-component velocity distribution over the normalized water depth.

In the present study, dowels and naturally grown seedling trees were selected to model the debris. The length of seedling trees was nonuniform, with an average length of 40.1 cm and a stem diameter of 0.3 cm while the dowels were all uniform with a 30 cm length and diameter of 1.3 cm. As mentioned, given the nature of natural debris, dowels are thought to be their idealized, though inaccurate, representation as previously shown by Panici and Almeida (2020). The seedling trees and dowels are shown in Figure 6-3.

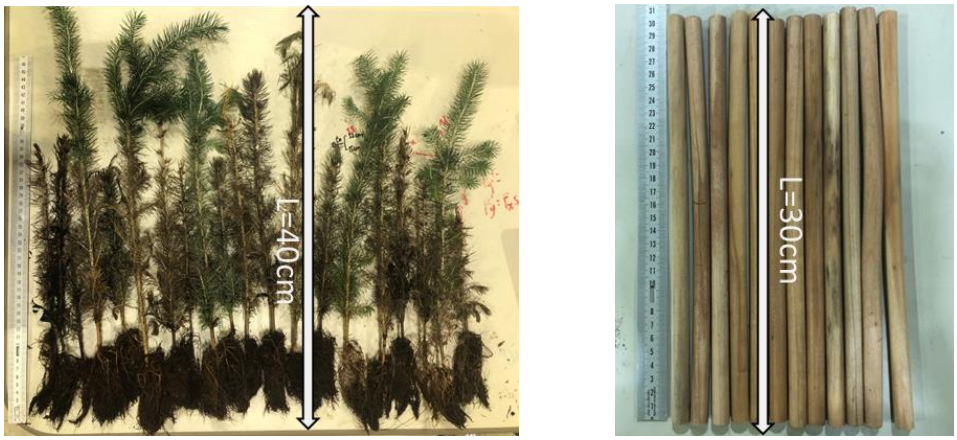

Figure 6-3 Seedling trees and dowels used in this debris loading test.

The test matrix was designed to investigate the influence of the mean velocity, water depth, individual pieces release, and dowel density. Tests 1-4 had similar water depths but different mean velocities, while Tests 5-7 had similar mean velocities but different approaching water depths. In Test 8 the debris was released with a frequency of 3 pieces every 5 seconds. In addition, Tests 3, 9, and 10 were repetition tests performed to investigate the random debris jam formation. Dowels for tests 1-10 were submerged in water for over 1 day to ensure that their density during the tests did not change significantly; the wet density of dowels was around 881.15-920 kg/m^3. However, Test 11 was conducted with dry dowels with a density of 526 kg/m^3. The flow Froude number of the present study was in the range of 0.16-0.30, while the Reynolds number was in the range of 5×10^4 - 9.8×10^4. The details of the test matrix are shown in Table *6-2*.

Table 6-2 Test matrix for the experimental debris loading tests

Test number	Mean velocity U (m/s)	Water depth h (m)	F_r number	R_e number $\times 10^4$	Debris type	Specific features
1	0.23	0.30	0.16	5.00	Dowels/Trees	Mean velocity
2	0.31	0.30	0.21	6.74	Dowels/Trees	
3R	0.37	0.30	0.26	7.99	Dowels/Trees	
4	0.44	0.30	0.30	9.51	Dowels/Trees	
5	0.37	0.25	0.27	6.98	Dowels/Trees	Water depth
6	0.37	0.35	0.24	8.93	Dowels/Trees	
7	0.38	0.40	0.24	9.81	Dowels/Trees	
8	0.38	0.30	0.26	8.13	Dowels/Trees	Congested release
9R	0.37	0.30	0.26	8.03	Dowels/Trees	Repeat tests
10R	0.39	0.30	0.26	8.31	Dowels/Trees	
11	0.38	0.31	0.26	8.20	Dowels	Lower density

Note: R means the repeating tests; lower dowels density ρ_d =526.27kg/m^3

6.2.3 Experiment procedures and scale effects

The procedures for all tests followed the same sequence. First, the flume pump was turned on using low flow to ensure the physical stability of the experimental setting and instruments. After the water level reached the submergence depth of all instruments, the discharge was gradually increased to the designed value. Once the water level reached its set flow condition, GoPro cameras started recording video data and the data acquisition system (DAQ) started recording data. Approximately 2 mins after the start of the video recording, debris pieces started to be manually released from 2.2 meters upstream of the pier location. When each test finished, debris captured by a retention wire mesh located at the entrance in the flume drain was recuperated and used in the next test. The duration of each test was about 60min. The dowels and seedling trees were released using the same flow condition for each test. A seedling tree jam and a dowels jam were shown, respectively, in Figure 6-4.

Figure 6-4 A debris jam formed by the (a) seedling trees and (b) side view for dowels.

Scaling in the present study used Froude similitude as it was widely used in previous debris tests (Schalko et al. 2019). A geometric scale factor, λ, (Prototype/Model) of 30 was used in the present study similar to (Schalko 2018). As such, the prototype flow condition was in the range of 1.2-2.4 m/s for velocity and 7.5m-11.99 m for the water depth. The cylindrical pier diameter of the prototype was 2.7 m. Debris pieces

would have prototype lengths of 9 m (dowels) and 12 m (seedling trees). According to the field report of (Diehl 1997), the lengths of individual debris pieces in real debris jams on single piers ranged from 0 to 18 m. Thus, the sizes of the selected debris pieces were deemed representative of this test series. The GoPro images were orthorectified to ensure that the correct debris jam dimensions were measured from the images.

6.3 Results and Analysis

6.3.1 Dimensions of dynamic debris jam

The spatio-temporal evolution and dimensions of the dynamic debris jams were captured by the GoPro cameras through conducting orthorectified. The evolution of the dimensions of dynamic debris jam data was averaged over one-minute timesteps. The evolution of the debris jam dimension of all tests is presented in the supplementary Figure S1. The height of the dynamic debris jam, h_d, was defined as the distance between the debris jam base and the water surface. The length of the debris jam, l_d, was set as the maximum longitudinal distance from the debris upstream edge to the pier face at the centerline. In addition, the width of the debris jam w_d was set as the maximum width of the debris jam in the transverse direction at the upstream face of the pier. The projected frontal area, A_{vc}, was calculated as the frontal area of the triangular shape (Panici and de Almeida 2018; Panici and de Almeida 2020) defined by the length and width of the dynamic debris jam as follows:

$$A_{vc} = 0.5 h_d w_d \tag{6-2}$$

The time-history of the dimensions of dynamic debris jams was investigated for both the dowel and tree jams. The results of Tests 1 and 2 are presented in Figure 6-5 at one-minute intervals. Generally, the dimensions of the dowel jam were larger than those of the seedling tree jam. The dynamic debris jam formed by dowels exhibited three peaks (including the process of formation, growth, and failure) during the tests, and each debris jam lasted about 15-20 mins before breakup which was also observed in (Zhang et al. 2022). By contrast, seedling tree jams were more stable and grew continuously except for only one Test 1 that partly failed.

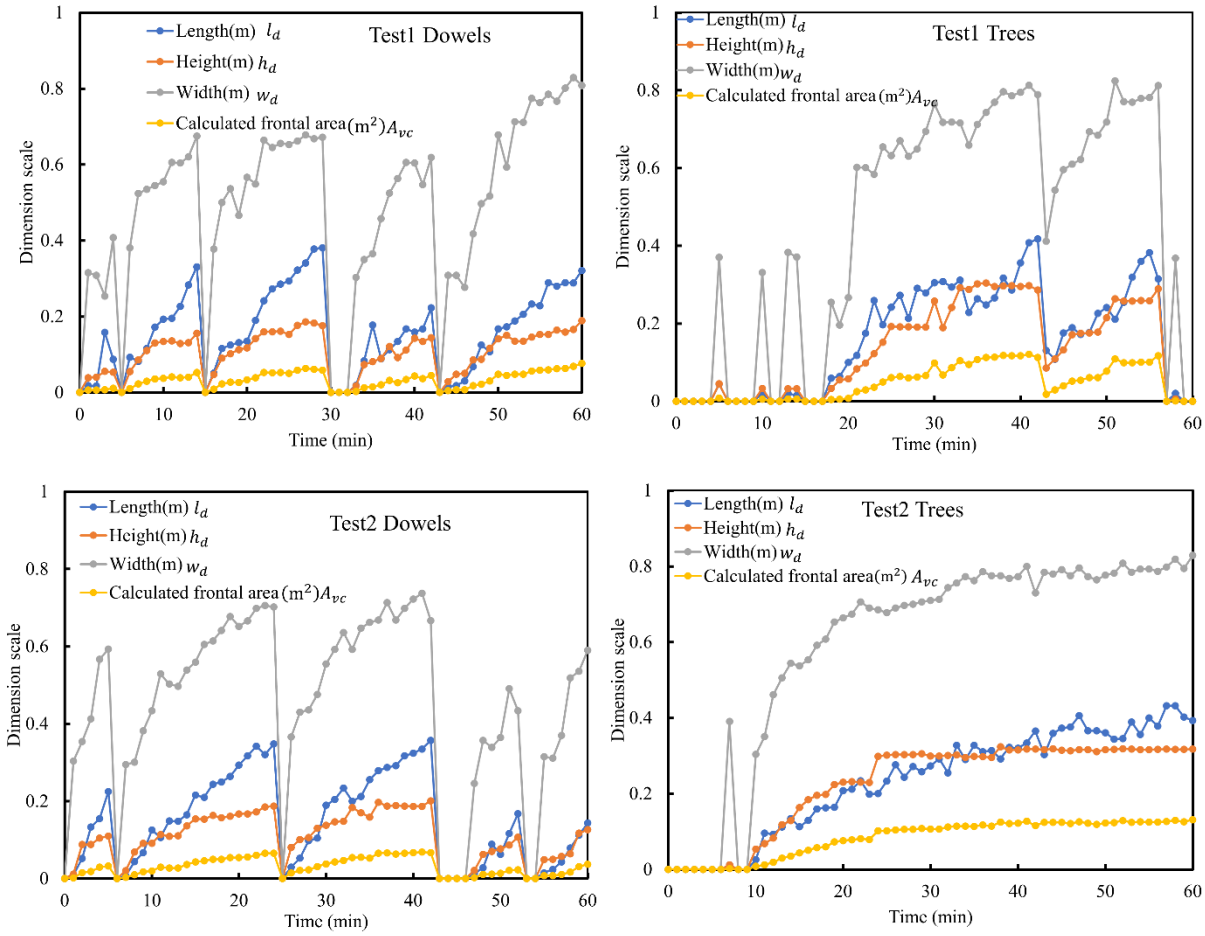

Figure 6-5 Spatio-temporal evolution of the dimensions of the dynamic debris jams for Test 1 and Test 2.

Considering the difficulty of determining the projected frontal area of debris jam in field conditions, it was feasible to establish the relationship between the planar horizontal area and the frontal projected area which indicated a potential convenient method to obtain the frontal area of debris jam. The planar horizontal area A_p of debris, the jam was obtained by the top GoPro camera. All test data were integrated to check the relation between dowels and trees jam respectively (Figure 6-6). Thus, the linear correlation between the horizontal area and the frontal projected area A_{vc} can be described as:

$$A_{vc} = 0.44A_p \qquad \text{for dowels} \tag{6-3}$$

$$A_{vc} = 0.53A_p \qquad \text{for seedling trees} \tag{6-4}$$

However, the correlation between the planar horizontal area and frontal vertical area might not continue keeping a linear relation when the height of the debris jam reached the water depth in the fixed bed.

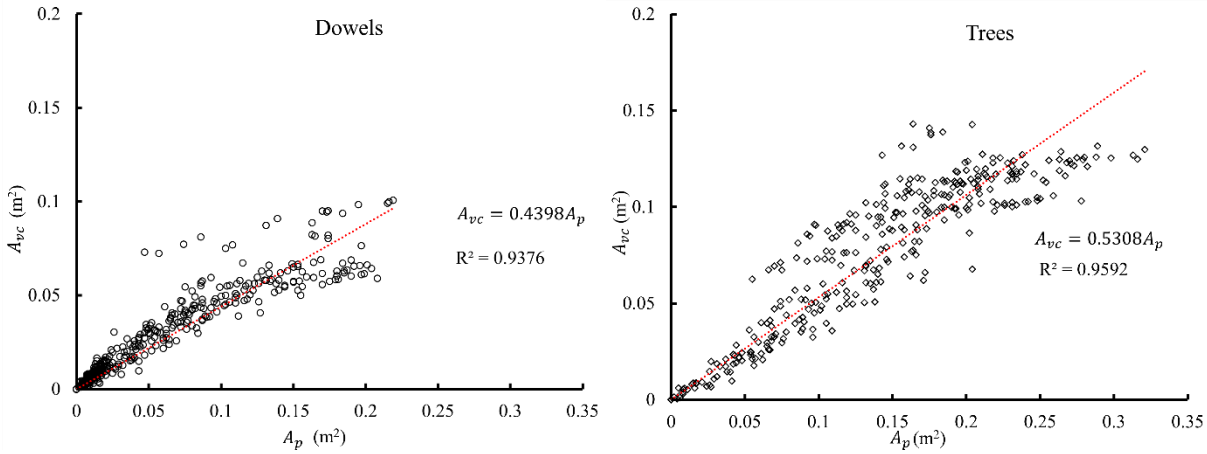

Figure 6-6 the plan horizontal area A_p and the frontal vertical area A_{vc} of all tests, (a) dowels and (b) trees.

6.3.2 Time-history of loading onto the bridge pier

The data for the load and hydraulic head were averaged over one-minute timesteps in order to be consistent with the data detailing the time-history of the loading due to debris jam. The evolution of loading due to dynamic debris jam of all tests is presented in the supplementary Figure S2. Loading caused by the dynamic debris jam was recorded using the load cell and the results obtained during the development of the debris jam of Test 1 and Test 2 are presented in Figure 6-7. For clarity, only these two tests are presented herein. As expected, it was observed that the higher approach flow velocity leads to higher loading in the presence of the debris jam, irrespective of whether the dowel or tree jams were used. In addition, the authors infer that the dynamic debris jam formed by seedling trees could exert a greater load compared to the one generated by the dowel jams due to the higher stability of seedling tree jams. As expected, the increasing exerted load correlated with the size of the dynamic debris jam. Furthermore, it also observed that load spikes occurred over a short time for both the dowel and tree jams. This phenomenon occurred several times and is discussed in the Discussion section.

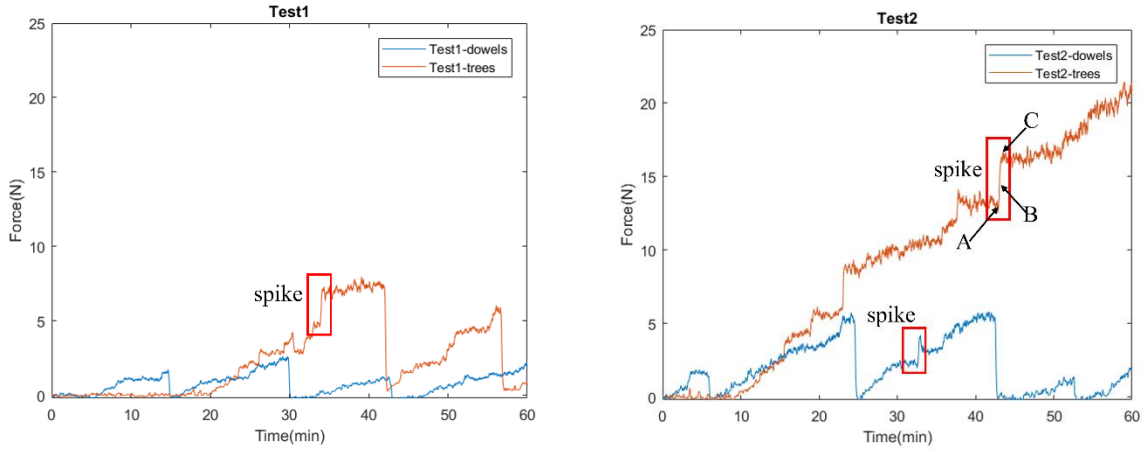

Figure 6-7 Time-history of the evolution of loading on the pier for (a) Test 1 and (b)Test 2

The calculation of the drag coefficient, C_d, was performed with the goal of estimating the load caused by the debris jam. The drag coefficient was calculated by the following equation (Panici and de Almeida 2018).

$$C_d = \frac{2F_x}{\rho U^2 A_d} \tag{6-5}$$

where ρ = the water density (1000kg/m^3); U = the mean velocity of the approach flow (without debris jamming); F_x = the increase in load caused by debris jam; $A_d = A_{vc} - h_d D_p$ = the increased projected area due to the presence of the debris jam; D_p = the pier diameter.

The definition of the blockage ratio generated by the debris jam was based on the study (Parola et al. 2000), and the blockage ratio here was calculated by $B = A_d/bh$, which b is the width of flume and h is the water depth before obstruction due to the debris jam. In present study, the blockage ratio is applied by

$$\Delta A = (A_{vc})/hb \tag{6-6}$$

The drag coefficient calculated for all tests is presented in Figure 6-8 as a function of the blockage ratio. It was observed that debris jams formed by seedling trees can generate a greater blockage ratio than that generated by the dowels. There was a fair amount of variance in the calculated drag coefficients for both the seedling tree jams and the dowel jams, especially when the debris jam size was small, with little clear correlation with the blockage ratio. Nonetheless, it can be seen that the drag coefficient converged to a constant value as the blockage ratio increased. The drag coefficient average, standard deviation, and coefficient of variation for the dowels (trees) were 2.37, 4.05, and 1.70 (2.62, 1.53, and 0.59). The trendline for the drag coefficient for the dowels (trees) had an intercept of 1.898 (2.75). The coefficient of variation of dowels was high due to variable calculated drag in the initial stages of debris jam development. This may in part be due to the assumption of triangular geometry when calculating debris jam dimensions, whereas initial jams comprised of dowels had irregular dimensions. More reasonable drag coefficients were obtained once the blockage ratio exceeded 0.1, for which the drag coefficient average and coefficient of variation for dowels (trees) were 1.79 and 0.34 (2.64 and 0.23).

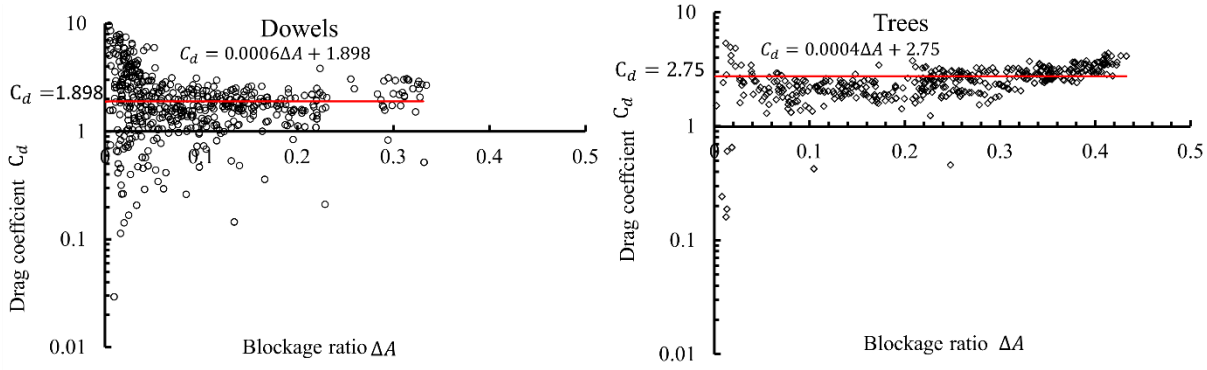

Figure 6-8 Calculated drag coefficient by the load caused by dynamic debris jam of (a) dowels and (b) seedling trees.

6.3.3 Time-history of debris-induced hydraulic head

The presence of debris jams can also lead to a water level increase upstream of the pier and result in an increase in flood risk upstream of the bridge. The debris-induced hydraulic head, (Δh), was calculated as the difference between the water level upstream and the water level downstream of the pier. Specifically, for example, the water level of sensor #1 minus the water level of sensor #3 provided the hydraulic head across the pier (Δh_1), and similarly Δh_2 was the difference between water level sensors #2 and #4. The debris-induced hydraulic head, (Δh), was calculated by the average of Δh_1 and Δh_2. The time-history of the debris-induced hydraulic head is presented for Tests 1 and 2 in Figure 6-9. It was observed that the debris jam formed by seedling trees was able to induce a greater hydraulic head compared to the debris jam

formed by dowels. In addition, spikes were also observed in the temporal evolution of debris jam-induced hydraulic head both in the seedling tree jam and dowel jam. The evolution of the hydraulic head due to dynamic debris jam of all tests is presented in the supplementary III Figure S3.

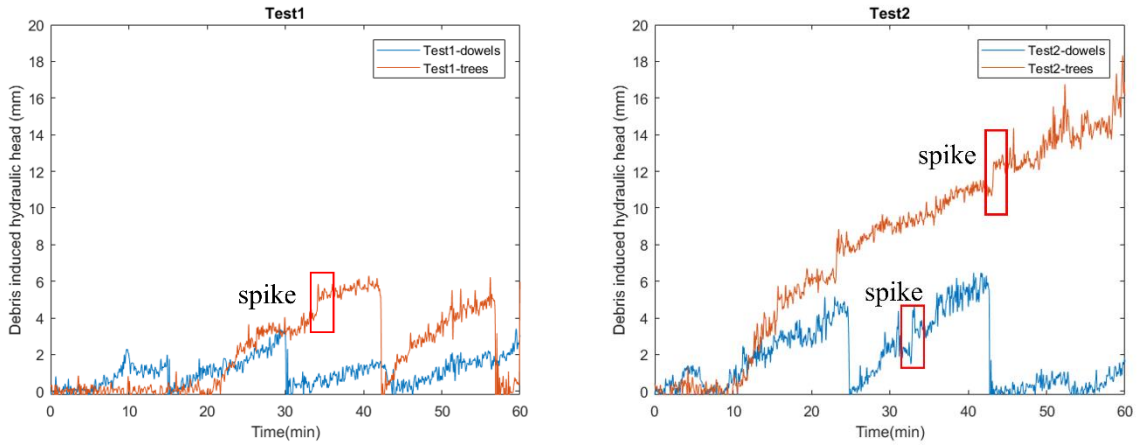

Figure 6-9 Time-history of the debris jam-induced hydraulic head for (a) Test 1 and (b) Test 2.

All data for the debris-induced hydraulic head (Δh) were normalized by the water depth before the debris jam-induced obstruction, and then by considering the influence of flow conditions through the Froude number. These normalized hydraulic head values are plotted versus the blockage ratio in Figure 6-10. The resulting functions for the dowels and seedling tree's dynamic debris jams are, respectively,

$$\Delta h = 0.32\Delta A F_r h \quad \text{for dowels} \tag{6-7}$$

$$\Delta h = 0.45\Delta A F_r h \quad \text{for seedling trees} \tag{6-8}$$

where ΔA = the blockage ratio caused by the debris jam; F_r = the Froude number; h = the water depth before the debris jams obstruction.

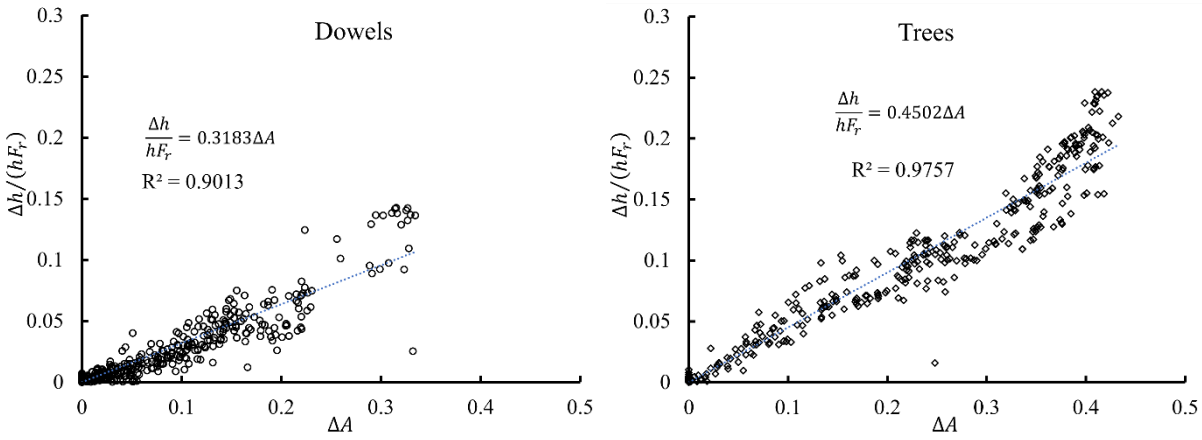

Figure 6-10 Variation of the normalized hydraulic head $\Delta h/(hF_r)$ as a function of the blockage ratio ΔA for (a) dowel and (b) seedling tree dynamic debris jams.

6.4 Discussion

The repeatability of the tests was also verified by Tests 3, 9, and 10 which were conducted in approximately similar flow conditions in terms of mean velocity and water depth, as was Test 11 but with lower density dowels. The load, hydraulic head, and frontal vertical area of debris were used to monitor their development over time (Figure 6-11). The load F_x and induced hydraulic head Δh were also highly related to the size of the debris jam. It was observed that the debris jam formed by dowels showed a similar trend for Tests 3 and 10 which exhibited two peaks of the debris jam size which lasted at least 20 minutes for each peak. However, it was also found that the size of the dowel jam in Test 9 was much smaller than that in other tests; nonetheless, two main peaks in jam development were still observed. According to the study of (Panici and de Almeida 2018), the randomness of the critical dimensions of debris jam (height h_d and length l_d) were generally higher with coefficients of variation greater than 0.24, so the differences observed in Test 9 could be attributed to the randomness of the temporal evolution of debris jams. In addition, Test 11 using dowels with a lower density is also presented in Figure 6-11. Debris pieces with a lower density reduced the stability of the debris jam and led to a much smaller size of debris jam. The debris jam peak in the lower density case lasted much less time (about 10 minutes), and the load was also much less.

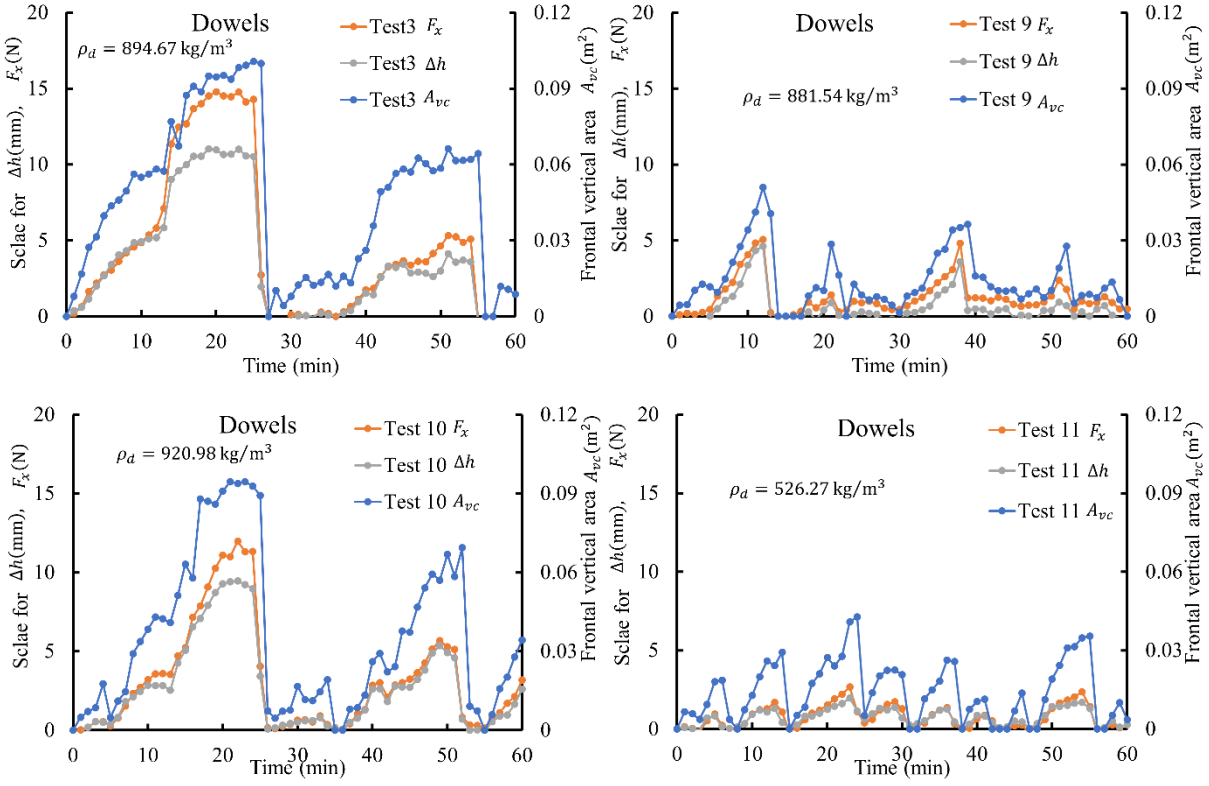

Figure 6-11 Temporal evolution of dynamic debris jam for the repeating tests of dowel and lower density.

The temporal evolution of the debris jam formed by seedling trees was checked for repeatability, and the time-histories of the force in the x-direction for Tests 3, 9, and 10 are shown in Figure 6-12. Firstly, all tests generally showed one force peak of the debris jam. Once the debris jam formed, the structure of the debris jam was relatively stable. However, the time for the formation of the debris jam varied significantly, and there was significant randomness in the formation process of the debris jam.

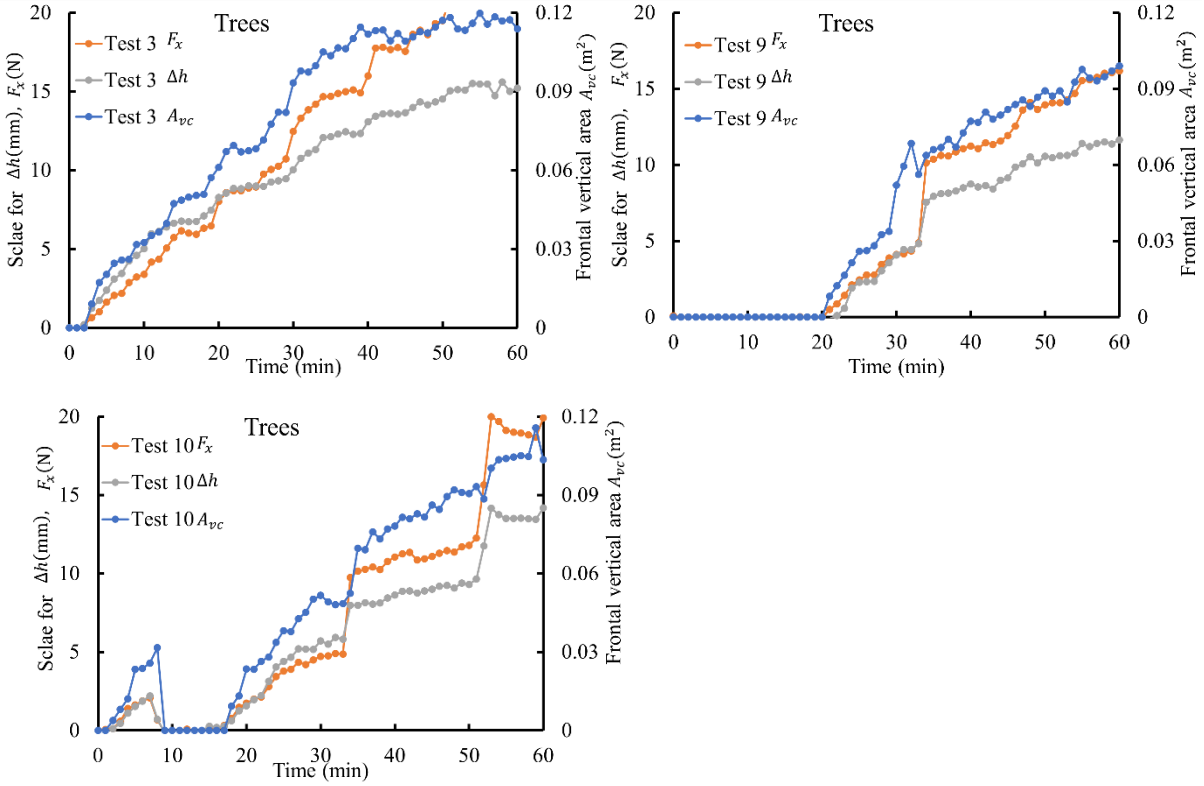

Figure 6-12 Time-history evolution of dynamic debris jam for the repeating tests of seedling trees.

The congested release, with higher debris releasing intensity, attempted to reproduce the greater debris transport in a flood event, and the result of the temporal evolution of debris jam size, load, and hydraulic head induced by debris jam is presented in Figure 6-13. It was observed that the load generated by the debris jams formed using higher intensity debris release mechanisms did not modify the development process of dynamic debris jams such as the duration time and the total time needed to start forming both the dowel and the seedling tree jam. However, the congested releasing debris technique led to a higher speed of load increase. In other words, the load caused by the debris jam reached a higher magnitude in a shorter time than that of slower debris release. This has important implications for bridge loading from dynamic debris jams during flood events or upstream debris jam release events, when large quantities of debris may be transported by the river.

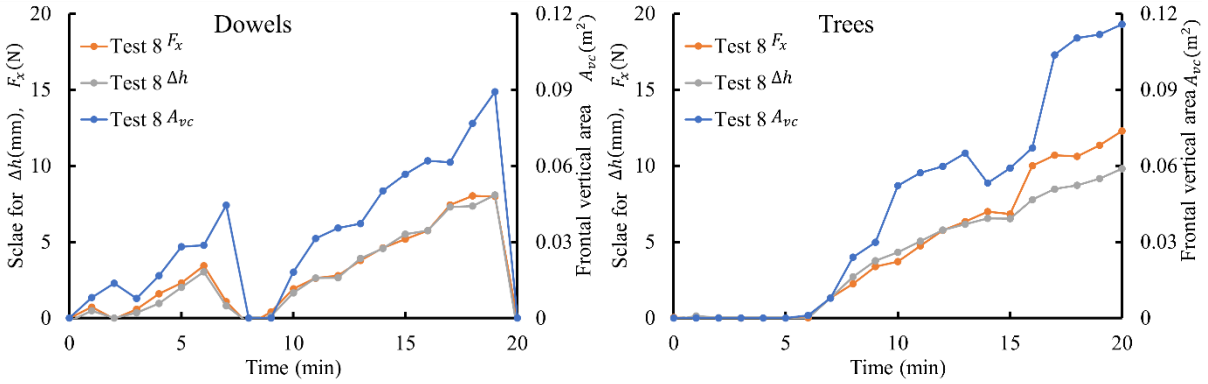

Figure 6-13 Time-history of the force due to dynamic debris jam for congested releasing technique.

Some spikes can be observed during the development of the dynamic debris jam – this was considered a potential factor attributed to the bridge failure as the load induced by the debris jam increased significantly in a very short period. A conceptual sketch is provided in Figure 6-14 to explain the formation of the force spikes. Supplementary Figures S4-7 were also presented to show the temporal evolution process of debris jam for dowels and trees. As debris pieces captured by the cylinder pier accumulated, and as the dimensions of the debris jam reached a certain size, the incoming floating debris pieces accumulated in larger numbers at the water surface at the upstream edge of the debris jam. As such, the speed of development of the debris jam in the longitudinal direction was faster than its speed of development in the vertical direction. Thus, the angle α characterizing the slope of this upstream portion of the debris jam was small and unstable; eventually, this frontal part of the debris jam was forced to roll downward. As the angle α increased to a greater value (β) this made the debris jam structure more stable. This increased the frontal obstruction area in a short time meanwhile the increasing obstructing area also induced a higher mean velocity in the section, thus, the load caused by debris jam, that exerts to the pier, formed a spike. These spikes could lead to impulse loads to the pier with the potential for bridge failure.

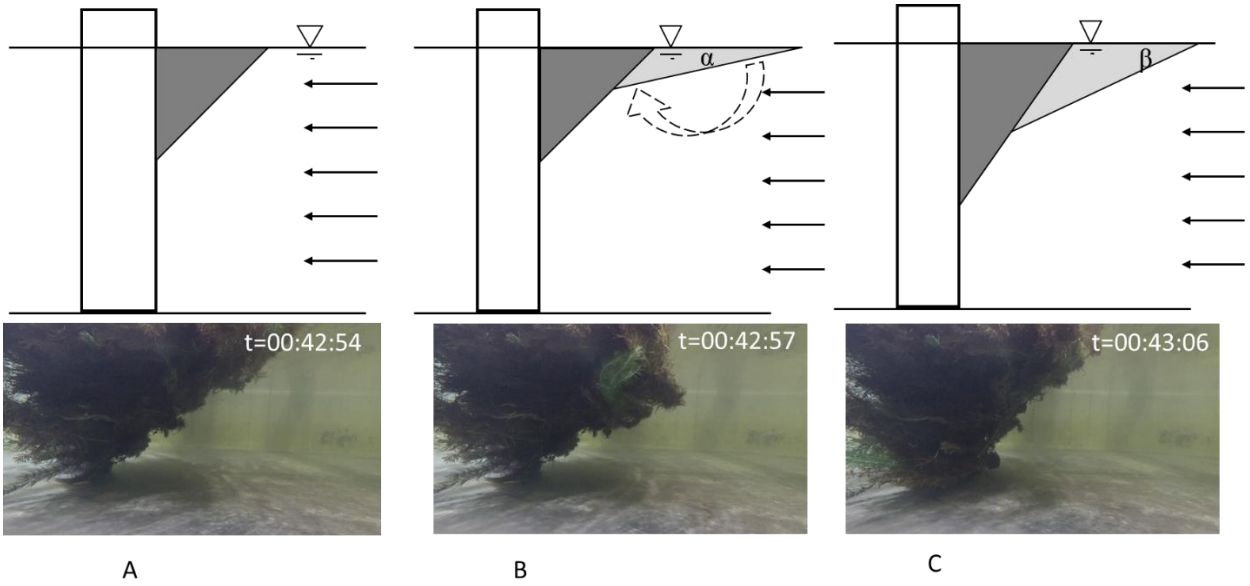

Figure 6-14 Mechanism of debris accumulation resulting in a force spike during the development of a dynamic debris jam, with an observed example over a period of 12 seconds during Test 2, with each image corresponding to points A, B, and C in Figure 7b.

6.5 Conclusions

In this study, either dowels or real seedling tree debris pieces were released upstream and captured by a single cylindrical pier to form dynamic debris jams. The evolution of the dynamic debris jam was monitored from a time-dependent perspective. Various flow conditions were used to record the load exerted on the bridge pier and upstream hydraulic head caused by the presence of the dynamic debris jam. The following results can be concluded:

(1) The horizontal plan area of the debris jam correlated linearly with its frontal vertical area. This correlation could provide a potential method to estimate the vertical debris jam area as it is relatively easier to obtain the horizontal plan debris jam area compared to its frontal vertical area.

(2) The type of debris influenced the formation of the debris jam: the debris jam formed by the seedling trees was significantly more stable than the debris jam formed by dowels. Consequently, dynamic debris jams formed from seedling trees accumulated to greater size and blockage ratio with corresponding greater induced load and hydraulic head.

(3) The temporal evolution provided insight into the behavior of the debris jams. Force spikes were observed when the debris jam reached a certain size and then consolidated.

Chapter 7. Experimental investigation of the hydrodynamic field around a debris jam on a bridge pier

7.1 Introduction

During flood events, wood logs or debris are often entrained into the river flow. When the debris pieces are attached to a bridge pier, the key log initiates the formation of a debris jam in front of the pier. Woody debris accumulated in front of the bridge pier imposes an extra load on the structure, and the load significantly increases the possibility of bridge failure. Bradley et al. (2005) provided an approach to estimate the load caused by debris damming, and the drag coefficient is considered to be dominated by the blockage ratio and Froude number. Previous laboratory studies have utilized idealized prismatic shapes to represent debris jams. However, a debris jam formed naturally in the field by individual debris pieces may have different roughness and porosity than an idealized debris jam. The intent of this study is thus to examine the influence of debris jam roughness on the local flow field, including the spatial distribution of vorticity and Reynold stress.

The hydrodynamics of bridge piers and associated scour have been studied for many years. Dargahi (1989) applied a hot film approach to measuring the flow field, and several vortices were observed to explain the mechanism in terms of velocity distribution. Graf and Yulistiyanto (1998) using an Acoustic Doppler Velocity Profiler (ADVP) measured the flow field including the velocity distribution, Reynold shear stress as well as the horseshoe vortex. The horseshoe vortex system exhibited positive vorticity at the base of the pier, and a counter-current with negative vorticity toward the outside. Okamoto et al. (2021), using particle image velocimetry (PIV), measured the flow field for evolving driftwood accumulation divided into four phases considering the accumulation process. Downward flow occurred in front of the debris jam and the magnitude of vertical velocity at the water surface was small at the end of the initial stage of the debris jam, but it increased and was stronger due to the carpet geometry of the debris jam.

The horseshoe vortex system is believed to be the primary cause of scour (Ettema et al. 2006; Graf and Istiarto 2002; Hager 2007). Lagasse et al. (2010) summarized idealized flow patterns for local scour in the presence of debris jam. Reduction of cross-sectional flow area due to the presence of triangular accumulation debris led to the acceleration of flow velocity, and finally, it caused the increase of scour hole depth. In the case of rectangular accumulation debris, a second scour hole formed in front of the bridge pier. These results conceptually described how the debris jam affected the scour process. Pagliara and Carnacina (2013) applied an Acoustic Doppler Velocimeter (ADV) to investigate the role of the debris jam by varying their dimensions and roughness. Flow accelerated and strengthened downwards as the flow area was constricted by the presence of debris jam, and the accumulation of debris formed a boundary layer that deflected the flow down to the base of the pier. However, the horseshoe-vortex system was not analyzed in these studies.

Numerical modeling has also been used to examine the turbulent flow structure around bridge piers. Kirkil et al. (2008) used LES to investigate the flow field around a circular cylinder located in a scour hole considering the interaction of the horseshoe vortex system. They found that the structure of the horseshoe vortex varied significantly with space and time even though a large and stable primary necklace vortex was evident in the scour hole. (Kirkil and Constantinescu 2012; Kirkil and Constantinescu 2015) further applied this model to simulate the necklace horseshoe vortex system in both laminar and turbulent flow, and the large-scale coherent structures (necklace vortices, vortex tubes shed in the separated shear layers (SSLs) and roller vortices shed in the wake) were well captured. However, the turbulence structure around a pier with a debris jam has not yet been investigated.

This paper presents the first experimental results for the velocity spatial distribution and the turbulence structure in four vertical sections around three debris jams of the same size and shape but with different roughness. The first objective of this study is to evaluate the influence of debris jam roughness on the flow field. Two debris jams were built with dowels of different lengths within the same size frame, while the third prismatic debris jam was built using a 3D printer. The same flow condition was applied for each debris jam in addition to a blank test (no debris). The second objective is to investigate the turbulence structure around a pier in the presence of a debris jam; these results could be potentially used for numerical modeling.

7.2 Methodology

7.2.1 Experimental setup and material

Laboratory experiments were conducted at the Hydraulic Laboratory of the University of Ottawa, Canada, in a 30m long, 0.7m deep, and 1.5m wide horizontal flume. A false concrete floor was constructed at the downstream end of the flume, and the height of the false floor was 0.2m. A circular pier with a diameter of 0.09m and a height of 0.6m in the centerline was placed 22.8m downstream of the water entrance (Figure 7-1).

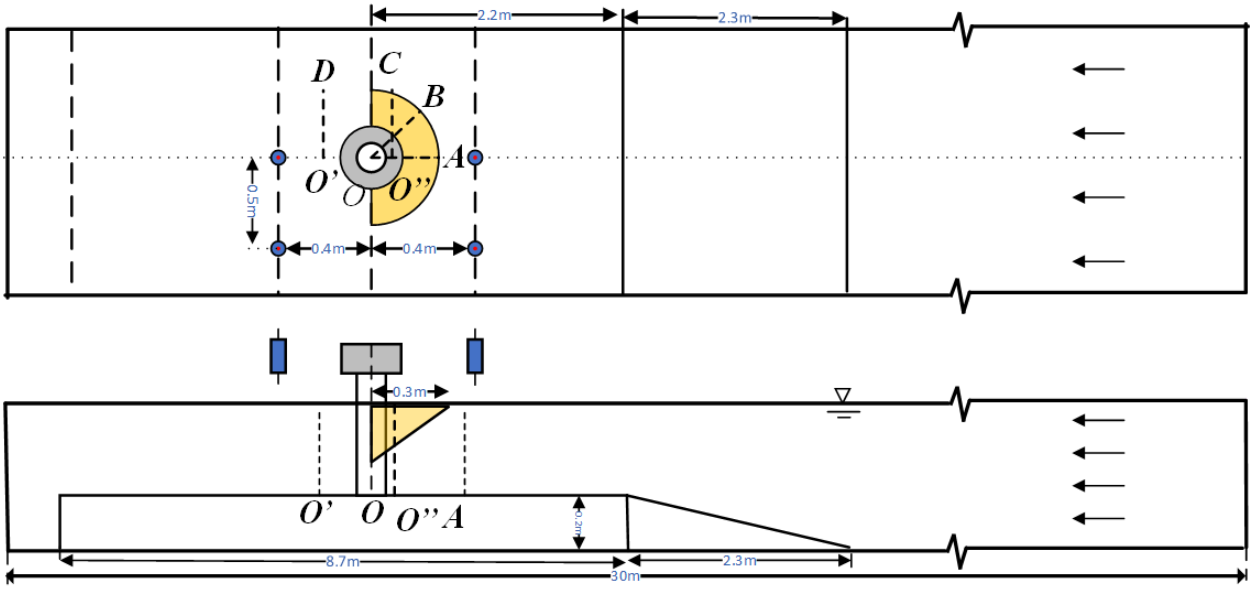

Figure 7-1 Experiment setup in plan view (top) and side view (bottom) (image not to scale).

Vectrino Acoustic Doppler Velocimeter (ADV) (https://www.nortekgroup.com/products/turbulent-flow) with a sampling rate of 100Hz was applied to measure point velocities with sampling periods between 75~90s, which was long enough to capture most of the largest eddies in the flow by means of spectral analysis. Considering the blockage of the debris jam, a cable-mounted ADV probe with a custom-designed 3-D mount was used for the measurements (Figure 7-2(a)), which enabled the capture of data in streamwise-vertical and cross-stream-vertical planes (sections) around the debris jam. The coordinate origin is defined in the center of the circular pier at the bottom of the flume (Figure 7-2(b)). Four sections around the pier were used to measure the flow field of each test case: OA, OB, O′′C, and O′D were represented in sections 1, 2, 3, and 4 (Figure 7-2). A filter developed by(Jamieson et al. 2010) as applied to remove the noise of ADV data. In each section, there were at least 5 vertical profiles, and the space between two points was 1-4cm, resulting in 79-119 points in one section. The mean velocity was obtained in the centerline at 1.0 m in front of the pier.

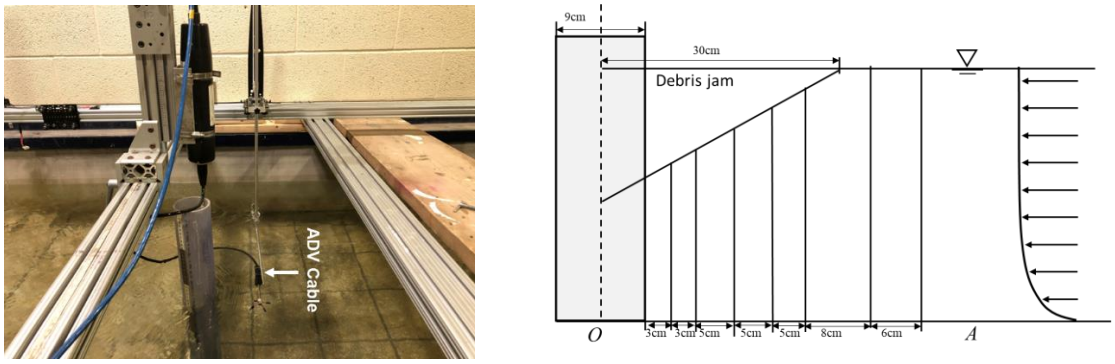

Figure 7-2 Flow field measurement set up for debris jam(a) ADV cable (b) Sketch of measurement distributions points

An Interface load cell was installed and connected to the bridge pier to measure the load due to debris jam. Interface's 6-axis (6A154B) (https://www.interfaceforce.com/) load cell can measure force simultaneously in three mutually perpendicular axes and three simultaneous torques about those same axes. Six full bridges provide mV/V output on six independent channels. The measurement was ±0.1%Fs, and the maximum nominal load in the x, y, and z-direction are 100N, 100N, and 200N, respectively.

In addition, four MassaSonic PulStar ultrasonic distance sensors (https://www.massa.com/industrial/ultrasonic-sensors/pulstar/) were applied to measure the water level around the debris jam. Two sensors were fixed 0.4m upstream of the pier and close to the centerline, while the other two were fixed 0.4 m behind the pier. The distance between the two sensors in the same longitudinal section was 0.5m (Figure 7-1).

Three debris jams were built to investigate the flow field around the pier. The debris jams were of equal geometric size and had the same half-cone shape geometry (Panici and de Almeida 2018). Two debris jams were built with dowels: one with 20cm long dowels and the other with 30cm long dowels. The third one was built using a 3D printer to generate an idealized half-cone debris jam. The height of the 3D-printed debris jam was 0.21m, and the diameter of the half-cone debris jam was 0.6m. As for the dowel's debris jam, a frame was made of dowels of the same size as the 3D-printed jam, and the dowels were put inside the frame. A total of 117 (264) dowels were used for the 30cm (20cm) dowel debris jam. The circular pier was placed in the center of the debris jam. A case without debris jams was also conducted as a blank test. The blank test is defined as "debris 00", and the 30 cm dowels jam is defined as "debris 01". Likewise, the 20cm debris jam is referred to as "debris jam 02", and the 3D printed debris jam is defined as "debris jam 03". The debris jams are presented in Figure 7-3.

Figure 7-3 (1)Debris jam built by 30 cm length dowels (2) Debris jam built by 20 cm length dowels (3) 3D printed debris jam

The flow condition stayed the same for all tests, and the depth average velocity was 0.376m/s with a depth of 0.36m. The Froude number in the flow condition was 0.24, and the Reynolds number was 91459 (Re(D) was 33840).

7.2.2 Data collection

A down-looker probe was set up to measure the velocity to avoid the effect of the flow, but this also caused a change in the measurement coordinate system as Figure 7-4 (a) was shown. A rotation matrix is required to transfer the measurement coordinate system to the standard coordinate system (Figure 7-4 (b)) to make it easy to understand which was also applied in (Carnacina et al. 2020).

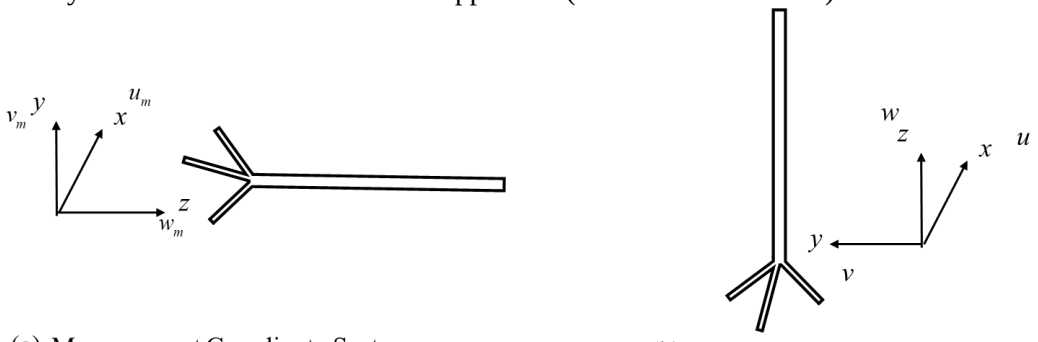

(a) Measurement Coordinate System (b) Standard Coordinate System

Figure 7-4 Measurement Coordinate system transfer to Standard Coordinate system

The matrix of counterclockwise rotation around the x-axis is used to finish the transformation.

$$R_x(\alpha) = \begin{bmatrix} 1 & 0 & 0 \\ 0 & \cos\alpha & -\sin\alpha \\ 0 & \sin\alpha & \cos\alpha \end{bmatrix} \tag{7-1}$$

where α is the degree angle in the counterclockwise direction around the x-axis.

Applying the rotation matrix to the measured velocity vector $\vec{u} \cdot R_x(90°)$, a velocity relation between the measurement coordinate and standard coordinate is obtained

$$u = u_m; v = -w_m; w = v_m \tag{7-2}$$

where $u, v,$ and w are the velocity components in the standard coordinate system; u_m, v_m, w_m are the velocity components in the measurement coordinate system.

The Reynolds stress indicates the turbulent exchange of fluid momentum, and it is related to the internal force of fluid and helps estimate its influence on the scouring. The three Reynolds shear stresses (RS) and the turbulence kinetic energy (k) were computed as

$$\tau_{uw} = -\rho\overline{u'w'}; \qquad \tau_{uv} = -\rho\overline{u'v'}; \qquad \tau_{vw} = -\rho\overline{v'w'} \tag{7-3}$$

$$k = 0.5\left[\overline{(u')^2} + \overline{(v'^2)} + \overline{(w')^2}\right] \tag{7-4}$$

where u', v', w' are the fluctuating velocity in the $x, y,$ and z directions respectively and the overbar indicates the mean. The relation of Reynold shear stress between the measurement coordinates and the standard coordinate is also updated accordingly. For each of the Reynolds shear stress, the directions and planes of action, as well as the associated velocity gradients, are summarized in Table 7-1 (Jamieson et al. 2013).

Table 7-1 Reynolds Stress Notation

Measurement	Stress component	Plane	Direction	Velocity gradient
$-\overline{\rho u' w'}$	τ_{uw}	yz	z	δ_w/δ_x
	τ_{wu}	yx	x	δ_u/δ_z
$-\overline{\rho u' v'}$	τ_{uv}	yz	y	δ_v/δ_x
	τ_{vu}	zx	x	δ_u/δ_y
$-\overline{\rho v' w'}$	τ_{vw}	zx	z	δ_w/δ_y
	τ_{wv}	yx	y	δ_v/δ_z

To have a comprehensive understanding of the turbulence structure, the turbulence integral time T_E and length scale L_E were also used to quantify the oscillations associated with large-scale eddies in the flow:

$$T_E = \int_0^{\mathcal{T}_m} \frac{\overline{u'(t)\cdot u'(t+\mathcal{T})}}{\overline{u'^2}} d\mathcal{T} \quad (7\text{-}5)$$

where $\mathcal{T}$ is the time lag of the velocity fluctuation between two measurement points; $\bar{u}$ is the mean local velocity.

7.3 Results and Analysis

7.3.1 Velocity magnitude and Reynold shear stress

The velocity magnitudes and vectors observed in the four measurement planes for each debris jam case are presented in Figure 7-5. In the case without debris jam, it was observed that the streamwise $\bar{u}$ component diminished in section 1 in front of the pier, and the vertical distribution of streamwise velocity tended towards uniformity as flow approached the pier. The $\bar{w}$ component was always downwards and increased considerably toward the bed, especially for the profile close to the pier. The $\bar{v}$ component was smaller than the other components and showed no pronounced trend which was consistent with the case observed in (Graf and Yulistiyanto 1998). In section 2, the $\bar{u}$ component increased slightly, and the velocity distribution became more uniform towards the bed. The $\bar{w}$ component continued going downward, while the magnitude of the $\bar{v}$ component increased considerably and was uniformly distributed in the outward direction. In section 3, flow acceleration around the pier was evident with flow directed outward, as well as down the flow immediately adjacent to the pier. In section 4, the region of flow acceleration continued beside the pier, as well as a low-velocity wake flow immediately behind the pier with upstream and inward-directed velocity vectors. In the presence of debris jam (20cm dowels jam, 30 cm dowels jam, and 3D printed jam), the $\bar{u}$ component in section 1 showed an inverted velocity profile with maximum velocity displaced downward within the flow due to the presence of the debris jam. The $\bar{w}$ component showed a downward flow, particularly in the upper part of the profile near the debris jam. The $\bar{v}$ component still had no apparent trend. In section 2, the flow began to accelerate with continuing downward flow below the jam. In section 3, the velocity below the jam beside the pier was further accelerated due to the flow constriction below the jam, resulting in a velocity magnitude greater than in the case without the jam. Finally, a large wake region of low velocity defined herein as a 'dead wake zone' occurred behind the debris jam in section 4. The geometry of the dead wake zone approximately matched the shape of the debris jam, although the dead wake zone was larger for the jams made of dowels than the 3D-printed jam. Below and adjacent to the dead wake zone there was a region of high-speed flow, with a sharp transition zone between the dead wake zone and accelerated high-speed zone.

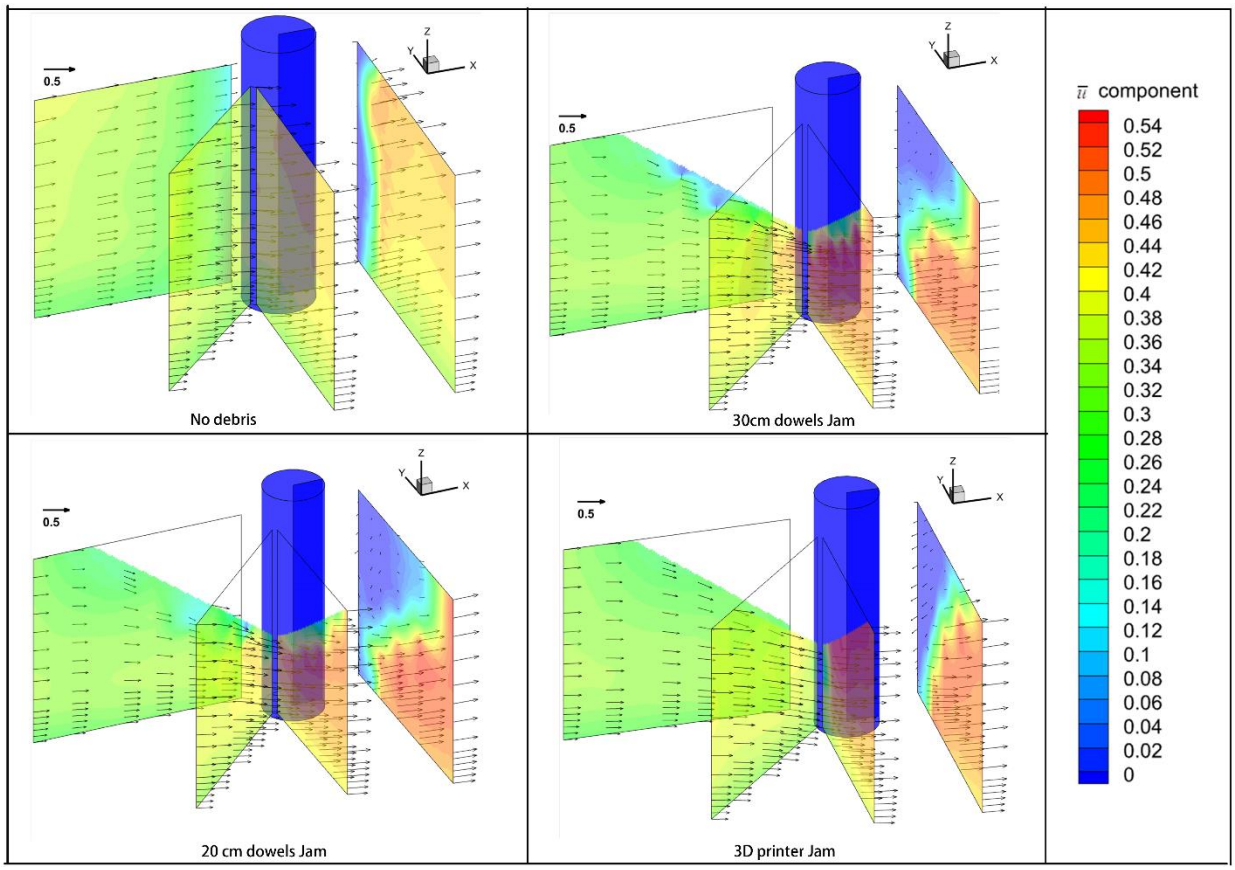

Figure 7-5 Mean U component velocity magnitude contours and vectors (m s^{-1})

The results of Reynolds shear stress τ_{uv} are presented in Figure 7-6. According to the definition of τ_{uv}, this stress comes from the cross-stream gradient of streamwise velocity and/or the streamwise gradient of cross-stream velocity (Table 7-1). It was also noticed that the negative or positive value co-existed in section 2 and section 3. This was probably caused by the roughness of the dowel jam due to the protrusion of dowel pieces; these protrusions affected the gradient of velocity in the lateral direction. Accordingly, the largest values of τ_{uv} were observed in section 4 in the transition zone between the wake or dead zone and the accelerated flow region. The peak value of τ_{uv} covered the projected pier area in section 4. High values of τ_{uv} also occurred along the edges of the debris jams, particularly for the jams comprised of dowels.

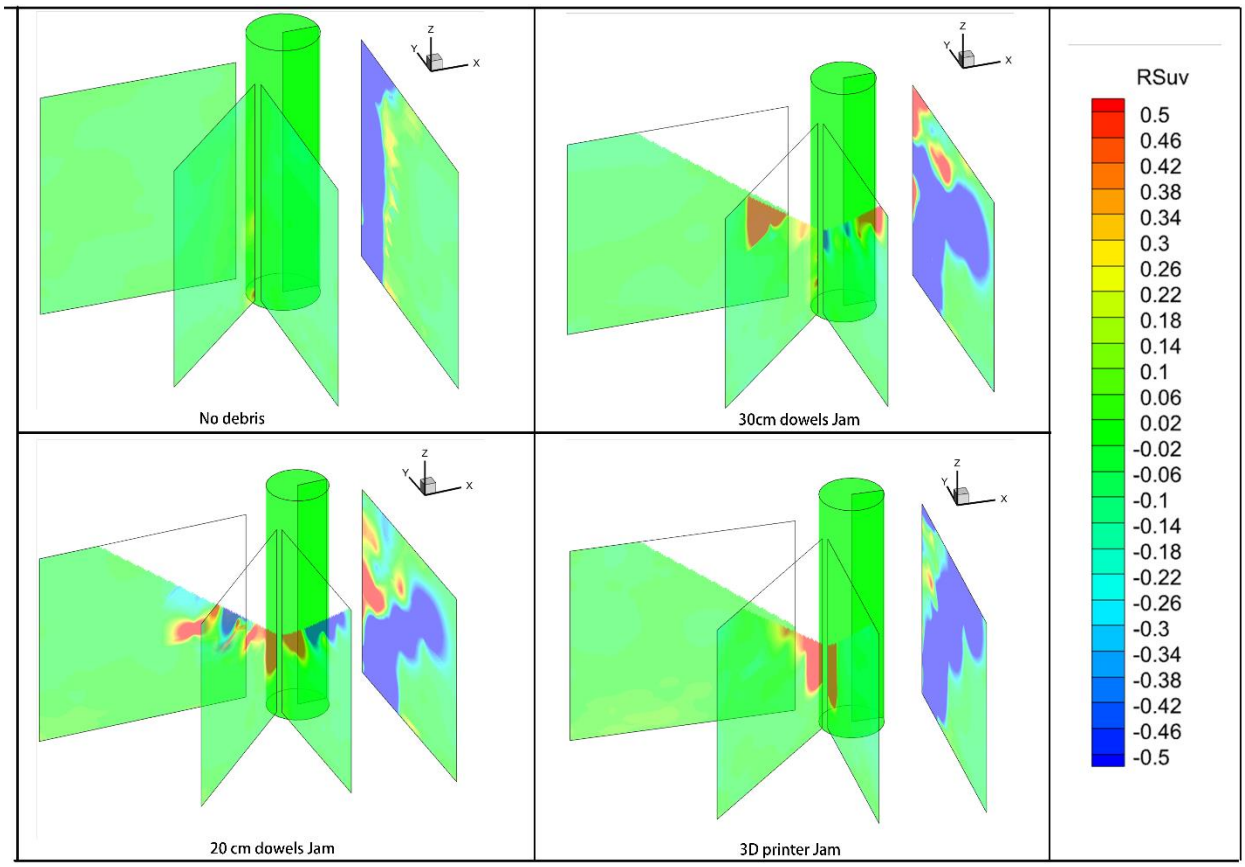

Figure 7-6 Contours of the τ_{uv} Reynolds stress (N m^{-2})

The principal Reynold shear stress τ_{uw} is presented in Figure 7-7. The vertical gradient of streamwise velocity plays a key role in τ_{uw} (Table 7-1). The magnitude of τ_{uw} was greatest near the fixed bed for all cases, but the magnitude and extent above the bed of elevated τ_{uw} diminished in all debris jam cases due to the constriction of debris jams. Sections 2 and 3 in cases of 20cm and 30cm dowels jams had negative τ_{uw} near the jam, which is consistent with development of a boundary layer below the jam. This did not occur in the 3D-printed jam case due to the smooth surface. In Section 4, both positive and negative values of τ_{uw} coexisted in the wake dead zone region behind the dowel debris jams, but positive values were observed only in the transition zone for the 3D-printed jam.

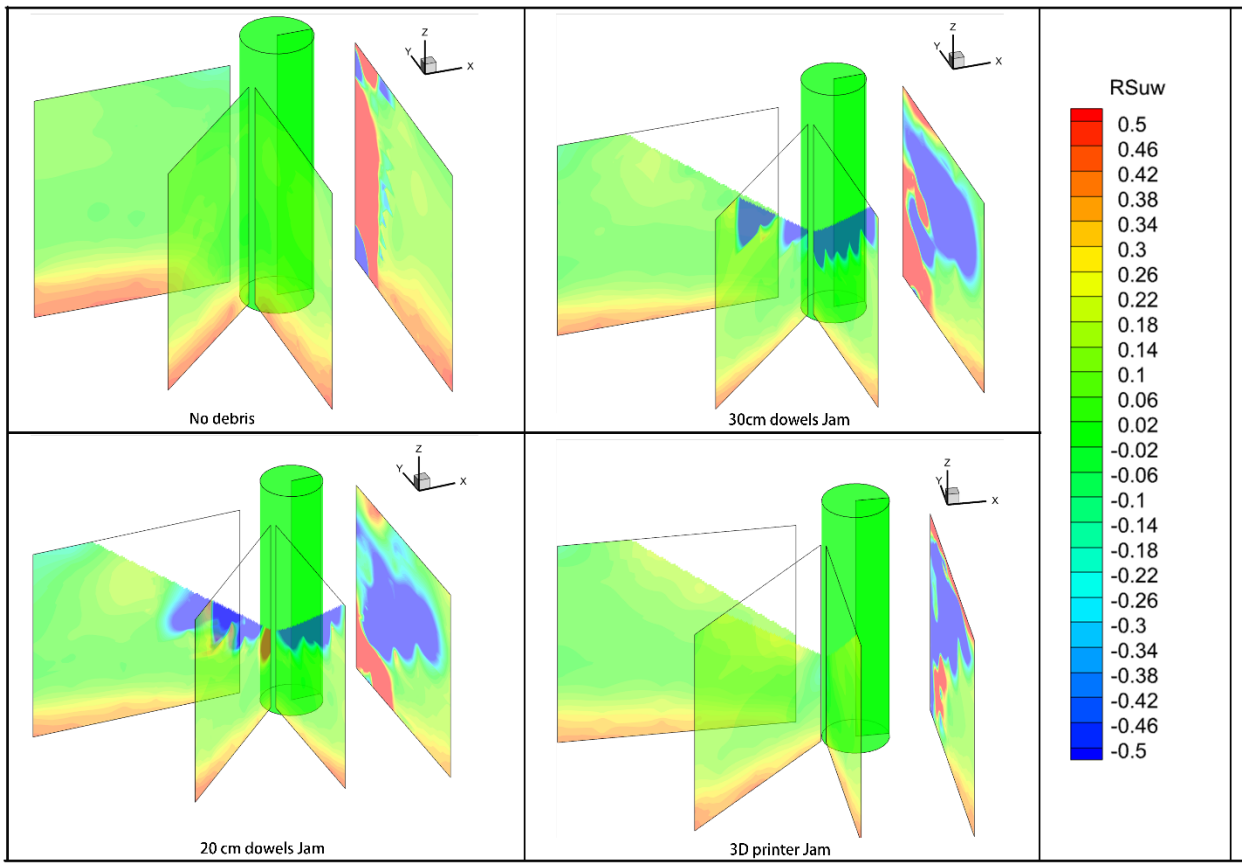

Figure 7-7 Contours of the τ_{uw} Reynolds stress (N m^{-2})

The results of Reynold shear stress τ_{vw} are presented in Figure 7-8. The δ_w/δ_y and δ_v/δ_z terms are both involved in the calculation of τ_{vw} shear stress. As Table 7-1 indicated, the positive value of τ_{vw} attributed to the greater velocity gradient of $\overline{w}$ the component along the y-axis and the $\overline{v}$ component along the z-axis. For the pier-only case, the Reynold shear stress τ_{vw} was quite uniform with a low value in sections 1-3. However, τ_{vw} was greater near to surface of dowel jam cases, and this is probably due to the protrusion of debris pieces. Large positive and negative values of τ_{vw} occurred in the wake dead zone region of section 4 for all cases. Large primarily negative values of τ_{vw} also occurred immediately adjacent to the debris jams comprised of dowels. The coexistence of positive and negative values also indicated the generation of vortices.

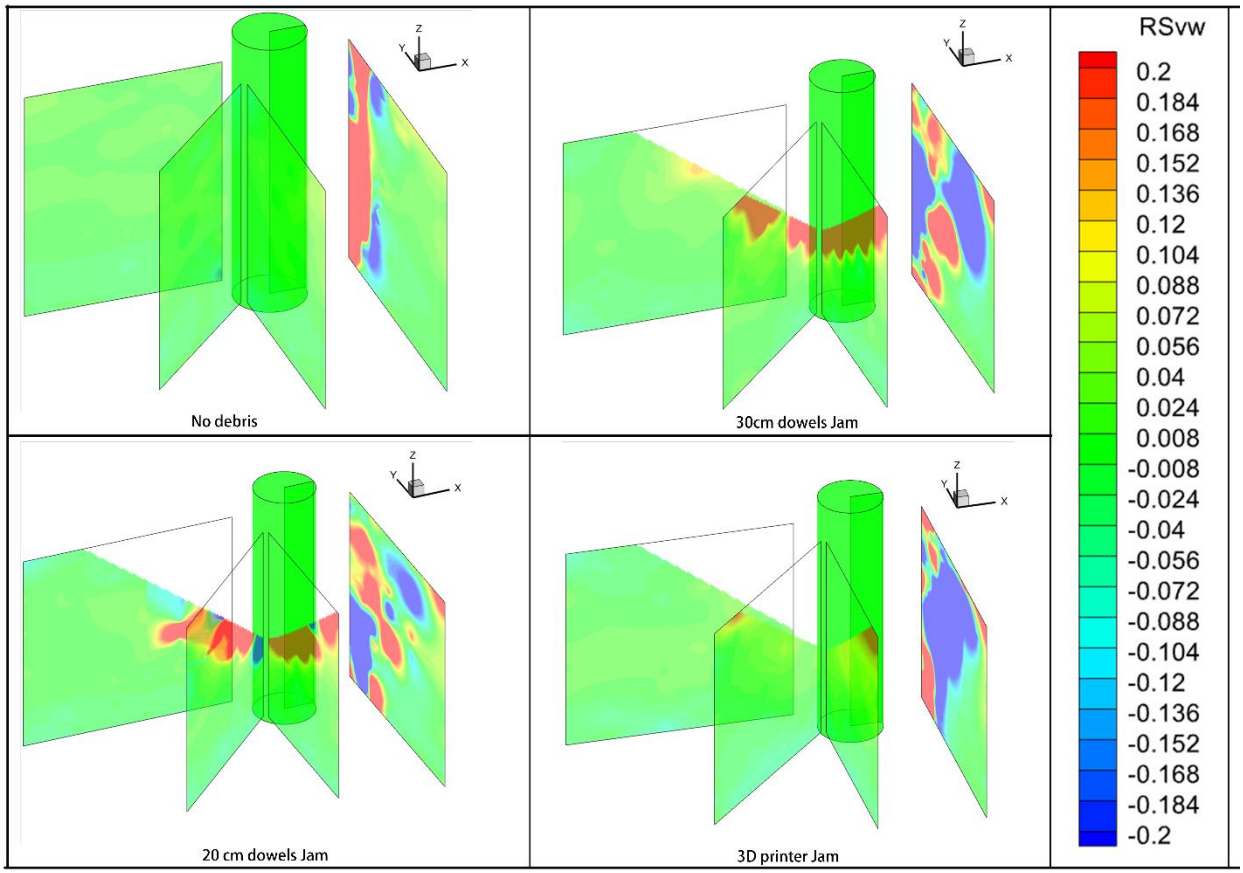

Figure 7-8 Contours of the τ_{vw} Reynolds stress (N m^{-2})

The distributions of turbulence kinetic energy measured for all cases are shown in Figure 7-9. For all cases, the highest turbulence energy was mainly observed in section 4. The magnitude of turbulence kinetic energy in the wake behind the pier without debris jam was greater than in the cases with debris jam. For the debris jam cases, the maximum turbulence kinetic energy occurred in the transition zone between the wake dead zone and the accelerated flow region. The momentum exchange in the transition zone is intensive due to shear induced by the high local velocity gradient resulting in greater turbulence kinetic energy.

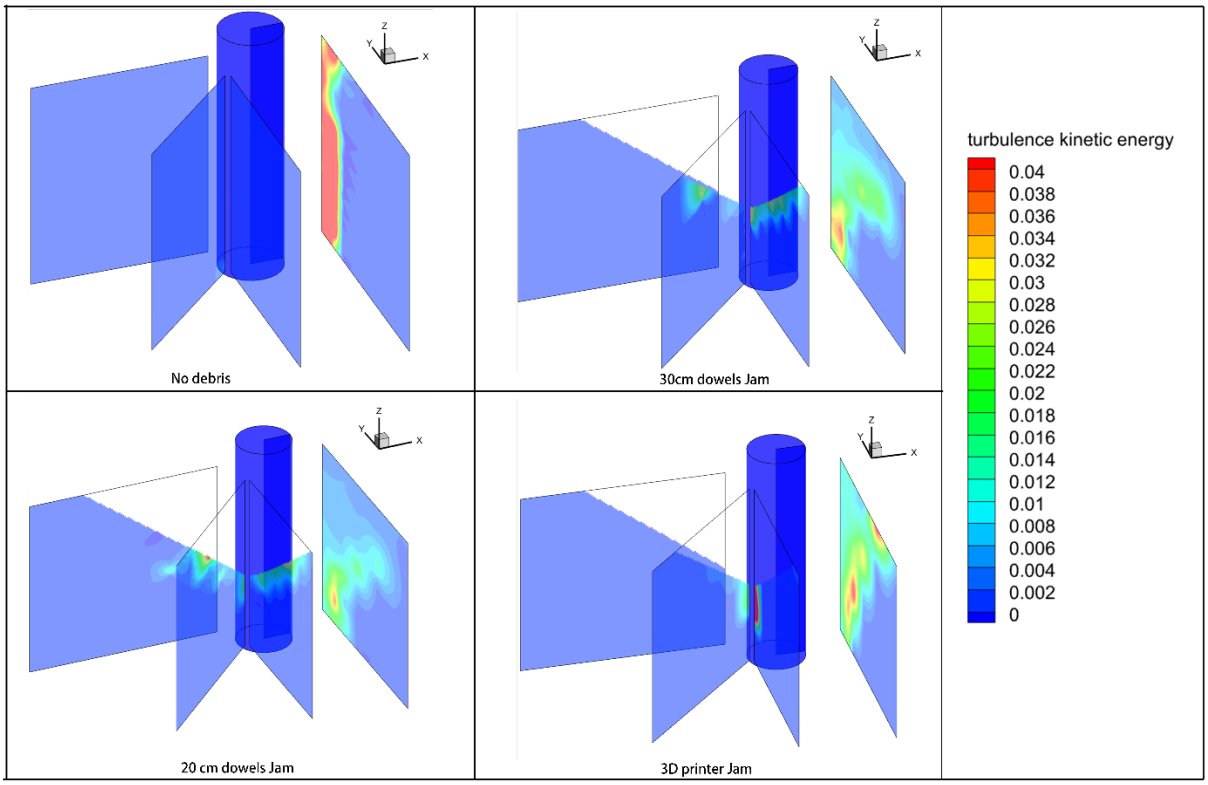

Figure 7-9 Contours of turbulence kinetic energy ($m^2\ s^{-2}$)

7.3.2 Integral time scale

The duration of velocity oscillations due to large turbulent structures can be represented by the integral time scale, and its distribution is shown in Figure 7-10 for all cases. The integral time scale tended to be greater in the region of flow acceleration for the case without debris jam, and lowest in the wake dead zone behind the pier. In contrast, for the cases with debris jams and particularly for the jams comprised of dowels, the magnitude of the integral time scale was greatest in the wake dead zone and lowest in the transition zone. This suggests that the dowel jams with greater permeability and roughness cause a greater temporal oscillation period behind the jam. Indeed, the integral time scale was sufficiently large in the dowel jam wake dead zone that a longer sampling period may have been required to capture it. This was likely due to minimal advection of eddies in the wake.

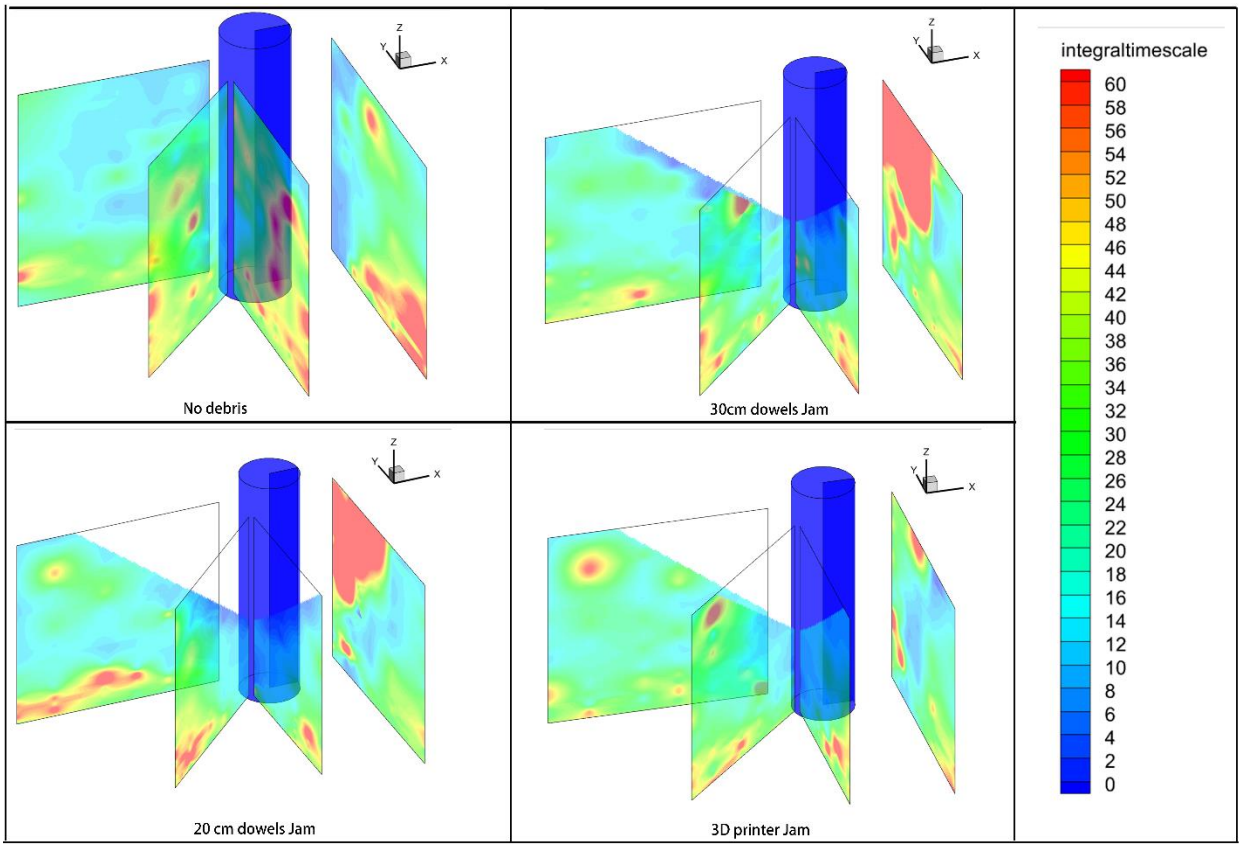

Figure 7-10 Contours of integral time scale (s)

7.3.3 Vorticity

The vorticity is also computed from the mean flow field data, and was calculated by

$$\begin{cases} \omega_x = \frac{1}{2}\left(\frac{\partial \bar{w}}{\partial y} - \frac{\partial v}{\partial z}\right) \\ \omega_z = \frac{1}{2}\left(\frac{\partial \bar{v}}{\partial x} - \frac{\partial \bar{u}}{\partial y}\right) \\ \omega_y = \frac{1}{2}\left(\frac{\partial \bar{u}}{\partial z} - \frac{\partial w}{\partial x}\right) \end{cases} \quad (7\text{-}6)$$

The magnitude of total vorticity and the vorticity around the Y-axis (ω_y) are shown in Figure 7-11 and Figure 7-12, respectively. Note that ω_y is generated in regions with a strong vertical gradient of streamwise velocity and/or streamwise gradients of vertical velocity. In all cases, section 4 had the greatest total vorticity, which is indicative of the flow circulation behind the pier and/or debris jam, particularly in the high shear transition zone. The dowel jams in sections 1, 2, and 3 also had high vorticity directly adjacent to the jam, presumably due to simultaneous downward flow deflection and the development of a boundary layer. This was not observed with the 3D-printed jam. Strong ω_y was also observed close to the bed for all cases in sections 1, 2, and 3, likely due to the bottom boundary layer. The thickness of this zone was slightly diminished when the debris jams were present. Although relatively mild in the present observations, elevated vorticity at the base of the pier is consistent with the horseshoe vortex system which was observed by (Graf and Yulistiyanto 1998).

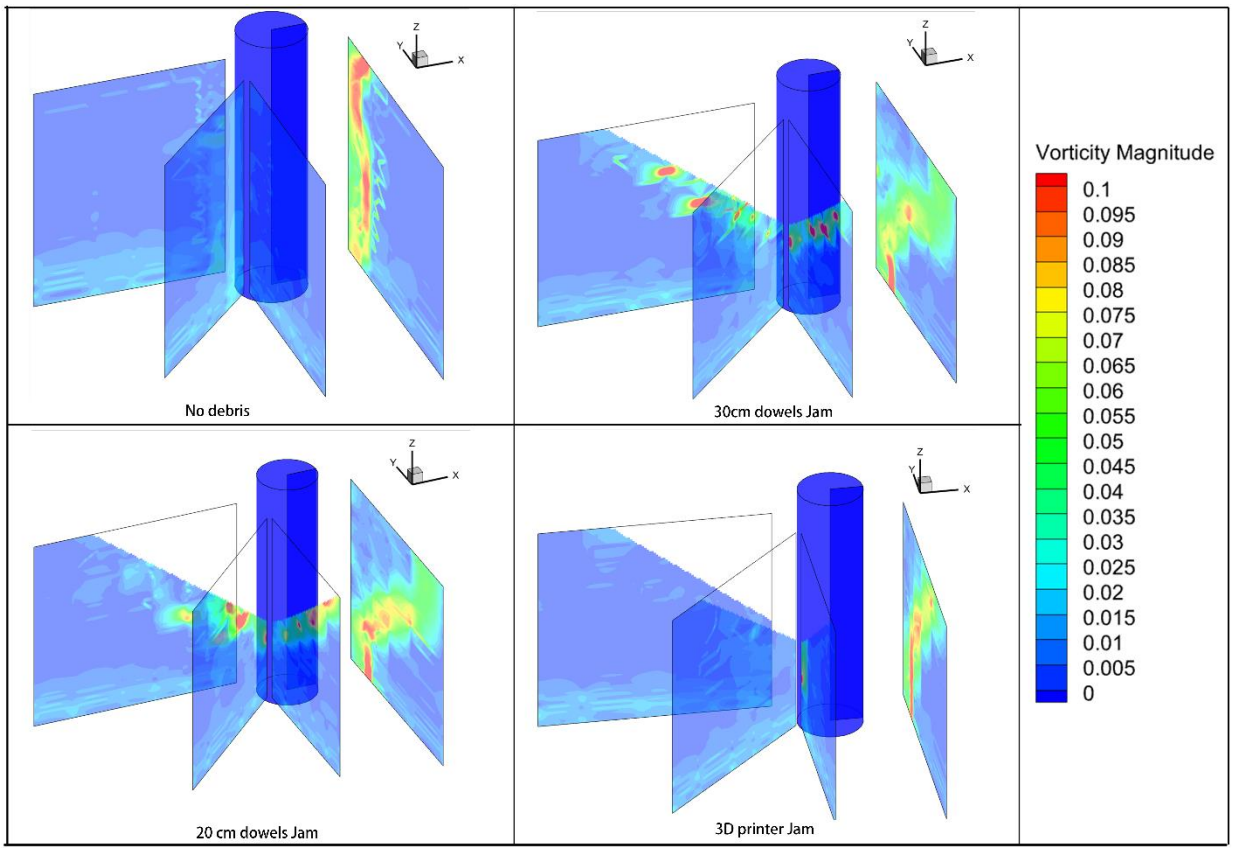

Figure 7-11 Vorticity magnitude contour (s^{-1})

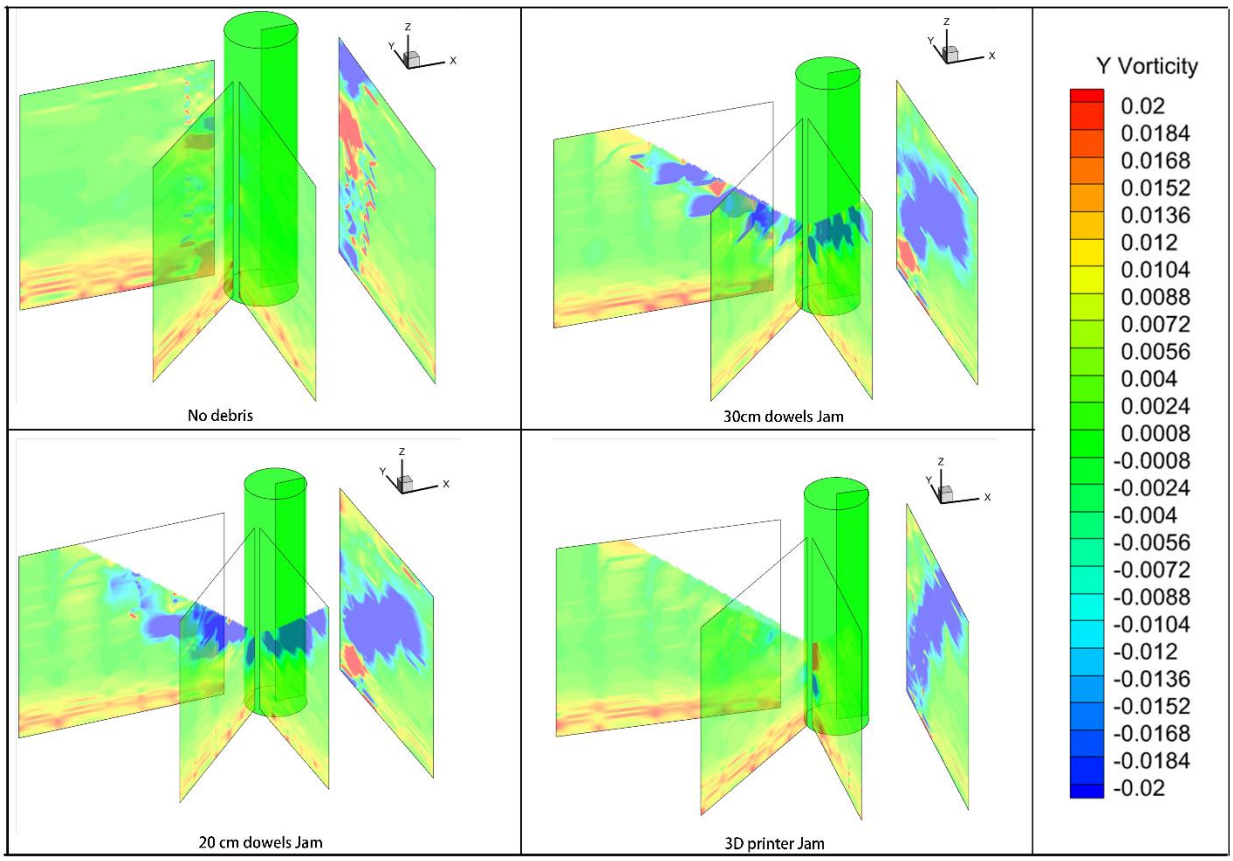

Figure 7-12 Contours of Y vorticity (s^{-1})

7.3.4 Drag coefficient and induced hydraulic head

The load caused by these debris jams is also an important concern to distinguish the difference between idealized debris jams and realistic debris jams. The drag force C_d is computed by the following equation:

$$C_d = \frac{F_d}{0.5\rho A_d U^2} \tag{7-7}$$

where ρ= the flow density; A_d = the projected vertical cross-section area of the debris jam in the direction of the flow subtracting the pier area; U = the approach flow velocity; F_d = the drag force subtracting the pier load.

The x-direction drag force was recorded using a load cell Interface's 6-axis (6A154B) (https://www.interfaceforce.com/) installed at the top of the pier and attached to a fixed beam fixed transversally across the top of the flume. , and the value of the drag coefficient is shown in Table 7-2. The three debris jams have the same projected area in the flow direction, and the calculated drag coefficients of the 20cm debris jam, 30cm debris jam, and 3D printed jam were 1.67, 1.70, and 0.88 respectively. The 3D-printed jam has a lower drag coefficient than the dowel jams. This difference is due to the difference in surface roughness of the debris jam. The 3D-printed jam had an idealized shape with a smooth surface compared with the dowel jams, which were formed by accumulated dowels and thus had higher roughness. Note that the 20 cm dowels jam and 30 cm dowels jam were built with dowels of the same diameter, and thus had similar roughness.

In addition, the hydraulic head (Δh) induced by each jam was non-dimensionalized by dividing it by the water depth (h) (Table 7-2). The $\Delta h/h$ caused by the presence of the 20 cm and 30 cm dowel jams were similar: 0.032 and 0.029, respectively. On the other hand, $\Delta h/h$ due to the presence of the 3D-printed jam

being smaller than the two, with a value of 0.02. This further demonstrates that the characteristics of dowel jams differed from those of the 3D-printed debris jam.

Table 7-2 Drag coefficient and induced hydraulic head of debris jam.

Debris type	Debris_00	Debris_01	Debris_02	Debris_03
C_d	1.14	1.70	1.67	0.88
$\Delta h/h$	0.0079	0.029	0.032	0.02

7.4 Discussion

A variety of debris jam geometries have been studied previously. Melville and Dongol (1992) applied a cylindrical debris jam around a circle pier, and the debris jam was idealized as a smooth, impermeable, regular shape in order to investigate the maximum scour depth caused by the debris jam. Pagliara (2010) used six types of debris jam with different porosity in the form of a rectangular shape to investigate its influence on scour depth but found a negligible influence of porosity on scour depth. Lagasse et al. (2010) and Ebrahimi et al. (2018) applied both rectangular and triangular shapes of debris jam to investigate sour depth. However, Lagasse et al. (2010) also pointed out the occurrence of the conical shape of debris jams in field observation. In addition, Panici and de Almeida (2018) applied a dynamic debris jam by continuously releasing debris pieces, and the shape of the debris jam was monitored and described as a half-cone shape. Furthermore, the failure condition of the debris jam was theoretically investigated for the half-cone debris jam (Panici and de Almeida 2020). Thus, the half-cone shape was assumed to be a reasonable choice to represent the geometry of a debris jam as it is commonly seen in the formation of debris jams. In addition, a debris jam built with a certain degree of porosity better represents actual debris jams.

The debris jam built from dowels was covered by their protrusions at the jam surface, which significantly affected the flow around the debris jam. The Reynold shear stress in section 1 (Figure 7-6) co-existed in the form of negative and positive values in the 20cm dowels jam, and this was attributed to the protrusion of the dowels out of the frame. These protrusions (the heads or tails on the surface of the dowels pieces) disturbed the flow structure and caused gradient changes in the velocity component, which was also reported in the study (Okamoto et al. 2021). In addition, these protrusions on the jam surface also led to the generation of vorticity as the sketch Figure 7-13 is shown. Figure 7-11 proved that vorticity occurred around the dowels jam surface while the vorticity was not observed in the 3D-printed jam surface. Bed shear stress caused the positive Y-axis vorticity ω_y, and the dowels jam surface generated the negative Y-axis vorticity. This suggested that the uneven surface of the woody debris jam could generate more vorticity around the pier. In turn, these vortices probably contributed to the stronger scour at the base of the bridge pier.

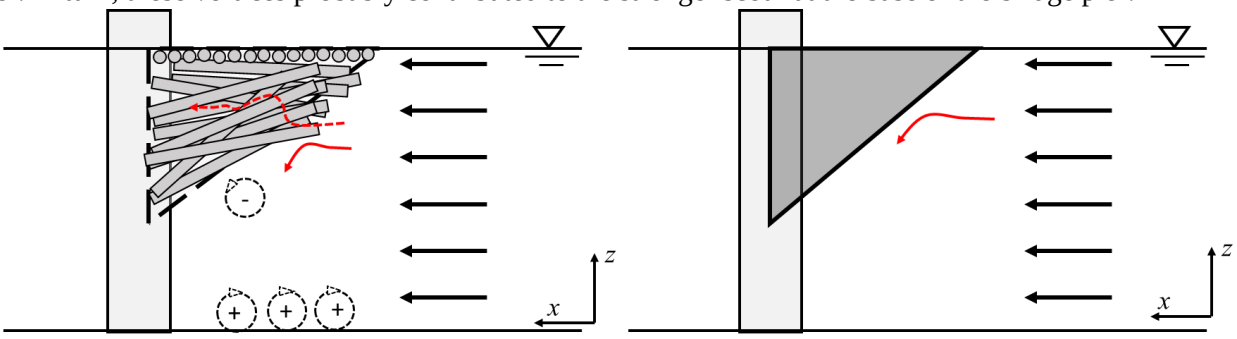

Figure 7-13 Sketch of the flow pattern for (a) dowels jam and (b) 3D-printed jam

The drag coefficient of a debris jam varies with the debris type. In previous studies, dowel jams were built using a quasi-random arrangement of debris pieces and thus were porous to some extent. Some water

would have flowed along irregular pathways through the dowel jams, although most of the water flowed below or around the jam. In contrast, all of the water flow went below or around the 3D-printed debris jam. A sketch of the flow structure around each debris jam is presented in Figure 7-13. Mauti et al. (2020) found that porosity did not strongly influence the drag coefficient of a debris jam. Parola et al. (2000) also investigated the drag coefficient of debris jams, finding that the drag coefficient is related to the blockage ratio of the debris jam. Panici and de Almeida (2018) also indicated that the drag coefficient of a debris jam was constant no matter the flow conditions. In the present study, the blockage ratio of all three debris jams was the same, and the drag coefficients of the dowel jams were similar but were greater than that of the 3D-printed jam. This must have been due to the increased roughness of the dowel jams, since any porosity would have reduced the drag coefficient.

The wake zone in section 4 for the dowels jam was quite different for the 3D-printed jam as the flow field indicated, and the sketch of the wake behind the debris jam is presented in Figure 7-14. Compared to the flow field without a debris jam, the flow field in the presence of debris jams has a greater magnitude gradient as the bridge opening area was reduced by the debris jam. The dead wake zone caused by the 3D-printed jam is approximated to be a triangular shape reaching the fixed bed which indicated that the wake started from the bed as the 3D-printed debris jam could cause a stronger downward flow. However, a deflection occurred at the bottom of the dowel jam which made the shape of the dead wake zone irregular, and this deflection might attribute to flow passing the dowel jam due to roughness. In addition, the wake area on the dowel jam is also observed to be greater than that on the 3d-printed jam due to protrusions on the dowel jam.

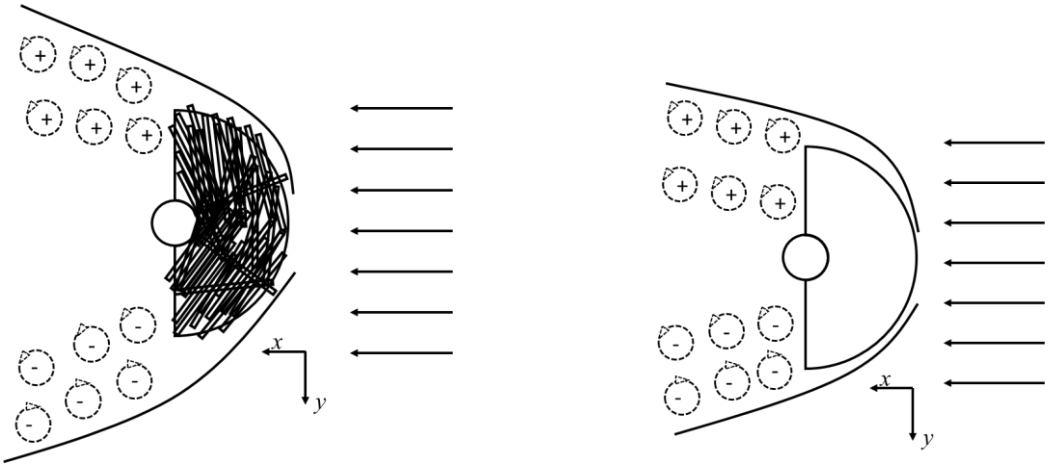

Figure 7-14 Sketch of the wake behind the debris jam (a) dowels jam (b) 3D-printed jam, noting that the position of separation, not the actual occurrence placed in the sketch

7.5 Conclusions

The change of the flow field around a pier due to a debris jam provides insight into debris jam mechanics and drag. Two 20cm and 30cm long dowel jams were built in the same size wood frame shaped in a half-cone, and a 3D printed debris jam was also made with the same geometry. A cable ADV was installed to measure the flow field across four sections around the three debris jams as well as a no-debris jam case. The load and hydraulic head caused by the debris jams were also measured. The conclusions of this study are:

(1) The flow field around the pier was significantly affected due to constriction caused by the debris jam. The approaching flow deflected by the debris jam increased the downward flow

compared to the pier-only case. The water flows partly propagated through the dowel jam and partly around it while the flow deflected smoothly around the 3D-printed jam. A greater wake was generated behind the dowels jam compared to that generated by the 3D-printed jam, and the wake provided a distribution of Reynold turbulence shear.

(2) The head or tail of the dowels forms protrusions on the surface of the dowels jam, and these protrusions increase the roughness of the dowels jam. The higher roughness of the dowels jam led to a greater drag coefficient and hydraulic head, and this indicated that the smooth jam structure might be not appropriate to represent the debris jam. In addition, the protrusions cause the extension of the surface of the debris jam leading to the strong change of Reynold shear stress and the generation of vorticity along the surface of the dowels jam.

(3) Porosity was considered another characteristic of dowel jam which was considered in this study, as it allowed the water flow to go through the debris jam for the dowel debris jams. This caused a longer integral time scale of velocity oscillations in turbulent structures. However, the porosity did not seem to significantly influence the magnitude of the calculated drag coefficient.

Chapter 8. A comparison of experimental results with the design codes

8.1 Debris jam Shape

According to HEC-18, debris jams are categorized into rectangular and triangular shapes, and rectangular debris shape indicates a greater blockage ratio resulting in greater scour at the base of the bridge pier. In addition, the design code points out that the largest scour occurs when the length of the debris jam reaches the water depth. The approaching flow mainly goes beneath the debris jam instead of going over the top of the debris jam.

Based on the present study, the shape of the debris jam is, generally most of the time, neither rectangular nor triangular shape. In addition, Lagasse et al. (2010) observed that the debris jam formed at mid-depth, which may be caused by an increase in debris density due to long-time submerging. Dynamic debris jam was applied in the present study, so it was formed based on local flow conditions and the characteristics of the debris pieces. A general half-cone shape is observed in the experiments, which is also observed in studies by (Panici and de Almeida 2018; Panici and de Almeida 2020).

Last but not least, the shape of a half-cone debris jam might also need to be included in the design code for the bridge pier.

8.2 Influence of Debris Jam on Scour

The HEC-18 equation for the pier scour depth is

$$\frac{d_{s0}}{h} = 2.0K_1K_2K_3\left(\frac{D_p}{h}\right)^{0.65} F_r^{0.43} \tag{8-1}$$

where K_1=correction factor for pier nose shape; K_2=correction factor for the angle of attack of flow; K_3=correction factor for bed condition; $F_r = U/(gh)^{0.5}$

The effective pier diameter is proposed in the design code, which is

$$D_p^* = \frac{K_4\left(h_d w_d\right) + D_p\left(h - K_4 h_d\right)}{h} \tag{8-2}$$

where K_4=0.79 for rectangular debris shape and 0.21 for triangular debris shape.

Then, the full equation for the estimation of scour depth in the presence of a debris jam is

$$\frac{d_s}{h} = 2.0K_1K_2K_3h^{-0.65}F_r^{0.43}\left(D_p^*\right)^{0.65} \tag{8-3}$$

$$\frac{d_s}{h} = 2.0K_1K_2K_3h^{-0.65}F_r^{0.43}\left(\frac{K_4\left(h_d w_d\right) + D_p\left(h - K_4 h_d\right)}{h}\right)^{0.65} \tag{8-4}$$

Thus, the influence of debris jam on scour depth ratio is

$$K_d = \frac{d_s}{d_{s0}} = \left(\frac{D_p^*}{D_p} \right)^{0.65} \tag{8-5}$$

$$K_d = \frac{d_s}{d_{s0}} = \left[\frac{K_4 \left(h_d w_d \right) + D_p \left(h - K_4 h_d \right)}{h D_p} \right]^{0.65} \tag{8-6}$$

K_4 = 0.21 for triangular debris jam, K_4 = 0.79 for rectangular.

According to the present study

$$R_d = \frac{0.5 h_d w_d - h_d P_d}{bh} \times 100\% \tag{8-7}$$

Then, the equation can be replaced by

$$h_d w_d = 2 \left(\frac{R_d bh}{100} + h_d D_p \right) \tag{8-8}$$

Finally, the relation between the blockage ratio and K_d for the triangular debris jam is:

$$K_d = \frac{d_s}{d_{s0}} = \left(\frac{0.42 \left(\frac{R_d bh}{100} \right) + 0.21 h_d D_p + h D_p}{h D_p} \right)^{0.65} \tag{8-9}$$

Likewise, the equation for rectangular debris is

$$R_d = \frac{h_d w_d - h_d D_p}{bh} \times 100\% \tag{8-10}$$

$$K_d = \frac{d_s}{d_{s0}} = \left(\frac{0.79 \frac{R_d bh}{100} + h D_p}{h D_p} \right)^{0.65} \tag{8-11}$$

Based on the (8-9) and (8-11), the HEC-18 equations are also presented to show the relation of debris jam blockage ratio and the influence on scour depth as Figure 8-1 is shown. The HEC-18 equation is derived from the data of the study (Melville and Dongol 1992). Generally, the equations are close to the study (Pagliara and Carnacina 2011) as the shapes of debris jam are consistent with the design code. However, the HEC-18 proposed the prediction equations for debris jam for rectangular and triangular shapes, respectively while Pagliara and Carnacina (2011) applied one equation for both rectangular and triangular debris shapes and proposed an additional equation for cylindrical debris shape. This might be due to different variables (blockage ratio (Pagliara and Carnacina 2011) and effective pier diameter (HEC-18)) applied to quantify the size of the debris jam. In addition, the seedling trees and the dowel debris jam shows a less scour depth compared with the static debris jam and dowels jam, probably it is caused by the shape of the debris jam and slowly development rate of size. The HEC-18 is conservative with respect to the current data. It might also need to point out that tree jams have a more stable structure and not yet reached

an equilibrium size in the present study due to time limitation, so the influence of debris jam formed by trees in field might be underestimated by present study.

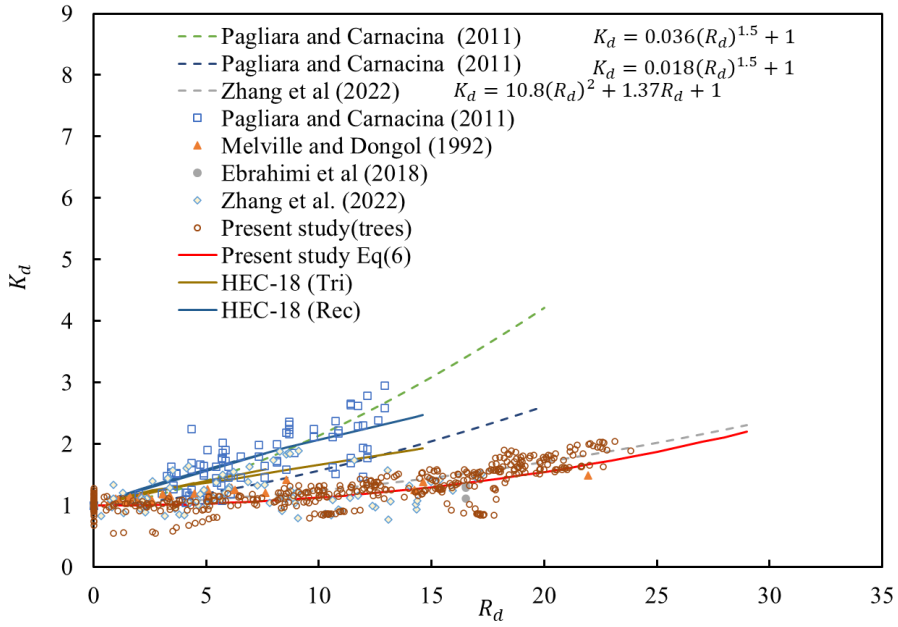

Figure 8-1 The relation of blockage ratio and the influence on scour depth (the data from (Melville and Dongol 1992)blockage percentage less than 20%)

In the HEC-18 (triangular debris shape), the effective pier diameter is used to quantify the influence of debris jam on scour depth, as shown in Figure 8-2. For the seeding trees jam, the effective pier diameter was generally consistent with the HEC-18 prediction, which has a greater value to protect the pier from scour. On the other hand, the debris jam formed by dowels has greater dispersion, but it was generally close to the prediction for the first dowel jam. However, the HEC-18 has very high dispersion and predicts less scour if the dowels jam included the subsequent debris jams.

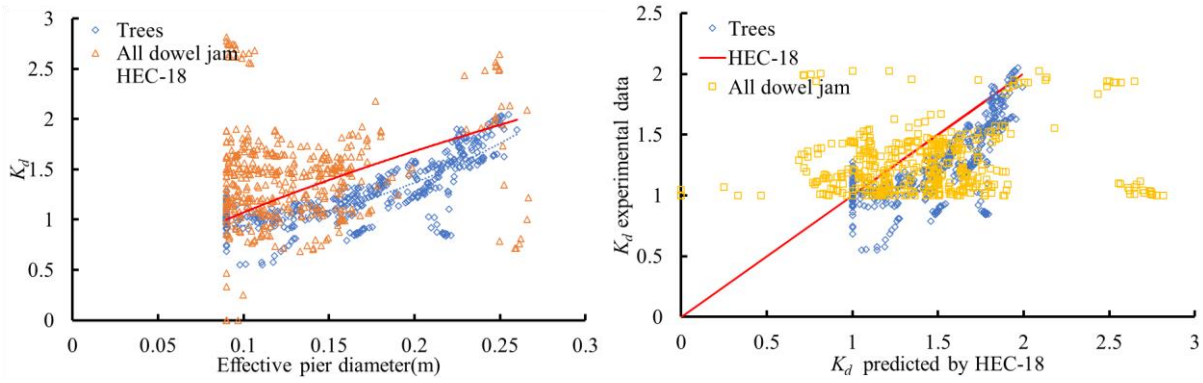

(a) Relation of effective pier diameter (all dowels jam data) with K_d (b) the predicted HEC-18 and experiments data

Figure 8-2 Quantify the influence of debris jam by effective pier diameter.

8.3 Influence of debris Jam on loading

HEC-09 provides the equation to estimate the dragging force and drag coefficient, and the equation is as follows:

$$F_d = C_d \rho g A_{vc} \frac{U_r^2}{2g} \tag{8-12}$$

where U_r =reference velocity depending on the blockage ratio; A_{vc} =wet projected area of debris jam in the pier upstream.

In the design code, the drag coefficient is affected by the blockage ratio and Froude number as Table *2-3* was shown. It suggests that the drag coefficient is 1.8 for the bridge pier when the blockage ratio is less than 0.36 and the Froude number is less than 0.4, which generally covers the present experimental conditions.

However, based on the present study, the drag coefficient for a dowels jam was 1.79, close to the suggested value, but this is not applicable for the debris jam formed by trees, which has a value of 2.64, much greater than the suggested value. Hereby, the drag coefficient suggestions might not be safe enough to resist different types of debris jams in the field.

Furthermore, the spiking phenomenon of dynamic debris jams observed in the present study requires attention for the protection of the bridge pier. The shape of the debris jam in the field also evolves in front of the pier if it continuously increases. Although this phenomenon has not yet been reported in field investigations, it still implies that a higher design standard for resisting debris loading should be taken into consideration.

Chapter 9. Conclusions and Recommendations for Future Work

9.1 Conclusions

Traditional experimental static debris jams did not consider the evolution of debris jams and thus did not reflect the fact that the debris jam might also take time to develop to reach a certain size. In contrast, the present experimental study reproduced the development of dynamic woody debris jams. Specifically, this thesis has examined the influence of dynamic debris jam, instead of traditional static debris jam, in terms of scour and load using physical modeling with a scale of 30. In addition, the flow field around the debris jam built by pieces of dowels was measured and compared to a traditional smooth block jam of equivalent size. The following conclusions could be drawn according to the results obtained with the examined experimental flow conditions:

(1) Compared to the traditional static debris jam, a dynamic debris jam involves the formation, growth, and failure processes. Interruption of the initiation of debris jams could provide a potential method to counter the development of debris jams. A dynamic debris jam may be removed by the water flow if the accumulation becomes unbalanced. Consequently, the debris jams built by dowels could last about 10-20 minutes whereas the debris jams formed by seedling trees, which have roots and branches, could last over 50 minutes. This demonstrated that the characteristics of debris pieces have a significant influence on the stability and formation of the debris jam.

(2) Dynamic debris jams increase the scour depth. No matter whether the dynamic debris jam was built by dowels or seedling trees, the debris jam enhanced the scour process. The first debris jam of dowels showed a significant influence on the scour depth, while the influence of subsequent debris jams on scour depends on their size, compared to the previous one. The influence of the first debris jam on scour depth had a clear correlation with the blockage of the debris jam. Meanwhile, seedling tree debris jams could lead to over twice the scour depth compared to the equivalent blank control test without a debris jam. This was due to the better stability of seedling tree debris jams in the tests.

(3) The presence of dynamic debris jam leads to much greater scour hole volume around the bridge pier, reaching 8 times that without debris. The removed scour hole volume at the base of the pier might also contribute to the instability of the bridge pier, and this indicated that the frontal scour depth of the bridge pier might not be enough to quantify the influence of debris jam.

(4) The AI tool of Multigene genetic programming (MGGP) was applied to develop the model for the temporal evolution of single pier scour depth based on the blank control test data without debris jams. The best performing MGGP models used the same terms as were used in previous empirical functions but obtained improved accuracy.

(5) The presence of debris jams also caused extra streamwise load on the pier. Generally, the seedling trees could cause a higher load on the pier than that of a dowel jam due to their better stability, and the drag coefficient of seedling trees was also higher than that of dowel jams. Individual debris impacts were observed in the tests. In addition, a load spiking phenomenon was observed in the tests, indicating that the load caused by a developing debris jam could significantly increase in a short time which might contribute to the bridge failure.

(6) Debris accumulated in front of the bridge pier or superstructure would also lead to the increase of water level upstream, and this could cause the flood risks to increase in the flood events.

According to the experiment results for both the seedling tree and dowel debris jams, the induced hydraulic head was correlated to the blockage of the debris jam and the Froude number.

(7) The horizontal plane area of the dynamic debris jam was also measured in the experiment, and it was found that the horizontal plane area of the dynamic debris jam was correlated to the projected frontal vertical area of the debris jam which might provide a potential method to estimate the blockage of debris jam. However, this correlation might still require further demonstration in various flow conditions.

(8) The flow field around the debris jam was also measured, and it was found that the flow fields around the 20 cm length dowel jam and the 30 cm length jam were similar but differed from that of the 3D printer-built debris jam, especially in the section behind the pier. Three zones were identified within the section behind the pier in the presence of a debris jam the accelerated high-speed zone, the higher shear transition zone, and the wake dead zone. The protrusions of debris dowels were observed to contribute to the roughness of the debris jam surface and caused higher vortices and shear stress near the surface of the debris jam. In addition, the drag coefficient of both jams constructed of dowels was approximately 1.7, while the 3D printer-built debris jam had a value of 0.88, smaller than the dowels jam.

9.2 Recommendations for Future Work

This study has examined dynamic debris jams comprised of dowels or seedling trees and monitored their influence on the temporal evolution of scour depth and the extra load on the pier. However, there remains much to be studied regarding static or dynamic debris jams, as the problem of debris jams is complicated due to the various characteristics of debris, the fluvial flow condition, and the structure of the pier design. Further studies to continue exploring this topic could include:

(1) Scour depth is widely used to quantify the danger of scour, whereas force or torque imbalances are the ultimate causes of structural instability. Scour depth is a simplified approach to explaining structural failures. Thus, future experiments could monitor the forces or torque on the pier during the development of scour, as well as the dynamic debris jam.

(2) Longer experimental time could be done for further tests, as the reason to choose one hour was just due to the limitations of instruments and feasibility. A one-hour test might not be sufficient to obtain an equilibrium scour depth for the case without debris jam. Additionally, one hour may be insufficient to develop fully and assess a dynamic debris jam and associated scour.

(3) Debris jams are built by pieces of debris and their porosity could also evolve during their development. The development of techniques to monitor continuously the debris jam porosity could be considered for future experiments. Similarly, porous medium studies might be applied to the accumulated jam, especially the dowels jam; the turbulent structure inside the dowels jam could be interesting work.

(4) In the present studies, random debris jam accumulation was minimized by reducing the distance between debris release and the pier to focus on the evolution of the debris jam. In fact, some studies have already indicated that debris pieces are randomly captured by debris jams or piers. It would be interesting to randomize the debris approach to consider statistically the evolution of a dynamic debris jam.

(5) Numerical studies for the dynamic debris jam could be worth investigating. This problem requires a dynamic boundary as the size of the debris jam evolves with time, and the porosity of the debris jam could also increase the difficulties to do the simulation. Furthermore, it would involve the fluid and structure interaction if a load of debris jam is included during the scour process.

References

Ahmed, F., and Rajaratnam, N. (1998). "Flow around Bridge Piers." *Journal of Hydraulic Engineering*, 124(3), 288-300.

Aksoy, A. O., Bombar, G., Arkis, T., and Guney, M. S. (2017). "Study of the time-dependent clear water scour around circular bridge piers." *Journal of hydrology hydromechanics*, 65(1), 26-34.

Alabi, P. D. (2006). "Time development of local scour at a bridge pier fitted with a collar." M.S. Thesis, University of Saskatchewan.

Ali, K. H. M., and Karim, O. (2002). "Simulation of flow around piers." *Journal of Hydraulic Research*, 40(2), 161-174.

Anderson, A. (1963). "Discussion of 'Sediment transportation mechanics: erosion of sediment'by Task Force on Preparation of Sedimentation Manual." *J. Hydraul. Div., Am. Soc. Civ. Eng*, 89, 237-248.

Arneson, L., Zevenbergen, L., Lagasse, P., and Clopper, P. (2012). "Evaluating scour at bridges." National Highway Institute (US).

Azamathulla, H. M. (2011). "Gene-expression programming to predict scour at a bridge abutment." *Journal of Hydroinformatics*, 14(2), 324-331.

Azamathulla, H. M. (2012). "Gene expression programming for prediction of scour depth downstream of sills." *Journal of Hydrology*, 460-461, 156-159.

Azamathulla, H. M., and Ghani, A. A. (2010). "Genetic Programming to Predict River Pipeline Scour." *Journal of Pipeline Systems Engineering and Practice*, 1(3), 127-132.

Azamathulla, H. M., Ghani, A. A., Zakaria, N. A., and Guven, A. (2010). "Genetic Programming to Predict Bridge Pier Scour." *Journal of Hydraulic Engineering*, 136(3), 165-169.

Baykal, C., Sumer, B. M., Fuhrman, D. R., Jacobsen, N. G., and Fredsøe, J. (2015). "Numerical investigation of flow and scour around a vertical circular cylinder." *Philosophical Transactions of the Royal Society A: Mathematical, Physical and Engineering Sciences*, 373(2033), 20140104.

Bocchiola, D., Rulli, M. C., and Rosso, R. (2006). "Flume experiments on wood entrainment in rivers." *Advances in Water Resources*, 29(8), 1182-1195.

Bocchiola, D., Rulli, M. C., and Rosso, R. (2006). "Transport of large woody debris in the presence of obstacles." *Geomorphology*, 76(1), 166-178.

Bradley, J., Richards, D., and Bahner, C. (2005). "Debris Control Structures-Evaluation and Countermeasures: Hydraulic Engineering Circular 9." United States. Federal Highway Administration. Office of Bridge Technology.

Braudrick, C. A., and Grant, G. E. (2000). "When do logs move in rivers?" *Water Resources Research*, 36(2), 571-583.

Braudrick, C. A., and Grant, G. E. (2001). "Transport and deposition of large woody debris in streams: a flume experiment." *Geomorphology*, 41(4), 263-283.

Braudrick, C. A., Grant, G. E., Ishikawa, Y., and Ikeda, H. (1997). "Dynamics of Wood Transport in Streams: A Flume Experiment." *Earth Surface Processes and Landforms*, 22(7), 669-683.

Breusers, H. "Time scale of two dimensional local scour." *Proc., Proc. 12th Congress IAHR, vol 3, paper C32*, IAHR.

Breusers, H. N. C., Nicollet, G., and Shen, H. W. (1977). "Local Scour Around Cylindrical Piers." *Journal of Hydraulic Research*, 15(3), 211-252.

Cantero-Chinchilla, F. N., Almeida, G. A. M. d., and Manes, C. (2021). "Temporal Evolution of Clear-Water Local Scour at Bridge Piers with Flow-Dependent Debris Accumulations." *Journal of Hydraulic Engineering*, 147(10), 06021013.

Carnacina, I., Lescova, A., and Pagliara, S. "A Methodology to Measure Flow Fields at Bridge Piers in the Presence of Large Wood Debris Accumulation Using Acoustic Doppler Velocimeters." Springer Singapore, 17-25.

Chabert, J., and Engeldinger, P. (1956). "Etude des affouillements autour des piles de points (Study of scour at bridge piers)." *Bureau Central d'Etudes les Equipment d'Outre-Mer, Laboratoire National d'Hydraulique, France*.

Chang, W.-Y., Constantinescu, G., Lien, H.-C., Tsai, W.-F., Lai, J.-S., and Loh, C.-H. (2013). "Flow Structure around Bridge Piers of Varying Geometrical Complexity." *Journal of Hydraulic Engineering*, 139(8), 812-826.

Chang, W.-Y., Lai, J.-S., and Yen, C.-L. (2004). "Evolution of Scour Depth at Circular Bridge Piers." *Journal of Hydraulic Engineering*, 130(9), 905-913.

Chen, S.-C., Tfwala, S. S., Wang, C.-R., Kuo, Y.-M., and Chao, Y.-C. (2019). "Incipient motion of large wood in river channels considering log density and orientation." *Journal of Hydraulic Research*, 1-14.

Chen, X., Zhang, X., Liu, X., Zhang, F., Yan, J., and Wang, H. (2022). "Experimental study of scour characteristics and scour hole dimensions in consolidated silt sediment under a current." *Ocean Engineering*, 266, 112801.

Claps, P. (2018). "Formation and growth of debris accumulations at bridge piers and its influence on local scour and flooding Formazione e crescita di accumuli detritici alle pile dei ponti ed influenza sull'erosione locale e." university of southampton.

Comiti, F., Lucía, A., and Rickenmann, D. (2016). "Large wood recruitment and transport during large floods: A review." *Geomorphology*, 269, 23-39.

Crosato, A., Rajbhandari, N., Comiti, F., Cherradi, X., and Uijttewaal, W. (2013). "Flume experiments on entrainment of large wood in low-land rivers." *Journal of Hydraulic Research*, 51(5), 581-588.

Daniels, M. D. (2006). "Distribution and dynamics of large woody debris and organic matter in a low-energy meandering stream." *Geomorphology*, 77(3), 286-298.

Dargahi, B. (1989). "The turbulent flow field around a circular cylinder." *Experiments in Fluids*, 8(1), 1-12.

Dargahi, B. (1990). "Controlling Mechanism of Local Scouring." *Journal of Hydraulic Engineering*, 116(10), 1197-1214.

Davidson, S. L., MacKenzie, L. G., and Eaton, B. C. (2015). "Large wood transport and jam formation in a series of flume experiments." *Water Resources Research*, 51(12), 10065-10077.

Derschum, C., Nistor, I., Stolle, J., and Goseberg, N. (2018). "Debris impact under extreme hydrodynamic conditions part 1: Hydrodynamics and impact geometry." *Coastal Engineering*, 141, 24-35.

Dey, S. (1999). "TIME-VARIATION OF SCOUR IN THE VICINITY OF CIRCULAR PIERS." *Proceedings of the Institution of Civil Engineers*, 136(2), 67-75.

Dey, S., Bose, S. K., and Sastry, G. L. N. (1995). "Clear Water Scour at Circular Piers: a Model." *Journal of Hydraulic Engineering*, 121(12), 869-876.

Dey, S., and Raikar, R. V. (2007). "Characteristics of Horseshoe Vortex in Developing Scour Holes at Piers." *Journal of Hydraulic Engineering*, 133(4), 399-413.

Diehl, T. H. (1997). *Potential drift accumulation at bridges*, US Department of Transportation, Federal Highway Administration, Research and Development, Turner-Fairbank Highway Research Center.

Ebrahimi, M., Kripakaran, P., Prodanović, D. M., Kahraman, R., Riella, M., Tabor, G., Arthur, S., and Djordjević, S. (2018). "Experimental Study on Scour at a Sharp-Nose Bridge Pier with Debris Blockage." *Journal of Hydraulic Engineering*, 144(12), 04018071.

Escauriaza, C., and Sotiropoulos, F. (2011). "Initial stages of erosion and bed form development in a turbulent flow around a cylindrical pier." *Journal of Geophysical Research: Earth Surface*, 116(F3).

Escauriaza, C., and Sotiropoulos, F. (2011). "Lagrangian model of bed-load transport in turbulent junction flows." *Journal of Fluid Mechanics*, 666, 36-76.

Escauriaza, C., and Sotiropoulos, F. (2011). "Reynolds Number Effects on the Coherent Dynamics of the Turbulent Horseshoe Vortex System." *Flow, Turbulence and Combustion*, 86(2), 231-262.

Ettema, R. (1980). "Scour at bridge piers. Rep. No. 216." *Auckland: School of Eng., Univ. of Auckland*.

Ettema, R., Constantinescu, G., and Melville, B. W. (2017). "Flow-Field Complexity and Design Estimation of Pier-Scour Depth: Sixty Years since Laursen and Toch." *Journal of Hydraulic Engineering*, 143(9), 03117006.

Ettema, R., Kirkil, G., and Muste, M. (2006). "Similitude of Large-Scale Turbulence in Experiments on Local Scour at Cylinders." *Journal of Hydraulic Engineering*, 132(1), 33-40.

Ferreira, C. (2001). "Gene expression programming: a new adaptive algorithm for solving problems." *Complex Syst*, 13(2), 87-129.

Franzetti, S., Larcan, E., and Mignosa, P. (1982). "Influence of tests duration on the evaluation of ultimate scour around circular piers."

Garg, A., Garg, A., Tai, K., Barontini, S., and Stokes, A. (2014). "A computational intelligence-based genetic programming approach for the simulation of soil water retention curves." *Transport in porous media*, 103(3), 497-513.

Gippel, C. J., O'NEILL, I. C., FINLAYSON, B. L., and Schnatz, I. (1996). "Hydraulic guidelines for the re - introduction and management of large woody debris in lowland rivers." *Regulated Rivers: Research & Management*, 12(2 - 3), 223-236.

Graf, W. H., and Istiarto, I. (2002). "Flow pattern in the scour hole around a cylinder." *Journal of Hydraulic Research*, 40(1), 13-20.

Graf, W. H., and Yulistiyanto, B. (1998). "Experiments on flow around a cylinder; the velocity and vorticity fields." *Journal of Hydraulic Research*, 36(4), 637-654.

Gurnell, A., Piégay, H., Swanson, F., and Gregory, S. (2002). "Large wood and fluvial processes." *Freshwater Biology*, 47(4), 601-619.

Haehnel, R. B., and Daly, S. F. (2004). "Maximum Impact Force of Woody Debris on Floodplain Structures." *Journal of Hydraulic Engineering*, 130(2), 112-120.

Haga, H., Kumagai, T. o., Otsuki, K., and Ogawa, S. (2002). "Transport and retention of coarse woody debris in mountain streams: An in situ field experiment of log transport and a field survey of coarse woody debris distribution." *Water Resources Research*, 38(8), 1-1-1-16.

Hager, W. H. (2007). "Scour in hydraulic engineering." *Proceedings of the Institution of Civil Engineers - Water Management*, 160(3), 159-168.

Hager, W. H., and Unger, J. (2010). "Bridge Pier Scour under Flood Waves." *Journal of Hydraulic Engineering*, 136(10), 842-847.

Hasanpour, A., Istrati, D., and Buckle, I. (2021). "Coupled SPH–FEM Modeling of Tsunami-Borne Large Debris Flow and Impact on Coastal Structures." *Journal of Marine Science and Engineering*, 9(10), 1068.

Hasanpour, A., Istrati, D., and Buckle, I. G. "Multi-Physics Modeling of Tsunami Debris Impact on Bridge Decks." *Proc., Proceedings of the 3rd International Conference on Natural Hazards & Infrastructure, Athens, Greece*, 5-7.

Istrati, D., Hasanpour, A., and Buckle, I. "Numerical investigation of tsunami-borne debris damming loads on a coastal bridge." *Proc., Proceedings of the 17 World Conference on Earthquake Engineering, Sendai, Japan*.

Jamei, M., and Ahmadianfar, I. (2019). "Prediction of scour depth at piers with debris accumulation effects using linear genetic programming." *Marine Georesources & Geotechnology*, 1-12.

Jamieson, E. C., Post, G., and Rennie, C. D. (2010). "Spatial variability of three-dimensional Reynolds stresses in a developing channel bend." *Earth Surface Processes and Landforms*, 35(9), 1029-1043.

Jamieson, E. C., Rennie, C. D., and Townsend, R. D. (2013). "Turbulence and Vorticity in a Laboratory Channel Bend at Equilibrium Clear-Water Scour with and without Stream Barbs." *Journal of Hydraulic Engineering*, 139(3), 259-268.

Kandasamy, J. K., and Melville, B. W. (1989). *Bridge damage due to Cyclone Bola*, Department of Civil Engineering, University of Auckland.

Kandasamy, J. K., and Melville, B. W. (1998). "Maximum local scour depth at bridge piers and abutments." *Journal of Hydraulic Research*, 36(2), 183-198.

Kang, T., Kimura, I., and Shimizu, Y. (2020). "Numerical simulation of large wood deposition patterns and responses of bed morphology in a braided river using large wood dynamics model." *Earth Surface Processes and Landforms*, 45(4), 962-977.

Kaydani, H., Mohebbi, A., and Eftekhari, M. (2014). "Permeability estimation in heterogeneous oil reservoirs by multi-gene genetic programming algorithm." *Journal of Petroleum Science and Engineering*, 123, 201-206.

Khan, M., Azamathulla, H. M., and Tufail, M. (2011). "Gene-expression programming to predict pier scour depth using laboratory data." *Journal of Hydroinformatics*, 14(3), 628-645.

Kimura, I., and Kitazono, K. (2019). "Effects of the driftwood Richardson number and applicability of a 3D–2D model to heavy wood jamming around obstacles." *Environmental Fluid Mechanics*, 1-23.

Kirkil, G., and Constantinescu, G. (2009). "Nature of flow and turbulence structure around an in-stream vertical plate in a shallow channel and the implications for sediment erosion." *Water Resources Research*, 45(6).

Kirkil, G., and Constantinescu, G. (2012). "A numerical study of the laminar necklace vortex system and its effect on the wake for a circular cylinder." *Physics of Fluids*, 24(7), 073602.

Kirkil, G., and Constantinescu, G. (2015). "Effects of cylinder Reynolds number on the turbulent horseshoe vortex system and near wake of a surface-mounted circular cylinder." *PHYSICS OF FLUIDS*, 27(7), 075102.

Kirkil, G., Constantinescu, G., and Ettema, R. (2009). "Detached Eddy Simulation Investigation of Turbulence at a Circular Pier with Scour Hole." *Journal of Hydraulic Engineering*, 135(11), 888-901.

Kirkil, G., Constantinescu, S. G., and Ettema, R. (2008). "Coherent Structures in the Flow Field around a Circular Cylinder with Scour Hole." *Journal of Hydraulic Engineering*, 134(5), 572-587.

Klaar, M. J., Hill, D. F., Maddock, I., and Milner, A. M. (2011). "Interactions between instream wood and hydrogeomorphic development within recently deglaciated streams in Glacier Bay National Park, Alaska." *Geomorphology*, 130(3), 208-220.

Koken, M., and Constantinescu, G. (2008). "An investigation of the flow and scour mechanisms around isolated spur dikes in a shallow open channel: 1. Conditions corresponding to the initiation of the erosion and deposition process." *Water Resources Research*, 44(8).

Koken, M., and Constantinescu, G. (2008). "An investigation of the flow and scour mechanisms around isolated spur dikes in a shallow open channel: 2. Conditions corresponding to the final stages of the erosion and deposition process." *Water Resources Research*, 44(8).

Kothyari, U. C., Garde, R. C. J., and Raju, K. G. R. (1992). "Temporal Variation of Scour Around Circular Bridge Piers." *Journal of Hydraulic Engineering*, 118(8), 1091-1106.

Kothyari, U. C., Hager, W. H., and Oliveto, G. (2007). "Generalized Approach for Clear-Water Scour at Bridge Foundation Elements." *Journal of Hydraulic Engineering*, 133(11), 1229-1240.

Kothyari, U. C., and Kumar, A. (2010). "TEMPORAL VARIATION OF SCOUR AROUND CIRCULAR BRIDGE PIERS." *ISH Journal of Hydraulic Engineering*, 16(sup1), 35-48.

Kothyari, U. C., Ranga Raju, K. G., and Garde, R. J. (1992). "Live-bed scour around cylindrical bridge piers." *Journal of Hydraulic Research*, 30(5), 701-715.

Lagasse, P. F., Clopper, P. E., Zevenbergen, L. W., Spitz, W. J., and Girard, L. G. (2010). "Effects of debris on bridge pier scour." Transportation Research Board, Washington,Dc.

Lagasse, P. F., Zevenbergen, L. W., and Clopper, P. E. "Impacts of debris on bridge pier scour." *Proc., Geotechnical Special Publication*, 854-863.

Lai, J.-S., Chang, W.-Y., and Yen, C.-L. (2009). "Maximum Local Scour Depth at Bridge Piers under Unsteady Flow." *Journal of Hydraulic Engineering*, 135(7), 609-614.

Lança, R., Fael, C., and Cardoso, A. (2010). "Assessing equilibrium clear water scour around single cylindrical piers." *River Flow 2010*, 1207-1214.

Lança, R. M., Fael, C. S., Maia, R. J., Pêgo, J. P., and Cardoso, A. H. (2013). "Clear-Water Scour at Comparatively Large Cylindrical Piers." *Journal of Hydraulic Engineering*, 139(11), 1117-1125.

Link, O., Castillo, C., Pizarro, A., Rojas, A., Ettmer, B., Escauriaza, C., and Manfreda, S. (2017). "A model of bridge pier scour during flood waves." *Journal of Hydraulic Research*, 55(3), 310-323.

Liu, H.-K., Chang, F. M., and Skinner, M. M. (1961). "Effect of bridge constriction on scour and backwater." Colorado State University. Libraries.

López, G., Teixeira, L., Ortega-Sánchez, M., and Simarro, G. (2006). "Discussion of "Further Results to Time-Dependent Local Scour at Bridge Elements" by Giuseppe Oliveto and Willi H. Hager." *Journal of Hydraulic Engineering*, 132(9), 995-996.

López, G., Teixeira, L., Ortega-Sánchez, M., and Simarro, G. (2014). "Estimating Final Scour Depth under Clear-Water Flood Waves." *Journal of Hydraulic Engineering*, 140(3), 328-332.

Lu, J.-Y., Shi, Z.-Z., Hong, J.-H., Lee, J.-J., and Raikar, R. V. (2011). "Temporal Variation of Scour Depth at Nonuniform Cylindrical Piers." *Journal of Hydraulic Engineering*, 137(1), 45-56.

Lyn, D. A., Cooper, T. J., Condon, C. A., and Gan, L. (2007). "Factors in debris accumulation at bridge piers."
Lyn, D. A., Cooper, T. J., Yi, Y.-K., Sinha, R. N., and Rao, A. R. (2003). "Debris accumulation at bridge crossings: laboratory and field studies."
Macabuag, J., Raby, A., Pomonis, A., Nistor, I., Wilkinson, S., and Rossetto, T. (2018). "Tsunami design procedures for engineered buildings: a critical review." *Proc. Inst. Civil Eng.-Civil Eng.*, 171(4), 166-178.
Manes, C., and Brocchini, M. (2015). "Local scour around structures and the phenomenology of turbulence." *Journal of Fluid Mechanics*, 779, 309-324.
Manners, R. B., and Doyle, M. W. (2008). "A mechanistic model of woody debris jam evolution and its application to wood-based restoration and management." *River Research and Applications*, 24(8), 1104-1123.
Mauti, G., Stolle, J., Takabatake, T., Nistor, I., Goseberg, N., and Mohammadian, A. (2020). "Experimental Investigation of Loading due to Debris Dams on Structures." *Journal of Hydraulic Engineering*, 146(5), 04020029.
Mazzorana, B., Hübl, J., Zischg, A., and Largiader, A. (2011). "Modelling woody material transport and deposition in alpine rivers." *Natural Hazards*, 56(2), 425-449.
Mazzorana, B., Hübl, J., Zischg, A., and Largiader, A. J. N. H. (2011). "Modelling woody material transport and deposition in alpine rivers." *Natural Hazards*, 56(2), 425-449.
Mazzorana, B., Zischg, A. P., Largiader, A., and Hübl, J. (2009). "Hazard index maps for woody material recruitment and transport in alpine catchments." *Natural Hazards and Earth System Sciences*, 9(1), 197-209.
Mehr, A. D., and Safari, M. J. S. (2020). "Application of Soft Computing Techniques for Particle Froude Number Estimation in Sewer Pipes." *Journal of Pipeline Systems Engineering and Practice*, 11(2), 04020002.
Melville, B. W. (1992). "Local Scour at Bridge Abutments." *Journal of Hydraulic Engineering*, 118(4), 615-631.
Melville, B. W. (1997). "Pier and Abutment Scour: Integrated Approach." *Journal of Hydraulic Engineering*, 123(2), 125-136.
Melville, B. W., and Chiew, Y.-M. (1999). "Time Scale for Local Scour at Bridge Piers." *Journal of Hydraulic Engineering*, 125(1), 59-65.
Melville, B. W., and Dongol, D. M. (1992). "Bridge pier scour with debris accumulation." *Journal of Hydraulic Engineering*, 118(9), 1306.
Melville, B. W., and Raudkivi, A. J. (1977). "FLOW CHARACTERISTICS IN LOCAL SCOUR AT BRIDGE PIERS." *Journal of Hydraulic Research*, 15(4), 373-380.
Melville, B. W., and Sutherland, A. J. (1988). "Design Method for Local Scour at Bridge Piers." *Journal of Hydraulic Engineering*, 114(10), 1210-1226.
Mendonça, I. S. P., Canilho, H. D. L., and Fael, C. M. S. "Flow-3D Modelling of the Debris Effect on Maximum Scour Hole Depth at Bridge Piers." *Proc., 38th IAHR World Congress*, 2813-2821.
Meninno, S., Persi, E., Petaccia, G., Sibilla, S., and Armanini, A. (2019). "An experimental and theoretical analysis of floating wood diffusion coefficients." *Environmental Fluid Mechanics*.
Mia, M. F., and Nago, H. (2003). "Design Method of Time-Dependent Local Scour at Circular Bridge Pier." *Journal of Hydraulic Engineering*, 129(6), 420-427.

Mohammadpour, R., Ghani, A. A. B., and Azamathulla, H. M. (2013). "Estimation of dimension and time variation of local scour at short abutment." *International Journal of River Basin Management*, 11(1), 121-135.
Muzzammil, M., Alama, J., and Danish, M. (2015). "Scour Prediction at Bridge Piers in Cohesive Bed Using Gene Expression Programming." *Aquatic Procedia*, 4, 789-796.
Naito, C., Cercone, C., Riggs, H. R., and Cox, D. (2014). "Procedure for Site Assessment of the Potential for Tsunami Debris Impact." *Journal of Waterway, Port, Coastal, and Ocean Engineering*, 140(2), 223-232.
Nistor, I., Goseberg, N., and Stolle, J. (2017). "Tsunami-Driven Debris Motion and Loads: A Critical Review." *Frontiers in Built Environment*, 3(2).
Nistor, I., Goseberg, N., Stolle, J., Mikami, T., Shibayama, T., Nakamura, R., and Matsuba, S. (2017). "Experimental Investigations of Debris Dynamics over a Horizontal Plane." *Journal of Waterway, Port, Coastal, and Ocean Engineering*, 143(3), 04016022.
Nistor, I., and Palermo, D. (2015). "Chapter 20 - Post-Tsunami Engineering Forensics: Tsunami Impact on Infrastructure—Lessons from 2004 Indian Ocean, 2010 Chile, and 2011 Tohoku Japan Tsunami Field Surveys." *Handbook of Coastal Disaster Mitigation for Engineers and Planners*, M. Esteban, H. Takagi, and T. Shibayama, eds., Butterworth-Heinemann, Boston, 417-435.
Okamoto, T.-a., Tanaka, K., Matsumoto, K., and Someya, T. (2021). "Influence of velocity field on driftwood accumulation at a bridge with a single pier." *Environmental Fluid Mechanics*.
Oliveto, G., and Hager, W. H. (2002). "Temporal Evolution of Clear-Water Pier and Abutment Scour." *Journal of Hydraulic Engineering*, 128(9), 811-820.
Oliveto, G., and Hager, W. H. (2005). "Further Results to Time-Dependent Local Scour at Bridge Elements." *Journal of Hydraulic Engineering*, 131(2), 97-105.
Olsen, N. R. B., and Kjellesvig, H. M. (1998). "Three-dimensional numerical flow modeling for estimation of maximum local scour depth." *Journal of Hydraulic Research*, 36(4), 579-590.
Olsen, N. R. B., and Melaaen, M. C. (1993). "Three-Dimensional Calculation of Scour Around Cylinders." *Journal of Hydraulic Engineering*, 119(9), 1048-1054.
Oudenbroek, K., Naderi, N., Bricker, J. D., Yang, Y., Van der Veen, C., Uijttewaal, W., Moriguchi, S., and Jonkman, S. N. (2018). "Hydrodynamic and Debris-Damming Failure of Bridge Decks and Piers in Steady Flow." *Geosciences*, 8(11), 409.
Pagliara, S., and Carnacina, I. (2010). "Temporal scour evolution at bridge piers: Effect of wood debris roughness and porosity." *Journal of Hydraulic Research*, 48(1), 3-13.
Pagliara, S., and Carnacina, I. (2011). "Influence of large woody debris on sediment scour at bridge piers." *International Journal of Sediment Research*, 26(2), 121-136.
Pagliara, S., and Carnacina, I. (2011). "Influence of Wood Debris Accumulation on Bridge Pier Scour." *Journal of Hydraulic Engineering*, 137(2), 254-261.
Pagliara, S., and Carnacina, I. (2013). "Bridge pier flow field in the presence of debris accumulation." *Proceedings of the Institution of Civil Engineers - Water Management*, 166(4), 187-198.
Pagliara, S., Carnacina, I., and Cigni, F. (2010). "Sills and gabions as countermeasures at bridge pier in presence of debris accumulations." *Journal of Hydraulic Research*, 48(6), 764-774.
Pagliara, S. C., Iacopo (2010). "Temporal scour evolution at bridge piers: effect of wood debris roughness and porosity " *Journal of Hydraulic Research*, 48(1), 3-13.
Paik, J., Escauriaza, C., and Sotiropoulos, F. (2007). "On the bimodal dynamics of the turbulent horseshoe vortex system in a wing-body junction." *Physics of Fluids*, 19(4), 045107.

Pandey, M., Zakwan, M., Sharma, P. K., and Ahmad, Z. (2018). "Multiple linear regression and genetic algorithm approaches to predict temporal scour depth near circular pier in non-cohesive sediment." *ISH Journal of Hydraulic Engineering*, 1-8.

Panici, D., and Almeida, G. A. M. d. (2020). "Influence of Pier Geometry and Debris Characteristics on Wood Debris Accumulations at Bridge Piers." *Journal of Hydraulic Engineering*, 146(6), 04020041.

Panici, D., and de Almeida, G. A. M. (2018). "Formation, Growth, and Failure of Debris Jams at Bridge Piers." *Water Resources Research*, 54(9), 6226-6241.

Panici, D., and de Almeida, G. A. M. (2020). "A theoretical analysis of the fluid–solid interactions governing the removal of woody debris jams from cylindrical bridge piers." *Journal of Fluid Mechanics*, 886, A19.

Panici, D., and Kripakaran, P. (2021). "Trapping Large Wood Debris in Rivers: Experimental Study of Novel Debris Retention System." *Journal of Hydraulic Engineering*, 147(3), 04020101.

Parola, A. C., Apelt, C. J., and Jempson, M. A. (2000). *Debris forces on highway bridges*, Transportation Research Board.

Persi, E., Petaccia, G., Sibilla, S., Brufau, P., and García-Palacin, J. I. (2020). "Experimental dataset and numerical simulation of floating bodies transport in open-channel flow." *Journal of Hydroinformatics*.

Persi, E., Petaccia, G., and Sibilla, S. J. N. H. (2018). "Large wood transport modelling by a coupled Eulerian–Lagrangian approach." *Nat Hazards*, 91(1), 59-74.

Rennie, C. D., and Church, M. (2010). "Mapping spatial distributions and uncertainty of water and sediment flux in a large gravel bed river reach using an acoustic Doppler current profiler." *Journal of Geophysical Research: Earth Surface*, 115(F3).

Rennie, C. D., and Hay, A. (2010). "Reynolds stress estimates in a tidal channel from phase-wrapped ADV data." *Journal of Coastal Research*, 26(1 (261)), 157-166.

Rennie, C. D., and Hay, A. (2010). "Reynolds Stress Estimates in a Tidal Channel from Phase-Wrapped ADV Data." *Journal of Coastal Research*, 2010(261), 157-166, 110.

Richardson, J., and Richardson, E. "The fallacy of local abutment scour equations." *Proc., Hydraulic Engineering*, ASCE, 749-754.

Richardson, J. E., and Panchang, V. G. (1998). "Three-Dimensional Simulation of Scour-Inducing Flow at Bridge Piers." *Journal of Hydraulic Engineering*, 124(5), 530-540.

Rijn, L. C. v. (1984). "Sediment Pick-Up Functions." *Journal of Hydraulic Engineering*, 110(10), 1494-1502.

Rijn, L. C. v. (1984). "Sediment Transport, Part I: Bed Load Transport." *Journal of Hydraulic Engineering*, 110(10), 1431-1456.

Roulund, A., Sumer, B. M., FredsØE, J., and Michelsen, J. (2005). "Numerical and experimental investigation of flow and scour around a circular pile." *Journal of Fluid Mechanics*, 534, 351-401.

Ruiz-Villanueva, V., Bodoque, J. M., Díez-Herrero, A., and Bladé, E. (2014). "Large wood transport as significant influence on flood risk in a mountain village." *Natural Hazards*, 74(2), 967-987.

Ruiz-Villanueva, V., Piégay, H., Gurnell, A. M., Marston, R. A., and Stoffel, M. (2016). "Recent advances quantifying the large wood dynamics in river basins: New methods and remaining challenges." *Reviews of Geophysics*, 54(3), 611-652.

Salaheldin, T. M., Imran, J., and Chaudhry, M. H. (2004). "Numerical Modeling of Three-Dimensional Flow Field Around Circular Piers." *Journal of Hydraulic Engineering*, 130(2), 91-100.

Schalko, I. (2018). "Modeling hazards related to large wood in rivers." ETH Zurich.

Schalko, I., Schmocker, L., Weitbrecht, V., and Boes, R. M. (2018). "Backwater Rise due to Large Wood Accumulations." *Journal of Hydraulic Engineering*, 144(9), 04018056.

Schalko, I., Schmocker, L., Weitbrecht, V., and Boes, R. M. (2019). "Laboratory study on wood accumulation probability at bridge piers." *Journal of Hydraulic Research*, 1-16.

Searson, D. P. (2015). "GPTIPS 2: An Open-Source Software Platform for Symbolic Data Mining." *Handbook of Genetic Programming Applications*, A. H. Gandomi, A. H. Alavi, and C. Ryan, eds., Springer International Publishing, Cham, 551-573.

Shahriar, A. R., Ortiz, A. C., Montoya, B. M., and Gabr, M. A. (2021). "Bridge Pier Scour: An overview of factors affecting the phenomenon and comparative evaluation of selected models." *Transportation Geotechnics*, 28, 100549.

Spreitzer, G., Gibson, J., Tang, M., Tunnicliffe, J., and Friedrich, H. (2019). "SmartWood: Laboratory experiments for assessing the effectiveness of smart sensors for monitoring large wood movement behaviour." *CATENA*, 182, 104145.

Spreitzer, G., Tunnicliffe, J., and Friedrich, H. (2020). "Large wood (LW) 3D accumulation mapping and assessment using structure from Motion photogrammetry in the laboratory." *Journal of Hydrology*, 581, 124430.

Spreitzer, G., Tunnicliffe, J., and Friedrich, H. (2020). "Porosity and volume assessments of large wood (LW) accumulations." *Geomorphology*, 107122.

Stolle, J., Derschum, C., Goseberg, N., Nistor, I., and Petriu, E. (2018). "Debris impact under extreme hydrodynamic conditions part 2: Impact force responses for non-rigid debris collisions." *Coastal Engineering*, 141, 107-118.

Stolle, J., Goseberg, N., Nistor, I., and Petriu, E. (2018). "Probabilistic Investigation and Risk Assessment of Debris Transport in Extreme Hydrodynamic Conditions." *Journal of Waterway, Port, Coastal, and Ocean Engineering*, 144(1), 04017039.

Stolle, J., Takabatake, T., Nistor, I., Mikami, T., Nishizaki, S., Hamano, G., Ishii, H., Shibayama, T., Goseberg, N., and Petriu, E. (2018). "Experimental investigation of debris damming loads under transient supercritical flow conditions." *Coastal Engineering*, 139, 16-31.

Sung-Uk, C., and Wonjun, Y. "Numerical Simulations of 3-D Flows Around Bridge Piers." *Proc., First International Conference on Scour of Foundations. November 17-20, 2002, College Station, USA*, 206-217.

Sutherland, A. (1986). "Reports on bridge failure." *RRU Occasional Paper, National Roads Board, Wellington, New Zealand*.

Tonon, A., Picco, L., and Rainato, R. (2018). "Test of methodology for developing a large wood budget: A 1-year example from a regulated gravel bed river following ordinary floods." *CATENA*, 165, 115-124.

Tseng, M.-H., Yen, C.-L., and Song, C. C. S. (2000). "Computation of three-dimensional flow around square and circular piers." *International Journal for Numerical Methods in Fluids*, 34(3), 207-227.

Uncuoglu, E., Citakoglu, H., Latifoglu, L., Bayram, S., Laman, M., Ilkentapar, M., and Oner, A. A. (2022). "Comparison of neural network, Gaussian regression, support vector machine, long short-term memory, multi-gene genetic programming, and M5 Trees methods for solving civil engineering problems." *Applied Soft Computing*, 129, 109623.

Wallerstein, N., and Thorne, C. R. (1997). "Impacts of woody debris on fluvial processes and channel morphology in stable and unstable streams." NOTTINGHAM UNIV (UNITED KINGDOM) DEPT OF GEOGRAPHY.

Wang, C., Yuan, Y., Liang, F., and Tao, J. (2022). "Experimental investigation of local scour around cylindrical pile foundations in a double-layered sediment under current flow." *Ocean Engineering*, 251, 111084.

Whitehouse, R. (1997). "Scour at marine structures: a manual for engineers and scientists." *Res. Rep. SR417, HR Wallingford Limited, Wallingford, UK*.

Xiong, W., Cai, C. S., Kong, B., and Kong, X. (2016). "CFD Simulations and Analyses for Bridge-Scour Development Using a Dynamic-Mesh Updating Technique." *Journal of Computing in Civil Engineering*, 30(1), 04014121.

Yan, X., and Mohammadian, A. (2019). "Multigene Genetic-Programming-Based Models for Initial Dilution of Laterally Confined Vertical Buoyant Jets." *Journal of Marine Science and Engineering*, 7(8), 246.

Yanmaz, A. M. (2006). "Temporal variation of clear water scour at cylindrical bridge piers." *Canadian Journal of Civil Engineering*, 33(8), 1098-1102.

Yanmaz, A. M., and Altinbilek, H. D. a. (1991). "Study of Time-Depenbent Local Scour around Bridge Piers." *Journal of Hydraulic Engineering*, 117(10), 1247-1268.

Yanmaz, A. M., and Kose, O. (2009). "A semi-empirical model for clear-water scour evolution at bridge abutments." *Journal of Hydraulic Research*, 47(1), 110-118.

Yeh, H., Barbosa, A. R., Ko, H., and Cawley, J. G. (2014). "Tsunami loadings on structures: Review and analysis." *Coastal Engineering Proceedings*, 1(34), 4.

Yilmaz, M., Yanmaz, A. M., and Koken, M. (2017). "Clear-water scour evolution at dual bridge piers." *Canadian Journal of Civil Engineering*, 44(4), 298-307.

Zeng, J., and Constantinescu, G. (2017). "Flow and coherent structures around circular cylinders in shallow water." *Physics of Fluids*, 29(6), 066601.

Zhang, W., Nistor, I., Rennie, C. D., and Almansour, H. (2022). "Influence of Dynamic Woody Debris Jam on Single Bridge Pier Scour and Induced Hydraulic Head." *Journal of Marine Science and Engineering*, 10(10), 1421.

Zhao, M., Cheng, L., and Zang, Z. (2010). "Experimental and numerical investigation of local scour around a submerged vertical circular cylinder in steady currents." *Coastal Engineering*, 57(8), 709-721.

Zhao, W., and Huhe, A. (2006). "Large-Eddy Simulation of Three-Dimensional Turbulent Flow Around a Circular Pier." *Journal of Hydrodynamics*, 18(6), 765-772.

Supplementary I Figures for MGGP

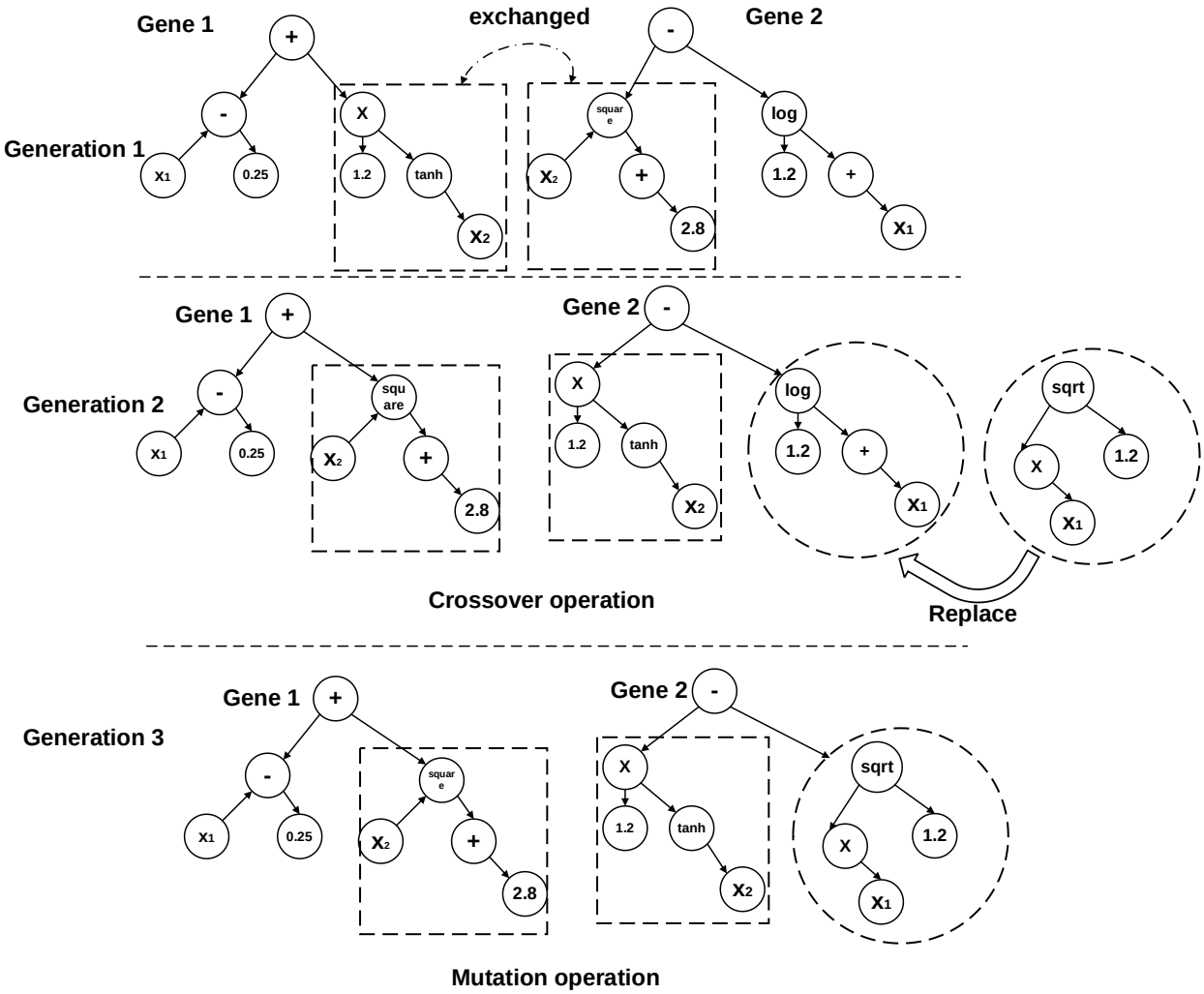

Figure S0 An example of the process of crossover and mutation operation in MGGP

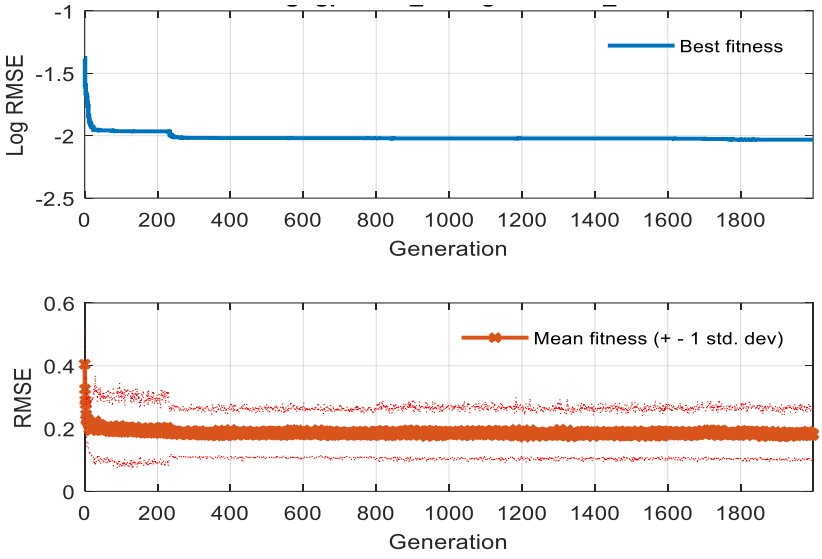

Figure S1 Evolution generations for the evolution of the MGGP model

Supplementary II Tables for MGGP

Table S0 Flow conditions

set number	water depth h (m)	mean velocity U(m/s)	shear velocity u^* (m/s)	Froude number F_r	U/u_c
1	0.284	0.223	0.0129	0.134	0.506
2	0.278	0.311	0.0150	0.188	0.707
3	0.281	0.273	0.0119	0.164	0.620
4	0.286	0.250	0.00959	0.149	0.566
5	0.184	0.256	0.0112	0.191	0.617
6	0.234	0.246	0.0105	0.162	0.573
7	0.326	0.257	0.0106	0.144	0.572

Note: Critical mean velocityu_c is determined by the method referred in Aksoy et al. (2017)

Table.S1 Parameters for GEP setup

Parameter	Value
Population size	500
Max Generations	2000
Max Genes	4
Probability of Pareto tournament	0.3
ERC probability	0.05
Function set	+, -, *, /, exp, log, abs, cube, exp, square, tanh, sqrt, neg

Table S2 Buckingham non-dimensional method

Deactivated variable	Function of the model	
——	$\Pi_7 = 0.08268\ln\left(\Pi_3^2\Pi_5\Pi_6/\Pi_1\right)-\left(4.866\Pi_1+2.433\Pi_6+2.433\Pi_1\Pi_4+2.433\Pi_5/\Pi_3\right)/0.5629\left(\Pi_1-\Pi_4\right)$ $+200.4\Pi_2\tanh\left(\Pi_2-\Pi_4\right)\ln\left(\Pi_5\Pi_6\right)/\Pi_3\left(\Pi_1+0.2571\right)-0.03452\Pi_1^2\left(\Pi_3+15.52\Pi_2\Pi_5-29.35\right)/\Pi_4^2-2.359$	S0(0)
Π_1	$\Pi_7 = 1.408\ln\left(\tanh\Pi_6/\tanh\Pi_4\right)+0.1636\ln\left(\Pi_3\left(2.0\Pi_4+\Pi_5\right)/\Pi_2\Pi_6\right)$ $+26.37\Pi_2\tanh\left(2.0\Pi_4+\Pi_5\right)\tanh^3\left(\Pi_4\right)-13.66\Pi_2\tanh\left(\tanh\left(\Pi_4\right)\right)\exp\left(\tanh\left(\Pi_4\right)\right)\tanh^2\left(\Pi_4\right)$ -0.3438	S0(1)
Π_2	$\Pi_7 = 0.0005621\Pi_5/\Pi_4-0.001477\Pi_1^2\ln\left(\Pi_1\Pi_3\Pi_5\right)\left(2.0\Pi_5+\Pi_3\right)+0.0002811\Pi_4^3$ $+6.39\Pi_6^2\Pi_4\left(\Pi_1+\Pi_4+\Pi_6\right)/0.0004503\Pi_3+0.0011\Pi_4+0.0005498\Pi_3/\Pi_5-0.8107$	S0(2)
Π_3	$\Pi_7 = 0.434\tanh\left(\Pi_1\Pi_2\Pi_5\right)-6.804\tanh\left(\tanh\left(10.97\Pi_1\right)\right)-0.06263\ln\left(\left(\Pi_5+2\Pi_1\right)/\Pi_1\Pi_5^2\right)$ $+2.512\tanh\left(\Pi_1+\Pi_6+\sqrt{\Pi_1}+\Pi_6^2\right)-10.06\Pi_6/\left(\Pi_1-\Pi_6\right)+3.846\Pi_6/\Pi_4^2-10.57$	S0(3)
Π_4	$\Pi_7 = 7.666\sqrt{\Pi_1\Pi_2-7.095\Pi_1\Pi_6+\sqrt{\Pi_6}}-5.721\sqrt{\Pi_2\Pi_6^2/\Pi_1\Pi_3\Pi_5}-23.87\left(\tanh\left(\Pi_1\right)+\Pi_1^2\right)$ $+0.1418\left(\Pi_2^2\Pi_5\right)^{0.25}+23.87\sqrt{\Pi_6}/\left(\Pi_3\Pi_5^2\right)-4.802$	S0(4)
Π_5	$\Pi_7 = 0.1259\ln\left(\Pi_1\Pi_4\right)\ln^2\left(\Pi_1\right)\tanh^3\left(\Pi_6\right)\left(\Pi_6-2.031\right)-1.125\exp\left(\Pi_6\Pi_1^2+\tanh\Pi_4\right)+2.88$ $-24.78\ln\Pi_4/\Pi_6^3\left(\Pi_2-2.179\right)\left(\Pi_3-10.55\right)-0.3479\Pi_1\Pi_4^2\Pi_6\ln\left(\Pi_1\right)\ln\left(\Pi_4\right)\left(\Pi_2-\Pi_4\right)/\left(\left(\Pi_2-3.702\right)\left(\Pi_2-3.747\right)\right)$	S0(5)
Π_6	$\Pi_7 = 7181.\tanh^2\left(\Pi_1\right)/\ln^2\left(\Pi_4\right)-2.27\tanh\left(\Pi_1+\Pi_2\right)-1.135\tanh\left(\Pi_4\right)/\sqrt{\Pi_2}$ $+0.891\sqrt{\Pi_2}\ln\left(\Pi_5-\Pi_1\right)/\ln\left(\Pi_3\right)-21022\Pi_1^2/\Pi_4^2+3.188$	S0(6)

Table S3 Sensitivity analysis of error evaluation for input data

Deactivated variable		RMSE	NRMSE	NASH	R^2
——	$\Pi_7 = \Pi_1\Pi_2\Pi_3\Pi_4\Pi_5\Pi_6$	0.011	0.160	0.909	0.909
Π_1	$\Pi_7 = \Pi_2\Pi_3\Pi_4\Pi_5\Pi_6$	0.013	0.187	0.877	0.879
Π_2	$\Pi_7 = \Pi_1\Pi_3\Pi_4\Pi_5\Pi_6$	0.010	0.146	0.924	0.925
Π_3	$\Pi_7 = \Pi_1\Pi_2\Pi_4\Pi_5\Pi_6$	0.012	0.179	0.886	0.887
Π_4	$\Pi_7 = \Pi_1\Pi_2\Pi_3\Pi_5\Pi_6$	0.016	0.234	0.807	0.807
Π_5	$\Pi_7 = \Pi_1\Pi_2\Pi_3\Pi_4\Pi_6$	0.028	0.399	0.436	0.437
Π_6	$\Pi_7 = \Pi_1\Pi_2\Pi_3\Pi_4\Pi_5$	0.017	0.253	0.774	0.790

Table S4 Sensitivity analysis of error evaluation for validating data

Deactivated variable		RMSE	NRMSE	NASH	R^2
—	$\Pi_7 = \Pi_1\Pi_2\Pi_3\Pi_4\Pi_5\Pi_6$	0.032	0.452	0.703	0.822
Π_1	$\Pi_7 = \Pi_2\Pi_3\Pi_4\Pi_5\Pi_6$	0.076	1.072	-0.672	0.077
Π_2	$\Pi_7 = \Pi_1\Pi_3\Pi_4\Pi_5\Pi_6$	0.031	0.434	0.726	0.792
Π_3	$\Pi_7 = \Pi_1\Pi_2\Pi_4\Pi_5\Pi_6$	0.038	0.534	0.586	0.763
Π_4	$\Pi_7 = \Pi_1\Pi_2\Pi_3\Pi_5\Pi_6$	0.031	0.433	0.728	0.819
Π_5	$\Pi_7 = \Pi_1\Pi_2\Pi_3\Pi_4\Pi_6$	0.063	0.886	-0.141	0.015
Π_6	$\Pi_7 = \Pi_1\Pi_2\Pi_3\Pi_4\Pi_5$	0.068	0.965	-0.353	0.026

Table.S5 MGGP model based on Melville and Chiew (1999) Eq. (7) group one

	Function of the model	
Single Gene, 1.0 training data and 0.0 testing data	$d_9 = 0.08265\ln d_7 - d_6/0.685 + 0.787/\left(d_6^{-2} + 2.0d_7/d_6\right) + 0.9168$	S (1)
0.6 training data and 0.4 testing data	$d_9 = 1.557\tanh\left(d_6^{-3} + d_6^{-2} - 4.527\right) - 1.553\tanh\left(d_6^{-3} + d_6^{-2} - 4.306\right) + 0.08832\ln\left(d_6^{-5}d_7\right) + 1.263\exp\left(-d_6^{-1} - 2d_7\right)/d_6^{-2} + 0.3788$	S (2)
0.75 training data and 0.25 testing data	$d_9 = 0.05169\ln\left(d_7^2\left(2d_6^{-1} + d_7\right)/d_6^{-2}\right) - 2.947\exp\left(-d_6^{-3}\right) + 26300.0\exp\left(-27d_6^{-3}\right) + 25.56\exp\left(-2.0d_6^{-1}\right)\exp\left(-d_7\right)\exp\left(-\exp\left(-d_7\right)\right)\exp\left(-d_6^{-1}d_7\right) + 0.6333$	S (3)
0.9 training data and 0.1 testing data	$d_9 = 3.081\exp\left(-\left\lvert\ln d_6^{-1}\right\rvert\right) + 13000.0\exp\left(-\exp\left(3.0d_6^{-1}\right)\right) - 1.162\exp\left(-d_6^{-6}\ln d_6^{-1}\right) + 0.009975\left(\exp d_6^{-1} - \ln d_7\right)\left(3.0d_6^{-1} + d_7 + \ln d_7 + 1.364\right) - 1.542$	S (4)
1.0 training data and 0.0 testing data	$d_9 = 3.774\left(\ln d_6^{-1}\right)^2/d_6^{-3} - 0.1023\ln\left(0.3084/d_7 - 6.073d_6^{-1} + 13.48\right) - 3.101\tanh\left(d_6^{-6}\right) - 0.5769\ln\left(d_6^{-1}\right)/\left(d_6^{-9}\tanh d_6^{-1}\right) + 3.119$	S (5)

Table S6 Error of the MGGP model based on Eq. (7) group one

		RMSE	NRMSE	NASH	R^2
Eq. (S1)	Input data	0.025	0.369	0.519	0.542
	validating data	0.046	0.649	0.388	0.816
Eq. (S2)	Input data	0.021	0.307	0.667	0.683
	validating data	0.024	0.340	0.832	0.877
Eq. (S3)	Input data	0.025	0.365	0.529	0.601
	validating data	0.039	0.544	0.570	0.810
Eq. (S4)	Input data	0.025	0.358	0.546	0.611
	validating data	0.033	0.472	0.676	0.874
Eq. (S5)	Input data	0.025	0.365	0.529	0.594
	validating data	0.038	0.540	0.576	0.840

Noted that the input data includes both the training and testing data.

Table S7 MGGP model based on Oliveto and Hager (2002) Eq (7) group two

	Function of the model	
Single Gene, 1.0 training data and 0.0 testing data	$d_{10} = 0.00001917 \exp\left(d_3/d_4\right)\left(\ln d_5\right)^2\left(2\exp d_3 + \ln d_5\right) + 0.29834$	S (6)
0.6 training data and 0.4 testing data	$d_{10} = 1.909\ln d_3 - 17500\tanh d_4^9 - 1.369\left(\ln d_4^3\right)^3 + 1.909 d_4^3 + 1.909\, d_4/\ln d_5 + \sqrt{d_4 - d_3 + \ln d_5} + 0.7602\ln d_5 + 17500$	S (7)
0.75 training data and 0.25 testing data	$d_{10} = \left(0.007078 d_3^3 d_4^{12} + 0.01044 d_3 d_4^{12}\left(\ln d_4\right)^2 \ln\left(d_3 d_4 d_5\right)\right)\Big/ d_4^{12}\left(\ln d_4\right)^3 - \left(14.11 d_3^3 - 44.88 d_4^3\left(\ln d_3\right)^3\right)\Big/ d_4^{12} + 0.02922$	S (8)
0.9 training data and 0.1 testing data	$d_{10} = 391.6\tanh\left(d_4^6\right) - 32000\tanh\left(d_4^9\right) + 0.006491 d_3^2 \ln d_5\left(d_5 - 13.83\right)/d_5 + 0.008262 d_3 \ln d_5\left(d_5 + 32.14\right)/\left(d_5 \ln d_4 \tanh d_3\right) + 31600.0$	S (9)
1.0 training data and 0.0 testing data	$d_{10} = 0.001513 d_3^3/\left(\ln d_4\right)^3 + 0.1598\sqrt{\exp\left(d_3\right)\ln d_5} - 0.9536 d_3^2/\ln d_4^3 + 3.553\left(1.525 d_3 - 1.525 d_4\right)/d_4^{1.5} + 0.9283$	S (10)

Table S8 Error of the MGGP model based on Eq. (7) group two

		RMSE	NRMSE	NASH	R^2
Eq. (S6)	Input data	0.025	0.356	0.550	0.612
	validating data	0.048	0.672	0.344	0.636
Eq. (S7)	Input data	0.016	0.239	0.798	0.806
	validating data	0.019	0.262	0.900	0.935
Eq. (S8)	Input data	0.015	0.223	0.825	0.834
	validating data	0.022	0.314	0.857	0.913
Eq. (S9)	Input data	0.014	0.199	0.860	0.864
	validating data	0.035	0.499	0.639	0.972
Eq. (S10)	Input data	0.021	0.300	0.682	0.707
	validating data	0.028	0.390	0.779	0.913

Table S9 MGGP model based on Aksoy et al. (2017) Eq. (7) group three

	Function of the model	
Single Gene, 1.0 training data and 0.0 testing data	$d_{11} = 0.1674 d_2^{-2} d_6^2 \ln\left(3.0 d_8\right) \tanh\left(5.277 d_2 d_6\right) + 0.1272$	S (11)
0.6 training data and 0.4 testing data	$d_{11} = 0.01834 d_2^2 d_6^2 \ln\left(d_2\right)\left(d_2 - 2.865\right)\left(d_6 - d_2 + \exp\left(d_6\right)\right) + 3.203\times10^{-5} \exp\left(2.835 d_6^4\right)$ $+0.3712 d_2^2 d_6^4 + 0.1278 \ln\left(\exp\left(-d_6\right)\right)\left(2.0 d_8 + 1.705\right) - 0.252$	S (12)
0.75 training data and 0.25 testing data	$d_{11} = -7.534\times10^{-6} \exp\left(2.0 d_2\right)\left(\ln\left(d_8\right) + 4.737\right) - 0.3768 \ln\left(d_2^2 + 2.0 d_6\right)$ $+0.1454 d_2 \tanh\left(d_6^2\right)\left(d_2 + \ln\left(d_8\right)\right) + 5.809\times10^{-8} \exp\left(8.775 d_6^2\right) + 0.5242$	S (13)
0.9 training data and 0.1 testing data	$d_{11} = 1.32 d_2 d_6 + 0.03523 d_6^{-2} \exp\left(2.0 d_6^2\right) + 0.3715 - 0.6799\left(d_2 d_6^5 + d_6 + d_2\right)$ $+0.06278\left(\ln\left(d_6 + 2.0 d_8\right) + d_2 d_6^2 \ln\left(d_8\right) + d_2 d_6 \ln\left(d_6\right)\left(d_2 - d_6\right)\right)$	S (14)
1.0 training data and 0.0 testing data	$d_{11} = 0.1748 d_6 \ln\left(d_8\right) d_2^2 + 0.002433 + 0.01855\left(\exp\left(\exp\left(d_6\right)\right) + d_6\left(d_2 + 2 d_6\right)\left(2 d_2 - 1.775\right)\right)$ $-0.001782 \ln\left(d_8\right)\left(d_2 + 1.298\right)\left(d_2 + d_6\right)\left(d_2 + 2 d_6 - \left(\ln\left(d_2\right)\right)^2\right) + 0.2532 d_2 d_6 \ln\left(d_2\right) \ln\left(d_6 / d_8\right)$	S (15)

Table S10 Error of the MGGP model based on Eq. (7) group three

		RMSE	NRMSE	NASH	R^2
Eq. (S11)	Input data	0.021	0.310	0.661	0.663
	validating data	0.036	0.501	0.635	0.892
Eq. (S12)	Input data	0.020	0.290	0.703	0.707
	validating data	0.035	0.497	0.641	0.822
Eq. (S13)	Input data	0.017	0.247	0.785	0.785
	validating data	0.032	0.447	0.709	0.887
Eq. (S14)	Input data	0.017	0.250	0.779	0.779
	validating data	0.029	0.404	0.762	0.910
Eq. (S15)	Input data	0.018	0.254	0.772	0.774
	validating data	0.034	0.479	0.666	0.829

Supplementary III Figures for the debris jam evolution

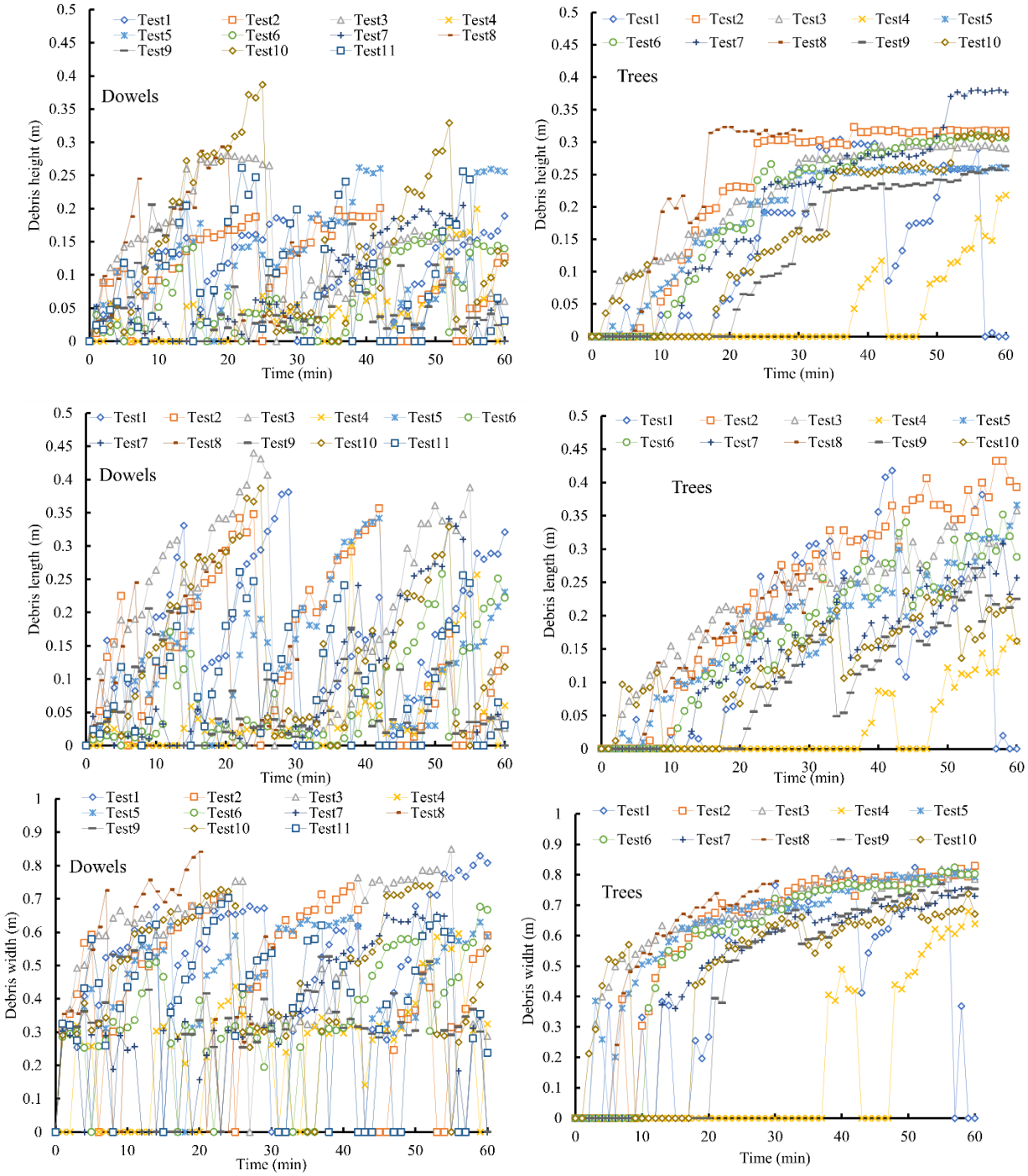

Figure S1 Evolution of debris jam in height h_d, in width w_d and in length l_d for both dowels and trees

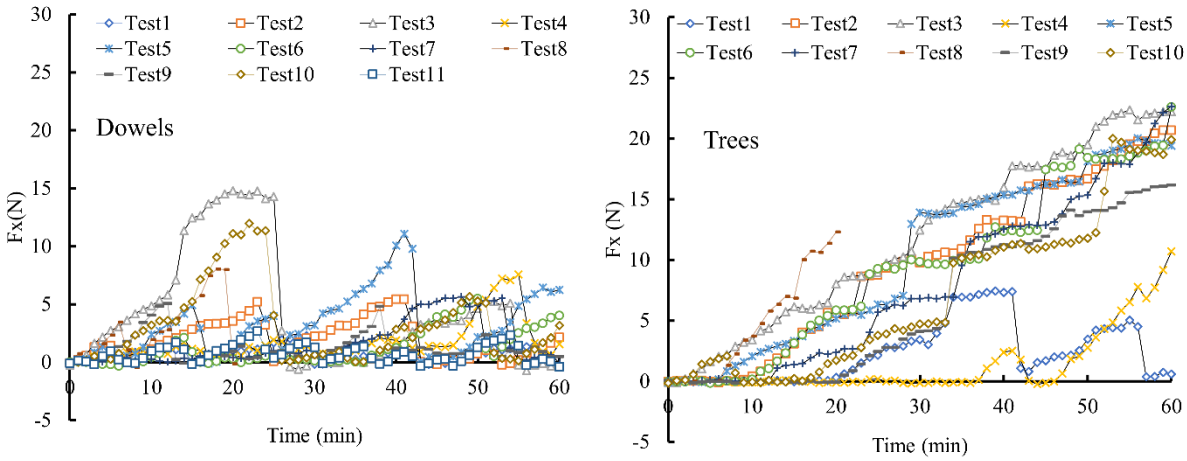

Figure S2 Evolution of loading on the pier for (a) dowels and (b) trees

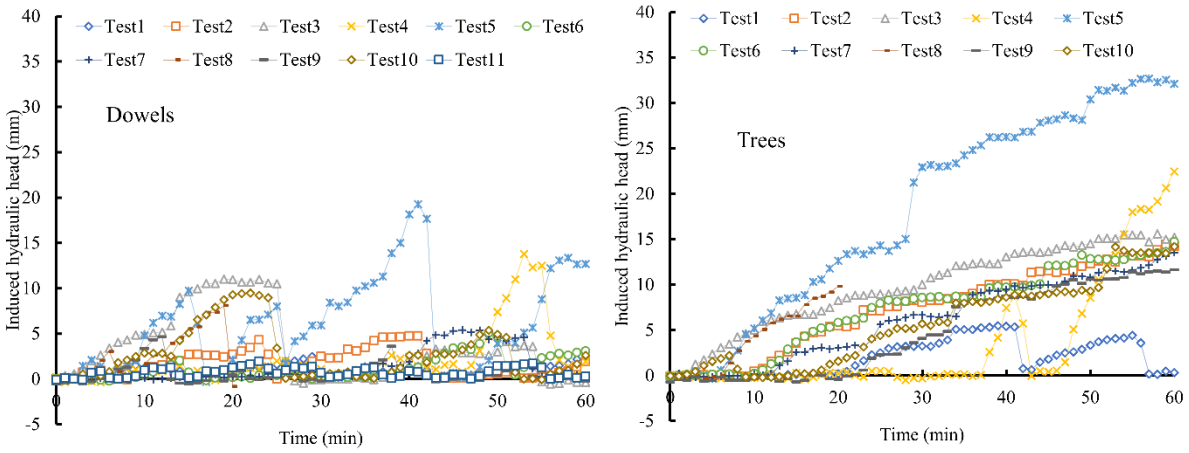

Figure S3 Evolution of the induced hydraulic head for (a) dowels and (b) trees

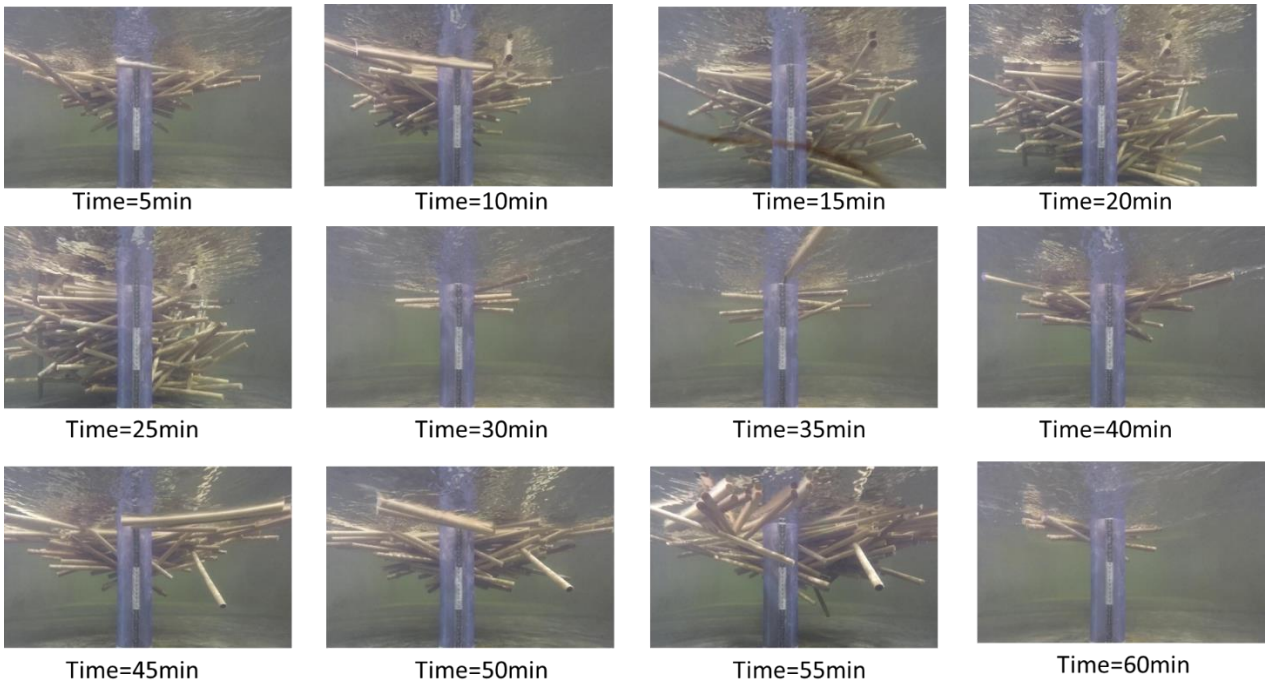

Figure S4 Evolution of dynamic debris jam of dowels of Test 3 from the behind GoPro camera

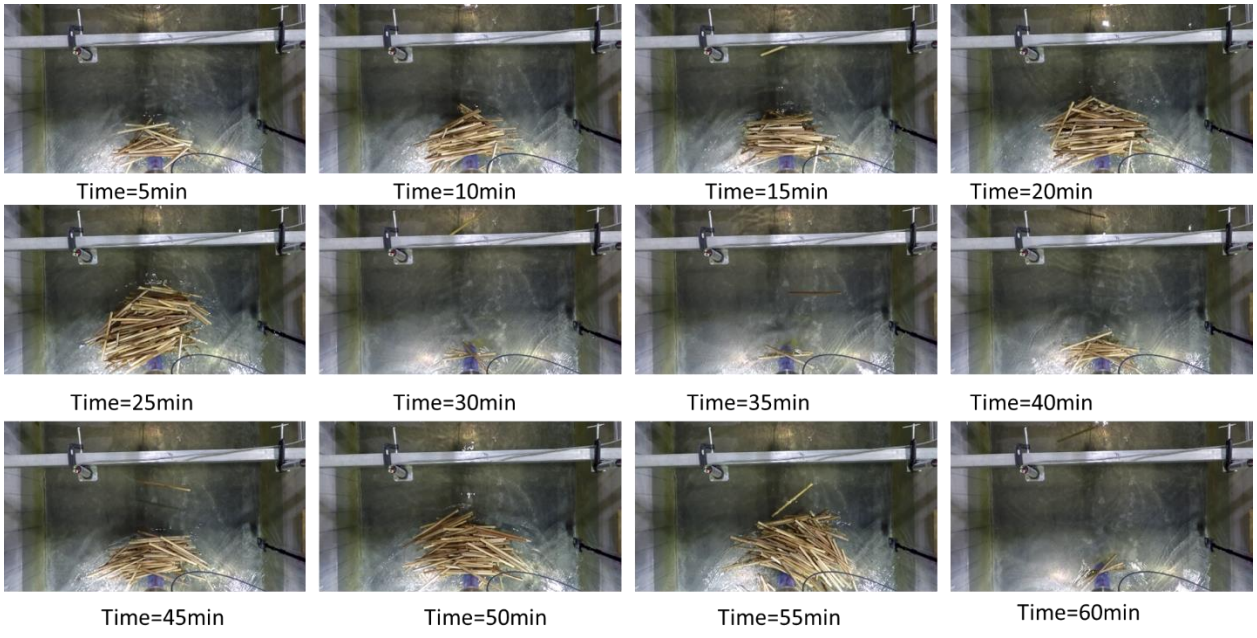

Figure S5 Evolution of dynamic debris jam of dowels of Test 3 from the top camera

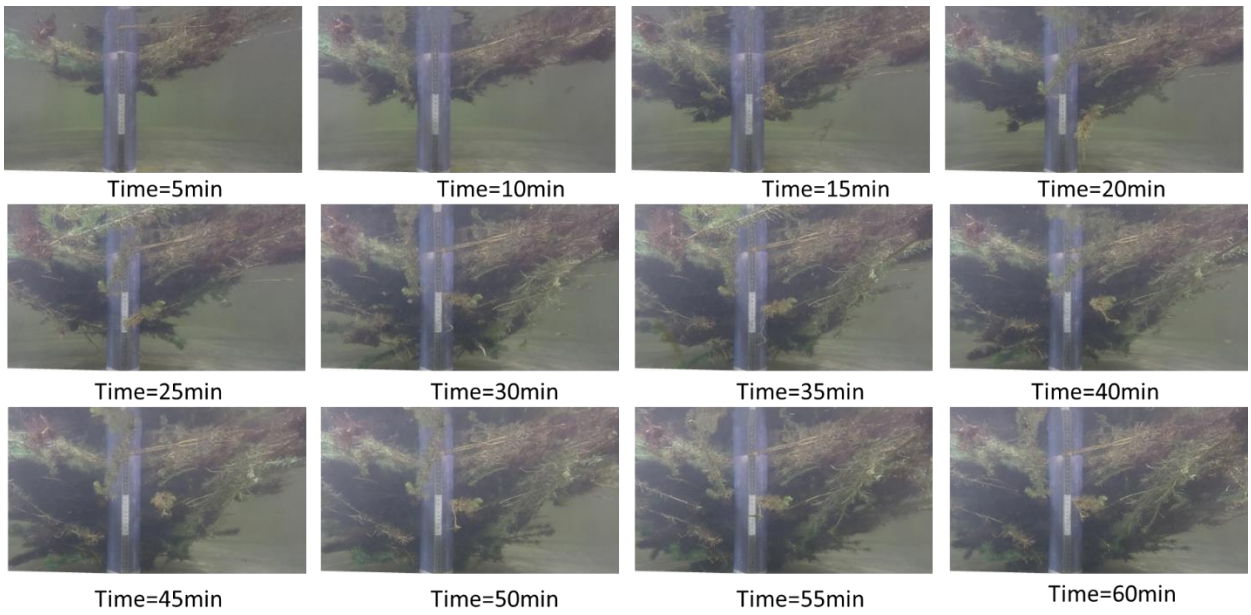

Figure S6 Evolution of dynamic debris jam of trees of Test 3 from the camera behind the pier

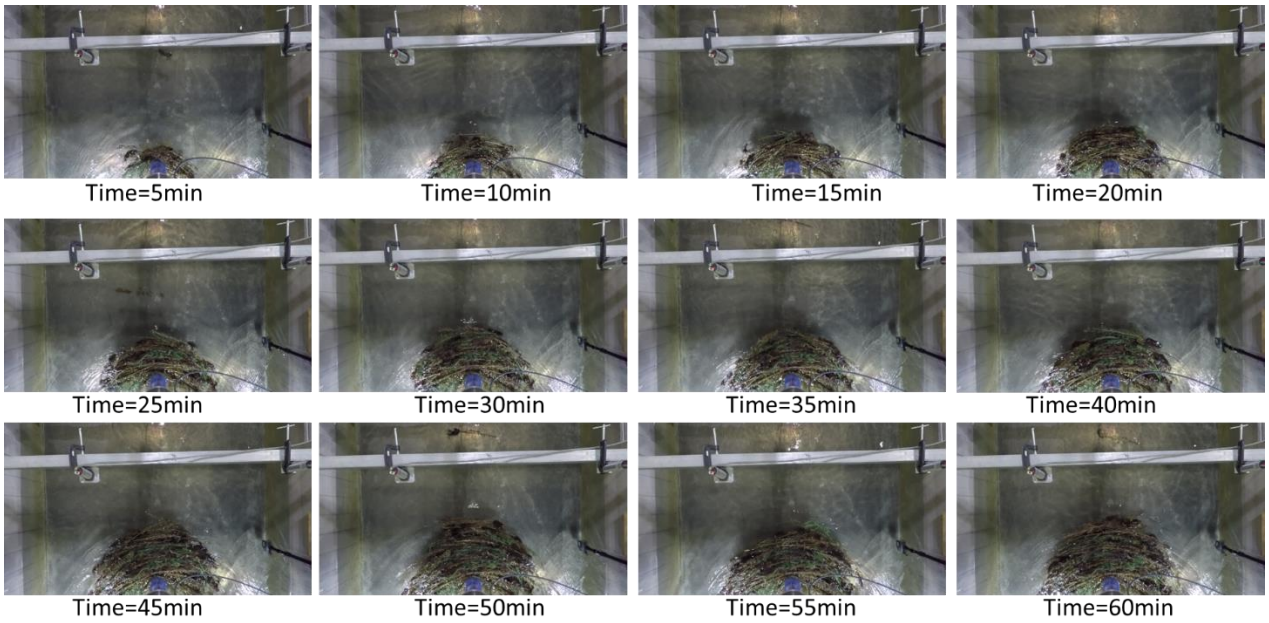

Figure S7 Evolution of dynamic debris jam of trees of Test 3 from the top camera